Pontifícia Universidade Católica
do Rio de Janeiro

Paulo Henrique Marangoni Feghali

Numerical Analysis and Experimental Mechanical Behavior of UHPC Beams with Optimized Cross-Section

Dissertação de Mestrado

Dissertation presented to the Programa de Pós-Graduação em Engenharia Civil of PUC-Rio in partial fulfillment of the requirements for the degree of Mestre in Engenharia Civil.

Advisor: Flávio de Andrade Silva

Co-Advisor: Pablo Augusto Krahl

Rio de Janeiro

April 2024

PONTIFÍCIA UNIVERSIDADE CATÓLICA
DO RIO DE JANEIRO

Paulo Henrique Marangoni Feghali

Numerical Analysis and Experimental Mechanical Behavior of UHPC

Beams with Optimized Cross-Section

Dissertation presented to the Programa de Pós-Graduação em Engenharia Civil of PUC-Rio in partial fulfillment of the requirements for the degree of Mestre in Engenharia Civil. Approved by the examination committee.

Flávio Andrade Silva
Advisor
Departamento de Engenharia Civil e Ambiental– PUC-Rio

Pablo Augusto Krahl
Co-Advisor
Universidade Presbiteriana Mackenzie – Campinas

Luís A. G. Bitencourt
University of São Paulo

Yi Shao
Co-Advisor
McGill University

Rio de Janeiro, April 10, 2024

Paulo Henrique Marangoni Feghali

Graduated in Civil Engineering from Universidade Federal do Rio de Janeiro – UFRJ in 2022.

Bibliographic data

Feghali, Paulo Henrique Marangoni

Numerical Analysis and Experimental Mechanical Behavior of UHPC Beams with Optimized Cross-Section / Paulo Henrique Marangoni Feghali ; advisor: Flávio Silva ; co-advisor: Pablo Krahl. _ 2024.

181 f. : il. color. ; 30 cm

Dissertação (mestrado)_Pontifícia Universidade Católica do Rio de Janeiro, Departamento de Engenharia Civil e Ambiental, 2024.

Inclui bibliografia

1. Engenharia Civil e Ambiental - Teses. 2. UHPC. 3. Ductilidade. 4. Elementos finitos. 5. Dano. I. Silva, Flávio. II. Krahl, Pablo. III. Pontifícia Universidade Católica do Rio de Janeiro. Departamento de Engenharia Civil e Ambiental. IV. Título.

CDD: 624

Acknowledgments

To my parents, who agreed to have me at home for a longer period than originally expected and always gave me the support to continue my journey as a researcher.

To Giovana for all the companionship during my entire life.

To my grandfather Jaurès for being my main inspiration in engineering and in life and to my grandmother Umbelina for always being such a warm figure during my life.

To Flávio and Pablo for all the help in developing this work and for being very present and patient supervisors during this entire year, with weekly meetings to decide the paths the study would take and discuss all the results.

To all the friends and technicians who divided the laboratory with me during the year of 2023 and helped me develop this study.

To all my friends from OLM, Santo Inácio, UFRJ, UTC and PUC.

To Luisa who accompanied me through great part of this journey.

To Conselho Nacional de Desenvolvimento Científico e Tecnológico – CNPq for the financial support to the research.

To FAPERJ for the financial support.

This study was financed in part by the Coordenação de Aperfeiçoamento de Pessoal de Nível Superior - Brasil (CAPES) - Finance Code 001.

Abstract

Feghali, Paulo Henrique Marangoni Feghali; Silva, Flávio; Krahl, Pablo. **Numerical Analysis and Experimental Mechanical Behavior of UHPC Beams with Optimized Cross-Section**. Rio de Janeiro, 2023. 181p. Dissertação de Mestrado _ Departamento de Engenharia Civil e Ambiental Pontifícia Universidade Católica do Rio de Janeiro.

Ultra-high performance concrete is a material which has been developed in the last decades to fulfill modern structures' need for a more resistant and durable material. Its highly nonlinear characteristics in both tension and compression leads to a complex behavior. In addition to that, the inhomogeneous distribution of the fibers and the high tensile strength when compared to conventional concrete result in reduced ductility for UHPC beams. Finite element analysis is shown to be an adequate tool to represent UHPC structural element's response but the model calibration must be correctly applied and coherent modeling techniques must be used to correctly model the post-peak branches of load-displacement curves for UHPC beams subjected to four-point load bending tests. An extensive material characterization in both tension and compression was conducted. Monotonic axial tests were conducted to obtain stress-strain curves in compression and stress-crack opening in tension and cyclic tests were made to determine the experimental damage evolution in compression and in tension. These data served as input to calibrate uniaxial models and damage evolution models according to analytical expressions available in the literature. Heterogeneous models simulating the material dispersion of the mechanical properties of the UHPC over structural beams were used to obtain a cross-section that presented optimized resistance while maintaining target ductility. Finally, five beams were tested, with different shapes and reinforcement ratios and the modeling strategies were benchmarked to the beams' experimental data.

Keywords

UHPC; Ductility; Finite element; Damage.

Resumo

Feghali, Paulo Henrique Marangoni Feghali; Silva, Flávio; Krahl, Pablo. **Análise Numérica e Comportamento Mecânico Experimental de Vigas de UHPC com Seção Transversal Otimizada**. Rio de Janeiro, 2023. 181p. Dissertação de Mestrado _ Departamento de Engenharia Civil e Ambiental Pontifícia Universidade Católica do Rio de Janeiro.

O concreto de ultra alto desempenho (UHPC) reforçado com fibras é um material que foi desenvolvido nas últimas décadas para atender à necessidade de estruturas modernas por um material mais resistente e durável. Suas características altamente não lineares tanto na tração quanto na compressão levam a um comportamento complexo. Além disso, a distribuição não homogênea das fibras e a alta resistência à tração, quando comparada ao concreto convencional, resultam em menor ductilidade para vigas de UHPC. A análise de elementos finitos mostra ser uma ferramenta adequada para representar a resposta de elementos estruturais de UHPC, mas a calibragem do modelo deve ser aplicada corretamente e técnicas de modelagem coerentes devem ser usadas para representar corretamente os tramos pós-pico de curvas força-deslocamento para vigas de UHPC submetidas a testes de flexão de quatro pontos. Foi realizada uma extensa caracterização do material tanto em tração quanto em compressão. Testes axiais monotônicos foram conduzidos para obter curvas tensão-deformação na compressão e tensão-abertura de fissura na tração. Testes cíclicos foram realizados para determinar a evolução do dano experimental em compressão e na tração. Esses dados serviram como referência para calibrar modelos uniaxiais e modelos de evolução de dano de acordo com expressões analíticas disponíveis na literatura. Modelos heterogêneos simulando a dispersão do material nas propriedades mecânicas do UHPC ao longo do volume das vigas foram utilizados para obter uma seção transversal que apresentasse resistência otimizada, mantendo a ductilidade desejada. Finalmente, cinco vigas foram testadas, com diferentes formas e porcentagens de reforço, e estratégias de modelagem foram comparadas aos dados experimentais das vigas.

Palavras-chave

UHPC; Ductilidade; Elementos finitos; Dano.

Figure List

List of Tables

SUMMARY

1 INTRODUCTION

1.1 Motivation

Due to its high strength and self-compacting nature, fiber reinforced ultra-high performance concrete (UHPC) has been employed in various situations. One great potential this material has if to reduce structural elements' cross-sections. Its enhanced mechanical properties make it possible to produce thinner beams and still withstand the same loads as ordinary beams. However, this material has a complex behavior leading to difficulties to describe its behavior.

In addition to reducing cross-sections, this material's superior tensile strength makes it possible to reduce steel reinforcements or even build unreinforced structural elements [1], where the only post-cracking tensile reinforcement is provided by the fibers inside the matrix. Because of that, very thin structural elements may be produced. However, structural safety may still be an issue because of ductility related problems [2]. Manufacturers take advantage of this potential to produce thin panels of unreinforced UHPC [3], [4], [5].

In addition to enhanced mechanical properties, UHPC has a superior durability due to increased crack resistance and denser packing, resulting in less penetration on moisture and chlorides [6].

Figure 1 illustrates the year-to-year evolution of articles mentioning UHPC in the title or keywords. Its strongly nonlinear behavior and reduced ductility at low reinforcement ratios, make numerical modeling a suitable methodology to represent its complex behavior.

To highlight the relevance of the material in recent decades, a simplified bibliometric analysis was conducted to quantify the number of UHPC articles published each year. Searches were performed in the SCOPUS and Web of Science scientific repositories. The search was conducted using the following search strings, with keywords appearing in the title, abstract, or keywords:

uhpc OR (ultra-high AND performance AND concrete)

- SCOPUS search: The search results were limited to the fields of "Engineering" and "Materials Science," returning a total of 7,180 articles.

- Web of Science search: The search results were limited to "Engineering Civil," "Construction Building Technology," "Materials Science Multidisciplinary," or "Materials Science Composites," returning a total of 2,472 articles.

The encountered bibliometric data was exported in CSV and BibTeX formats. Duplicates appearing in both databases were removed, and the data was imported into the Bibliometrix [7] package developed in the R language. Finally, the evolution of the number of publications per year was obtained using this tool. It was also observed that the countries with the highest number of publications on UHPC are China followed by the United States, Germany, and Canada. Figure 1 illustrates the progression of articles year by year, highlighting a significant increase in publications from the 2000s onwards, with a constant growth trend. Until this moment, Brazil has 53 published articles until this moment.

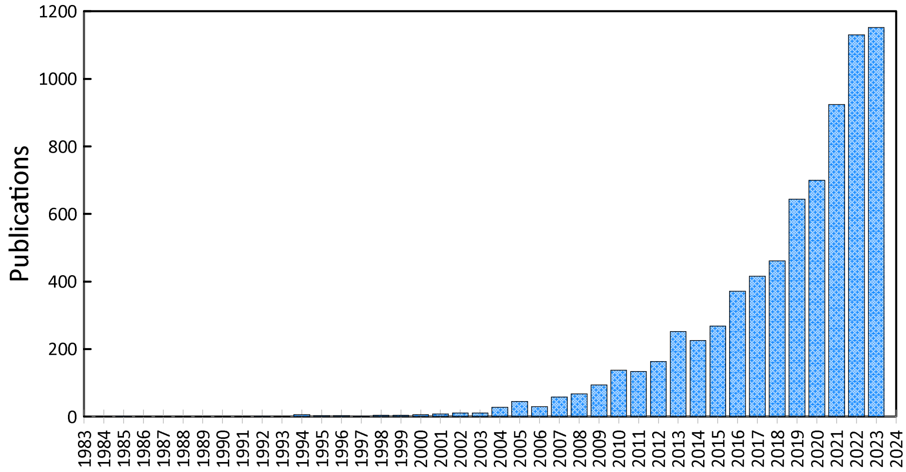

Figure 1 - Number of articles published worldwide by year mentioning UHPC in title, abstract or keywords (Source: Author).

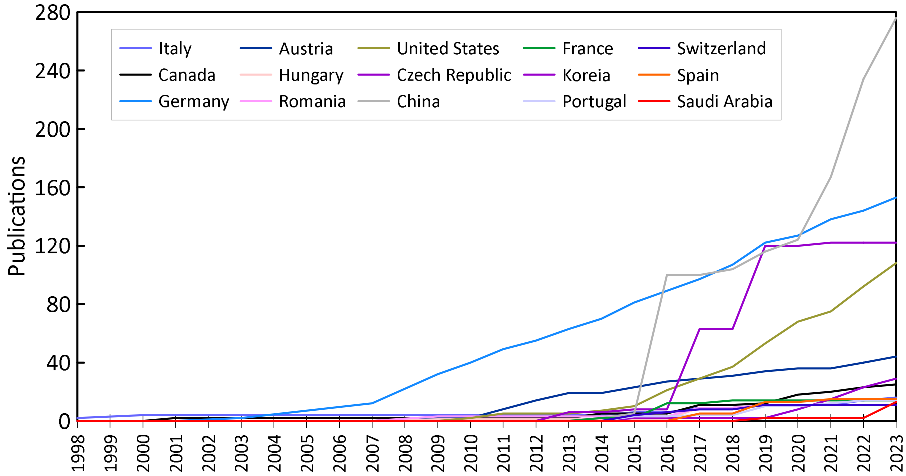

Figure 2 - Evolution of the number of publications year by year for the fifteen countries with the highest number of publications on UHPC (Source: Author).

Although China appears as the leading country in terms of the number of publications, the year-to-year evolution separated by each country (Figure 2) shows that this number comes from more recent articles, with China becoming the country with the highest number of publications only in 2020. France, Switzerland, and the United States are also notable among the countries with a high number of publications, with these being the first countries to present specifications for UHPC.

In order to assess the relevance of finite element modeling in this subject, a new search was conducted in the databases with a modification to the search string by adding keywords to obtain only articles that reference numerical modeling. The search was performed using the following modified search string:

(uhpc OR (ultra-high AND performance AND concrete)) AND (numerical OR (finite element))

Maintaining the same search refinements, the search on the SCOPUS database returned 1,498 articles, and the search on the Web of Science database returned 504 articles. This indicates that approximately 21% of the found articles for UHPC reference numerical models as a way to describe the complex behavior of this material. The temporal evolution shown in Figure 3 demonstrates that only from the year 2010 onwards did a significant number of publications involving numerical modeling emerge, approximately a decade later than the beginning of relevant publications on UHPC.

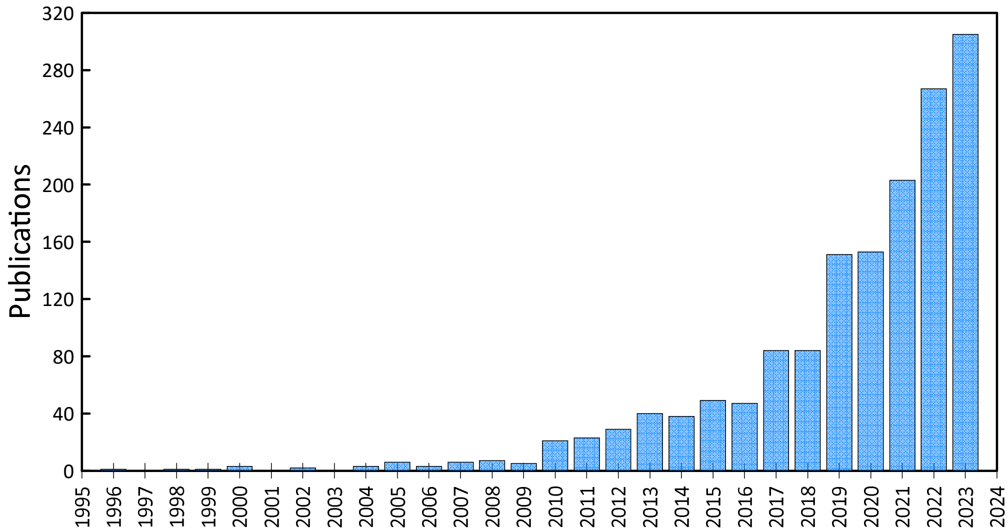

Figure 3 - Number of articles published worldwide by year mentioning UHPC and numerical models in title, abstract or keywords.

Bibliometric metadata was input into VosViewer [8] tool to generate word clouds for the set of articles on UHPC (shown in Figure 1) considering the time period before and after 2010. The following figures illustrate the clouds generated for the 50 most recurrent keywords in each case. In Figure 4 (a), which corresponds to the period before 2010, there is a predominance of terms related to the characterization of mechanical properties, such as "compressive strength," "deformation and ," "shrinkage"... and those related to material production, such as "fibers," "silica fume," "concrete mixes." In Figure 4 (b), the presence of the finite element method is connected to properties, such as "ductility," "bearing capacity," and to structural elements, such as "bridge decks," "concrete beams and girders," and "concrete slabs." The semantic difference in keywords illustrates a first phase related to articles on UHPC production and characterization at the material scale. In the second phase, a larger portion of articles at the structural level is observed, with the finite element method emerging as an important tool for describing the behavior of structural elements.

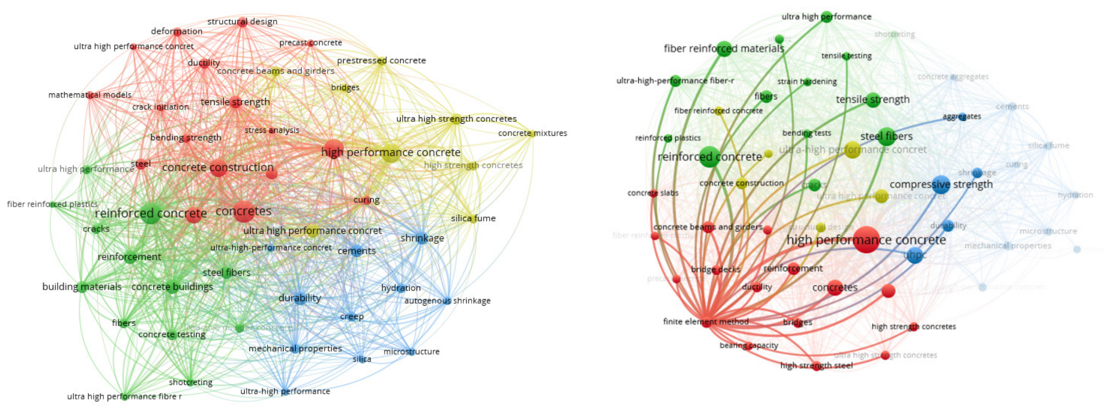

(a) (b)

Figure 4 – Word cloud for the fifty most recurring key-words in the set of articles published before 2010 (a) and after 2010 (b).

There is not one clear definition on what is the minimum compressive strength for UHPC, with different codes around the world specifying different compressive strengths. These standards are summarized in Figure 5, where it can be seen that standards such as the ASTM C1856 [9], CSA 23.1/2 [10] and SIA 2052 [11] consider as minimum compressive strength 120 MPa, while the French standard NFP18-470 [12] considers 130 MPa. Finally, the specifications from the Federal Highway association and the Japanese specification (JSCE) [13] consider 150 MPa for minimum compressive strength. It is worth noticing that even inside a same country, the American standard from ASTM and the FHWA [14] specifications diverge on the topic.

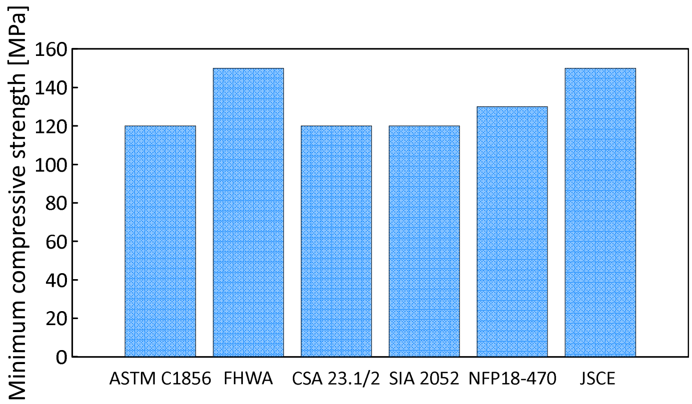

Figure 5 - Minimum compressive strength according to each standard.

1.2 Objectives

The objectives for this work are to conduct an extensive material characterization for the application in finite element models based in the "Concrete Damaged Plasticity" (CDP) constitutive model available in the Abaqus software. These models are then used for the optimization by genetic algorithms of a cross-section for UHPC beams to gain ductility with low reinforcement ratios.

A second experimental assessment is focused on testing the beams modeled in the numerical part of this study. A comparison of the experimental data and the numerical model results was performed to validate the strategy for numerical modeling of UHPC beams.

1.3 Structure of the work

This work is divided into five main parts, being the first one a comprehensive literature review (Chapter 2), where the main elements needed for the numerical modelling of concrete using the CDP material model are discussed, together with the mechanical properties and the corresponding testing methods for their determination, analytical models to describe uniaxial and damage evolution on UHPC and modeling strategies available on the literature.

Chapter 3 defines the modelling strategy used throughout the study, with random material properties being used to simulate the non-homogeneity of the properties in a beam's volume. Because at this point the material characterization was not completed yet, the optimization was made with the material properties from another study. Four beams are determined in this section as the beams to be tested in Chapter 5.

Chapter 4 describes the experimental program, passing through material level and structural level testing.

Chapter 5 shows the numerical study, passing through preliminary models to adjust the CDP parameters in compression and in tension. The material models used in Chapter 3 are recalibrated using the material properties determined in Chapter 4. Finally, the beams are modeled and the models' outputs are compared to the experimental data.

Chapter 6 presents the conclusions on the final remarks and the suggestions for future works.

2 LITERATURE REVIEW

2.1 Uses of UHPC in the Industry and the State of the Art

Although the construction industry may take more time than other industries to incorporate new technologies, UHPC has already been used in multiple scenarios. The website of the Federal Highway Administration, the agency responsible for managing federal highways in the United States, provides a compilation of all bridges in service in the country that use in some way UHPC elements. The location of each of these structures is shown in Figure 6 (a). Among the applications listed are: connection between prefabricated elements, bridge deck overlays, repairs of existing beams, repairs of connections between prefabricated elements, pre-stressed UHPC beams, pre-stressed UHPC piles, precast bridge decks and small localized repairs.

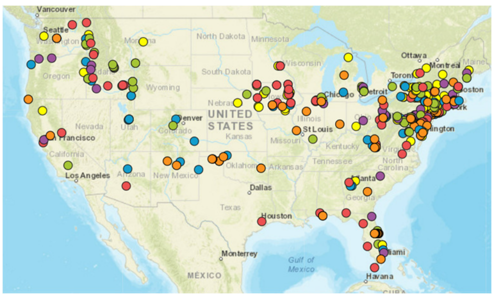

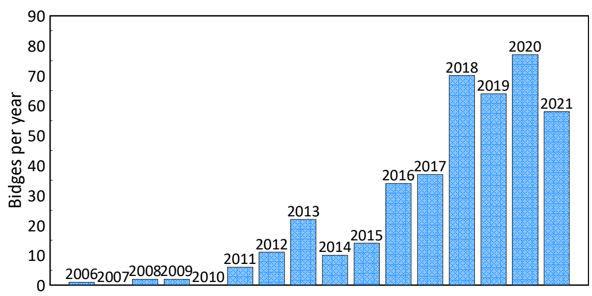

(a) (b)

Figure 6 - Projects using UHPB in bridges according to the Federal Highway Association [USA], spatial (a) and temporal (b) distribution [https://highways.dot.gov/research/structures/ultra-high-performance-concrete/deployments].

The histogram presented in Figure 6 (b) shows the evolution through time of these projects, with the first listed UHPC project in bridge structures initiated in 2006 in the USA. There is a notable increase starting from 2018, with the total number of projects in each year after 2018 approximately double that observed for 2016 and 2017.

The replacement of conventional concrete beams with UHPC beams results in elements with a smaller cross-sectional area, potentially leading to material savings and a reduction in the self-weight of structures. Lima et al. [2] demonstrated that rectangular UHPC beams, with approximately half the width of the cross-section, can withstand loads equivalent to those of conventional concrete beams. Figure 7 presents a diagram created by the manufacturer Lafarge Holcim, comparing the dimensions of conventional reinforced concrete beams, pre-stressed concrete, and steel beams with UHPC beams.

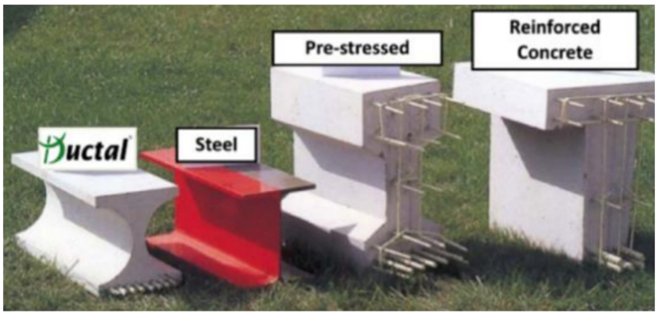

Figure 7 - Size comparison between conventional reinforced concrete, pre-stressed concrete, steel and UHPC girders to withstand the same load.

Azmee and Shafiq [15] list some of the notable projects which used UHPC around the world. The Sherbrook pedestrian bridge, located in Canada, being completed in 1997 (Figure 8 (a)), the Bourg-Les-Valence Viaduct, completed in 2001 in France (Figure 8 (b)), and the Seonyu Pedestrian Bridge, built in South Korea having the world's longest span using UHPC, measuring 120 meters (Figure 8 (c)).

(a) (b) (c)

Figure 8 - UHPC notable projects: Sherbrook pedestrian bridge (a), Bourg-les-Valence viaduct (b) and Seonyu arch (c) [15].

Some projects that used UHPC as reinforcement for existing structures are shown on the Ductal manufacturer's website. Among them, notable examples include the Yunnan Bridge, located in the Honghe province, China, which employed a layer of UHPC on the bridge deck to enhance its durability (Figure 9 (a)), and the Chillon Viaduct in Switzerland, where a UHPC layer was adopted on the slab to restore the load-carrying capacity of the element after damage caused by heavy vehicle traffic (Figure 9 (b)).

(a) (b)

Figure 9 - Bridge deck overlays in Switzerland (a) and China (b) [16].

The state-of-the-art research on finite element modeling of ultra-high performance concrete beams was conducted by gathering all articles from the last five years that mentioned "UHPC," "beams," and "finite element" or "numerical." The topics encountered are discussed as follows.

Articles addressing the application of UHPC in pre-stressed elements include full-scale bending tests of pre-stressed UHPC beams with spans ranging from 30 m [17] to 60 m [18] involving box and PI girders [17]. Li et al [19] investigated the effects of UHPC anchorage zones, highlighting a reduction in cracking due to concentrated forces.

The application of UHPC in composite beams has been studied in three contexts. In a more conventional approach, UHPC is considered as a collaborating deck in the compressed part, as explored by Zhu et al. [20], who investigated UHPC composite beams with a collaborating deck composed with a ribbed slab. Liu et al. [21] studied the effects of composite slabs consisting of precast slabs in conventional concrete and UHPC cast in situ. Another application in composite beams involves using UHPC as reinforcement in negative moment zones over supports, aiming to reduce tensile concrete cracking, enable moment redistribution, and limit deformation [22] [23] [21] [24] [20]. The third application in composite beams involves studying the interaction of different types of shear connectors and their behavior when embedded in UHPC [25] [26] [27] [28] [29].

Studies related to precast elements primarily focus on both the elements as well as on their connections. Baghdadi et al. [30] investigated different types of connections subjected to bending moments, Deng et al. [31] for the connection of precast beams in multi-beam decks, and Xue et al. [32] for connections between precast beams and columns subjected to seismic forces. Additionally, there are studies on the manufacturing of precast elements in UHPC, such as precast slabs studied by Mahdi et al. [33], and precast molds in the form of U-shaped beams that are retained as part of the structural element after concrete consolidation with conventional concrete poured in the inner part of the element [34].

Studies on UHPC-filled columns aim to increase load capacity and ductility for tall building columns while maintaining reduced section elements due to the enhanced strength of UHPC under confinement [35] [36] [37].

2.2 UHPC mix design

Ultra-high performance concrete (UHPC) allies great compressive strength with higher tensile strength compared to normal concrete (NC) and good durability. To achieve these excellent mechanical properties, UHPC mixes make use of low water-to-binder ratios, high cement consumption, and optimized packing densities. Usually supplementary cementitious materials are used in the mixes, such as pozolanic materials and optimized granulometric distribution is achieved by the use of mineral fillers. The low water-to-binder ratio is achieved without losing concrete's workability through the use of superplasticizers and water reducing agents.

UHPC minimum compressive strength vary by authors. While some authors state that compressive strength must be greater than 120 MPa [38], others assume it must be greater than 150 MPa [6]. In the selected papers for the literature review, the minimum compressive strengths considered for UHPC were 103 MPa [39],109 MPa [40], and 119 MPa [41], being below the specified minimum of 120 MPa. The maximum encountered compressive strength was 197 MPa [42].

UHPC's water to binder ratio ranges up to 0,25 [43]. Table 1 shows mass proportions for UHPC mixes for the selected articles. For these studies, water-to-cement ratio ranges from 0,12 to 0,298 [44]. The authors used supplementary cementitious materials, such as pozzolanic binders and hydraulic cements in addition to Portland cement as main binder.

Table 1 - Mass proportions for UHPC mixes.

Authors	Class	Water	Cement	Specification	Silica fume	Sand	Filler	Furnace Slag	Water reducer	W/b
Mahdi et al. [33]	C110	0.12	Sulfate	Sulphate resistant cement	0.21	1	-	-	0.06	0.12
	C100	0.19	1	Sulphate resistant cement	0.226	1	-	-	0.045	0.155
	C10	Sulfate	1	Sulphate resistant cement	0.226	1	-	-	0.045	0.155
Singh et al. [45]	C140	Sulfate	1	Sulphate resistant cement	0.266	1	-	-	0.045	0.141
Bahraq et al. [46]	C150	0.181	1	-	0.24	1.117	-	-	0.044	0.145
Li et al. [47]	C120	0.2	1	Portland Cement	0.25	1.1	0.3	-	0.02	0.160
Feng et al. [48]	C150	0.18	1	Portland Cement	0.37	1.1	0.25	-	0.04	0.131
Paschalis et al. [44]	C130	0.298	1	-	0.23	1.695	-	0.7	0.095	0.155
Sun et Liu [49]	-	0.2	1	-	0.3	1.34	0.3	-	0.013	0.154
Basha et al. [50]	C130	0.235	1	-	0.18	0.512	-	0.349	0.012	0.154
Teng et al. [22]	C120	0.233	1	-	0.14	0.792	-	0.43	0.034	0.204
Wang et al. [51]	C140	0.2	1	P·II 52.5 Portland cement	0.25	1.1	-	-	0.05	0.160
Gao et al. [52]	C140	0.24	1		0.3	1.34	0.3		0.018	0.185

As supplementary materials, all authors on Table 1 used silica fume, in mass proportions ranging from 0.17 to 0.37 of the cement mass. Bajaber and Hakeem [6] recommend the use of silica fume between the limit interval from 10% to 30% of the cement mass. Paschalis et al. [44], Basha et al. [50] and Teng et al. [53] specified additional hydraulic cement in the form of furnace slag to the mix. The water-to-binder ratio was computed for the mixes in Table 1 and its correlation to the compressive strength is shown in Figure 10, with the clear tendency of smaller w/b ratios resulting in higher compressive strengths [38] and all w/b ratios being under the upper limit specified in ACI 239R.

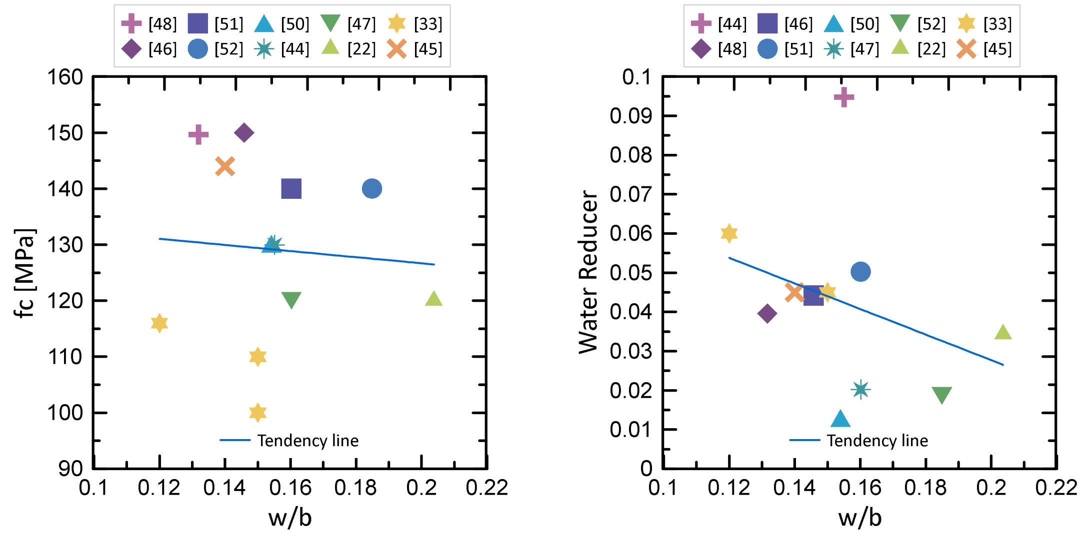

(a) (b)

Figure 10 - Correlation between compressive strength (a) and water reducer (b) with the water to binder ratio.

Due to the loss of workability for low w/b ratios, UHPC mixes use water reducing agents to maintain fluidity of the concrete mix in the fresh state. Figure 10 (a) shows the correlation between lower w/b ratios and higher compressive strengths for the mixes listed in Table 1. Figure 10 (b) shows mass proportions of water reducing agents ranging from 1.2% up to 9% of the cement mass, but mean value is 3.5%, with the correlation between lower w/b ratios and higher mass consumption of superplasticizers, resulting in clear inverse relation.

Fine aggregates used in the mixes comprised river sand, regular quartz sand and fine quartz sand. Gao et al. [52], Paschalis and Lampropoulos [44], Li et al . [47], Shi et al. [39] and Sun and Liu [49] all used quartz powder as mineral filler for denser packing.

Table 2 shows fiber specification for each author. All studies used steel fibers with aspect ratios ranging from 65 up to 100. UHPC mixes usually specify fiber contents around 2%, [51] [52] , but fiber contents as low as 1% until 3% were found on the studies.

Table 2 - Fiber properties used in the UHPC mixtures.

Authors	Fiber content (volume)	Specification	Aspect ratio	Fiber Factor
Mahdi et al. [33]	2.25%	Steel 35mm length 0.6mm diameter	64.00	1.44
Bahraq [46]	1.70%	Equal mass of straight and hooked	-	-
Li et al. [47]	2.00%	Steel 13 length 0.15mm diameter	86.67	1.73
Feng et al. [48]	-	Steel 16 length 0.2mm diameter	80.00	-
Paschalis [44]	3.00%	Steel 13 length 0.16mm diameter	81.25	2.44
Sun et Liu [49]	-	Steel 16 length 0.2 mm diameter	80.00	-
Basha [50]	1.90%	Steel 12 length 0.12 mm diameter	100.00	1.90
Teng et al. [53]	1.70%	Steel 13mm length 0.2 mm diameter	65.00	1.11
Wang et al. [51]	2.00%	Steel 13mm length 0.2 mm diameter	65.00	1.30
Xiao-Long [52]	2.00%	Steel 16 length 0.2 mm diameter	80.00	1.60
Kahdin et al. [54]	1.50%	Steel 13 length 0.16 mm diameter	81.25	1.22
Yuan et al. [53]	2.00%	Steel 13mm length 0.2 mm diameter	65.00	1.30
Sakr et al. [55]	2.00%	Steel 30mm length 0.8 mm diameter (hooked)	37.50	0.75

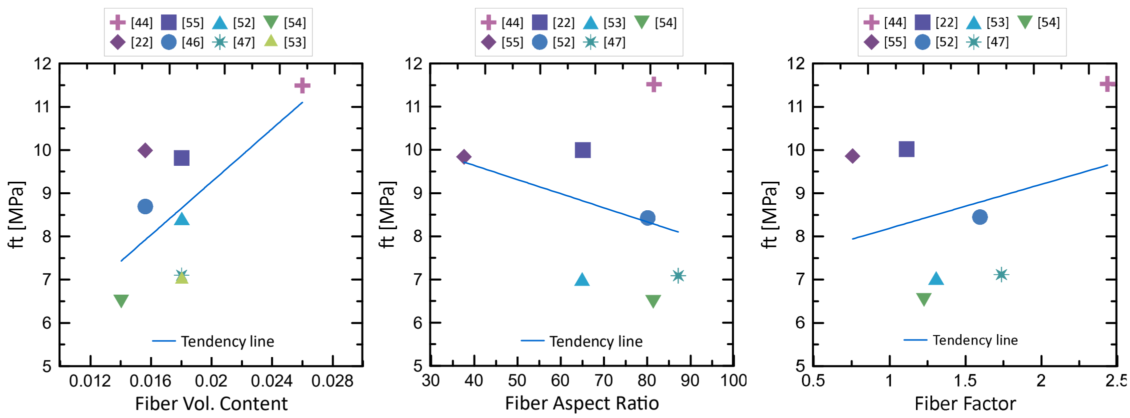

(a) (a) (c)

Figure 11 – Tensile resistance x fiber content (a) and tensile resistance x fiber aspect ratio (b) and tensile strength x fiber factor (c).

Figure 11 (a) plots the relation between tensile strength and fiber volumetric content and shows the relation where an increase in fiber content results in growth in tensile strength. Although Figure 11 (b) shows the inverse relation between the tensile strength and aspect ratio, with lower aspects ratios resulting in higher tensile strengths, Yang et al. [56] found that the tensile strength of UHPC increased with an increase in aspect ratio when the aspect ratio is within a reasonable range of less than 100.

Yang et al. [56] recommend the fiber factor as a more accurate indicator of the fibers influence on concrete, being the product of the fiber volume and the aspect ratio. Figure 11 (c) shows the correlation between fiber factor and tensile strength for the UHPC mixes listed in Table 2.

With respect to fiber aspect ratios, only one author used fibers with lower aspect ratio (37.50), corresponding to hooked fibers [55].

2.3 Uses of numerical models for specific for UHPC beams

A wide variety of concrete models were used on the selected articles and were able to simulate concrete behavior to certain degree of precision. These models predict permanent strains through fracture mechanics and material degradation through damage evolution, being the material damage evolution a factor for the analysis.

Among the categories of finite element models for modeling fiber-reinforced concrete, two types of categories can be listed. The first type refers to the explicit presence of fibers in the model, through truss or beam elements. Meso-scale models such as the ones developed by Wang et al. [51] model the concrete through tree-dimensional solid elements and the fibers through two-node truss elements. Hussein and Ahmed [57] list as mains steps for building meso-scale models (1) create a grid of points and connect them randomly with 2-node element trusses, (2) duplicate the nodes and generate the matrix elements through solid elements, (3) connect the original nodes and the duplicated nodes with non-linear springs to model the interfacial relation between the fibers and matrix.

These models can be used to study complex results due to fiber alignment in specific directions and other phenomena that arise due to fiber dispersion. The meso-scale models counterpart category are the macro-scale models. These models use as input material parameters that simulate the composite response of the fibers and matrix working together. These models are the most frequent in the literature because they are simpler to model and require less refined finite element mesh (Table 3).

From the perspective of representing cracking in concrete, two other categories of models can be identified. Rots and Blaauwendraad [58] divide models as "discrete crack models," where cracks are physically modeled by a discontinuity in the displacement field, and the separation between solid elements is controlled by interface elements. An alternative is the "smeared crack model" approach which represents concrete cracking through equivalent deformations, without a discontinuous representation.

The articles that include numerical models make reference to various commercial softwares with different implemented material models. Among the listed models are SBETA [59] implemented in the ATENA software, Karagozian and Case [60] implemented in the LS-DYNA software, Drucker-Prager based model in the Ansys software , Concrete 02 implemented in the OpenSees software, Disturbed Stress Field in the Vector 2 [61]software, Extended Finite Element Method in XFEM, and the most widely used model in the found articles, the "Concrete Damage Plasticity" [62] implemented in the Abaqus software.

Table 3 lists the material models, element types and corresponding mesh sizes used by each author. It can be seen that the smeared crack macroscale models found in the literature (CDP, SBETA, Karagozian and Case) adopted a less refined mesh, ranging from 10 to 30 mm, while the meso scale model developed by Wang et al. [51] required a mesh up to 2 mm and the non-local phase field model developed by Yuan et al. [53] needed a 0.5 mm discretization.

The implementation of the Drucker-Prager model in the Ansys software (version 17.2 or higher) exhibits behavior similar to traditional Drucker-Prager models, with improvements related to different failure criteria for tension and compression, nonlinear responses to compression, strain-softening/hardening in tension, and definition of post-cracking behavior. The Karagozian and Case model implemented in the LS-DYNA software is a simpler model with the only input parameter being compressive strength, with all other parameters obtained through internal conversions. The SBETA model implemented in the ATENA software presents its own uniaxial constitutive models. The "Concrete 2" and "Steel 01" models implemented in the OpenSees software are simplified models and cannot successfully represent strain-softening/hardening, crack opening, or sliding at the concrete-reinforcement interface. The model based on the Extended Finite

Element Method can accurately reproduce crack evolution but is dependent on the pre-definition of possible crack patterns and complex refinement techniques [53].

Table 3 – Material models, element types and corresponding mesh sizes found in the literature.

Authors	Material Model	Element Type	Mesh Size
Selim et al. [41]	CDP	8-node brick (C3D8R)	10 mm
Paschalis and Lampropoulos [44]	SBETA	8-node element	-
Mansour et al. [55]	CDP	8-node brick (C3D8R)	30 mm
Yin et al. [42]	Karagozian e Case	-	-
Sun and Liu [49]	-	8-node brick (C3D8R)	
Kadhim et al. [54]	Druker-Prager	8-node brick (SOLID 65)	20-25 mm
Bahraq et al. [46]	CDP	8-node brick (C3D8R)	-
Feng at al. [48]	CDP	8-node brick (C3D8R)	10 mm
Yuan et al. [53]	Concrete02/Steel01	Fiber discretized	800 fibers
Yuan et al. [53]	Nonlocal phase-field model	-	0.5 mm
Franssen et al. [63]	Disturbed Stress Field Model (DSFM)	2D quadrilateral	
Zhang et al. [64]	CDP	8-node brick (C3D8R)	30 mm
Song et al. [65]	CDP	-	
Basha et al. [50]	CDP	-	
Shi et al. [39]	CDP	8-node brick (C3D8R)	20 mm
Wang et al. [51]	Smeared crack model	8-node brick + discrete fibers	1-2 mm
Gao et al. [52]	CDP	8-node brick (C3D8R)	-
Elsanadedy et al. [40]	Model type 159 (continuous surface cap model)	8-node element	10-25mm

Table 4 - CDP parameters used by each author.

Author	Eccentricity	Stress ratio	Shape factor	Viscosity parameter	Dilation angle
Selim et al. [41]	0.1	1.16	0.667	0.001	36
Mansour et al. [66]	0.1	1.14	0.6667	-	38
Feng et al. [48]	0.1	1.16	0.6667	0.005	30
Zhang et al. [64]	0.1	1.16	0.667	-	33
Basha et al. [50]	0.1	1.16	0.667	-	45
Gao et al. [52]	0.1	1.07	-	0.01	54

Models based on Concrete Damaged Plasticity implemented in the Abaqus software depend on the definition of plasticity parameters, including dilation angle, viscosity parameter, equi-biaxial stress ratio, shape factor and eccentricity. Table 4 summarizes the parameters found in the literature review. Along with the CDP parameters, the CDP models need the definition for stress-strain curves and damage evolution curves in both tension and compression.

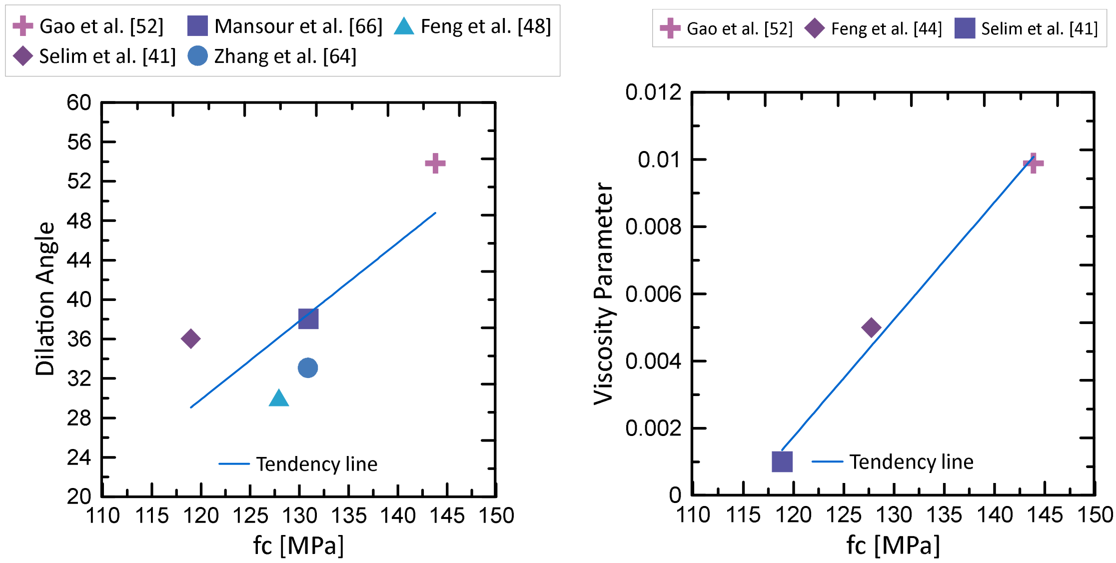

(a) (b)

Figure 12 - Relations between the CDP parameters of dilation angle (a) and viscosity parameter (b) with compressive strength.

Jabbar [67] studied the influence of parameters in the Concrete Damaged Plasticity (CDP) model on load-displacement curves for beams subjected to four-point load bending tests. It was observed that changes in eccentricity, shape factor, and equibiaxial ratio resulted in little influence on the obtained curves. From all the CDP parameters, dilation angle and viscosity parameter showed the greatest influence on the obtained curves and should be calibrated for each model. For dilation angles exceeding 30º, higher values lead to greater peak loads and corresponding displacements. An increase in the viscosity parameter also results in higher peak loads and displacements. Figure 12 (a) illustrates the relationship between compressive strength and dilation angle, and Figure 12 (b) illustrates the relationship between compressive strength and the viscosity parameter for the articles listed in Table 4. The tendency lines in Figure 12 show a relation in which higher resistance concretes imply in higher values for dilation angle and viscosity parameter.

Concrete Damage Plasticity (CDP) models often result in difficult convergence in the post-peak branch, with higher values for the damage variables. Because of that, specific techniques are necessary to ensure numerical convergence for obtaining consistent load-displacement curves. Bahraq et al. [46] employed explicit analysis to ensure convergence through a high number of small increments. The loading was configured to be applied within one second with the application of the "mass scaling" technique. Yuan et al. [53] used explicit analysis combined with the "nonlocal-phase field" model. Kadhim et al. [54] ensured model convergence through the use of a nonlinear iterative procedure based on the Newton-Raphson method. The load was applied in small steps to ensure simulation convergence.

Table 5- Bond consideration between rebar and concrete.

Author	Bond Consideration	Interface adopted in the model
Paschalis and Lampropoulos [44]	CEB FIB Model Code 90 [68]	Bond Slip
Mansour et al. [66]	Perfect bond	Embedded
Kadhim et al. [54]	Perfect bond	Merged nodes
Bahraq et al. [46]	Perfect bond	Embedded
Feng et al. [48]	Perfect bond	Embedded
Zhang et al. [64]	Perfect bond	Embedded
Yuan et al. [53]	Perfect bond	-
Shi et al. [39]	Perfect bond	Embedded

For rebar modelling, Mansour et al. [66], Kadhim et al. [54], Baraq et al. [46], Feng et al. [48], Zhang et al. [64], Shi et al. [39], Gao et al. [52] and Elsanadedy et al. [40] all used two node truss elements to model the beams' steel reinforcement. Mansour et al. [66], Bahraq et al. [46], Kadhim et al. [54], Feng et al. [48], Yujie et al. [64] and Shi et al. [39] considered the bond between steel reinforcement and concrete by means of a perfect bond considering "Embedded" constraint in Abaqus. Kahdin et al. [54] also considered a perfect bond constraint through the merged nodes tool in Ansys software. Paschalis et al. [44] considered the CEB FIB Model Code 90 for concrete-rebar bond strength through means of a bond-slip model. Table 5 shows each author's consideration for concrete-reinforcement bond.

2.4 Material characterization for CDP models

The finite element models used for UHPC simulations are based mainly on three steps: (1) Mechanical characterization through compressive and tensile tests and determination of concrete's post peak behavior in compression and post-crack in tension; (2) Selection of uniaxial constitutive models for concrete and steel in compression and in tension to match mechanical characterization; (3) Model calibration to take into account material's specificities, set deformations, mesh convergence and model accuracy.

Uniaxial curves created for conventional concrete usually cannot model precisely UHPC, leading to unreal peak deformations, overestimating elastic modulus and misleading post-peak behavior due to disregarding the fibers' influence in strain hardening/softening branches.

Table 6 - Experimental compressive strength with corresponding compressive test and selected compressive uniaxial model.

Authors	Experimental Compressive Strength [MPa]	Compressive Test	Uniaxial Model - Compression
Selim et al. [41]	119	Cubic (150 mm)	-
Paschalis and Lampropoulos [44]	136.5	Cubic (100 mm)	SBETA
Mansour et al. [66]	131	-	Zheng et al. [69]
Yin et al. [42]	153 -197	-	Internal Karagozian & Case implemented
Kadhim et al. [54]	133-140	-	Graybeal (Bilinear)
Bahraq et al. [46]	151,4	Cubic (50 mm)/Cylinder	Implemented experimental data
Feng et al. [48]	128	Cubic (100 mm)	Feng and Li [48]
Yuan et al. [53]	129	Cubic (100 mm)	OpenSees Implemented
Franssen et al. [63]	200	-	Vector 2 Implemented
Zhang et al. [64]	100-180	-	Lu et al. [70]
Song et al. [65]	144	-	Prem et al. [71]
Shi et al.[39]	103	Cubic (150 mm)	Parabolic
Gao et al. [52]	144.1	Cubic (100 mm)	Yang [72]
Elsanededy et al. [40]	109	Cylindric (150 × 300 mm))	-

Compressive and tensile strength of concrete should be determined through corresponding testing. Wang et al. [51] studied size effect on mechanical properties of UHPC specimens including compressive and tensile strength and flexural properties on notched prisms. Yuan et al. [53] tested the same concrete formulation on cubic and cylindrical specimens, encountering compressive strengths of 129.7 MPa for cubical specimens with 100 mm edges and equivalent compressive strength of 108.9 MPa for cylindrical specimens. Table 6 shows the correspondence between each authors concrete's compressive strength, the test specimen configuration and the uniaxial compressive model used for the finite element model. All authors except Elsanadedy [40] used cubic compressive test specimens ranging from 50 mm to 150 mm. Elsanadedy et al. [40] used cylindrical 150 x 300 mm specimens. Bahraq et al. [46] used cubic and cylindrical specimens for testing and implemented the the compressive uniaxial stress-strain curves after specimen's exposure to different temperature experimental data directly into the model. Selim et al. [41] determined experimentally to account for thermal damage on UHP-ECC to account for damage in PE fibers.

Table 7 shows the expressions for the uniaxial models used in the articles found in the literature. These are the models developed by Yang [72], Zheng [69], Lu [70], Feng [48] and Mansur [73].

Figure 13 shows the curves generated from the compressive uniaxial models listed in Table 7. These models being empirically determined formulas, all of them show a linear behavior for lower stress values followed by a nonlinear regime until peak load and a softening branch at post-peak. What differs these models are the estimates for initial modulus of elasticity, peak deformation and the inclination of the post-peak branch, with some of the models leading to a faster strain-softening than others. Models such as the one developed by Mansur [73] correlate the softening regime with the fiber properties and fiber content, with higher fiber contents leading to slower softening at post-peak.

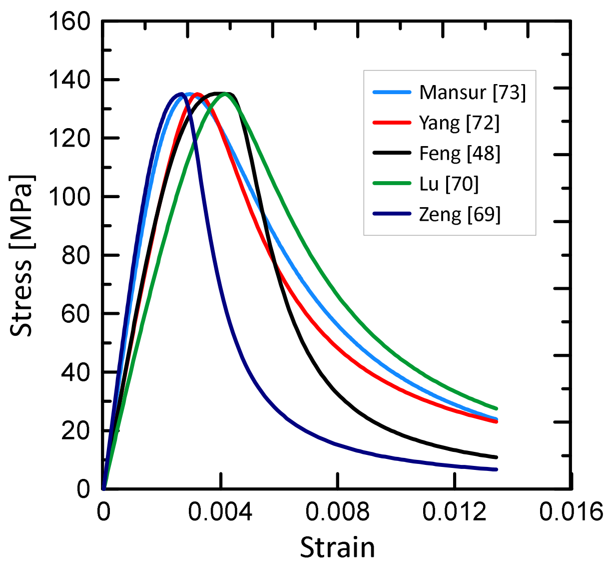

Figure 13 - Superposition of the curves for the models exhibited in Table 7.

Table 7 - Uniaxial compressive models found in the literature.

Uniaxial compression model	Expression
Yang (2007) [72]	$\sigma_c = \begin{cases} f_{cu}\dfrac{n\xi - \xi^2}{1+(n-2)\xi} & (0 < \varepsilon_c < \varepsilon_{co}) \\ f_{cu}\dfrac{\xi}{2(\xi-1)^2+\xi} & (\varepsilon_{co} < \varepsilon_c < \varepsilon_{cu}) \end{cases}$ $\xi = \dfrac{\varepsilon}{\varepsilon_{co}}; n = \dfrac{E_c}{E_{cs}}; E_{cs} = \dfrac{f_{cu}}{\varepsilon_{co}}$
Zheng et al. (2011) [69]	$\sigma_c = f_c\left(\left(\dfrac{1.55\varepsilon_c}{\varepsilon_0}\right) - 1.20\left(\dfrac{\varepsilon_c}{\varepsilon_0}\right)^4 + 0.65\left(\dfrac{\varepsilon_c}{\varepsilon_0}\right)^5\right) 0 \leq \dfrac{\varepsilon_c}{\varepsilon_0} < 1.0$ *(upward section)* $\sigma_c = f_c\left(\dfrac{\dfrac{\varepsilon_c}{\varepsilon_0}}{6\left(\dfrac{\varepsilon_c}{\varepsilon_0}-1\right)^2 + \dfrac{\varepsilon_c}{\varepsilon_0}}\right)\dfrac{\varepsilon_c}{\varepsilon_0} \geq 1.0$ *(Descent section)*
Lu (2010) [70]	$\sigma_c = f_c'\left[\dfrac{(E_0/E_{SC})(\varepsilon_c/\varepsilon_{c0}) - (\varepsilon_c/\varepsilon_{c0})^2}{1+(E_0/E_{SC}-2)(\varepsilon_c/\varepsilon_{c0})}\right]$ *with* $0 \leq \varepsilon \leq \varepsilon_0$ $\sigma_c = \left[\dfrac{f}{1+1/4\,[\{(\varepsilon/\varepsilon_0)-1\}/(\varepsilon_L/\varepsilon_0)-1]^{1.5}}\right]$ *with* $\varepsilon_0 < \varepsilon$ $\varepsilon_L = \varepsilon_0\left[\left(\dfrac{1.25}{10}\dfrac{E_0}{E_{SC}} + \dfrac{4}{5}\right) + \sqrt{\left(\dfrac{1.25}{10}\dfrac{E_0}{E_{SC}} + \dfrac{4}{5}\right)^2 - \dfrac{4}{5}}\right]$ $\varepsilon_0 = 750(f_c')^{0.35} \times 10^{-6}$ $E_0 = 3840\sqrt{f_c'}$
Feng et al. (2021) [48]	$y = \begin{cases} Ax + (5-4A)x^4 + (3A-4)x^5 & 0 \leq x \leq 1 \\ \dfrac{x}{8(x-1)^2+x} & x \geq 1 \end{cases}$ $\begin{cases} x = \varepsilon/\varepsilon_{cu} \\ y = \sigma/f_c \\ A = E_c\,\varepsilon_{cu}/f_c \end{cases}$
Mansur (1999) [73]	$\dfrac{fc}{f'c} = \dfrac{k_1\beta\left(\dfrac{\epsilon}{\epsilon c'}\right)}{k_1\beta - 1 + \left(\dfrac{\epsilon}{\epsilon c'}\right)^{k_2\beta}}$ $k_1 = \left(\dfrac{50}{f'c}\right)^{3.0}\left[1 + 2{,}5\left(\dfrac{V_f L_f}{\emptyset_f}\right)^{2{,}5}\right]$ $k_2 = \left(\dfrac{50}{f'c}\right)^{1{,}3}\left[1 - 0{,}11\left(\dfrac{V_f L_f}{\emptyset_f}\right)^{-1{,}1}\right]$ $\beta = \dfrac{1}{1 - \dfrac{f'c}{\epsilon c' Ei}}$

For high strength concrete specimens, snapback in compressive stress-strain curves and displacement instability due to localized damage result in unreal uniaxial compressive curves [74]. RILEM TC 148-SSC [75] recommends three possible testing sets to reduce this effect: (1) control by circumferential or lateral displacement, (2) by means of a control function that combines longitudinal and lateral deformation or (3) by means of a feedback control [76]. Figure 14 shows the recommended test set for test control through lateral displacement.

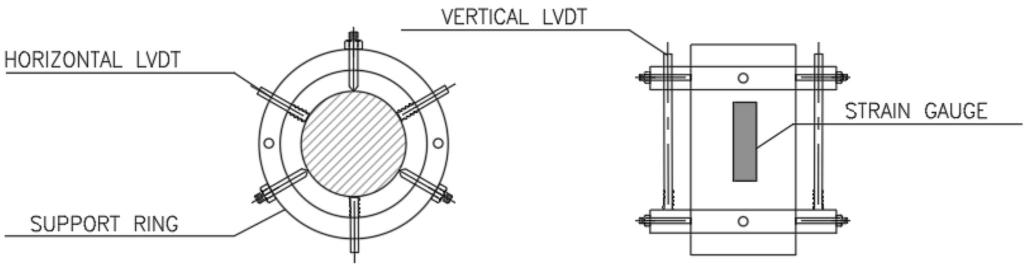

Figure 14 - Recommended test set to minimize snapback in compression curves for high resistance concretes.

The uniaxial behavior of high resistance concretes is of hard characterization due to damage localization, which leads to snapback in compressive stress-strain curves. Jansen and Shah [76] studied a method to obtain a stable feedback signal by rotating the test results with localized damage. Pressmair et al. [77] developed compressive tests according to the set in Figure 14 and included the translation of the measured signal before the rotation of the feedback signal to eliminate initial LVDT slips. Figure 16 (a) compiles the recommendations of Jansen and Shah [76] and Pressmair [77].

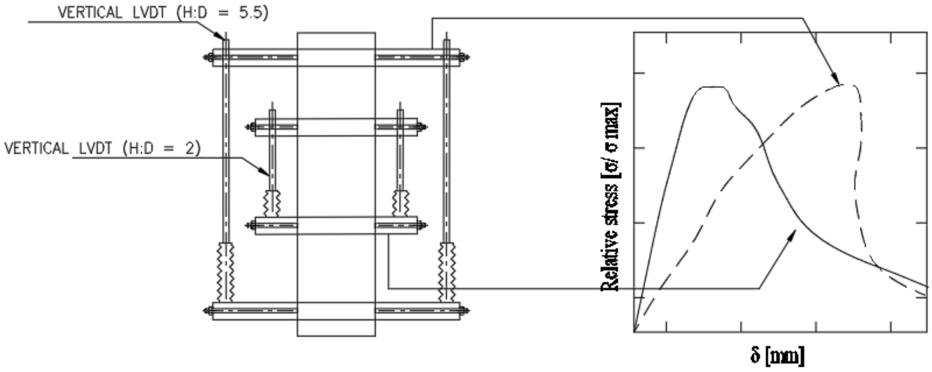

Figure 15 - Impact of gauge length on load-displacement curves in compressive tests. [Adapted from Jansen and Shah [76]].

Jansen and Shah [76] attribute this snapback phenomenon to the occurrence of localized failures in the concrete, that are more likely to occur when bigger gauge lengths are used to obtain load-displacement curves. The variation of LVDTs gauge lengths from H:D = 5.5 to H:D = 2 produced the difference in curves shown in Figure 15.

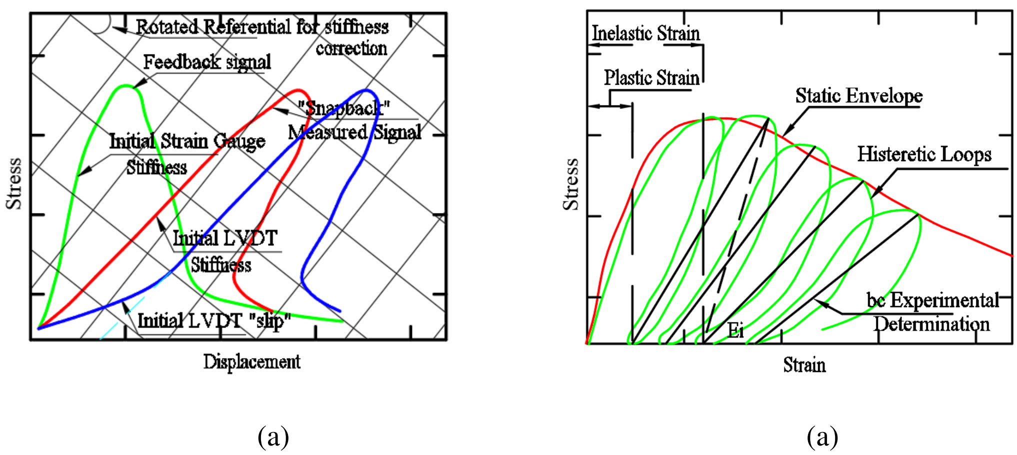

Figure 16 – Feedback control for snapback effect correction in compressive tests (a) and compression test for damage parameter determination (b) [Adapted from Birtel and Mark [78].

The feedback signal is obtained by the expression (1), where δ is the displacement in the horizontal axis, F is the force, K0 is the initial stiffness and α is a parameter that must be calibrated so the initial stiffness curve obtained by the LVDT matches the initial stiffness measured by the strain gauge.

$$FS = \delta - \alpha \frac{F}{K0} \quad (1)$$

Compressive uniaxial stress-strain models varied by author, and there were no repetitions found. Mansour et al. [66] implemented the model proposed by Zheng et al. [69] which specifies two separate expressions for an ascending branch and descending post-peak branch. Paschalis et al. [44] used the SBETA constitutive model, internally implemented in ATENA software. Yin et al. [42] used the Karagozian and Case [60] method implemented in LS-Dyna. Kadhim et al. [54] implemented the bilinear model proposed by Graybeal [79] [80], with an ascending branch and a descending branch connected by the compressive strength and peak strain. Feng et al. [48] used the model proposed by Feng and Li [48] with calibrated expressions for pre and post peak branches. Zhang et al. [64] applied the expressions of Lu et al. [70] for ascending and descending branch of the compressive stress-strain curve, peak strain, elastic modulus, secant modulus and limiting strain. Song et al. [65] modelled concrete in compression based on the expressions of Prem et al. [71] for the modified Carreira et Chu model for UHPC. Shi et al. [39] applied a parabolic stress strain curve. Gao et al. [52] applied the equations proposed by Yang, [72] separating pre and post-peak branches.

Table 8 - Experimental tensile strength with corresponding tensile test and selected tensile uniaxial model.

Authors	Experimental Tensile strength [MPa]	Tensile Test	Uniaxial Model - Tension
Selim et al. [41]	8.7	Dog-bone shaped	-
Paschalis and Lampropoulos [44]	11.5	Dog-bone shaped	SBETA
Mansour et al. [66]	5.2	-	Zheng et al. [69]
Yin et al. [42]	10.5	-	Internal Karagozian & Case implemented [60]
Kadhim et al. [54]	-	-	Bilinear
Bahraq et al. [46]	8.7	Dog-bone shaped	Implemented experimental data
Feng et al. [48]	7.4	Dog-bone shaped	Feng and Li [48]
Yuan et al. [53]	7	Dog-bone shaped	OpenSees Implemented
Franssen et al. [63]	-	-	Franssen et al. [63]
Zhang et al. [64]	-	-	Trilinear
Song et al. [65]	-	-	Zhang et al. [83]
Li et al. [47]	7.1	Prisms specimens (100 mm × 100 mm × 400 mm)	Zhang et al. (2018)
Shi et al. [39]	-	-	Bilinear
Wang et al. [51]	-	CMOD	Linear
Gao et al. [52]	-	Dog-bone shaped	Gao [52]

The original Carreira et Chu [81] model for plain concrete has the advantage of modelling concrete in compression through one sole equation. The post peak branch in UHPC is governed by fiber characteristics and content, not considered in the original method. Studies have been made by Prem et al. [71], Mansur [73] and Krahl [82] to propose modified Carreira and Chu models for FRC and UHPC.

Uniaxial tensile constitutive models vary in complexity. Simpler models utilize polygonal forms to represent the elastic pre-cracking phase, strain hardening and fiber pull-out. Some authors even disregard the strain softening phase [52].

$$fc_t = fct, fl_{El}\left(\frac{2\left(\frac{h}{h0}\right)^{0,7}}{1+2\left(\frac{h}{h0}\right)^{0,7}}\right) \tag{2}$$

For studies such as the ones developed by Li et al. [47] and Lima et al. [2] in with the tensile strength was determined indirectly from flexural tests, the French standard [12] offers the equation (2) to convert flexural tensile strength into direct tensile strength. For the expressions listed in Table 8 the direct tensile strength must be used. For Expression (2), fct, fl_{El} is the flexural tensile strength at the limit of proportionality, h is the height of the prism, and h0 is 100 mm.

Concrete in tension first behaves elastically, with a linear load-deformation relation almost until the peak load. At a macro scale, the stresses and strains are homogeneously distributed throughout the sample's body and the load-deformation behavior can accurately be described by the stress-strain relationship in pre-crack phase. However, when stresses reach peak load they tend to localize in zones of micro-cracks. The process will occur in the weakest part subjected to tensile stresses. Due to the fact that the stresses are governed by crack opening, Hordijk [84] recommends splitting the tensile curve in stress-strain for bulk material and stress-crack opening for the cracking phase because since the failure occurs locally, while part of the specimen enters the softening phase during crack growth, the other parts of the specimen will receive a lower stress and will actually develop lower strain values. Because of that, the stress-strain curves are influenced by gauge length, and curves obtained using longer gauge-lengths may result in the aspect shown in Figure 17.

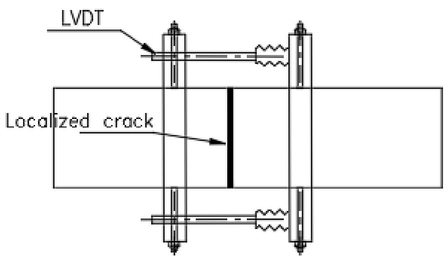

(a)

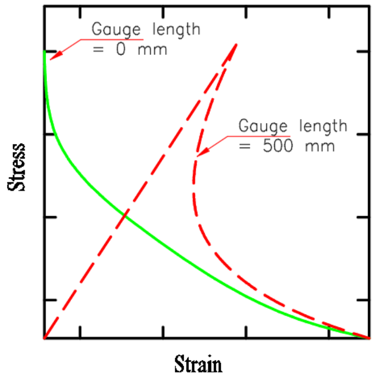

(b)

Figure 17 – Localizef failure in tensile tests (a) and influence of gauge-length in stress-strain curves in tension (b) [Adapted from Hordjik [84]].

Hillerborg's "Fictitious Crack Model" [85] permits to transform crack opening to equivalent inelastic strain by assuming a theoretical average elongation throughout the gage length (mean element length), by dividing the crack opening by the characteristic length [78]. This method has the advantage so that finite element analysis can be performed with a relatively coarse mesh since there are no stress singularities [85]. The relationship between inelastic strain and crack opening is given by equation (3), where W is the equivalent crack opening, Lt if the characteristic length and ε_{in} is the inelastic strain. The Characteristic length used in the conversion is a relation between the Young's (E) modulus, the cracking energy (G) and the tensile strength (ft) of the concrete (equation (4)). Bazant reached the conclusion that the characteristic length is an upper limit for the size of the finite element mesh to assure the energy equilibrium [86].

$$W = Lt \times \varepsilon_{in} \tag{3}$$

$$Lt = \frac{EG}{ft^2} \tag{4}$$

Table 8 shows selected articles experimental tensile strengths, tensile tests and the chosen uniaxial tensile model to represent concrete in tension. The most applied tensile characterization methodology was through dog-bone shaped specimens. Authors used different sections with different tests speeds. Paschalis et al. [44] and Bahraq et al. [46] both used displacement control, with the former's specimen having 15x50 mm cross section and test speed of 0.42 mm/min and the latter a 0.5 mm/min load speed. Wang et al. [51] used notched beam specimens to obtain flexural tension x Crack Opening relationships through DIC analysis. The fracture energy was calculated through the fitting process of SEL and a linear stress-crack opening curve was obtained with resulting area comprised by the curve equal to the obtained cracking energy.

The first step for tensile constitutive model choosing is the characterization of concrete's tensile behavior as strain hardening or strain softening. Franssen et al. [63] formulated a model for concrete in tension, including crack spacing formulations for both behaviors. The post cracking curve is determined by the fiber volume and the difference in hardening/softening depends on the fiber critical volume.

The critical volume is a function depending on the fibers' aspect ratio and fiber orientation factor. The resulting curve combines the tension softening regime of the matrix with fiber activation regime through crack opening.

The fiber critical volume is the minimum volume so that the composite can present multiple cracking and pseudo-ductility. Aveston [87] presents expressions for the fiber critical volume in the cases for 1D aligned fibers, 2D and 3D randomly oriented fibers.

Selim et al. [41] entered directly mean tensile stress-strain curves obtained through dog-bone tests. Paschalis et al. [44] used SBETA constitutive model implemented in ATENA software, which represents tensile behavior through a strain-hardening behavior and the descending portion corresponding to fiber pullout is represented bi-linearly. Mansour et al. [54] used the equations provided by Zheng [69], considering two separate equations for ascending and descending branch with smooth transition to strain softening. Yin et al. [42] used the Karagozian and Case method implemented in LS-Dyna. Kadhim et al. [54] implemented a bilinear stress-strain curve with ascending portion until first crack strain. Bahraq et al. [46] implemented directly mean tensile stress-strain curves obtained through dogbone tests. Feng et al. [48] implemented the model of Feng and Li [48], considering three phases (1) elastic phase until tensile strength, (2) strain hardening represented by a plateau, and (3) strain softening phase represented by a descending expression. Franssen et al. [63] developed a stress-crack opening relation for strain-hardening or strain softening concretes depending on a critical volume relation. Zhang et al. [64] considered a trilinear stress-strain model to simulate strain hardening with 1% inclination until maximum fiber activation and later linear fiber pull-out strain softening. Song et al. [65] and Li et al. [47] considered the model proposed by Zhang et al. [83] in terms of tensile inelastic (cracking) strain and in terms of crack opening. Shi et al. [39] considered a bi-linear model consisting of only elastic pre-cracking branch and strain-hardening plateau, with no strain softening. Gao et al. [31] applied the model proposed by Gao [52].

Table 9 shows the expressions for the tensile uniaxial models found in the literature that describe concrete in tension in terms of stress-crack opening curves. Figure 18 presents the curves for comparison of these models, being the main difference how the fibers enter the softening branch at post cracking stage and at which crack opening the stress comes to zero, with Li and Leung's [88] model at about one quarter of the fiber's length and at the model developed by Pyfl [89] at half of this length. Fehling et al. [90] recommend using the latter for UHPC.

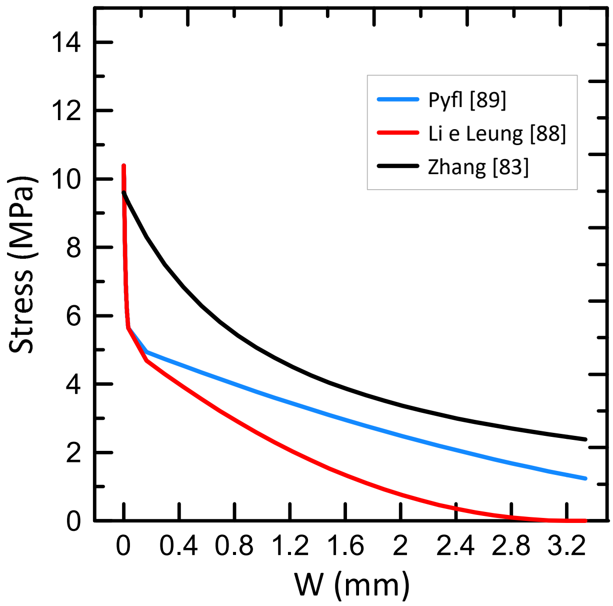

Figure 18 - Curves for the uniaxial tensile models developed in terms of stress-crack opening given in Table 9.

The damage evolution represents material degradation through the loading stages, being a normalized value with a one value corresponding to the material with no degradation and zero value corresponding to a completely degraded material. The elastic phase corresponds to zero damage phase, with total strain corresponding to elastic strain. When a material enters the no-linear regime, inelastic strains start to develop and this results in damage evolution. Part of the inelastic strains correspond to plastic strains, which are the permanent strains when the material is unloaded.

Table 9 - Uniaxial tensile models developed in terms of stress-crack opening.

Uniaxial compression model	Expression
Li and Leung (1992) [88]	$\sigma_f(w) = \begin{cases} \sigma_{f0}\left(2\sqrt{\dfrac{w}{w_0}} - \dfrac{w}{w_0}\right) \mathit{for}\ w \le w_0 \\ \sigma_{f0}\left(1 - \dfrac{4w}{L_f}\right)^2 \mathit{for}\ w > w_0 \end{cases}$
Pyfl (2003) [89]	$\sigma_f(w) = \begin{cases} \sigma_{f0}\left(2\sqrt{\dfrac{w}{w_0}} - \dfrac{w}{w_0}\right) \mathit{for}\ w \le w_0 \\ \sigma_{f0}\left(1 - \dfrac{2w}{L_f}\right)^2 \mathit{for}\ w > w_0 \end{cases}$
Zhang (2015) [83]	$\sigma_f(w) = \dfrac{\mathrm{fct}}{\left(1 + \dfrac{W}{Wp}\right)^p}$ $Wp = 1$ $p = 0.95$

Mansour et al. [66], Bahraq et al. [46] and Song et al. [65] all used Birtel and Marks formulations for damage in both tension and compression. These formulations depend on the factors bt (Table 12) and bc (Table 11) in tension and compression, respectively, that relate plastic and inelastic strains in tension and compression. These parameters define the amount of plastic strain for a corresponding inelastic strain. A bc parameter specified with a zero value corresponds to no plastic strains for a material subjected to compression, and a bc parameter with a one value meaning that all inelastic strains correspond to plastic strains. None of the authors specified the bt and bc parameters used. Although for conventional concretes the recommended values are 0,7 for bc and 0.5 for bt, these values may result in unrealistic damage evolution for UHPC. These factors must be determined through cyclic damage evolution tests. Zhang et al. [64] used the model proposed by Singh [45] in compression and the model proposed by Mahmud [91] in tension. These models do not depend on supplementary testing for damage determination.

Table 10 - Damage models used by the authors in tension and compression.

Author	Damage Tension	Damage Compression
Mansour et al. [66]	Birtel e Mark [78]	Birtel e Mark [78]
Bahraq et al. [46]	Birtel e Mark [78]	Birtel e Mark [78]
Yujie et al. [64]	Mahmud [91]	Singh [45]
Song et al. [65]	Birtel e Mark [78]	Birtel e Mark [78]
Gao et al [31]	Krahl et al.[92]	Wang [52]

Damage evolution with different damage models was plot in Figure 19 and Figure 20. Figure 19 (a) corresponds to the concrete in compression considering the modified Carreira and Chu model by Mansur [73] as uniaxial model and different damage models applied to this stress-strain curve. Figure 19 (a) represents traction model considering Li and Leung's [88] model, with fiber activation phase. Figure 19 (b) shows damage in compression for Birtel and Mark's [78] model, Singh's [45] model for UHPC, Wang's [52] model and the simplified model proposed by Pavlovich [93].

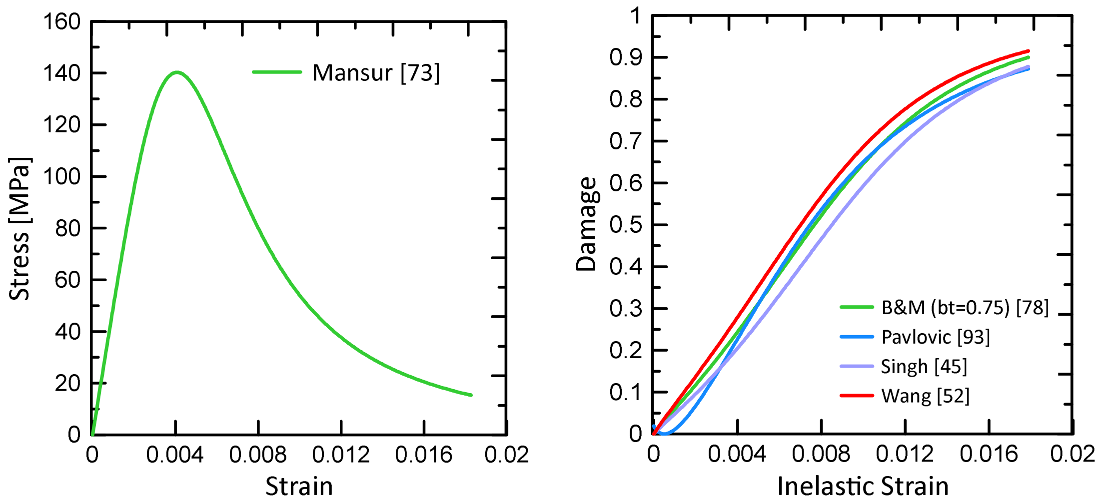

(a) (b)

Figure 19 – Compressive stress-strain curve (a) and corresponding compressive damage evolution according to different damage models (b).

It can be noted that values of bc used for CC can result in good approximations for UHPC in compression. From Figure 20 (b) it can be noted that higher bt values must be used to coincide with Krahl's [92] model for a fasta damage evolution, being the originally proposed value for conventional concrete 0.5. Also, the maximum damage value is limited to 0.9 in this model, whereas in the other models damage tends to 1.

Table 11 - Expressions for the compressive damage evolution models used in the literature.

Compression damage evolution models	Expression
Birtel and Mark (2006) [78]	$d_c = 1 - \dfrac{\left(\frac{\sigma_c}{E_c}\right)}{\varepsilon_{pl}\left(\frac{1}{b_c} - 1\right) + \left(\frac{\sigma_c}{E_c}\right)}$
Pavlovich (2013) [93]	$d_c = 1 - \sigma_c/\sigma_{max}$
Wang (2018) [52]	$d_c(\varepsilon_c^{in}) = \dfrac{(1-0.7)\varepsilon_c^{in}E_c}{\sigma_c + (1-0.7)\varepsilon_c^{in}E_c}$
Singh (2018) [45]	$d_c = 1 - \dfrac{\left(\frac{\sigma_c}{E_c}\right)}{\varepsilon_{in}(0.2) + \left(\frac{\sigma_c}{E_c}\right)}$

Table 11 and Table 12 list the expressions for the damage evolution models used in the literature for compression and tension respectively. Mahmud [91] and Pavlovich's [93] models are simplified while the others are real empirical models calibrated from cyclic testing. For the model developed by Krahl [92], the parameters needed for a concrete with 2% fiber content in volume are Y0 = -0.11437, A1 = 0.87236, A2 = 0.18508, t1 = 5.0235E-4, t2 = 0.01417.

Table 12- Expressions for the tensile damage evolution models used in the literature.

Tensile damage evolution models	Expression
Birtel and Mark (2006) [78]	$d_t = 1 - \dfrac{\left(\frac{\sigma_t}{E_c}\right)}{\varepsilon_{pl}\left(\frac{1}{b_t} - 1\right) + \left(\frac{\sigma_t}{E_c}\right)}$
Alfarah (2016) [95]	$d_{\mathrm{t}} = 1 - \dfrac{1}{2+a_{\mathrm{t}}}\begin{bmatrix} 2(1+a_{\mathrm{t}})\exp\left(-b_{\mathrm{t}}\varepsilon_{\mathrm{t}}^{\mathrm{ck}}\right) - \\ a_{\mathrm{t}}\exp\left(-2b_{\mathrm{t}}\varepsilon_{\mathrm{t}}^{\mathrm{ck}}\right) \end{bmatrix}$ $b_{\mathrm{t}} = \mathrm{fct} \times \dfrac{Lc}{Gf}(1 + 0{,}5 \times at)$ $at = 1$
Mahmud (2013) [91]	$d_t = 1 - \sigma_t/\sigma_{max}$
Krahl (2018) [92]	$d_t(\varepsilon) = y_0 + A_1\left(1 - e^{-\varepsilon/t_1}\right) + A_2\left(1 - e^{-\varepsilon/t_2}\right)$

Tian et al. [94] conducted monotonic and cyclic tensile loading tests to characterize damage evolution in UHPC specimens. The tests were conducted in a manner that the dog-bone specimens were subjected to displacement control load of 0,05 mm/min and unloaded to zero with constant displacement speed of 1 mm/min. Reloading was conducted with a 0,1 mm increment in total cycle displacement, representing a strain increment of 0,05% compared to the residual displacement of the previous cycle. The resulting envelope curve connecting all cycle maximum stresses result in a curve similar to the monotonic response.

Figure 21 (a) illustrates the damage evolution obtained using Birtel and Mark's [78] model for different gauge lengths for the calculation of the correspondent inelastic deformation. To compare the effects of different LVDT openings, the curves obtained by Krahl et al. [92] with an opening of 5 cm and Tian et al. [94] with an opening of 20 cm for UHPCs with 2% fiber content were selected. Finally, the Birtel and Mark models were compared with the experimental damage evolution data obtained by Tian et al. [94] and Krahl et al. [92] considering inelastic deformations for these LVDT openings (Figure 21 (b)), highlighting that the more localized the damage measurement, the faster will the observed damage evolution be.

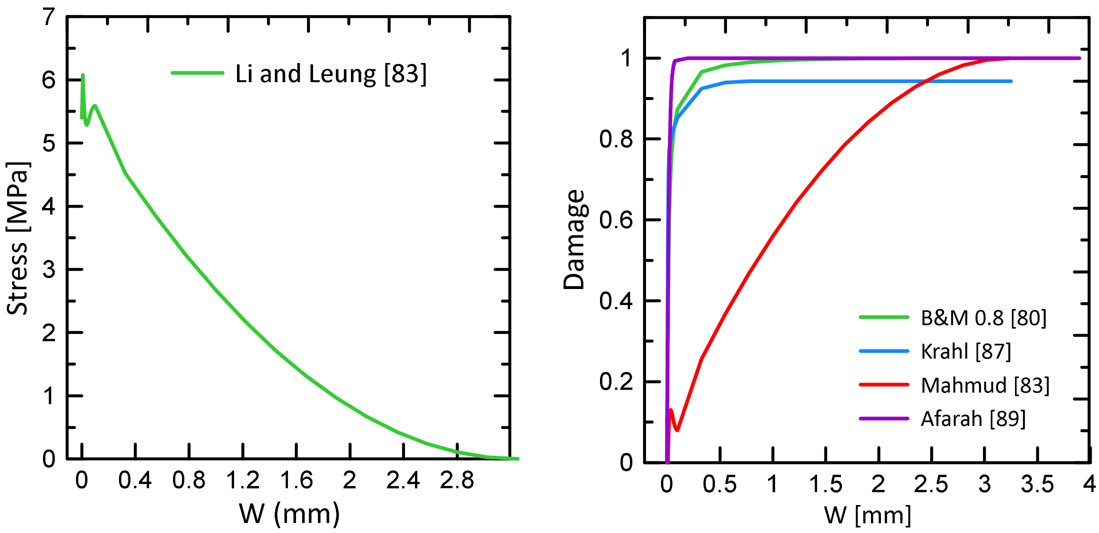

(a) (b)

Figure 20 - Damage evolution according to different models (b) for the same tensile stress-strain curve (a).

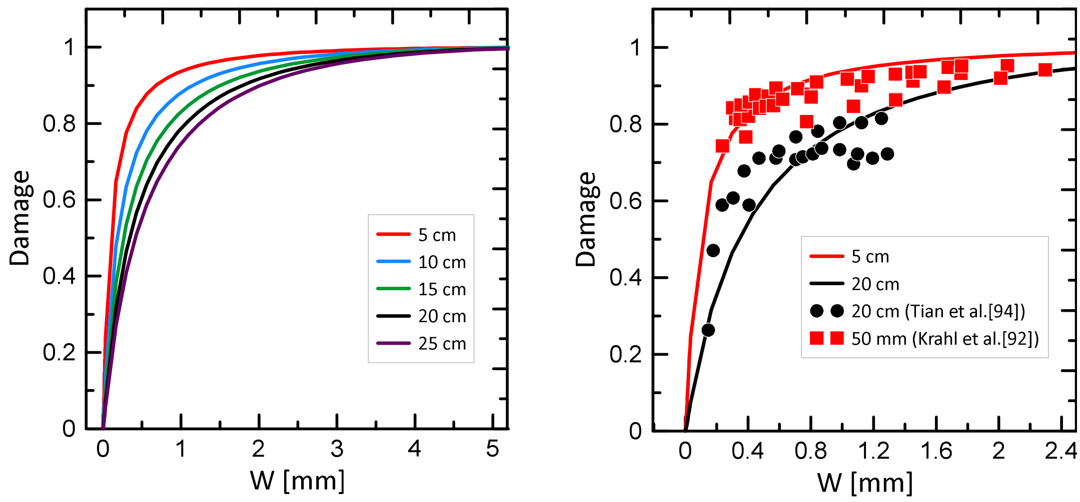

(a) (b)

Figure 21 - Birtel and Mark's model considering different gauge lengths (a) and the superposition of the curves corresponding to 5 cm and 20 cm with the experimental data of Krahl et al. [92] and Tian et al. [94] (b).

2.5 Ductility of UHPC beams

Conventional concrete beams retrofitted with UHPC layers were studied by Paschalis et al. [44], Yin et al. [42], Song et al. [65] and Yuan et al. [53]. Paschalis et al. [44] and Yuan et al. [53] compared load-deflection curves derived from experimental results and FEM models for conventional concrete beams retrofitted with UHPC layers on the tension side and jacketing on three sides. All models showed good agreement concerning peak loads observed in experimental data. For these cases, the perfect bond was an adequate representation of the physical model. The jacketed beam models exhibited the greatest difference compared to experimental results, with a clear yield point in the model, compared to smooth transition on experimental results, and higher post-peak stiffness in the model compared to experimental results. Yin et al. [42] compared CC beams retrofitted with UHPC layers on the tensile side. Song et al. [65] studied over-reinforced CC beams retrofitted with UHPC layers on the compression side. The numerical models were able to reproduce the distributed cracking pattern on the CC portion of the beams with good overall correspondence between experimental and numerical results. The results showed that greater UHPC layers result in higher bearing capacity due to UHPC greater crushing resistance and increment the beams ductility until a certain limit. After this limit, greater UHPC layers correspond to the beams loosing ductility. Yuan et al. [53] were able to reproduce crack localization phenomena through their numerical model.

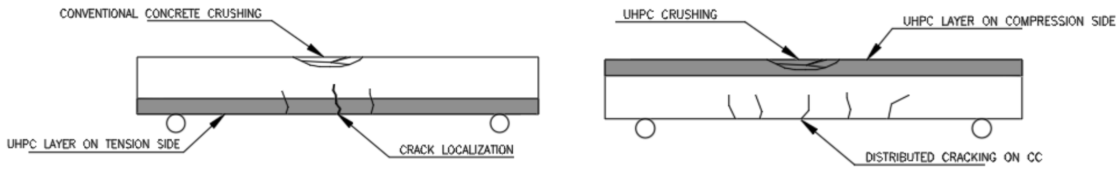

(a) (b)

Figure 22 - Retrofitting configurations and crack patterns of the beams studied by Yuan et al. (Yuan et al. 2022) (a) and Song et al. (Song et al. 2022) (b).

Load deflection curves from UHPC beams with 0,53% to 1,71% reinforcement ratio developed by Yin et al. [42] show that lower reinforcement ratios correspond to poor correspondence between numerical models and experimental results in post-peak branches and the lower the reinforcement ratio, more reduced will be the ductility of the UHPC beam.

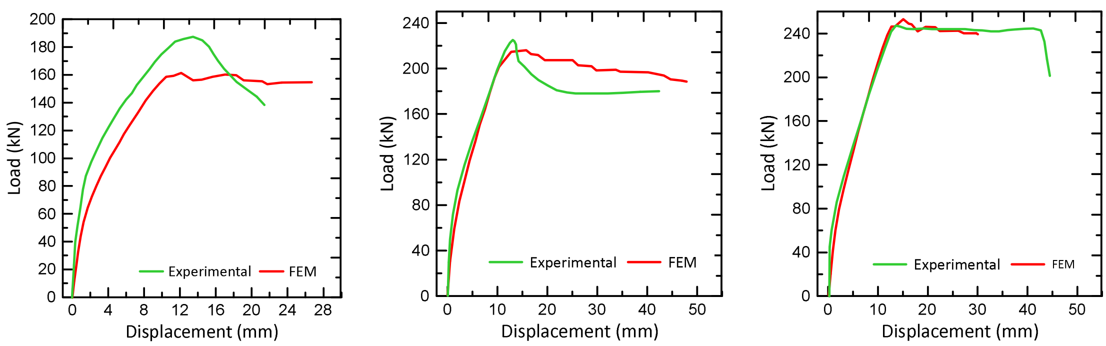

(a) (b) (c)

Figure 23 – Comparison between load-deflection curves for non-composite UHPC beams with 0.53% (a), 1.06% (b) and 1.71% (c) reinforcement ratios [42].

Dancygier and Berkover [96] showed the importance of ductility studies for fiber reinforced concrete beams with low reinforcement ratios, with reinforcement ratio playing an important role on post peak behavior, but also fiber content having a minor role, with higher fiber contents resulting in specimens with lower ductility indexes. Dancyngier and Karinski [97] studied crack localization phenomena in tensile fibrous steel-reinforced bars and proposed analytical expressions for determination of the number of cracks and of those, how many would develop into major crack localization. A “weak section” can be defined with a length of half the fiber’s length. Yang and Xu [98] proposed a heterogeneous model for brittle materials based on a correlation length and its effect on the crack path. Lima et al. [2] used random material properties throughout the specimens' volume on finite element analysis to simulate non-homogeneity of the fibers, resulting in post-peak drop, which reflects the beam's ductility and crack localization as well as the plastic deformation on steel reinforcement concentrating on the localized cracks.

Ductility parameters were used by Yuan et al. [53] and Song et al. [65] to study UHPC layers effect over CC beams' ductility. Yuan et al. [53] used the model reproduced in Figure 24 (a), with the resulting ductility index being the relation between the ultimate load deflection and the yield deflection. In this model, the yield deflection is defined as the deflection in the pre-peak branch of the curve corresponding to the point where a line passing through 75% of the peak load and a horizontal line passing through the peak load meet. Song et al. [65] used the ductility index according to Figure 24 (b). The yield point is defined as the most distant point to the line connecting the origin to the peak of the load-deflection curve. Shao and Billington [99] studied UHPC beams' ductility in the form of a drift capacity defined by the deflection corresponding to post-peak load of 20% divided by the shear span. A minimum drift capacity of 2.5% was proposed to assure ductile flexural failure for UHPC beams.

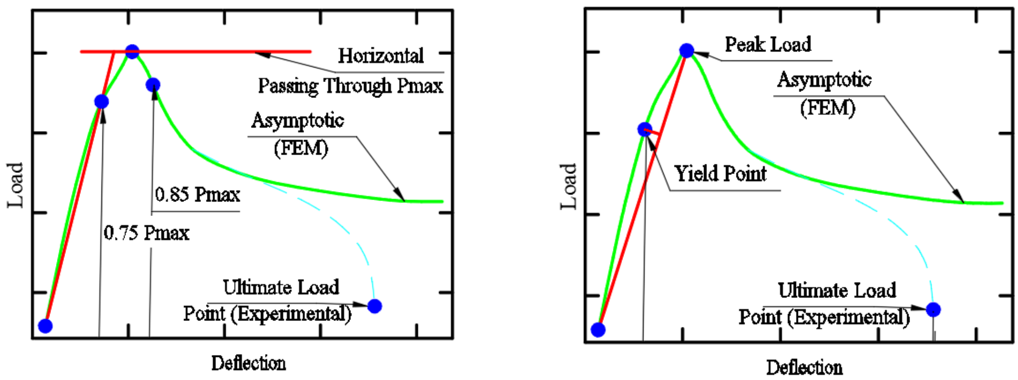

(a) (b)

Figure 24 - Ductility indexes calculated by Yuan et al. [53] (a) and Song et al. [65] (b)

The main reason for the differences in finite element models post-peak behavior and the experimental results is that smeared crack models result in distributed failure for fiber reinforced concrete while the experimental results [3] [12] show that the distributed crack pattern corresponds to service level loads, while the beam failure is associated with fiber pull-out resulting in localized failure modes. To obtain the localization of the failure through smeared crack models, Lima et al. [2] modeled the beams considering random properties throughout the beams volume, which led to a non-homogeneous damage evolution in the numerical model. Figure 25 shows the process of generating random uniaxial tensile curves and the corresponding damage evolution curves.

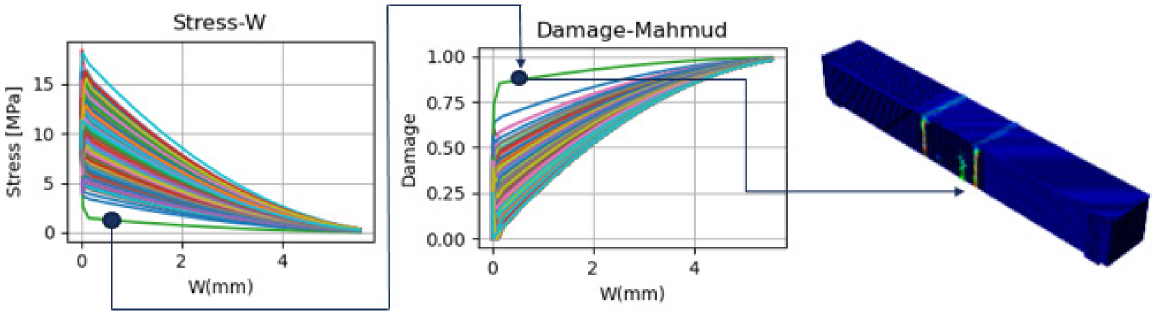

Figure 25 - Strategy for crack localization modelling through smeared crack models with correspondence between uniaxial tensile models and damage evolution models' variability influence on failure localization in numerical models.

The damage model specified in this model [Figure 25] presents an inverse relationship with the tensile stress curve, with the stress-crack opening curves corresponding to the fastest post-cracking drop resulting in the fastest damage evolution. The material partition cell to which this material is assigned represents the point at which the damage localization process will start, resulting in the post-peak branch obtained in load-displacement curves numerically with softening post-peak branch.

This process shows that to obtain crack localization on the numerical model, a "band" of curves must be generated, and the thicker the generated band, the higher the tendency of the model to generate localization. A similar process mas made to evaluate the variation of the other tensile damage models found in literature. The graphs shown in Figure 26 are all generated from the same set of 500 tensile uniaxial curves.

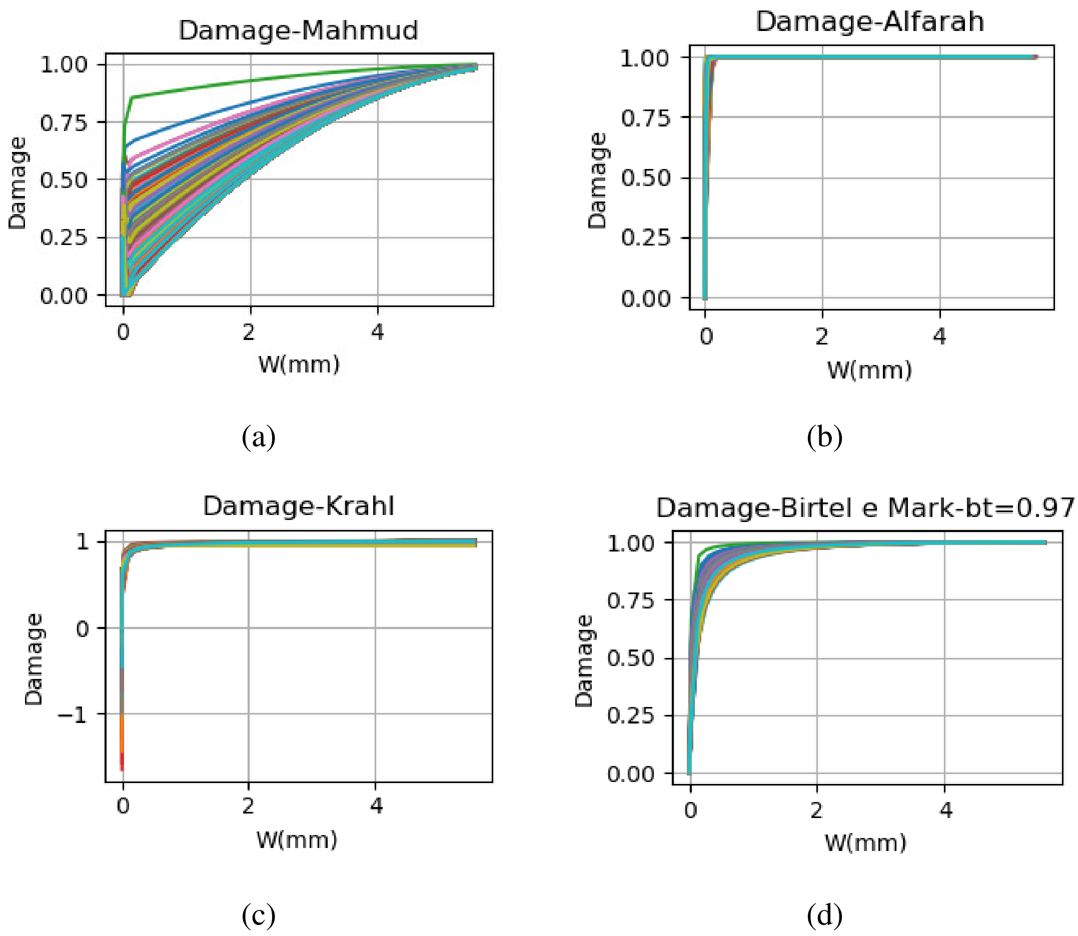

Figure 26 - Variability of the damage evolution considering Mahmud's (a), Alfarah's [95] (b) Krahl's [92] (c) and Birtel and Mark's [78] model (d).

It can be seen in Figure 26 that from the models calibrated to have a rapid damage evolution after the crack formation, only Birtel and Mark's [78] model actually had some relevant differentiation in the generated curves. This happens because it is the only model that corresponds the damage state to the tensile state at each point of the curve. While Krahl's [92] model is independent from the tensile stress evolution, Alfarah's [95] model is dependent only on the tensile-strength and the cracking energy, but not on the tensile stress evolution on the uniaxial model. Another set of curves was generated to investigate the influence of the bt parameter in the variability of the damage evolution (Figure 27).

It can be noted from Figure 27 that higher bt values result in more dispersion of the damage evolution curves and that the bt parameter represents not only the relationship between plastic and inelastic strains as it would be for homogeneous models, but also indicate the tendency for damage localization in heterogeneous models with higher bt values generating higher dispersion of the tensile damage evolution curves. As it was shown in Figure 25, the differentiation of the damage variable in definition of the material properties in each partition cell is what results in the localized failure.

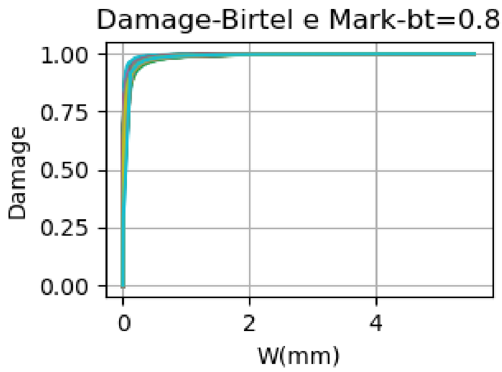

(a)

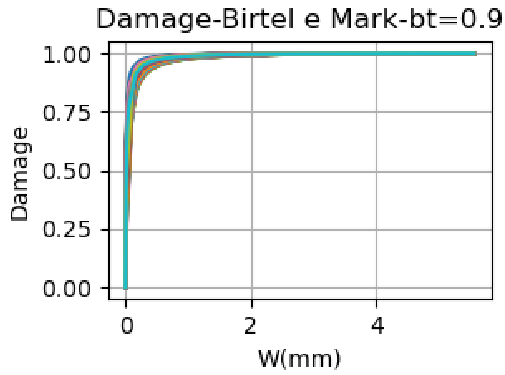

(b)

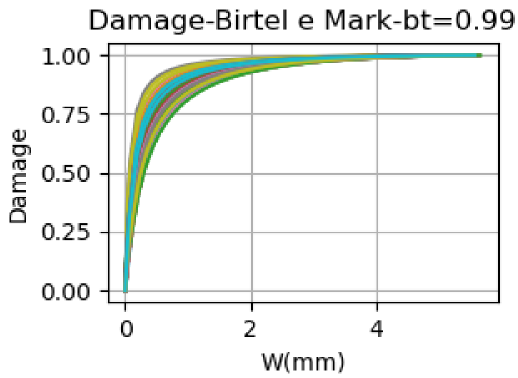

(c)

Figure 27 - Influence of the bt parameter in the damage evolution variability.

2.6 Contributions of this work

After the review of the literature, it was identified as a knowledge gap a validation of the material models for UHPC both through material and structural scale testing, with the correct identification of the bc and bt parameters for Birtel and Mark's model in compression and tension.

Also, a new approach is conducted to determine the CDP parameters through material level numerical models benchmarked to the material characterization results. This benchmark considers both axial and lateral strains for comparison and failure pattern.

Also, the investigation on the effects of changing the cross-section's shape over the ductility of UHPC creates new insight over UHPC beams' reduced ductility.

3 PRELIMINARY NUMERICAL PROGRAM - DEFINITION OF THE STUDIED BEAMS

For the definition of the studied beams, a numerical program was conducted based on the work developed by Lima et al. [2], where a novel modeling strategy was settled to correctly model the post-peak behavior of four-point load bending tests in UHPC beams and study the ductility of those beams through finite element models. The present study represents and advance in relation to this previous one by presenting a careful study to justify the selected material models, with automation of the division of the structural element to make possible the specification of many material properties at once and study its effect on the models' results.

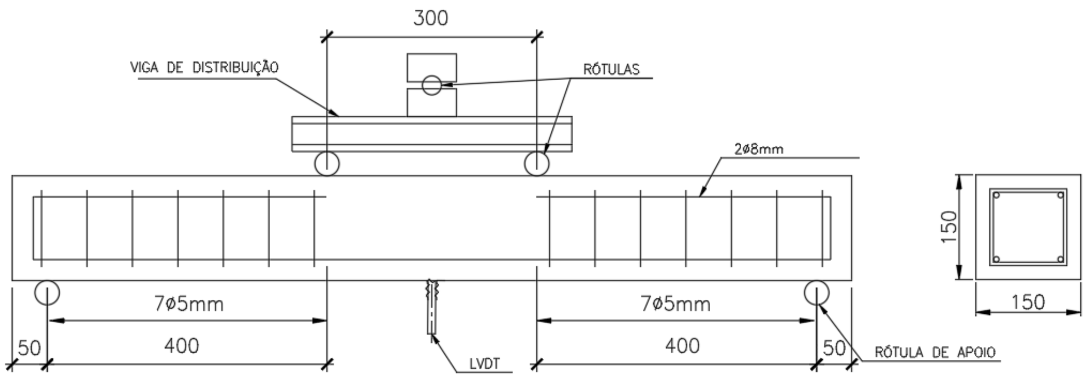

Figure 28 - Test setup used by Lima et al. (2023).

A model calibration is presented to obtain the same results as Lima et al. [2] for a UHPC beam with a low reinforcement ratio. Then, this modelling strategy is used to obtain an optimized cross-section and three reference beams to be tested in the experimental part of this study. The material properties for the modelled concrete in the preliminary numerical program are given by a compressive strength of 142 $\pm$ 6 MPa, and elastic modulus of 38 $\pm$ 4 GPa. As tensile strength a value of 9.04 with coefficient of variation of 0.149 was obtained through flexural tests.

The used steel fibers were the Dramix OL type with 13mm length and 0.2 mm diameter with 2% volume fraction. For the fiber-matrix equivalent bond a value of 8 MPa was used. A coefficient of alignment of the fibers was considered as 0.6 [100] representing a slight alignment compared to the random distribution factor of 0.5.

3.1 Calibration of the numerical model

The calibration of the modeling strategy used as a basis the study of Lima et al. [2], in which non-homogeneous models based on the concrete damage plasticity model (CDP) were implemented in Abaqus commercial software. The modelling strategy consists in dividing the beam into partition cells and creating different material properties attributed to each of those cells, with the difference that Lima et al. used only vertical partitions whereas in this study, partitions were made along the three axis, following the studies presented by Benedicto [100].

3.1.1 Constitutive model

For the creation of the material properties, the material characterization used by Lima et al. [2] was used as input. The interface between Abaqus commercial software and Python programming language was used to generate random material properties through programming scripts and then attribute these properties to material sections and these sections are then attributed to parts of the model in an automated manner. This automation made it possible to test a large number of models with a large number of material curves defined, in a way that is not time consuming. Also, since the random material properties would result in slightly different results every time a model is remade, once the set of material properties was defined, they were used to all the models.

The constitutive model adopted for concrete in compression was the Carreira and Chu method adapted by Mansur [73] for fiber-reinforced concretes due to its simplicity in describing the entire compressive behavior of concrete with just one formulation. The model formulation is based on the parameter β (

Table 7), which depends on the relationship between the peak strain and the modulus of elasticity. The concrete used in the reference work has a modulus of elasticity lower than estimated by Mansur's method, and to use the experimental modulus of elasticity, the peak strain had to be adjusted.

The calibration of the peak strain was made considering the relationship between the peak strain and the corresponding strain of the concrete in elastic regime (fc/Ei). According to Mansur's expressions for initial modulus of elasticity and peak strain for concrete with 2% fibers and the properties adopted by Lima et al. [2], the peak strain results in 8% higher than the ratio considering elastic properties.

The compression damage model was adopted according to Birtel and Mark's formulation considering the parameter bc = 0.7.

For the definition of the curves to be used as input in the material definition for the numerical model, for each material created, a limit of elasticity was defined as the first point in which the material starts to develop inelastic strains. This point is obtained through successive iteration specified in the Python script, starting from 40% of the peak load as an initial guess for the elastic limit [78]. The successive iterations followed until the first positive value for inelastic strain is obtained. Figure 29 (b) shows the evolution with the inelastic strains with a negative first branch, becoming zero in the defined limit of elasticity. Figure 29 (a) shows the corresponding damage evolution curve following the same path. From this point on, it is assumed that the material starts to exhibit compression damage and the corresponding points are used as input parameters for the material definition in the Abaqus software.

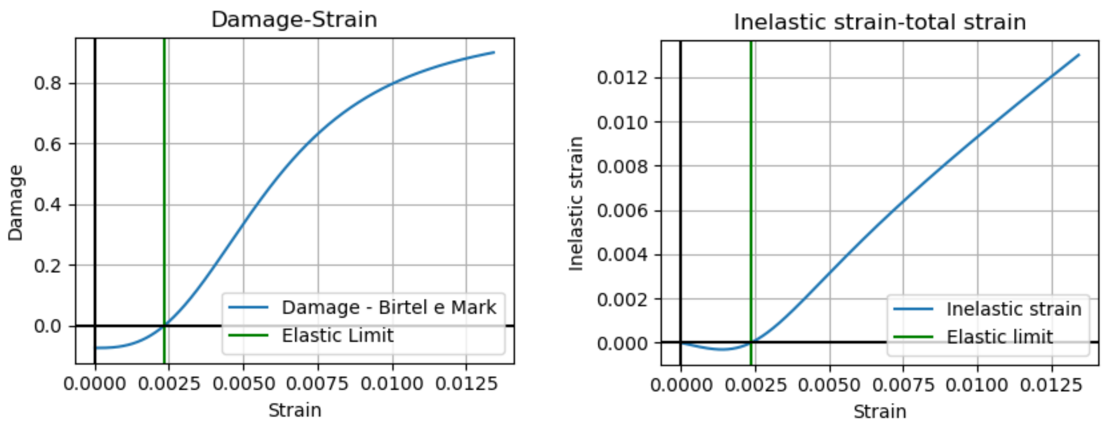

(a) (b)

Figure 29 - Definition of the fist deformation to generate the curves used as input parameters in the material definition for the model through damage-strain curves (a) and the corresponding curve in terms of inelastic strain – total strain (b).

The constitutive model adopted for concrete in tension was the Li and Leung's [88] model. The model considers the behavior of fiber-reinforced concrete through two formulations that aim to represent the behavior of the matrix (σm) and the fibers (σf). The behavior of the composite is given by the sum of those two contributions. In the absence of corresponding information for the parameter bt for the implementation of the Birtel and Mark's model in tension, a simplified damage model proposed by Pavlovic [93] was adopted.

The tensile cracking energy (Gf) is obtained according to the fib Model Code (2010), through equation 5 . σf0 and w0 represent the stress at the maximum activation of fibers, and the corresponding crack opening. The fiber-matrix equivalent bond was adopted with an average value of 8 MPa and a standard deviation of 1.6 MPa, [2]. The coefficient related to the orientation of fibers within the beam (n) was chosen with a value of 0.6 and a standard deviation of 0.1 [100] , representing a slight orientation of fibers to calibrate the peak load in load-displacement curves. For equations (5) to (7), fcm is the average compressive strength, η is the orientation factor, L_f and d_f are the fiber's length and diameter, V_f is the fiber volume fraction, τ_{eq} is the fiber-matrix equivalent bond and E_f is the fiber's Young's modulus.

$$G_f = 73 {f_{cm}}^{0.18} \tag{5}$$

$$\sigma_{f0} = \eta \times \frac{L_f}{d_f} \times V_f \times \tau_{eq} \tag{6}$$

$$w_0 = \frac{\tau_{eq} \times L_f^2}{E_f \times d_f} \tag{7}$$

The beam modeling involved dividing its volume into 500 parts, with each part having a different material property assigned. The material generation was carried out through the Abaqus interface with the Python programming language, automating the creation of random properties. Figure 30 shows the set of curves obtained for the 500 materials. From the random values generated for compressive strength, tensile strength, fiber volume fraction, fiber alignment coefficient, and fiber matrix equivalent bond, the uniaxial models in compression and tension were generated. From these uniaxial models, the corresponding damage evolution models were obtained.

The fields corresponding to the plasticity parameters adopted in the model are shown in the table below, where φ is the dilation angle, ϵ is the eccentricity, fbc/fc is the biaxial ratio, Kc is the shape factor, μ is the viscosity parameter, and ν is the Poisson's ratio.

Table 13 - CDP parameters used by Lima et al. [2].

φ	ϵ	Fbc/fc	Kc	μ	ν
30º	0.1	1.16	0.667	0.0001	0.2

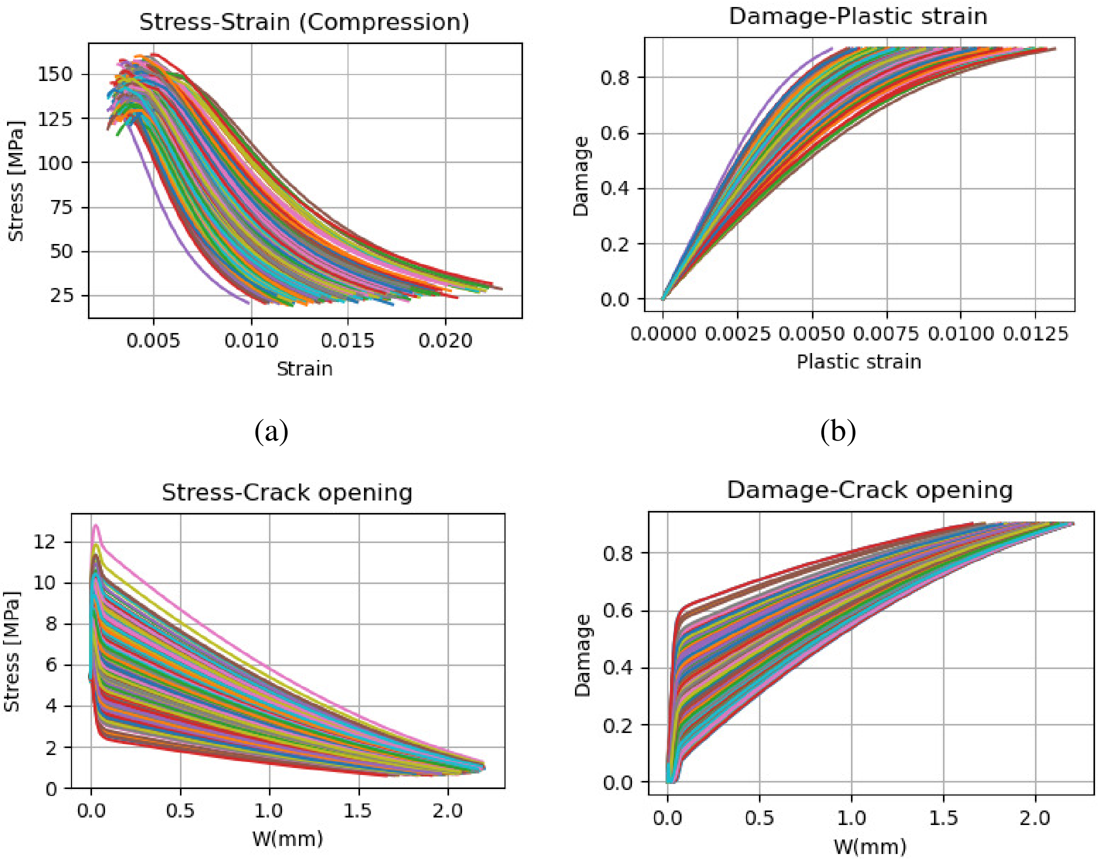

(a) (b)

(c) (d)

Figure 30 - Sets of curves generated for the total of 500 materials (uniaxial curves in compression (a), damage evolution curves in compression (b), stress-crack opening curves in tension (c) and damage evolution curves in tension (d).

The Python codes for the generation of uniaxial and damage evolution curves and their definition in the Abaqus software are shown in Annex C.

3.1.2 Mesh and finite elements

The reinforcements were modeled considering a perfectly plastic model with von Mises yielding criteria, using two-node truss elements (T3d2) [101]. The bond between concrete and reinforcements was assumed to be perfectly bonded through the use of the "Embedded" tool. The constitutive model for the steel reinforcement was a perfectly plastic material, with a nominal yield stress of 500 MPa. The concrete was modeled through 8-node brick elements with reduced integration and 10 mm mesh average size according to the convergence study conducted by Lima et al. [2].

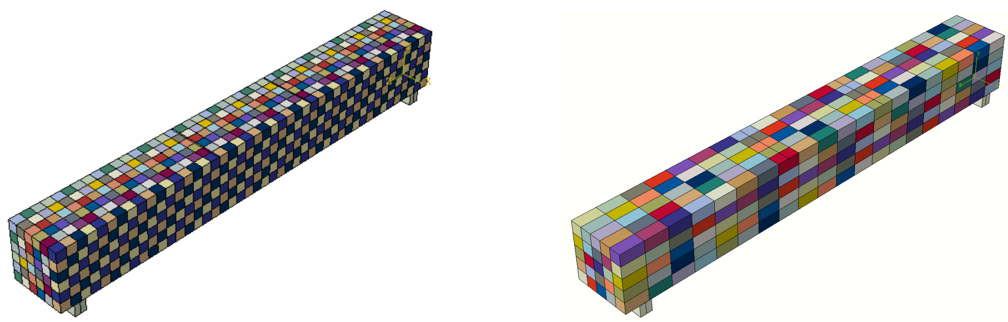

(a) (b)

Figure 31 - Numerical model with the different regions with materials assigned, considering the original size for the partitions (a) and the final adopted size (b).

Originally, a model considering partition cells of approximately twice the fibers' length [100] was implemented with 1620 material properties, however, this model's processing was time consuming and the load-displacement curves resulted in poor correspondence to the experimental load-displacement curves.

It was observed that smaller meshes resulted in losses on the localization tendency on the model, since a weaker cell's contribution over the behavior of the model is lower for smaller partition cells. Because of that, the partition size should be defined by the size of the greatest heterogeneity of the material.

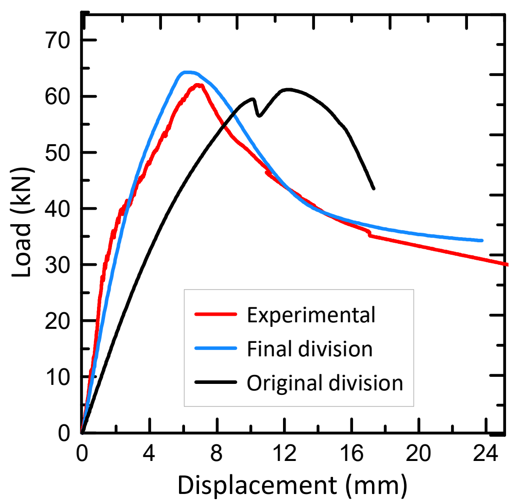

Figure 32 - Comparison between the original partition size model and the final model with bigger partition cells.

Figure 33 - Reinforcement inside the beam's model.

3.1.3 Loading and boundary conditions

Explicit analysis was adopted to ensure model convergence in post-cracking through a large number of small increments. For the explicit analysis, density values of 2500 kg/m³ for concrete and 7850 kg/m³ for steel were used and the loading was applied as a prescribed displacement, with 25 mm over 120 seconds.

The deformations of the test support elements, the distribution beam, and other elements of the setup were simulated by creating fictitious supports in the model. The machine compliance was then matched by the calibrated stiffness of these supports. These supports were assigned an elastic material with its modulus of elasticity calibrated so the initial slope of the load-displacement curve obtained from the numerical model matched the curve obtained experimentally. Figure 34 (a) illustrates the evolution of the curves obtained by the model through the calibration of the supports, and Figure 34 (b) compares the final curve with the one obtained experimentally.

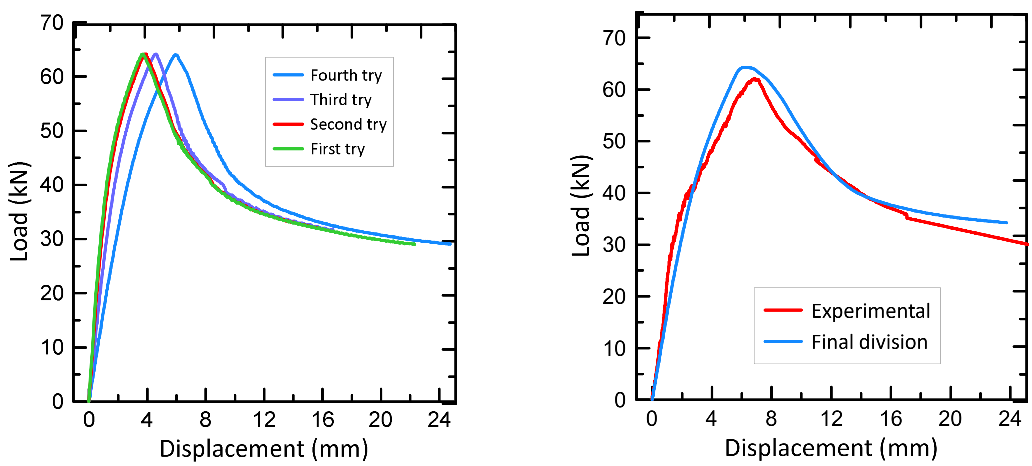

(a) (b)

Figure 34 - Calibration of the stiffness of the support elements (a) and the comparison between the calibrated model and the experimental curve obtained by Lima et al. [2].

The damage patterns observed in the numerical model reflect the UHPC beams' tendency to exhibit localized failure in flexure for beams with low reinforcement ratios due to fiber pullout in the softening branch of the load-displacement curves (Figure 35 (a)). Figure 35 (b) shows the plastic deformations in the reinforcements for the final load, showing the localization in the areas with high damage values. These pattern occurs because the damage evolution starts at the partition cells with the fastest damage evolution and are contained in specific sections of the beam as the stiffness of these sections is decreased with damage evolution in the model.

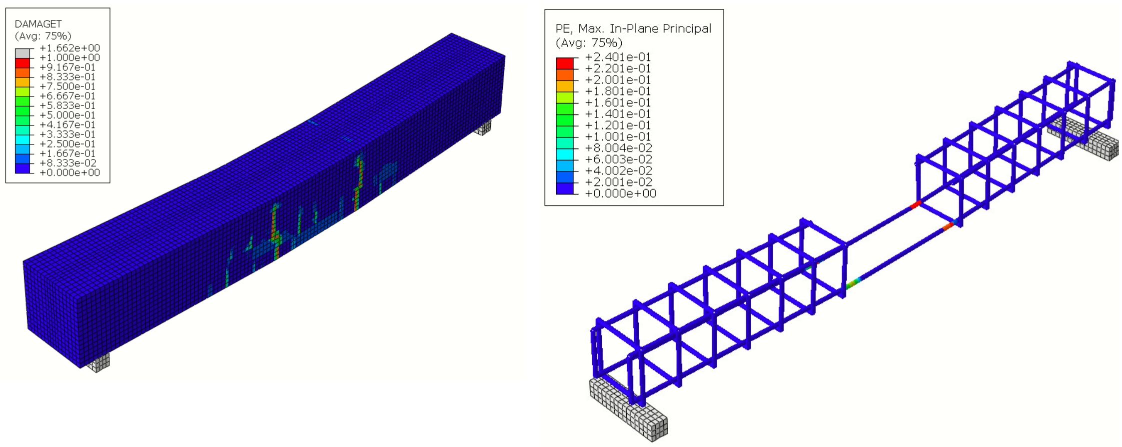

(a) (b)

Figure 35 - Damage pattern in the concrete material (a) and plastic deformations in the reinforcements (b).

3.2 Definition of the optimized cross-section

3.2.1 Methodology

Genetic algorithms is a method developed in the 1950s by computer scientists to determine an optimization routine based in the evolution of a population of candidate solutions to a specific problem using natural selection concepts [102]. The evolution of the variables governing the problem is given in terms of treating these variables as chromosomes, which are passed through the generations and subjected to natural selection.

Individuals which best approximate the solution for the problem are ranked in a way that the best ranked individuals have a higher probability of passing their chromosomes for the next generation. The ranking of individuals is made according to their performance as a solution for the selected problem. This performance is quantified in terms of a fitness function [103].

Sastry et al. [104] define the steps of evolution after the definition of a fitness function:

(1) Initialization: the original population is generated with the chromosomes defined randomly to occupy a certain domain which contains the solution;
(2) Evaluation: the fitness function is used to evaluate how well an individual performed as a solution for the problem;
(3) Selection: the selection of the individuals is an application of the “survival of the fittest” mechanism in which the individuals with higher fitness are preferable to give their chromosomes for the following generation;
(4) Recombination: the chromosomes of two or more selected individuals are combined to create a new, and desirably better, solution of the problem;
(5) Mutation: after the recombination and the selection of the chromosomes that form a new individual, a percentage of these chromosomes are changed to evaluate the vicinity of the fitness function, permitting shifts in the convergence tendency from a local optimal solution to a global optimal solution in the given domain;
(6) Replacement: The previous population is replaced with the new generated population.
(7) Repeat steps 2-6 until a termination condition is met.

The evaluation of the individuals may be made in terms of two steps. Other than the fitness function, a penalty function may be applied to reduce the fitness value of an individual if certain defined constraints are violated. Adibaskoro and Suarjana [105] define as constraints for the optimization of prestressed I girders the service conditions, ultimate flexural limit state resistance, ductility requirements, ultimate shear resistance, web slenderness ratio. Siripong et al. [106] applied the penalty function in terms of the minimum flexural strength.

For the selection phase, a roulette wheel is applied for the choosing of the parents that will give the chromosomes for a new individual. The probability of an individual being picked is given by the ratio of its fitness and the summation of the fitness of the generation [105], [107] [108].

Elitism was a concept introduced in the optimization routine to prevent the work of rediscovering fit individuals of previous generations by keeping them when a new generation is created.

In total, three generations were created by this routine comprising 80 models in total, being 30 models in the first and second generations each and 20 models in the third generation. Although a greater number of models would be recommended, the time consuming processing through explicit analysis resulted in a limitation of the numer of generations.

3.2.1.1 Initialization

An initial population of 30 beams was randomly generated and subjected to numerical analyses simulating four-point bending tests to determine load-displacement curves. The generation of each cross-section in this phase occurred randomly from the original beam following five steps: (1) selection of the dimensions of the upper flange, (2) selection of the dimensions of the lower flange; (3) selection of the thickness of the web; (4) definition of the point at the intermediate height between the bottom face of the upper flange and the top face of the lower flange; (5) connection of the extreme points of the inner faces of the flanges and the intermediate point on the web face through parabolic curves. This resulted in a new cross-section cut into the original rectangular one.

This simplified approach allows for optimization with a minimal number of variables. The five variables used in this routine were: the width and thickness of the lower and upper flanges, and the width of the web. While reducing the number of variables, the procedure results in smooth contours ensured by the alignment in parabolic shapes.

Figure 36 shows the coordinates used for the generation of the random cross-sections. The shape of the shear reinforcement was changed for open stirrups so that the thickness of the web of the beam could be generated without the need to adapt the transversal reinforcement. The modeling of the cross-sections was made automatically through a dedicated python script and the transversal bars in the top and bottom flanges were adapted to the geometries of the size of the flanges.

After simulating each beam, the load capacity is calculated from the peak point in the load-displacement curves. The ductility parameter used in this phase of the study was the drift capacity ratio as determined by Shao and Billington [99], dividing the displacement at the mid-span by the shear span of the four-point load bending test.

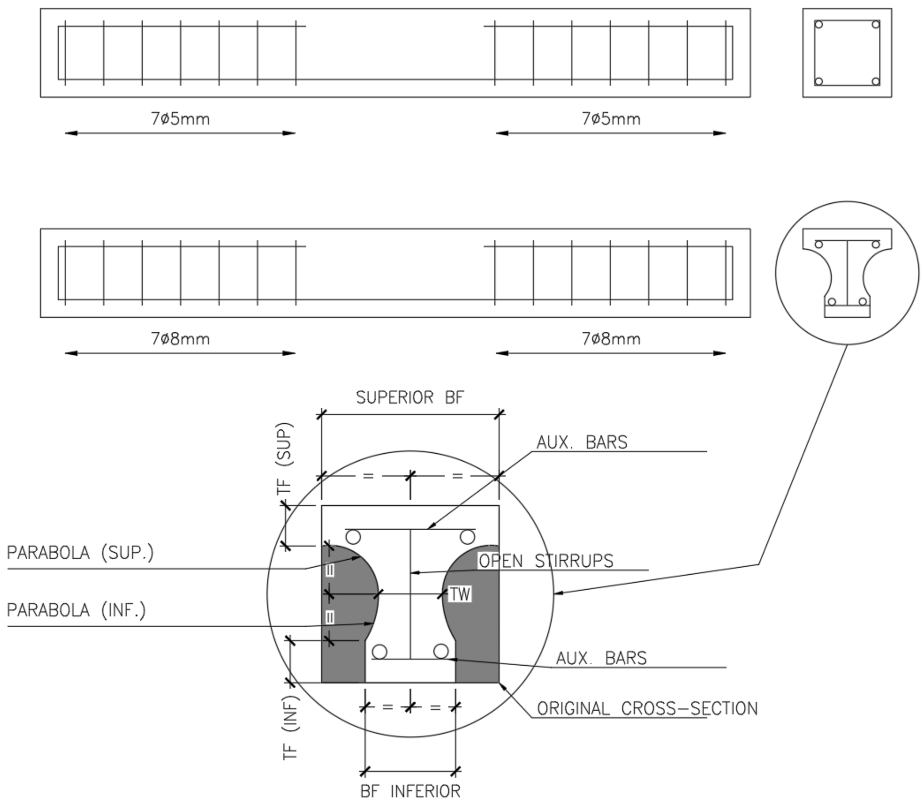

Figure 36 - Coordinates generated randomly for the initial population.

3.2.1.2 Evaluation

The studies presented by Yuan et al. [53] and Lima et al. [2] demonstrated that UHPC beams exhibit reduced ductility compared to conventional concrete beams with the same reinforcement ratios. This phenomenon is accentuated in beams with low reinforcement ratios, as they result in a lower capacity to redistribute stresses that would be resisted by the fibers after they enter the softening phase.

The study conducted by Lima et al. [2] indicated that the strength of conventional concrete beams can be matched by equivalent beams of the same height and half the width. This results in beams with a higher reinforcement ratio, reducing the drop in ductility caused by the change in material. The material exchange while maintaining the full section of the beam leads to increased strength with a significant decrease in ductility due to the inclination of the post-peak segment of the load-displacement curves.

Figure 37 depicts the models developed for the full-section beam (a) and the beam with half of the original section (b). For these models, the fictitious supports were eliminated to compare only the displacements obtained through the deformation and cracking of the elements, excluding contributions from the elastic displacement of the supports.

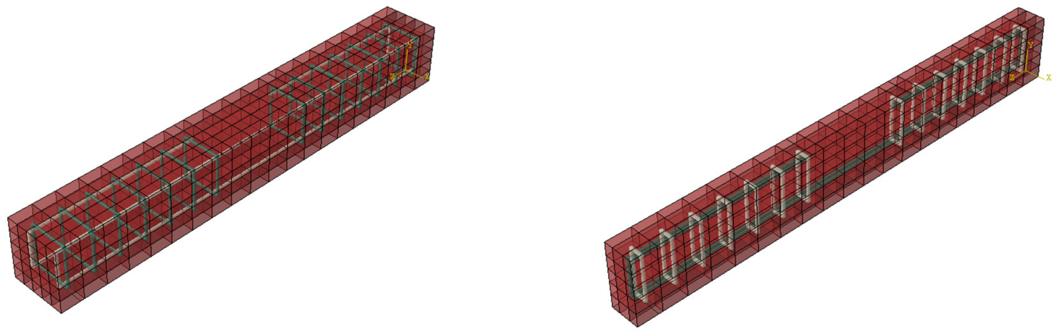

(a) (b)

Figure 37 - Numerical models developped for the beams investigated by Lia et al. (2023) with the original cross-sectio (a) and with half the original width (b).

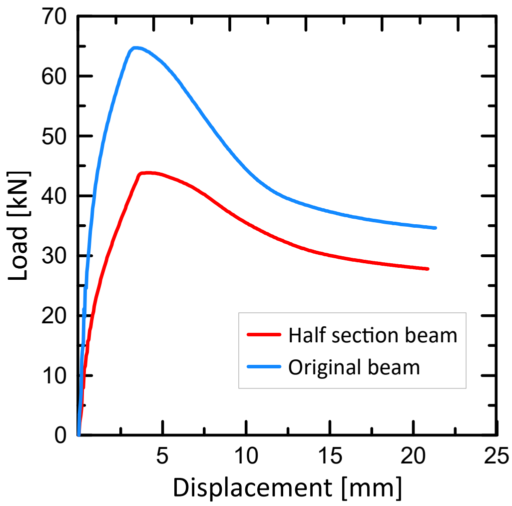

Figure 38 - Load displacement curves generated for the models with the original cross-section and with half of the original cross-section.

The optimization objective was to obtain an optimized cross-section with a higher load capacity than the beam with half of the original cross-section but still maintaining a minimum "drift capacity" of 2.5%. Figure 38 illustrates the load-displacement curves obtained for these beams with the methodology developed in item 3.1, with the half-section beam achieving a coefficient close to the recommended minimum and the full-section beam, despite representing a higher load capacity, resulting in an insufficient drift capacity.

The beams that meet the minimum requirements are ranked by fitness function, such that individuals with higher load capacities have a greater probability of being selected as parents for the next generation. The fitness function was defined according to equation (8), where the load capacity of the beam (P_i) is compared to a reference load capacity (P_{Ref}), adopted first as a value of 40 kN corresponding to the beam with half of the original cross-section. This value was then incremented when passing from the second to the third generation to 50 kN.

$$Fi = P_i - P_{Ref} \tag{8}$$

The minimum drift capacity and minimum load capacity were evaluated in terms of the penalty function, where the fitness of a beam with a drift capacity lower than 2.5% or load capacity lower than the reference stablished for that generation would be reduced to zero.

$$Fi = 0 \; if \begin{cases} P_{max} < P_{Ref} \\ DC < 2.5\% \end{cases} \tag{9}$$

3.2.1.3 Selection, recombination and mutation

The creation of the cross-sections for the next generation is done using a roulette function, where a number is randomly decided, and the interval in which this number is contained determines the parent to provide one of the chromosomes. To generate new individuals, five draws are executed to determine the five chromosomes that will form this individual, being the size of the superior flange (bfSup), size of the inferior flange (bfInf), width of the superior flange (tfSup), width of the inferior flange (tfInf), and width of the web (tw). To generate the recombination of chromossomes for the new individuals, intervals of probabilities were generated, being the intervals determined by the summation of the fitness functions of each beam, resulting in the probability given in equation (10), being P_i the load capacity of an individual and P_{Ref} the reference load capacity for a given generation.

$$i = \frac{P_i - P_{Ref}}{\sum(P_i - P_{Ref})} \tag{10}$$

When passing from the second to the third generation, elitism and mutation were included in the routine. Elitism was made by keeping at each generation, the individuals from previous generations that satisfied the final fitness function, with reference load capacity of 50 kN. Mutation was included by replacing 5% of the original chromosomes defined for the next generation.

3.2.2 Results

The compiled results for the beams of the initial generation is shown in Figure 39. The initial generation exhibited average values of 49.1 kN for load capacity and 2.42% for the ductility coefficient, both below the desired minimum final values.

After calculating the values of load capacity and drift capacity coefficient for the thirty models in the initial population, they are subjected to the penalty function for the selection of individuals that meet the eligibility criteria. For the first generation, in addition to the minimum drift capacity coefficient, the condition was added that the beams must have a higher load capacity than that found by Lima et al. [2] for the conventional concrete beam.

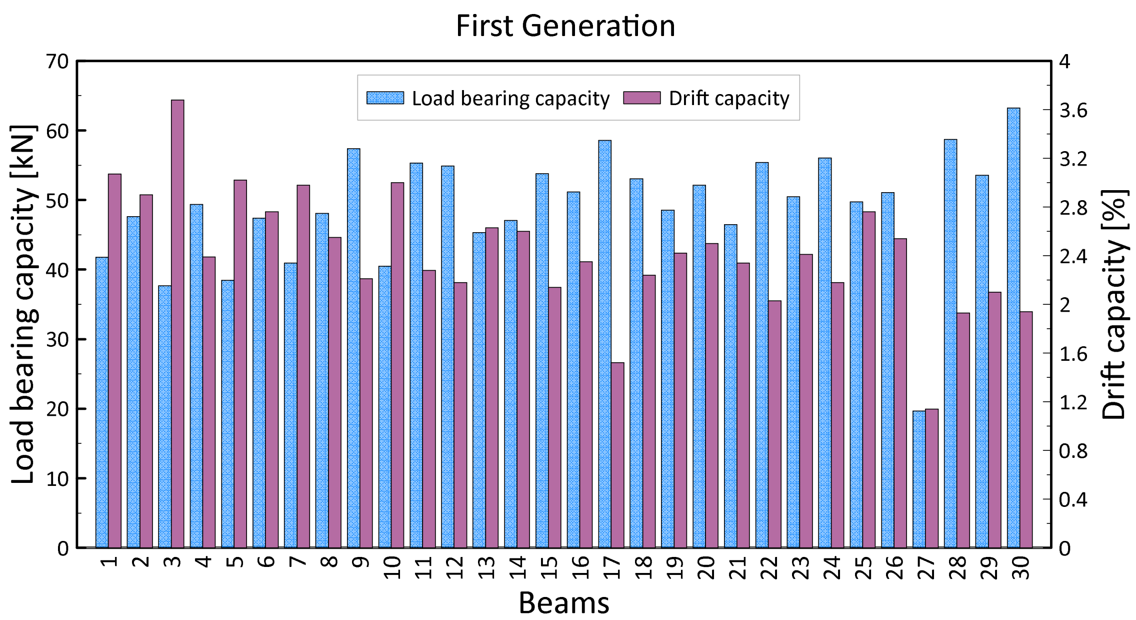

Figure 39 - Load capacity and drift capacity of the beams in the first generation.

Table 14 lists all individuals from the first generation that satisfy the requirements imposed by the penalty function, with a load capacity exceeding 40 kN and a minimum ductility of 2.5%. From these individuals, the roulette is used to select the chromosomes for the individuals of the second generation.

Table 14 - Results for the beams that satisfied the penalty conditions in the initial population.

Selected beams from the initial population		
Beam	Load Capacity [kN]	Drift capacity [%]
1	41.78	3.07
2	47.6	2.9
3	37.66	3.68
5	38.46	3.02
6	47.41	2.76
7	40.94	2.98
8	48.08	2.55
10	40.46	3
13	45.31	2.63
14	47.07	2.6
20	52.15	2.5
25	49.75	2.76
26	51.05	2.54
Average	45.21	2.85
Standard deviation	4.83	0.32

Figure 40 illustrates the results obtained for load capacity and drift capacity for individuals in the second generation. It can be observed that the second generation has less variation in the results than the initial population, indicating the convergence tendency of the optimization routine.

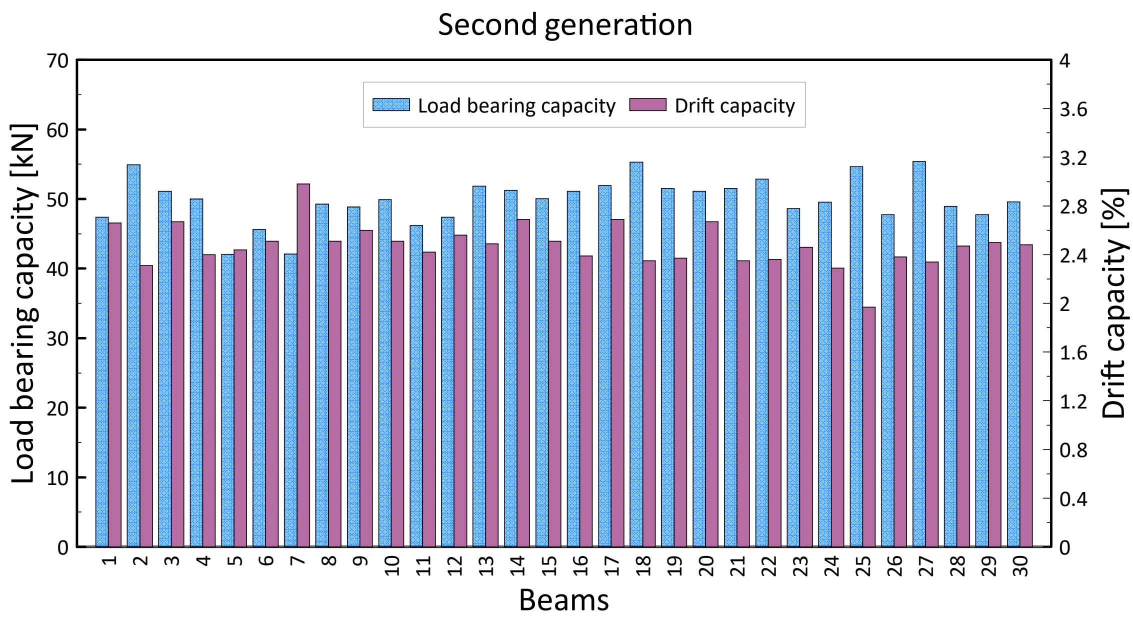

Figure 40 - Load capacity and drift capacity of the beams in the second generation.

Table 15 lists the individuals that satisfy the penalty function for the second generation, with the minimum load capacity for this generation increased from 40 kN to 50 kN. Finally, from the individuals selected in the second generation, chromosomes are chosen to form individuals in the third generation. The results for the beams of the third generation are shown in Figure 41.

Table 15 - Results for the beams that satisfied the penalty conditions in the second generation.

Selected beams from the second generation		
Beams	Load Capacity [kN]	Drift capacity [%]
1	47.39	2.66
3	51.09	2.67
6	45.61	2.51
7	42.1	2.98
8	49.27	2.51
9	48.86	2.6
10	49.91	2.51
12	47.37	2.56
14	51.26	2.69
15	50.03	2.51
17	51.92	2.69
20	51.09	2.67
Average	48.83	2.63
Standard deviation	2.83	0.13

The beams from the third generation that satisfy the imposed conditions of minimum drift capacity and load bearing capacity are listed in Table 16. It is observed that individual 5 from the third generation had the best overall result, exhibiting the highest load capacity and the second-highest ductility in the generation. Therefore, it is adopted as the most optimized cross-section from the optimization process.

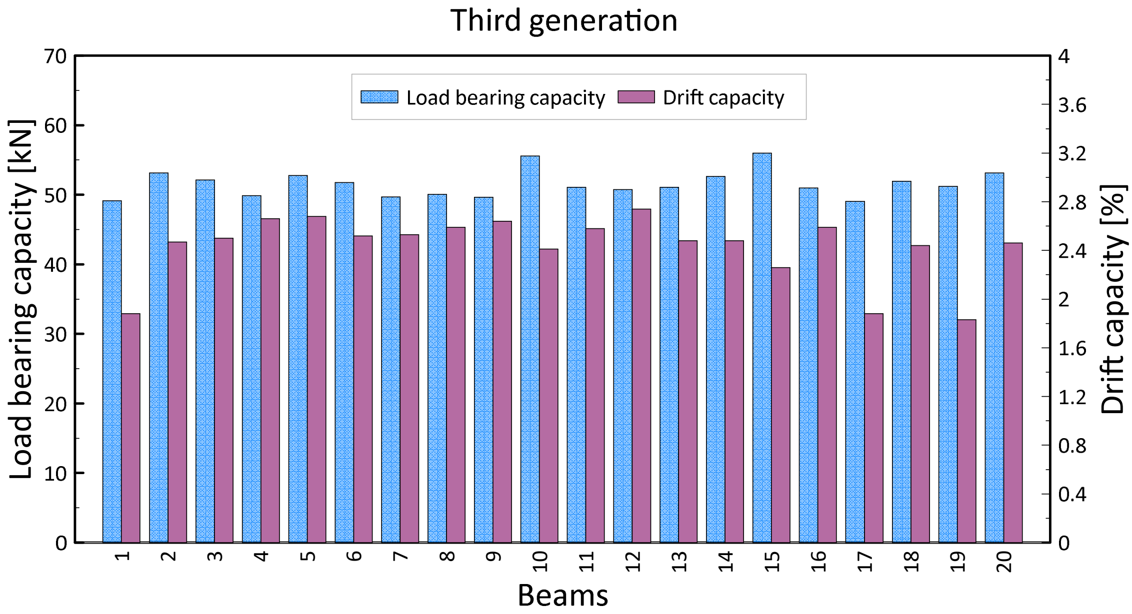

Figure 41 - Load capacity and drift capacity of the beams in the third generation.

Table 16 - Results for the beams that satisfied the penalty conditions in the third generation.

Selected beams from the third generation		
Beams	Load Capacity [kN]	Drift capacity [%]
3	52.13	2.5
5	52.79	2.68
6	51.75	2.52
7	49.68	2.53
8	50.05	2.59
9	49.65	2.64
11	51.06	2.58
12	50.75	2.74
13	50.98	2.59
Average	50.98	2.59
Standard deviation	1.09	0.078

The convergence trend throughout the optimization routine can be observed from the variation in the mean and standard deviation of the optimized parameters in each generation. While there is not a significant variation in the mean values of each generation, it is noticeable that with the progression of generations, in addition to a slight increase in the mean value of load capacity, the corresponding standard deviation decreases in each generation, indicating convergence to the maximum load capacity value that satisfies the condition imposed by the penalty function. Regarding drift capacity values, there is a small oscillation around the specified minimum value of 2.5% with an increase from the initial to the second generation. However, when transitioning from the second to the third generation, there is a slight decrease and an increase in the standard deviation. The main reason that influenced this decrease was the inclusion of mutations when transitioning from the second to the third generation. Figure 42 shows the general trend observed through the optimization process. Although the mutations guarantee that the optimization will not tend to a locally optimized set for the random variables that is not the globally optimized, it also creates deviations in the optimization process, increasing the dispersion of the results and delaying the convergence of the optimization routine.

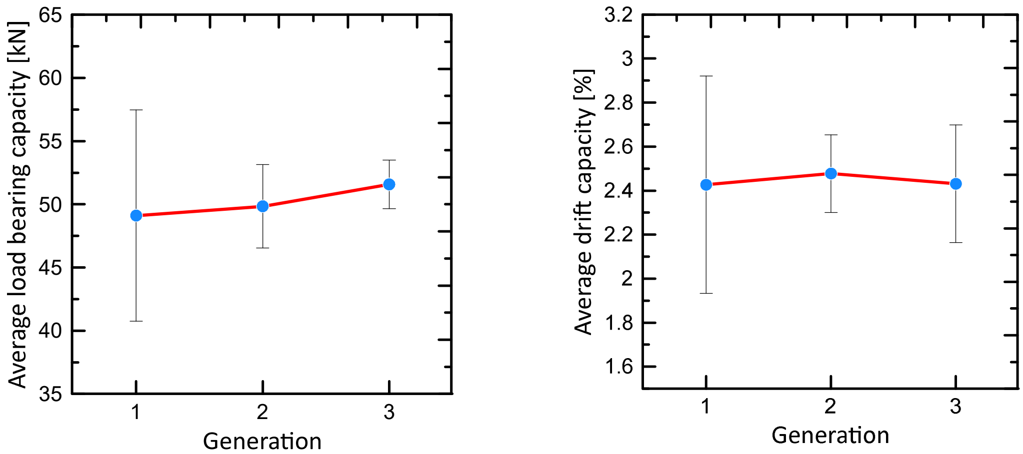

(a) (b)

Figure 42 - Evolution of average and standard deviation of load bearing capacity (a) and drift capacity (b) at each generation.

Figure 43 shows the results only for the beams that satisfy the requirements of the final penalty function in each generation, considering minimum load bearing capacity of 50 kN. Figure 43 (a) illustrates the evolution of the percentage of individuals in each generation that meet the minimum drift capacity requirement of 2.5% and a minimum load capacity of 50 kN, increasing from 6.7% in the first generation to 45% in the third generation. Figure 43 (b) displays the evolution of the mean load capacities of these individuals in each generation. There is an increment in each generation, simultaneously with a decrease in the standard deviation. Figure 43 (c) illustrates the evolution of the ductility of these individuals, showing a tendency towards the minimum drift capacity of 2.5% and a gradual decrease in the standard deviation, indicating convergence to this minimum value while there is an increase in load capacity.

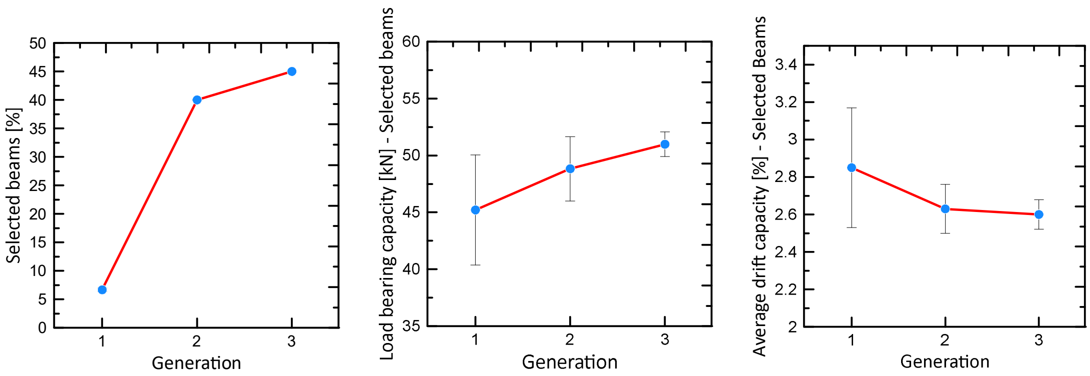

(a) (b) (c)

Figure 43 - Proportion of beams that fulfil the penalty laws (a), and average and standard deviation of the load bearing capacity (b) and drift capacity (c) of these beams at each generation.

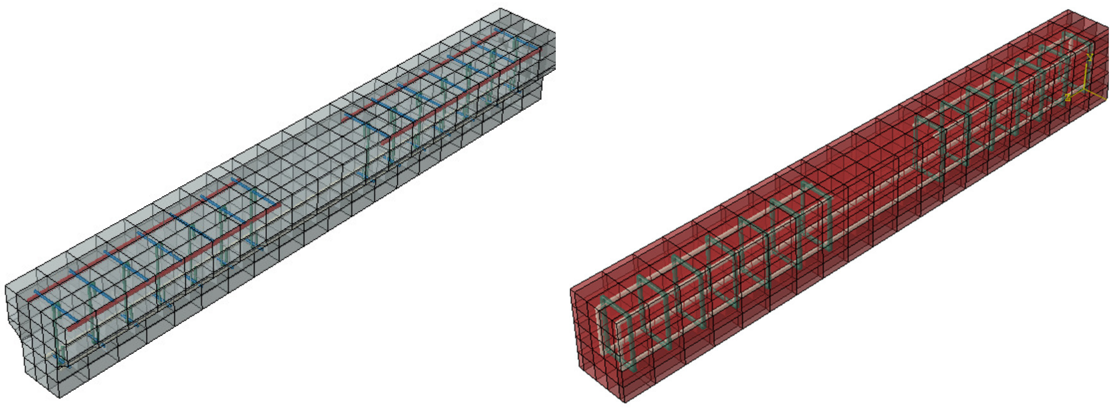

(a) (b)

Figure 44 - Beam with the optimized cross-section (a) and the equivalent rectangular beam (b).

As a result of the optimization, a section with a load capacity of 52.79 kN and a drift capacity coefficient of 2.68% was obtained, satisfying the minimum value for assuring ductility but still accounting for increase in load capacity. For comparison purposes, a rectangular section resulting in approximately the same load capacity as the optimized cross-section was obtained by successively manually changing the width of the cross-section resulting in a width of 112.5 mm. Both the optimized beam and the equivalent rectangular beam is shown in Figure 44.

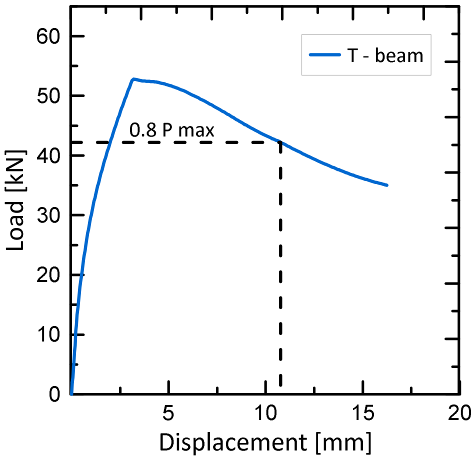

(a)

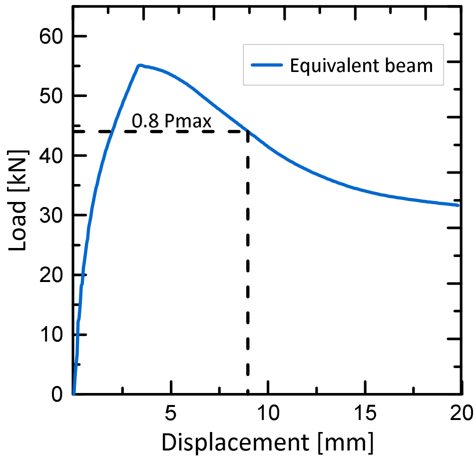

(b)

Figure 45 - Load-displacement curves for the optimized beam (a) and the equivalent rectangular beam (b).

The result of the optimization process indicates that the optimal section is a T-girder, where material was removed from the tensile part. This results in less redistribution of tensile stress to the reinforcements when the fibers enter the softening phase. At the same time, it is observed that the upper flange has been maintained with a width close to the original beam, resulting in a larger compression flange and a smaller tensile resultant in the tensile part due to the reduced web thickness.

Table 17 summarizes the results of load capacity and drift capacity ratio obtained for each of the modeled beams. It is observed that as a result of the optimization process, a beam with a load capacity 20.42% higher than the originally proposed half-section beam was obtained, and a ductility 17.54% higher than the equivalent rectangular cross-section beam.

The individual results for each of the individuals in each generation are given in Annex D, with the corresponding cross-section format and load displacement curves with load capacity, failure load and drift capacity computed in each case.

Table 17 - summary of the properties of the studied beams.

Viga	Load Capacity [kN]	Drift capacity
Original cross-section (150 mm)	64.73	1.96
Half width (75 mm)	43.84	2.56
Optimized cross-section	52.79	2.68
Equivalent rectangular section (112.5 mm)	55.14	2.28

4 EXPERIMENTAL PROGRAM – MATERIAL LEVEL

The experimental program is divided into three main topics. In the first one, the mix design for the UHPC is determined and a fine correction on the rheology is made for stabilization of the fibers in the structural element's volume to obtain a good fiber distribution preventing segregation while maintaining the enhanced material properties.

In the second part, a material characterization is conducted. The goal of this phase is to obtain a complete characterization of the UHPC mix in terms of its resistance, both in compression and in tension, and also to obtain is uniaxial behavior to serve as a base for the selection of adequate uniaxial and damage evolution models as input parameters for the constitutive model Concrete Damaged Plasticity (CDP).

In the third phase of the experimental program, the beams whose cross-sections were studied through a preliminary numerical program in the topic 3.2 are fabricated and subjected to testing to validate all the previously obtained hypothesis.

4.1 Mix design and rheology stabilization

The UHPC mix passed through a rigorous optimization process to ensure the stabilization of the fibers and obtain an adequate distribution in the concrete mix. For that, mixes containing different values of superplasticizer and viscosity modifying agent were used and subjected to compressive tests for the control of the compression strength. In addition, dogbone specimens were molded and broken with hammers to verify the distribution of the fibers inside the specimen's volume. The procedure is carefully detailed in Annex A.

Table 18 - Final mix adopted for UHPC after stabilization of the fibers.

Materials	Consumption (kg/m³)
Cement CPV-ARI RS	800.00
Industrialized Sand AG50/60	846.20
Pozofly fly Ash	80.00
Quartz powder SM325	200.00
Micro-silica 920U	80.00
Water	166.20
MasterGlenium 51 Super plasticizer	20.00
Viscosity modifying agent	3.00

For the final mix, values of 2% and 0.375% were adopted for mass consumption of the superplasticizer and viscosity modifying agent in relation to the cement mass. Table 18 summarizes the material consumption for the final mix. The final mix resulted in a slump reduction of approximately five centimeters compared to the original mixture with no VMA and no reduction on superplasticizer, resulting in a total of approximately 26 cm (Figure 46).

(a) (b)

Figure 46 - Spread result for the final mix.

The mixing procedure for molding a total of 130 L using a 600 L capacity mixer, model Cibi M600, followed the following procedure procedure:

1 - Dry materials were mixed in the mixer for about five minutes.

2 - Cement was added, and mixing continued for five minutes.

3 - Half of the water, followed by the addition of superplasticizer and VMA, and the remaining water (around 2 minutes) were added, and mixing continued for an additional five minutes.

4 - Fibers were added to the mix, and mixing continued for five more minutes

4.2 Test Methods

For the material characterization, a set of monotonic and cyclic tests was performed in both compression and tension for the determination of the uniaxial and damage evolution models.

4.2.1 Compressive tests

The characterization of concrete in compression was performed using two testing configurations. Four cylindrical specimens were subjected to compression tests with load control to determine compressive strength and modulus of elasticity. Another four specimens underwent tests controlled by circumferential displacement to determine the compressive uniaxial behavior with post-peak branch of the curve. The tests were conducted in a MTS universal testing machine model 311. Figure 47 depicts the adopted configuration for the tests controlled by circumferential displacement.

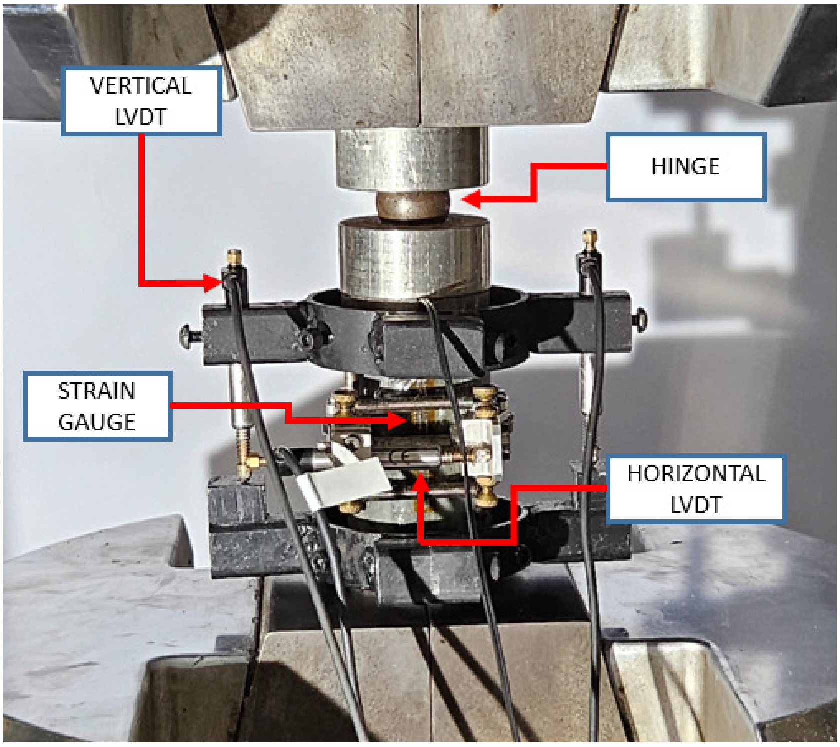

Figure 47 - Compression test setup for post-peak measurement.

The load-controlled tests were conducted at a rate of 0.3 MPa/s as specified in NBR 5739 [109]. Strains were measured using strain gauges attached to the side of the specimens. The modulus of elasticity was computed through a linear fit on the stress-strain curves calculated from the strain gauge readings.

The tests with circumferential displacement control were calibrated according to Pressmair [77] to eliminate the initial accommodation of the LVDTs and rotate the load-displacement curve to align the initial stiffness measured by both LVDTs and strain gauges. The loading was made with a circumferential displacement rate of 0.08 mm/min.

In addition to the monotonic tests, cyclic tests were conducted following the recommendations of Wang and Xu [110] for damage evolution determination. Initially, the specimens were loaded until exceeding the displacement corresponding to the peak load (determined according to monotonic tests). Unloading was performed by load control at a rate of 1 kN/s. A minimum load was maintained at 5 kN so that the actuator and the specimen did not lose contact [110].

The first unloading point was initiated from a 0.5 mm marking on the horizontal LVDT connected to the chain to ensure that the loading surpassed the peak load. Each reloading cycle was conducted at the same rate as the monotonic tests.

4.2.2 Tensile tests

For the tensile tests, dogbone specimens with the dimensions shown in Figure 48 were prepared and subjected to direct tension. The test setup is shown in Figure 49. The specimens were fixed to a MTS 311 machine using 10mm diameter steel bars attached to the ends of the specimens, with an embedded length of 10 cm. The attachment was performed using Sikadur 32.

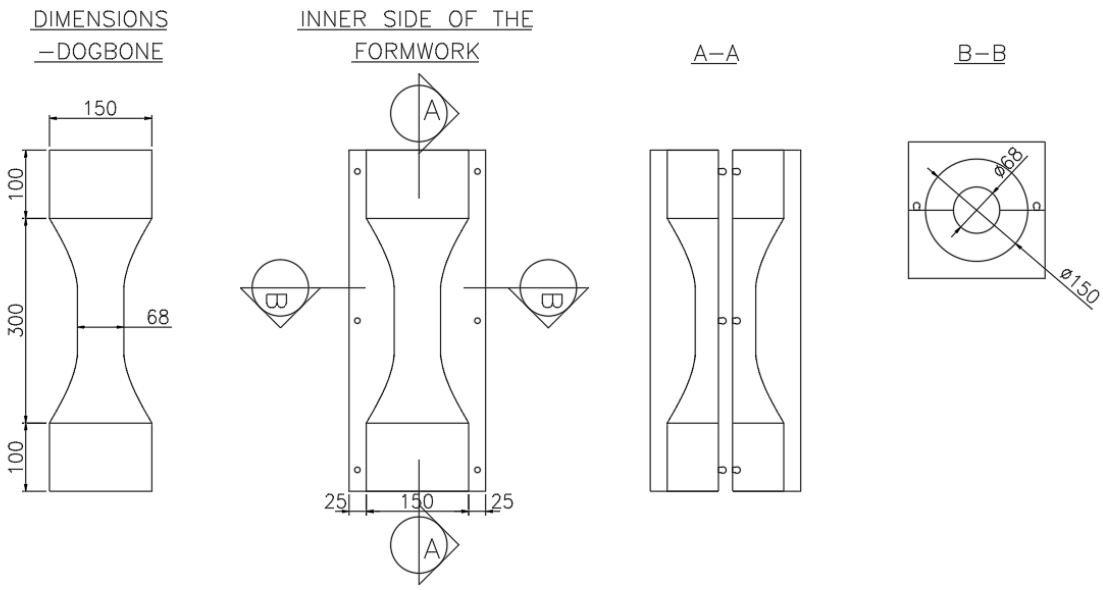

Figure 48 - Dimensions for the dog bone type specimens subjected to direct tension tests.

For crack opening measurements through DIC analysis, a speckle pattern was painted on the central part of the specimens, where the section reduction occurs. This pattern was selected for a total opening of 30 cm and captured with 5 MP cameras. Two cameras were used to capture photos every five seconds for the 3D DIC analysis. Photo processing was carried out using the VIC3D program. A set of calibration images was made before testing. After calibration images were taken, the analysis in the software was automated, specifying only the points for measurements with digital extensometers.

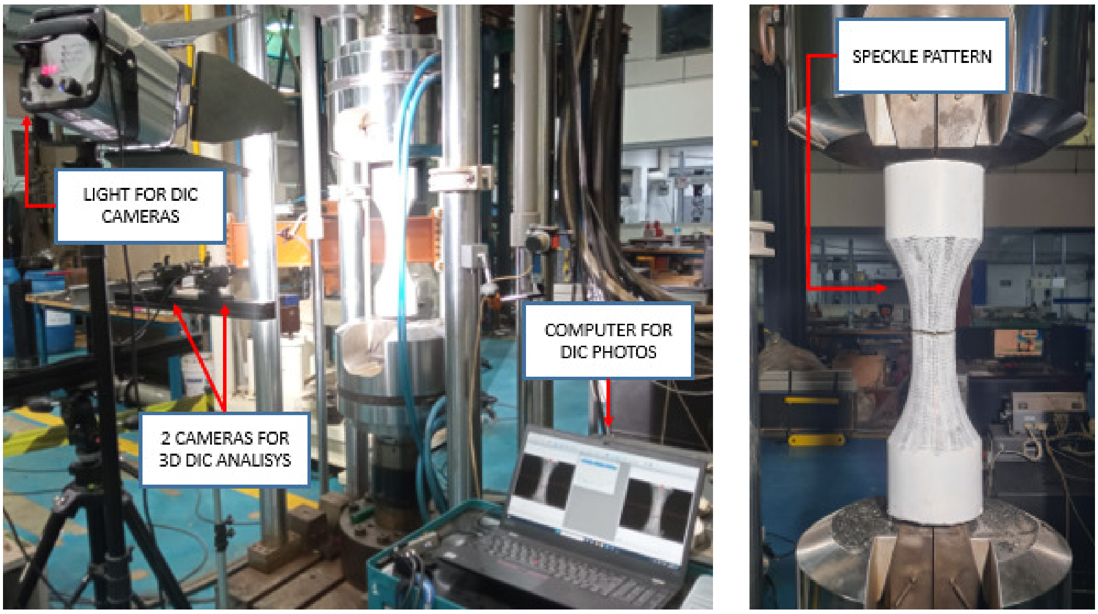

(a) (b)

Figure 49 - Direct tension tests setup (a) and dogbone specimen with speckle pattern fixed to the testing machine (b).

The fixation of the bars at the ends of the dogbone specimens followed the following steps:

(1) Measurement of the center of the end face of the specimen with a ruler, alignment of the drill with a laser, and drilling to a depth of 10 cm. The holes were cleaned with compressed air jets and a piece of cloth was inserted to remove any remaining concrete dust;

(2) Mixing Sikadur 32 with a 1:2 ratio of components A and B, respectively. The mixture was placed in the hole with a spoon, and air bubbles were expelled using a flexible rod;

(3) Application of Sikadur on the surface of the CA-50 steel bar with a diameter of 10 mm in the section that is anchored. The bar was positioned vertically with the help of a wooden mold;

(4) Painting the specimens with white paint and a speckle pattern for DIC analysis, with the pattern corresponding to a 5 MP camera and a total opening of 30 cm, corresponding to the section where the reduction occurs in the specimen.

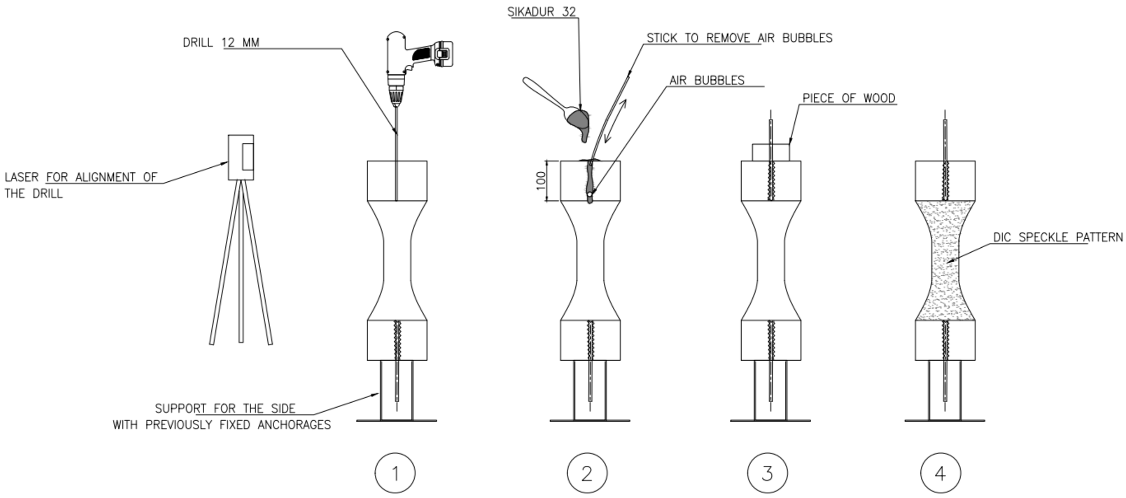

Figure 50 - Procedure for the preparation of the dogbone specimens.

The first attempts at anchoring that did not strictly follow this procedure resulted in the failure of the anchors without the formation of cracks in the center of the specimens. Figure 50 illustrates the procedure for bar anchoring, and Figure 51 depicts the failure in the anchors of the specimens.

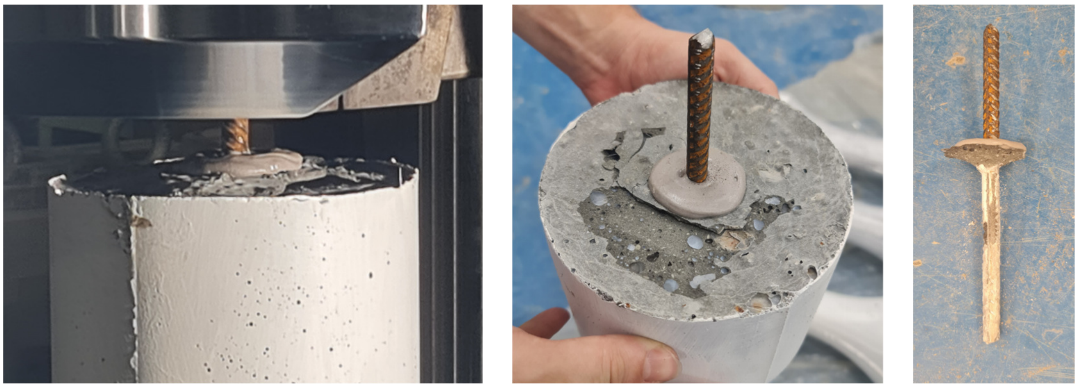

(a) (b) (c)

Figure 51 - Anchorage failure observed in the initial tests.

Specimens DB1 to DB5 were subjected to monotonic tensile tests, from which the Stress - Crack Opening curves were obtained. From these tests, the tensile strength of the matrix and the crack energy were obtained. The tensile strength of the matrix was taken from the image where the first crack appeared, and the crack energy was calculated by numerically integrating the stress - crack opening curve using the trapezoidal method.

The tests were conducted in a MTS universal testing machine model 311. Cyclic tests were conducted through displacement control considering increments of 0.1 cm in actuator's displacement at the end of each cycle. Each cycle consists of a loading stage with displacement control at a speed of 0.2 mm/min, followed by unloading with load control at 2 kN/s until a minimum load of 5 kN is reached. This load is maintained to prevent undesired compression that could compress the fibers in the crack. Linear extrapolation was performed in each cycle to calculate the residual crack openings corresponding to unloading with zero force on the actuator.

For each loading and unloading cycle, the slopes connecting the unloading point to the reloading point were calculated. The experimental damage evolution was calculated for each cycle by calculating the ratio between the slope defined in each cycle and the slope in the undamaged stage. Using the values of residual crack opening, damage in each cycle, and tensile stress at each unloading point, the bt parameter that best fits the Birtel and Mark damage curve to the dataset was interpolated.

The fibers' distribution in the failure section of each dogbone specimen is shown in Annex B.

4.2.3 Structural tests

4.2.3.1 Fabrication of the beams

For the investigation in the structural level, a total of five beams were casted based on the cross-sections modeled in Chapter 3. The casted beams are specified as follows:

1 - A beam with a 150 x 150 mm section without reinforcement to verify the behavior with only the Dramix OL 13/.20 steel fibers.

2 - A 150 x 150 beam with two 8 mm bars as longitudinal reinforcement representing the full-section beam (under-reinforced).

3 - A 75 x 150 mm beam with two 8 mm rebars as longitudinal reinforcement corresponding to the half-section beam.

4 - A beam with the cross-section shape resulting from the genetic algorithm optimization procedure.

5 - A 112 x 150 mm beam corresponding to the equivalent rectangular beam with the same load capacity as the T girder.

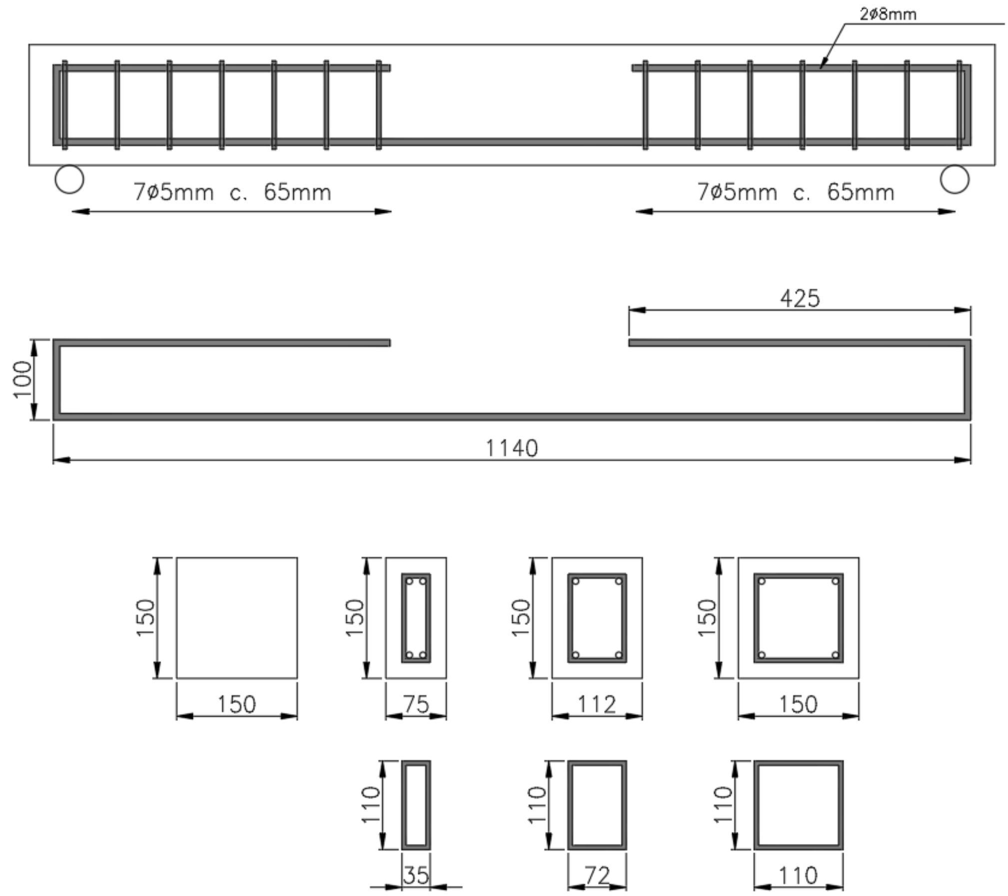

Figure 52 - Rectangular beams' cross-sections and reinforcement.

For the rectangular beams, a transversal reinforcement configuration was adopted with 5 mm stirrups spaced of 65 mm. The height of all sections was maintained at 150 mm, with a reinforcement cover of 20 mm. Thus, the rectangular section beams received stirrups with a height of 110 mm. Although the shortest beam showed small transverse spacing between the longitudinal rebars, this was considered acceptable for aggregate-free and self-consolidating concrete. Figure 52 illustrates the configurations adopted for the rectangular section beams.

For the T-girder, the configuration adopted during the modeling phase was maintained, with open stirrups and stirrup holders for the assembly of reinforcements. The stirrup holders were specified with different lengths in the upper and lower parts to accommodate the reinforcements in the T-section.

The longitudinal reinforcements were divided into upper and lower reinforcements due to the difference in width between the upper flange and the web of the beam, resulting in a total of two lower bars and four upper bars longitudinally. Figure 53 illustrates the scheme adopted for the T girder.

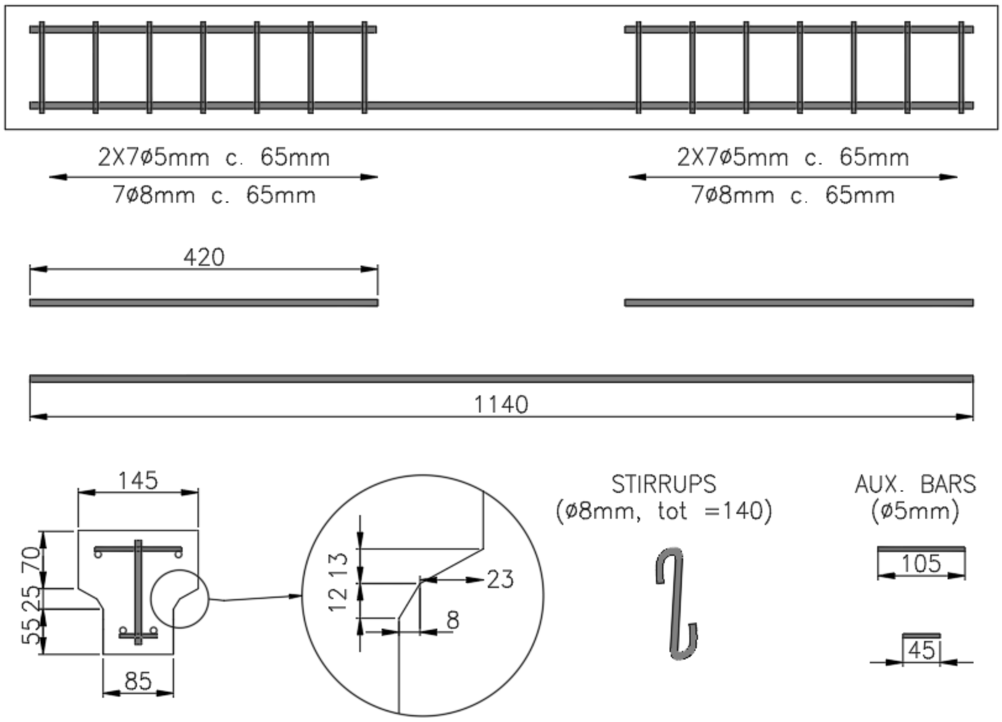

Figure 53 - T girder cross-section and reinforcements.

During the structural tests conducted by Lima et al. [2], the vertical displacement caused by the compliance of the test setup resulted in the need for the calibration of support stiffness to correct the load-displacement curves and make the comparison between the results from the numerical models and the experimental curves. To reduce this effect, the test setup used in this study comprised in addition to the DIC speckle in the constant moment region, the LVDT in the midspan of the beam and the distribution beam with hinges for the four-point load configuration, two additional LVDTs to measure the displacements on the supports.

Figure 54 depicts the configuration adopted for the four-point bending tests. A spacing of 300 mm between the load introduction points was adopted by using rods below the load distribution beam. The regions subjected to Digital Image Correlation (DIC) analyses are shown with a dotted pattern for the central region of 400 mm.

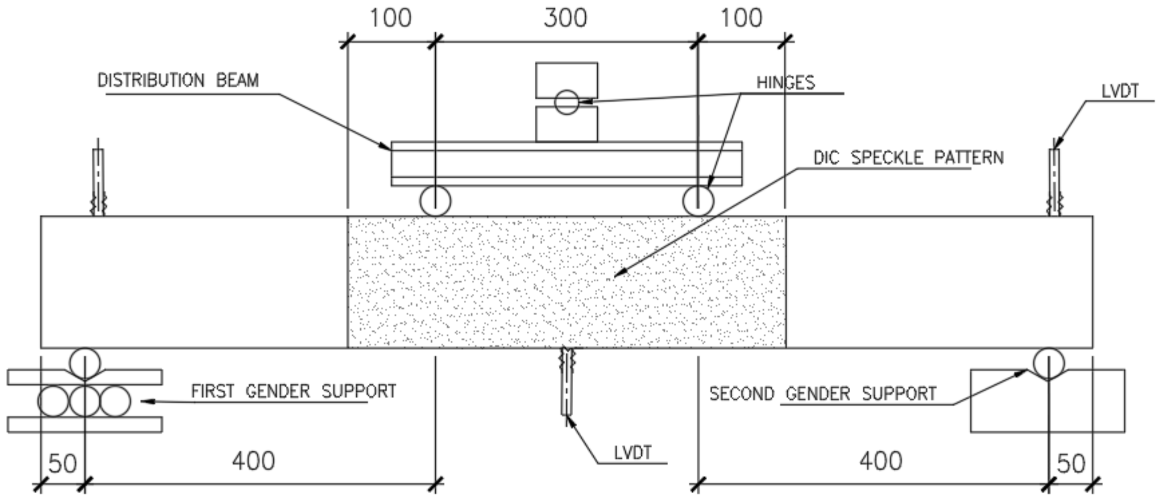

Figure 54 - Test setup for the four-point load bending tests.

For the fabrication of the T-section beam formwork, the following procedure was adopted (Figure 55):

1 - Construction of plywood forms with internal rectangular-shaped filling.

2 - Cutting strips of expanded polystyrene (EPS) to the required dimensions to fill the spaces between the rectangular forms.

3 - Gluing the EPS strips and sanding to create the rounded contour adopted in the modeling.

4 - Attaching plastic coating to smooth the surface of the formwork.

(a)

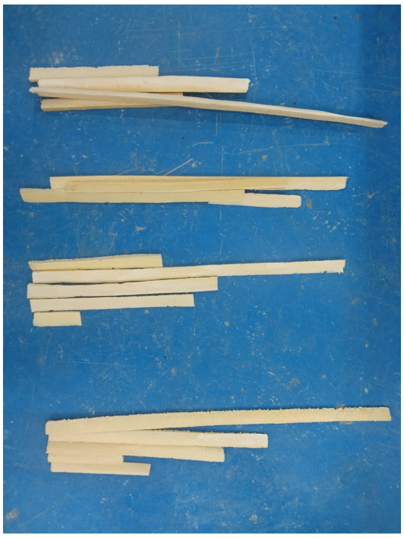

(b)

(c)

(d)

Figure 55 - Process for fabrication the formwork for the T-girder, with wooden plates (a), EPS strips (b) for the round contour (c) and final mold with plastic film in the interior (d).

The reinforcement of the T-beam was done with open stirrups and stirrup holders attached to the longitudinal reinforcements by wires. To provide greater stiffness to the system, a wire was added both in the longitudinal and vertical directions. Figure 56 illustrates the arrangement of the T-beam reinforcement.

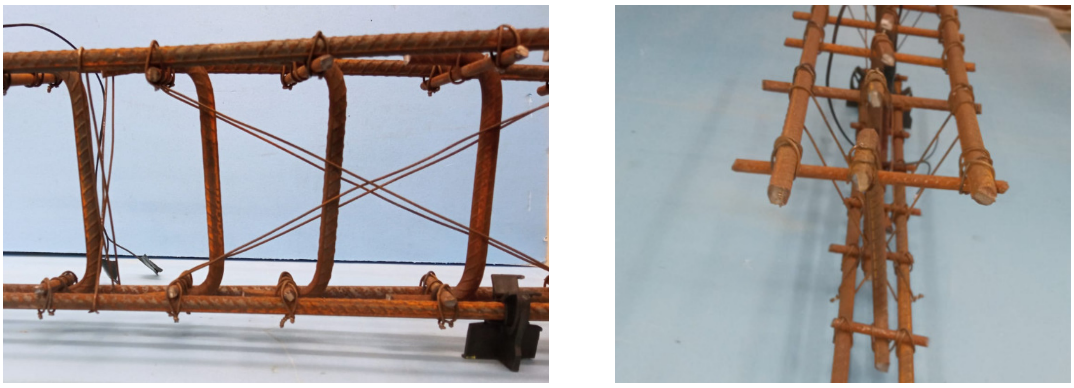

(a) (b)

Figure 56 - Reinforcement scheme of the T-girder in the longitudinal plane (a) and transversal plane (b).

For each beam, a pair of strain gauges was fixed to the reinforcements: one in the middle of the lower longitudinal reinforcements and one on a stirrup's leg in the middle of the shear span. The strain gauges were wrapped in insulating tape for protection during concrete pouring. The reinforcements were cleaned and smoothed with a micro grinder at the positions where the sensors were attached.

The casting of large quantities of UHPC proved to be challenging because this material loses its workability approximately one hour after water is added to the mix. Additionally, casting the beam in multiple batches presents the challenge of a dry layer forming quickly on the UHPC in its fresh state, preventing fibers from the more recent concrete from penetrating the layers already in the forms. Therefore, the decision was made to cast the beams in a single batch using a 600 L capacity mixer, model Cibi M600. A total of 130 L was casted.

At the end of the mixing time, the forms were positioned directly at the end of the mixer and were inclined so that the concrete was placed on one end of the form and flowed to the other side, resulting in preferential longitudinal alignment of the fibers. When the form was filled, the surface was smoothed. Figure 57 illustrates the form-filling procedure. The cast beams were covered with plastic film to prevent water from evaporating from the top layers. After 48 hours, the beams were demolded and placed in a curing chamber for 28 days.

(a) (b) (c)

Figure 57 - Pouring of the concrete in the formwork from one of the sides (a), regularization of the concrete in the formwork (b) and covering of the concrete with plastic film to prevent water from evaporating (c).

4.2.3.2 Testing of the beams

Figure 59 illustrates the setup adopted. For positioning the LVDTs (Linear Variable Differential Transformers), a metal beam was placed on a support separate from the rest of the test. Both the LVDTs at the supports and the central LVDT were fixed to this beam. The alignment of the support rollers of the distribution beam and the hinge was done using a laser to ensure that the assembly remained centered. Additionally, besides the strain gauges attached to the reinforcements, two supplementary strain gauges were glued to the upper and lower faces of the beams. The bonding of these strain-gauges was made using Araldite glue after the surface was smoothed with sandpaper.

The beam supports were assembled so that one of the supports simulated a fixed hinge support, with free rotation and restricted translation, and the other a roller support, with free rotation and translation in the horizontal direction. To achieve this, a plate was positioned over a roller box. A steel I-beam, with a length of 50 cm, was adopted as the distribution beam.

The tests were subjected to displacement control, with a 0.1 mm/min loading rate for the displacement of the actuator. The tests were conducted until at least 20% post-peak drop in the observed load-displacement curves, except for the half section beam to prevent the beam from damaging the test setup.

Figure 58 shows the entire test setup with the DIC equipment and Figure 59 shows the four-point load test setup with the DIC speckle pattern.

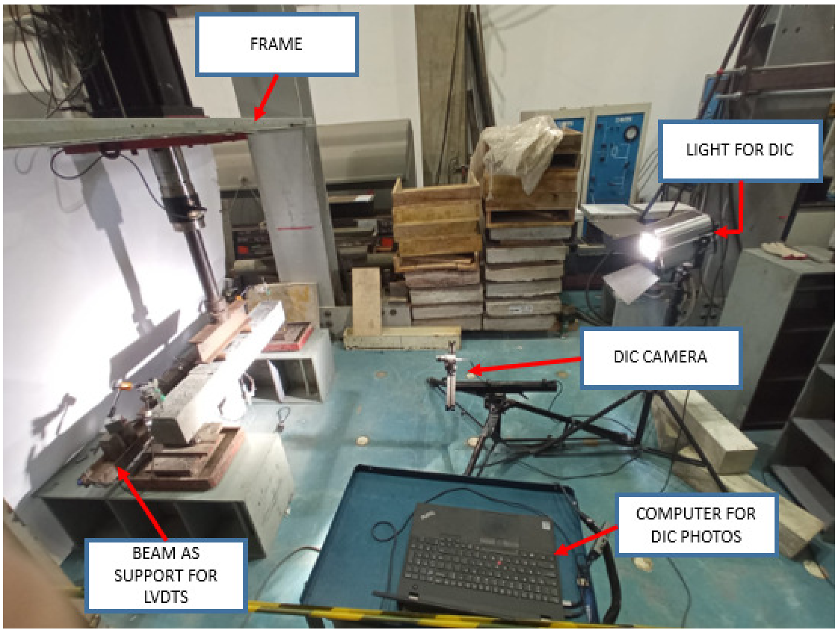

Figure 58 – Test setup for the four-point load bending tests on UHPC beams and measurement through DIC.

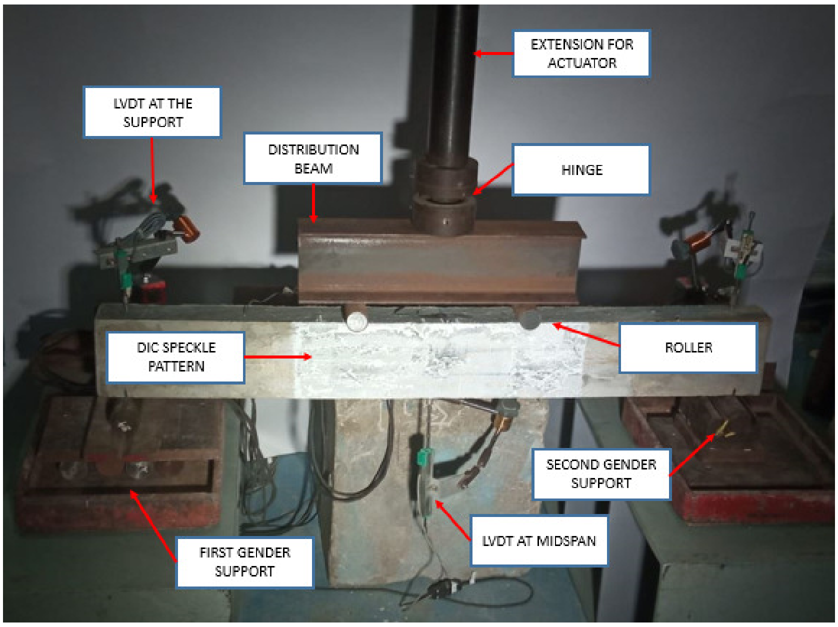

Figure 59 - Test setup for the four-point load bending tests on UHPC beams.

4.3 Results

4.3.1 Compressive tests

Table 19 summarizes the results obtained from the load-controlled tests, with average and standard deviation for compressive strength and Young's Modulus for specimens C1 to C4

Table 19 - Results for the load controlled compressive tests.

	C1	C2	C3	C4	Average	Standard deviation
fc [MPa]	139.2	142.3	131.9	150.8	141.05	7.83
Ei [GPa]	57.69	51.04	65.3	53.32	56.84	6.28

For the monotonic tests with the horizontal displacement control, initially, specimen CP 5 was loaded considering an opening of 0.008 mm/min for the horizontal LVDT, however, this test resulted in accommodation at some loading points, making it excessively long. The test was interrupted and restarted with a rate of 0.080 mm/min. The curves obtained considering this loading rate are shown in Figure 60.

Figure 60 shows all the stages for the determination of the feedback signal for C5 to C8, with the original reading obtained through the LVDTs, the correction of the original accommodation of the curve for lower stress values, the final feedback signal and the initial stiffness determined through the strain gauges.

Figure 61 shows the final stress-strain curves obtained for specimens C5 to C8 after the corrections shown in Figure 60, with the comparison of the initial stiffness calibrated through the feedback function and from the strain gauges fixed at the specimens body. It can be seen that the calibration resulted in an overlap of the strain gauge readings with the linear part of the stress-strain curves from the LVDT. The snapback in Figure 60 (a) in not present in Figure 61 (a) after the rotation of the curve.

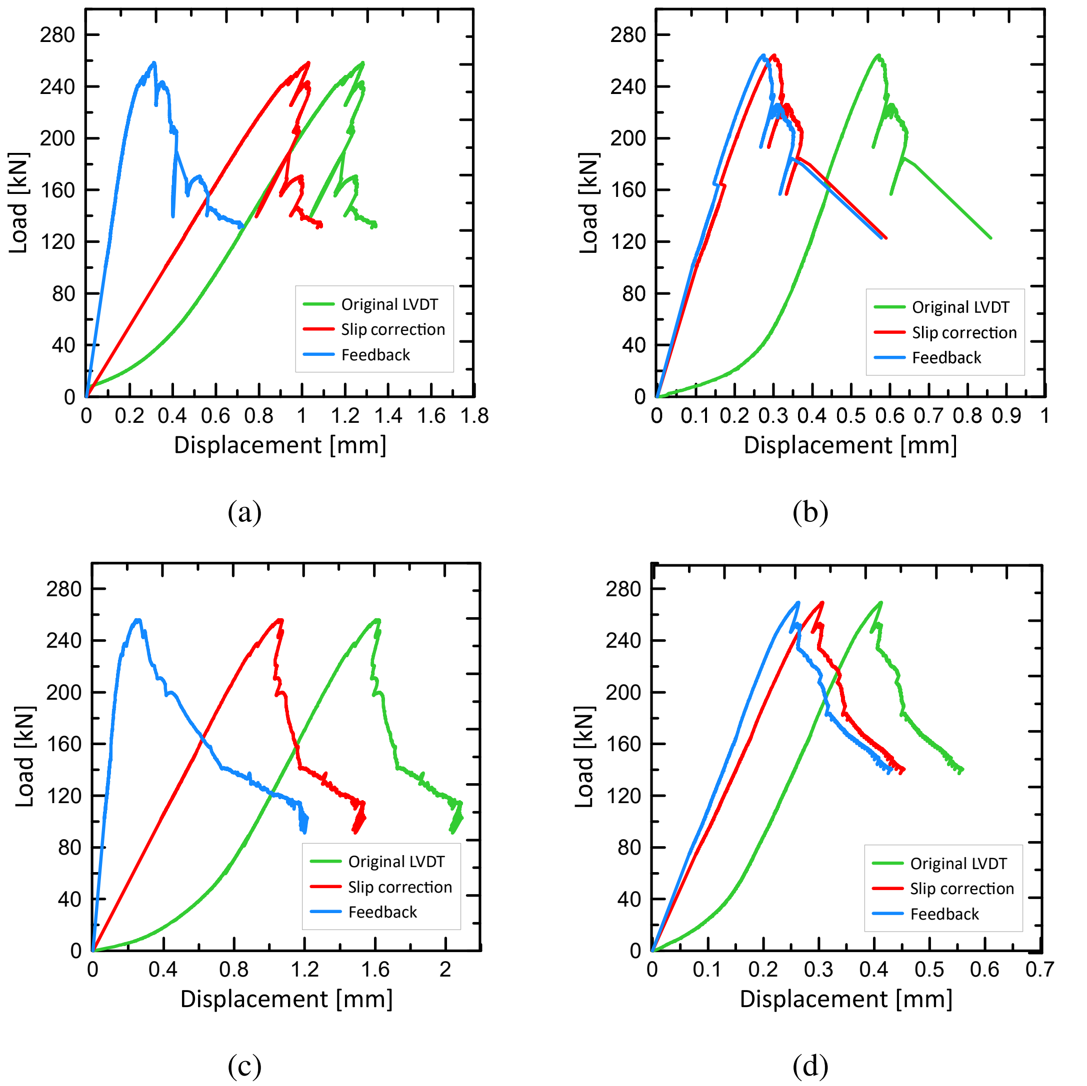

Figure 60 – Initial LVDT curves, correction for elimination of LVDT slip and rotation through feedback function for specimens C5 (a), C6 (b), C7 (c) and C8 (d).

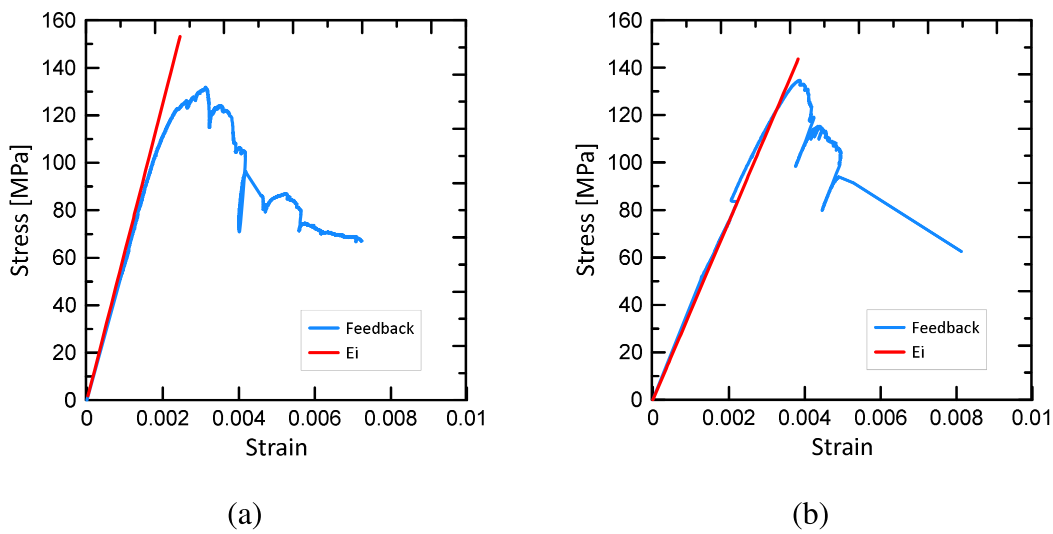

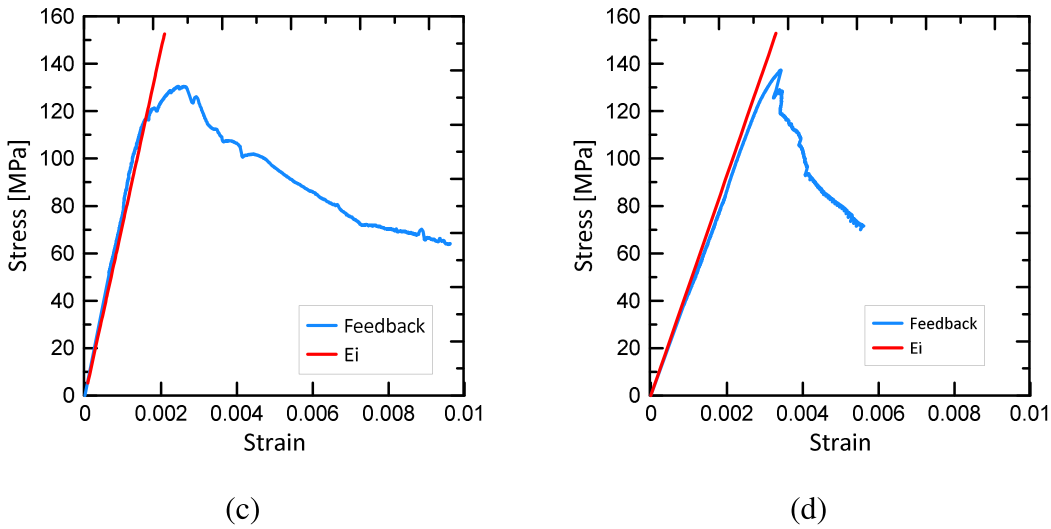

Figure 61 – Final stress-strain curves calibrated through the LVDTs and initial stiffness obtained through the strain gauges for specimens C5 (a), C6 (b), C7 (c) and C8 (d).

Table 20 summarizes the results for the monotonic compressive tests after correction of the curves. Average and standard deviation values are shown for compressive strength measured through the peak-load, Young's modulus measured through the strain gauges and the peak strain.

Table 20 - Compressive strength, modulus of elasticity and peak strain for the circumferential displacement controlled tests.

	C5	C6	C7	C8	Average	Standard Deviation
fc [MPa]	131.72	134.62	130.48	137.27	133.52	3.04
Ei [GPa]	62.53	37.54	72.95	46.40	54.86	15.89
Peak strain	0.0031	0.0039	0.0025	0.0034	0.0032	0.00059

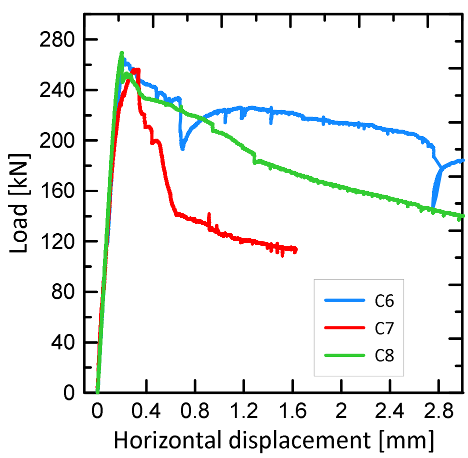

Figure 62 - Load - horizontal displacement measured by the horizontal LVDT.

Figure 63 shows the final curves obtained for the cyclic tests for specimens C9 to C14. For each cycle, the corresponding stiffness was determined and the experimental damage evolution was obtained through the relation between the initial stiffness at the first loading cycle and the measured stiffness at each cycle.

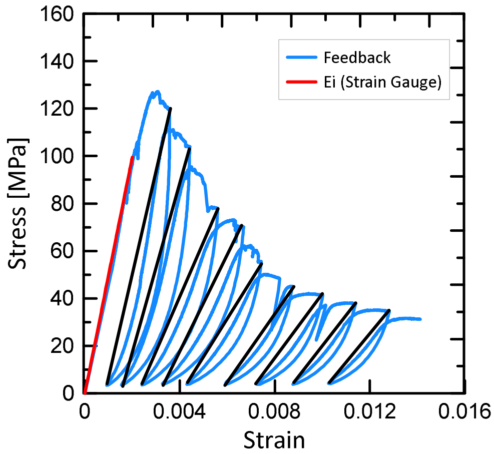

(a)

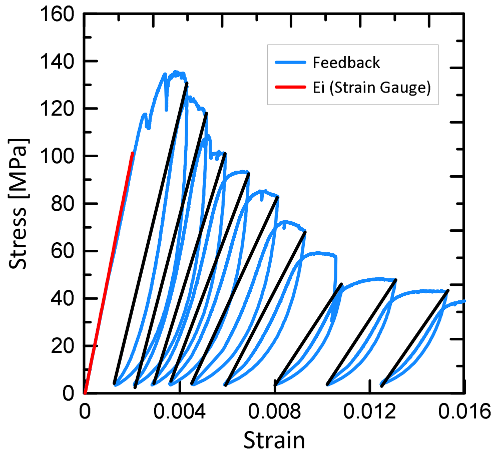

(b)

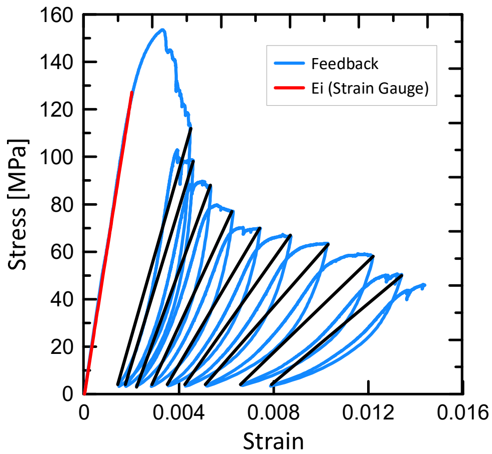

(c)

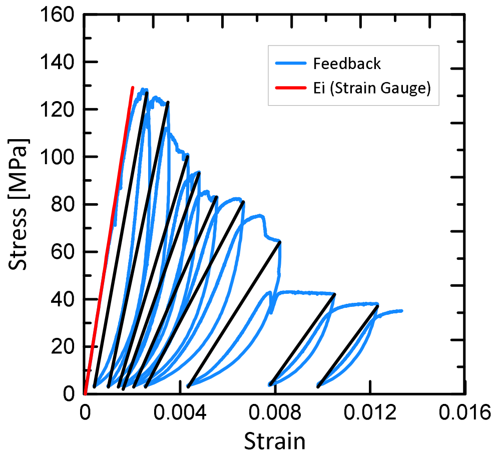

(d)

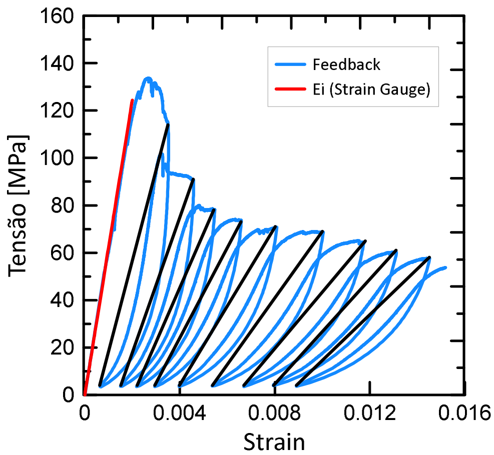

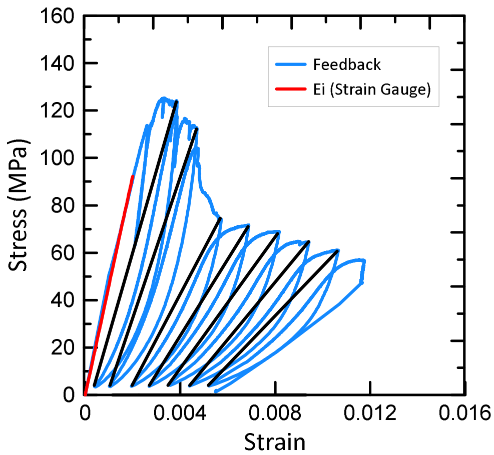

(e) (f)

Figure 63 - Stress - strain curves for the cyclic tests conducted for specimens C9 (a), C10 (b), C11 (c), C12 (d), C13 (e) and C14 (f) after correction of the LVDT curves through feedback function and initial stiffness measured through strain gauges.

Figure 63 shows the stiffness measurements through lines connecting the unloading and reloading points at each cycle.

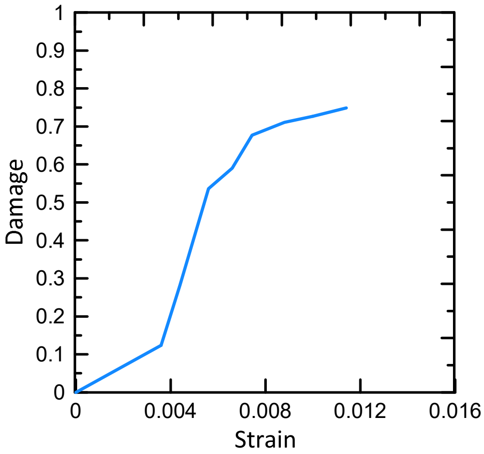

(a)

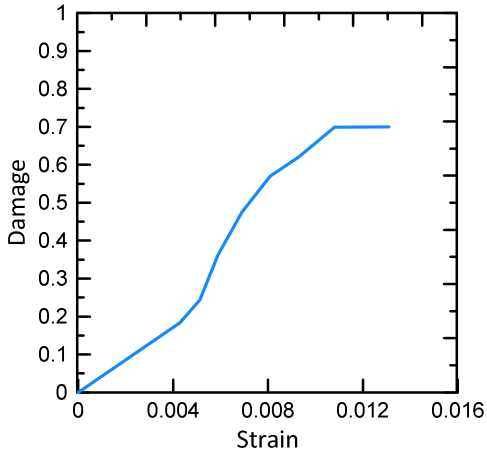

(b)

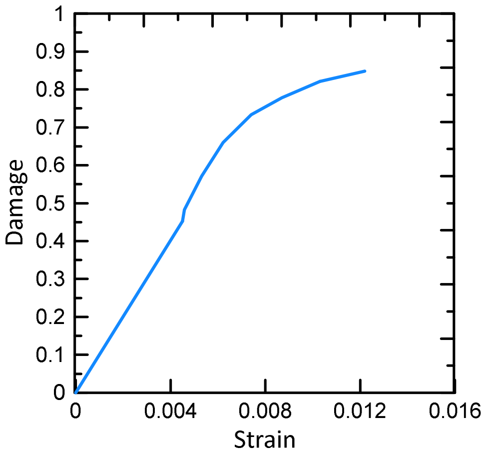

(c)

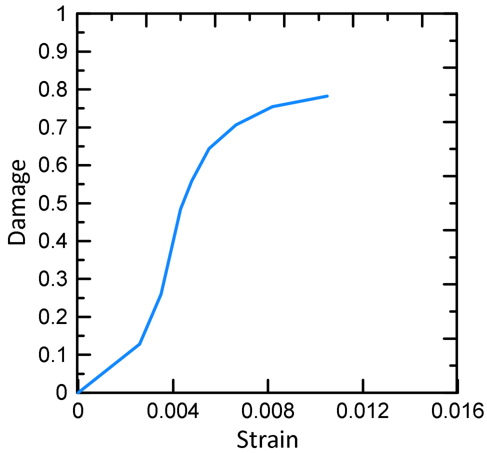

(d)

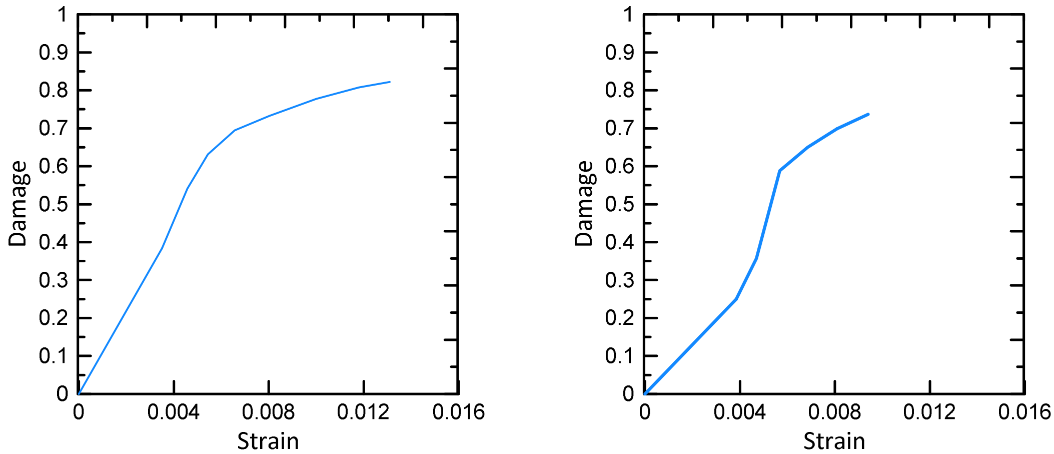

(e) (f)

Figure 64 – Damage evolution curves obtained from cyclic tests conducted in specimens C9 (a), C10 (b), C11 (c), C12 (d), C13 (e) and C14 (f).

Figure 64 shows the experimental damage evolution computed from the stiffness degradation at each loading cycle. The damage was calculated so that the experimental damage at each cycle was determined by di=1-Ei/E, where Ei is the stiffness at each cycle and E is the initial stiffness. It can be observed that the specimens failed before reaching a 1 value for damage in compression, with the highest measured damage value being 0.9.

Table 21 - Results for the cyclic tests.

	Cyclic tests							
	C9	C10	C11	C12	C13	C14	Average	Standard deviation
fc [MPa]	127.18	135.00	153.55	128.00	133.73	125.22	133.78	10.42
Ei [GPa]	49.75	50.52	63.58	64.62	62.18	46.1	56.13	8.21
Peak strain	0.0031	0.0038	0.0033	0.0024	0.0027	0.0034	0.0031	0.0005

The results of cyclic tests have been summarized in Table 21. The entire set of results was adopted for the compression characterization of concrete, including the results from load-controlled tests and the curves obtained in circumferential control tests.

Figure 65 illustrates the overlap of the envelope curve obtained from monotonic tests with the contours of cyclic tests. It is observed that the contours obtained coincide with the envelope of cyclic tests.

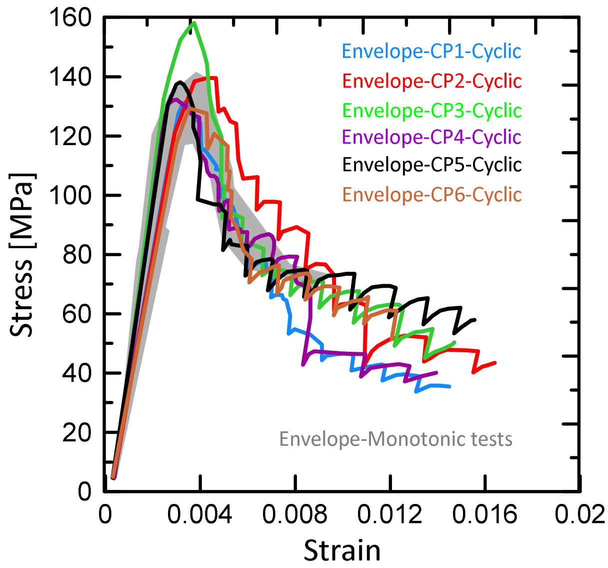

Figure 65 - Overlapping of monotonic curves and envelopes of the cyclic tests.

Table 22 summarizes the compressive tests characterization considering load-controlled tests, monotonic and cyclic tests. Results are obtained for compressive strength, Young's Modulus and peak strain.

Table 22 - Summary for all compressive tests.

	Average	Standard deviation
fc [MPa]	135.78	8.37
Ei [GPa]	55.97	9.69
Peak strain	0.0032	0.0005

For the damage evolution in compression according to Birtel and Mark's model, the bc parameter must be determined through the relationship between plastic and inelastic strains. Figure 66 shows the values obtained for the bc parameter at each cycle for each specimen.

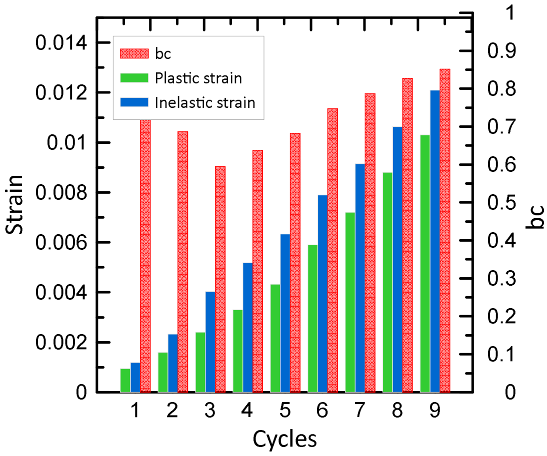

(a)

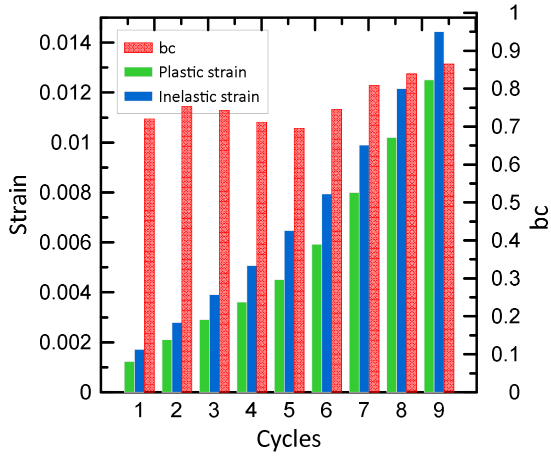

(b)

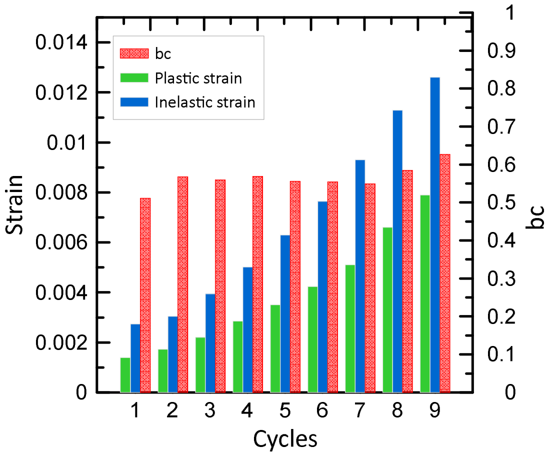

(c)

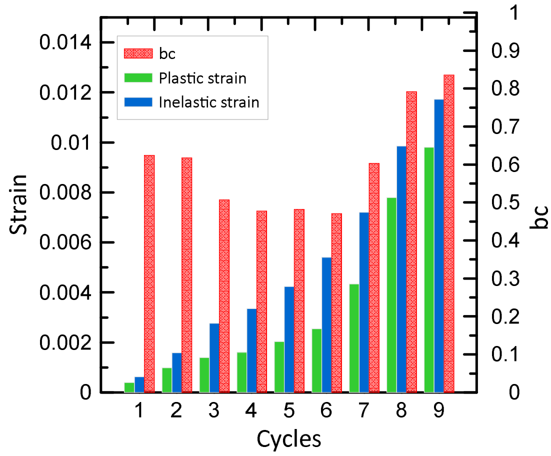

(d)

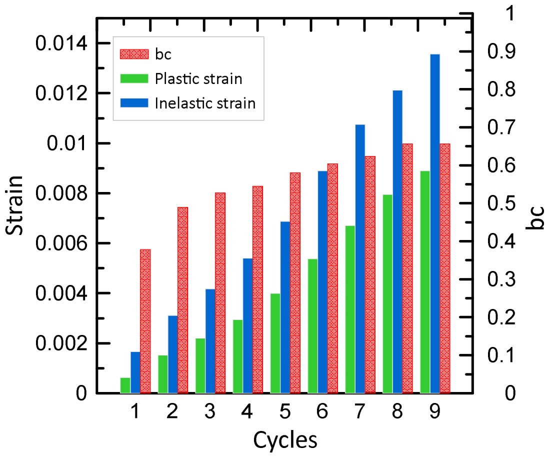

(e)

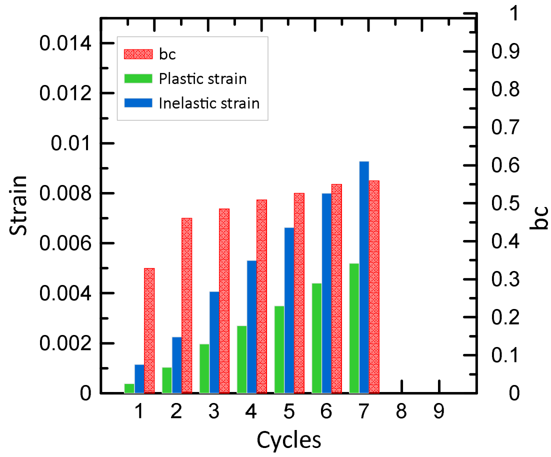

(f)

Figure 66 - Plastic and inelastic strains and bc parameter calculated for each cycle for specimens C9 (a), C10 (b), C11 (c), C12 (d), C13 (e) and C14 (f).

Figure 66 shows that the values determined for the bc parameter vary for each cycle as inelastic strains start to develop in the tests. For the calibration of Birtel and Mark's [78] model, one sole value must be determined for the whole set of cycles in each test. A fit was made using as input parameters the stress value in the discharging point at each cycle and the plastic strains at each cycle. For each test, one value for the bc parameter was determined to result in the best fit. Figure 67 shows the results for the damage evolution at each cycle and the result for the interpolation of the bc parameter and the resulting damage model value for each pair of stress and plastic strain at each cycle.

The resulting value of the bc parameter was assumed as the average of the interpolated values in Figure 67. The resulting value was assumed 0.7, being similar to the values recommended for conventional concrete.

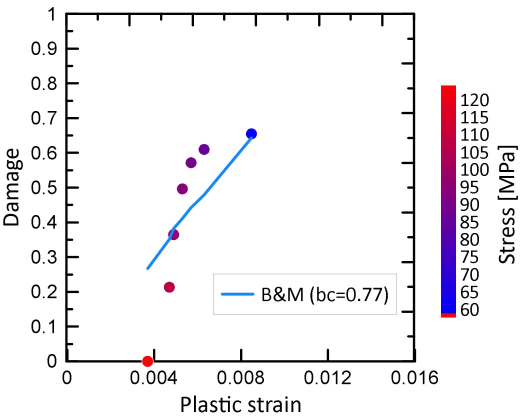

(a)

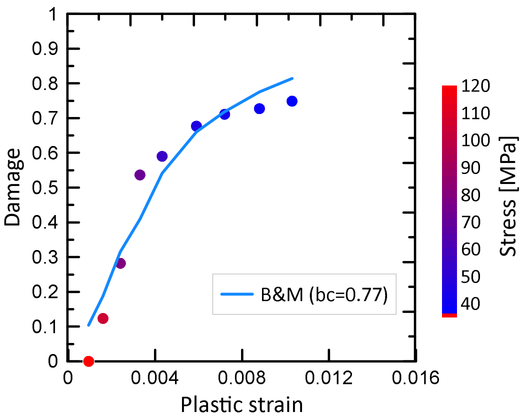

(b)

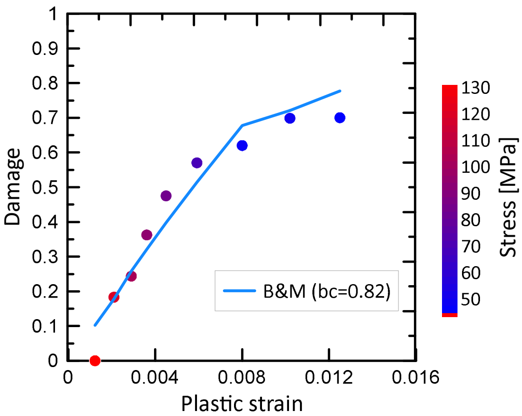

(c)

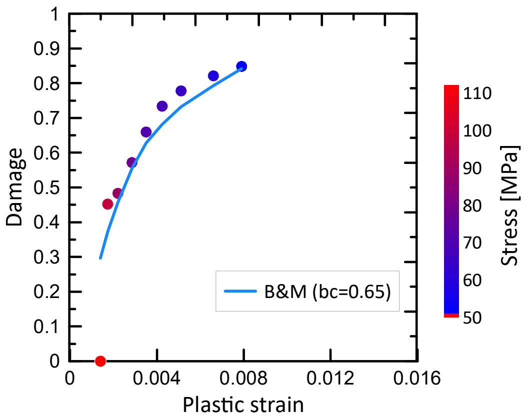

(d)

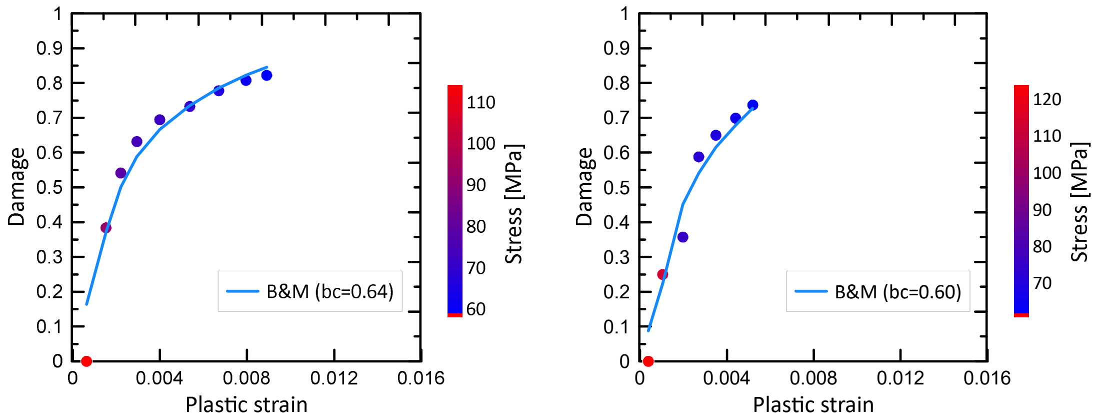

(e) (f)

Figure 67 - Damage evolution at each cycle and Birtel and Mark's [78] model with the interpolated bc parameter cycle for specimens C9 (a), C10 (b), C11 (c), C12 (d), C13 (e) and C14 (f).

4.3.2 Tensile tests

The tensile tests presented large values of slip in the anchorages, resulting in great difference between the displacements measured in the actuator and the crack openings measured through the DIC analysis. Figure 68 shows the superposition of the curves measured through digital extensometers and the curves obtained through the DIC analysis. It can be observed that the localized measurement results in totally different curves than the measured through the displacement at the actuator.

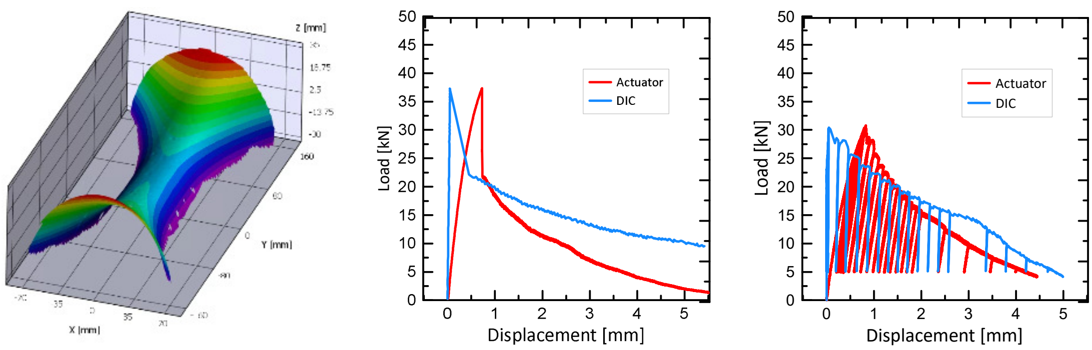

(a) (b) (c)

Figure 68 - 3D DIC analysis for dogbone specimen (3D coordinated) (a) and comparison of load-displacement curves measured through the actuator and through digital extensometers positioned at the crack for monotonic (b) and cyclic tests (c).

Figure 69 shows the failure modes and the position of the digital extensometers used for the crack opening measurements.

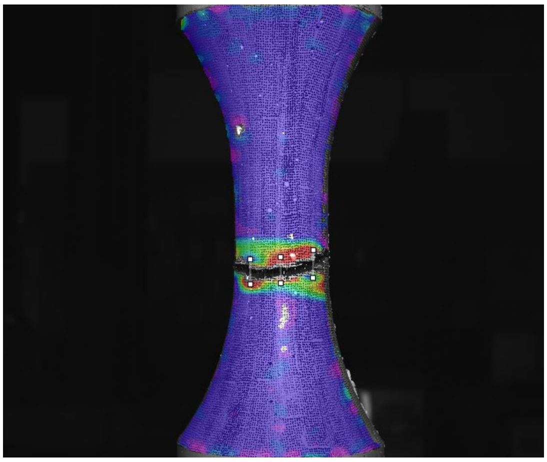

(a)

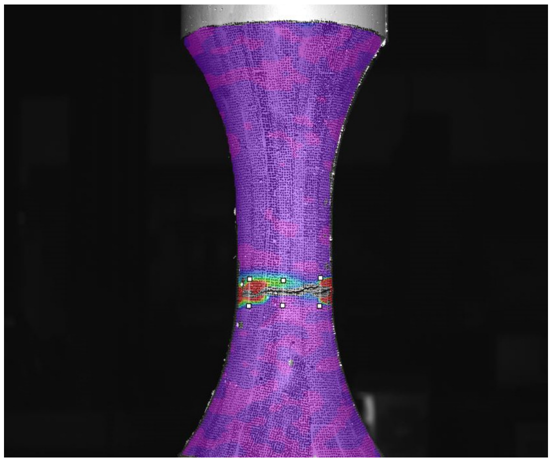

(b)

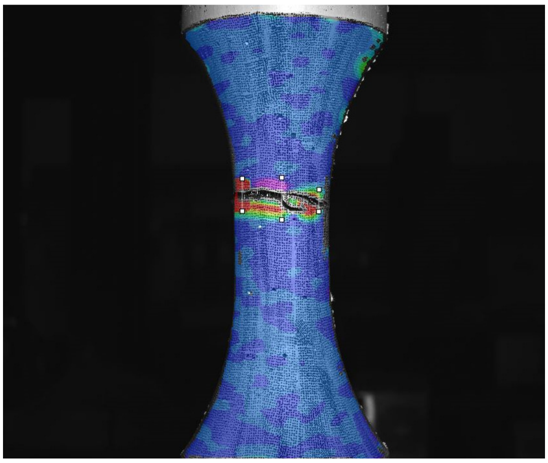

(c)

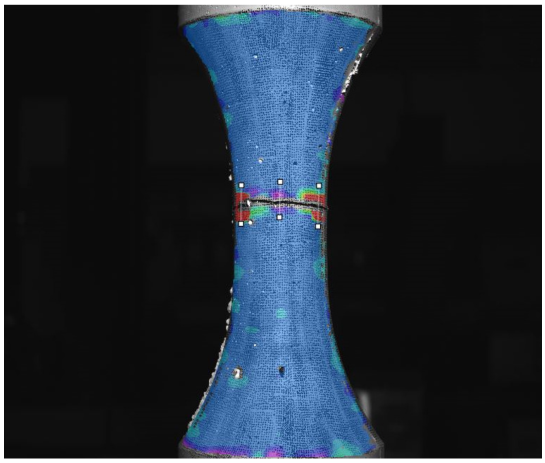

(d)

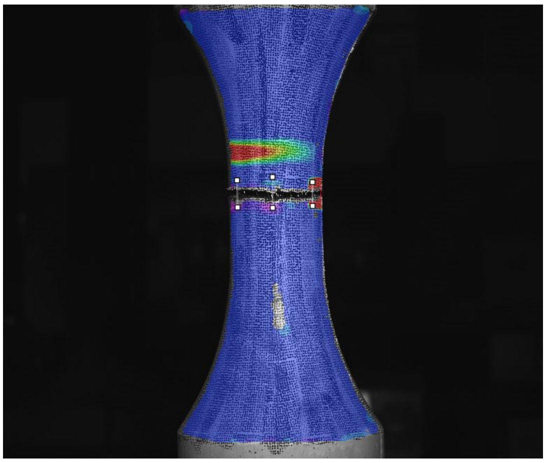

(e)

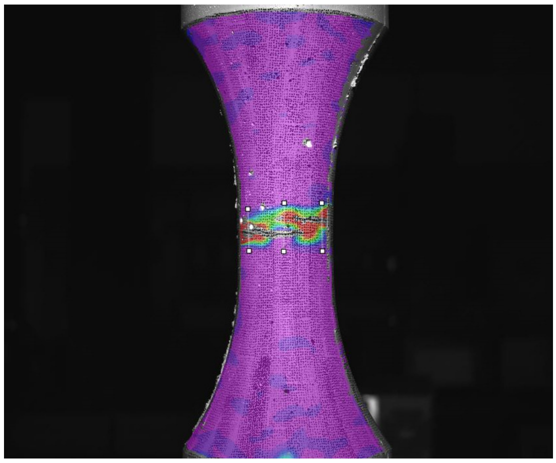

(f)

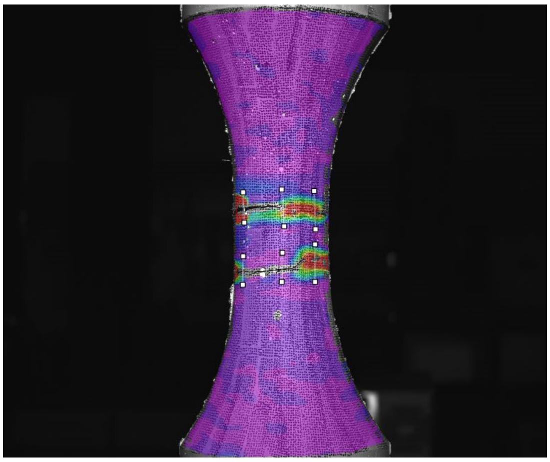

(g)

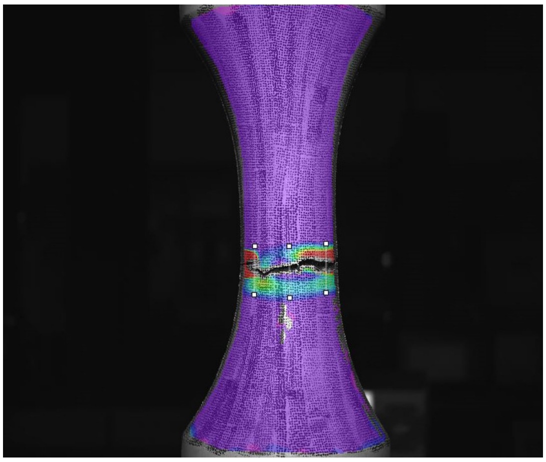

(h)

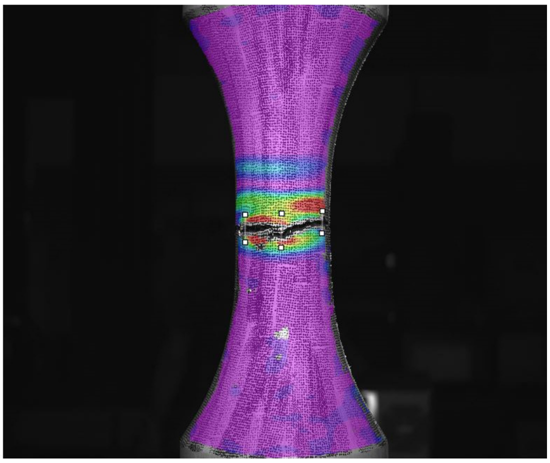

(i)

Figure 69 - Failure mode and positioning of the digital extensometers for crack opening measurement through digital image correlation for dogbone specimens DB1 (a), DB2 (b), DB3 (c), DB4 (d), DB5 (e), DB6 (f), DB7 (g), DB8 (h) and DB9 (i).

The stress-crack opening curves were obtained through the average opening of the three digital extensometers as shown in Figure 69. The curves were than considered from the first image where crack opening was observed through the DIC analysis. The corresponding curves are shown in Figure 70.

It can be observed that the use of large dogbone specimens resulted in a sudden post-peak drop as observed in Figure 70 (b) and (e) confirming the results obtained by Nguyen et al. [111], who showed that an increase in gauge length, section area and volume of the specimen result in reduction of the post-cracking strength. The reduction is associated with the larger probability of the specimen to contain defects.

Also, a bigger cross-section results in lower fiber alignment and a lower alignment results in a higher critical volume to assure the strain hardening in the post-cracking regime [87].

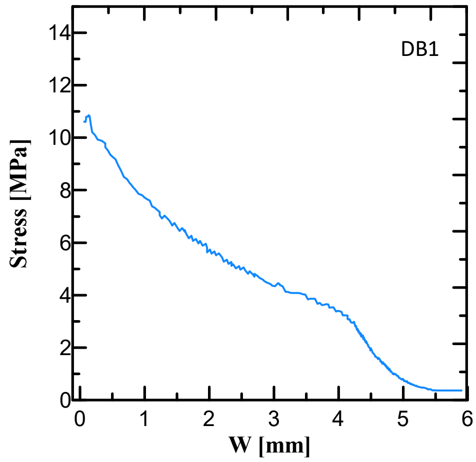

(a)

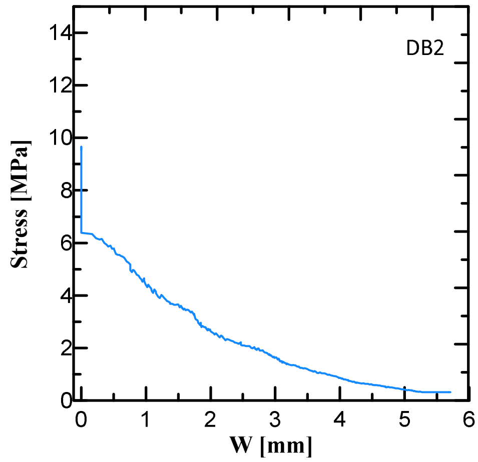

(b)

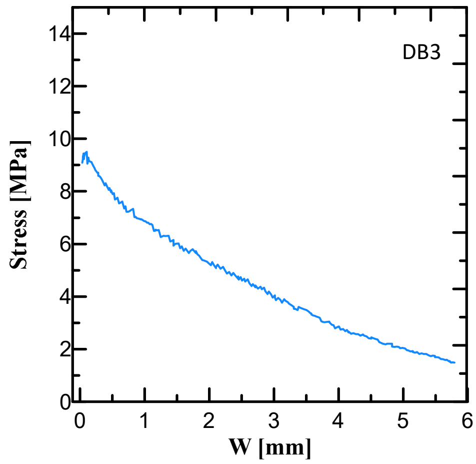

(c)

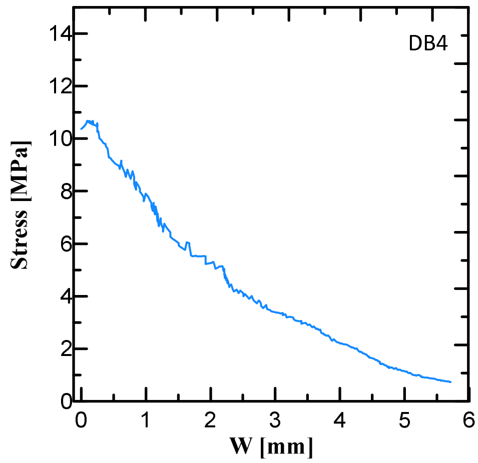

(d)

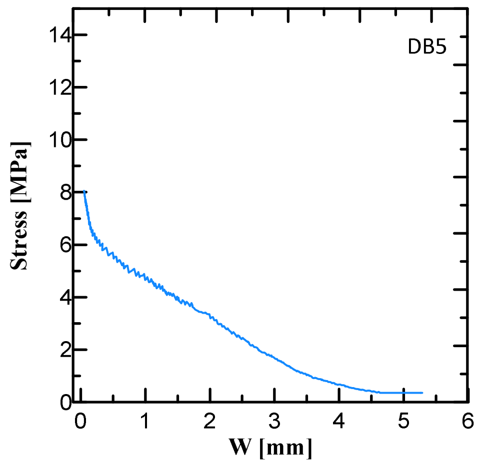

(e)

Figure 70 - Stress - crack opening curves for monotonic tests for specimens DB 1 (a), DB2 (b), DB3 (c), DB4 (d) and DB5 (e).

Table 23 summarizes the results for tensile strength, cracking energy and crack opening corresponding to maximum peak activation.

Table 23- Results for the monotonic tests for DB1 to DB5.

	DB1	DB2	DB3	DB4	DB5	Average	Standard deviation
fct [MPa]	10.613	9.660	9.083	10.373	8.026	9.551	0.852
Gf [kN/mm]	0.0266	0.0134	0.0273	0.0255	0.0134	0.0212	0.059
W0	0.132	0.005	0.095	0.102	0.054	0.078	0.04

Figure 71 compares the experimental results from the monotonic tests to the results from Wille et al.[112], Wille et al.[113], Krahl [92] and Tian [94]. The curves were obtained from stress-strain curves by the equivalent crack opening obtained multiplying each tensile strain by the gauge length of the LVDTs used in each direct tensile test.

A clear difference can be observed from the results obtained in Figure 70 when compared to the results found in the literature. The first difference observed is the dispersion of the results, with the experimental results presenting a bigger dispersion, while the results found in the literature presented lower dispersion regarding both the matrix tensile strength, and the fibers maximum activation.

Regarding the strain-hardening behavior of UHPC, the results found in the literature present a clear hardening behavior in the post cracking branch of the stress-crack opening curves, however, the results obtained in the direct tensile tests exhibited a much shorter strain-hardening branch. This can be explained in part by the size effect, with a greater section reduction length resulting in greater probability of localized failures in the specimen resulting in both a bigger dispersion of the results but also in a reduction of the tensile strength. In this case, the tensile tests conducted in this study resulted in lower tensile strength when compared to Wille et al. [112], Wille et al. [113] and Tian et al. [94]. The reduced section length from the test with the highest to the lowest tensile strength was 89 mm [112], 280mm [94], 203.2 mm [113] and 160 mm [92]. The total section reduction length in this study was 300 mm. Post-cracking strength reduction with gauge-length increment was also obtained by Nguyen et al. [111] when passing from 125 mm to 250 mm.

When it comes to the hardening behavior seen in the results found in the literature, it can be observed that the change in cross-section may lead to more or less fiber alignment, with the biggest cross-section used in this study resulting in a lower fiber alignment and in the loss of hardening behavior. A clear tendency when comparing the cross-sections of the dogbone specimens used by Wille et al. [113] (25x25 mm), Tian et al. [94] (30x30 mm), Wille et al. [112] (50.8x25.5 mm) and Krahl et al. [92] (30 x 30) resulting in lower dispersion of the results and a greater tendency for strain-hardening behavior when compared to the 68 mm in diameter cross-section here adopted. Similar results were obtained by Nguyen et al. [111], when incrementing cross-section area from 1250 mm² to 5000 mm², with reduction of the average post-cracking strength and increasing of the corresponding standard deviation.

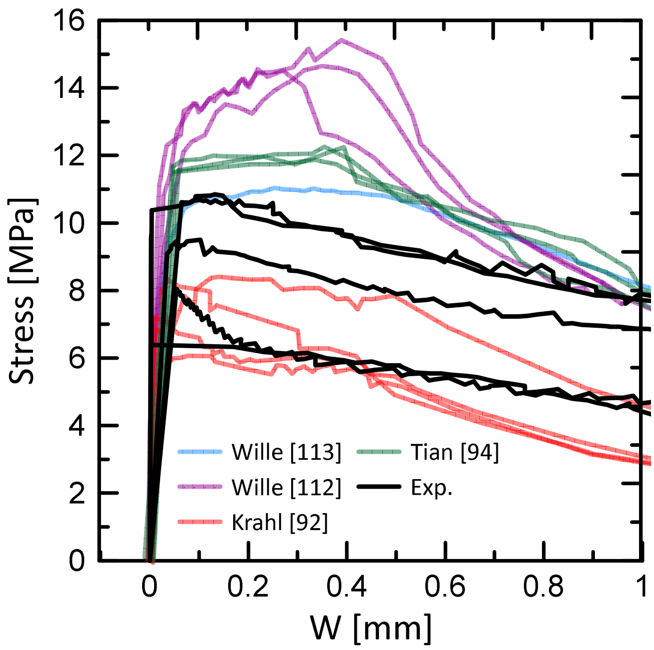

Figure 71 – Comparison of the stress-crack opening curves presented in Figure 70 with results found in the literature (Wille1 Wille2, Krahl and Tian).

Figure 72 shows stress-crack opening curves corresponding to cyclic tensile tests after the processing of the data through DIC analysis with the corresponding initial stiffness, and the stiffness computed at each cycle for the experimental damage determination through material stiffness degradation.

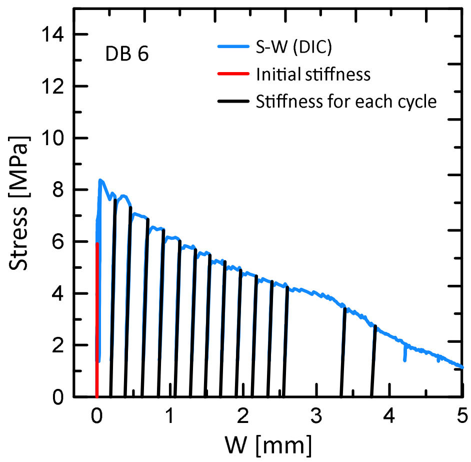

(a)

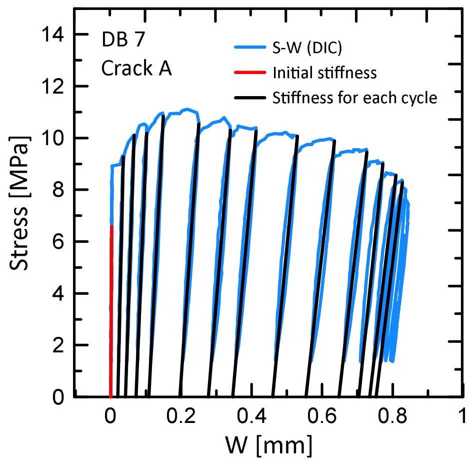

(b)

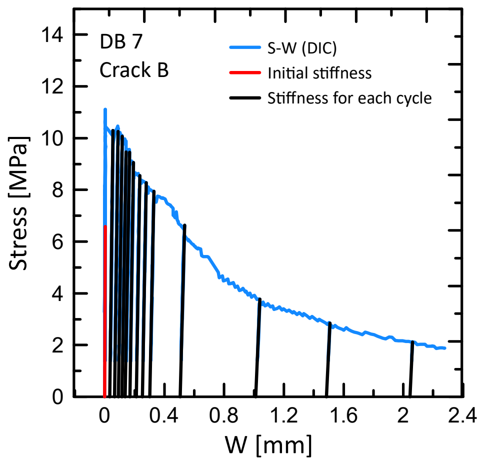

(c)

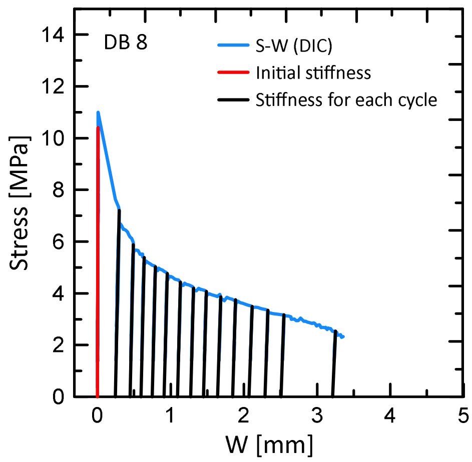

(d)

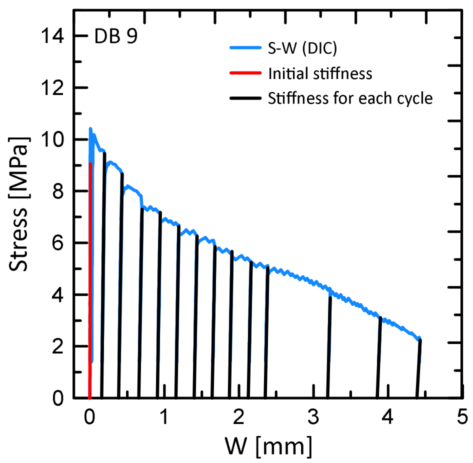

(e)

Figure 72 – Stress-crack opening curves for the cyclic tests after correction by the DIC analysis, with initial stiffness adopted as reference and corresponding stiffness' adopted at each cycle for the

experimental determination of the tensile damage evolution for dogbone specimens DB6 (a), DB7 (b) and (c), DB8 (d) and DB9 (e).

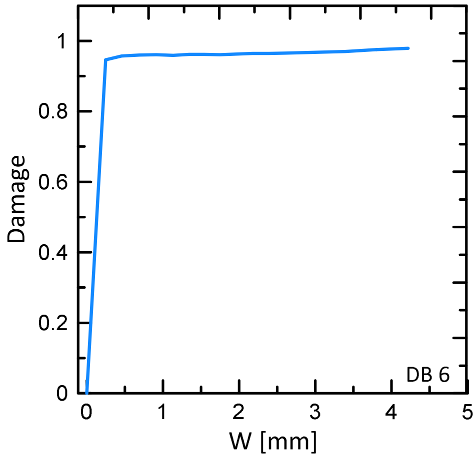

(a)

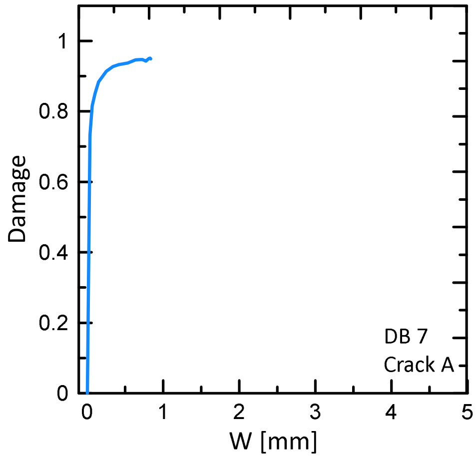

(b)

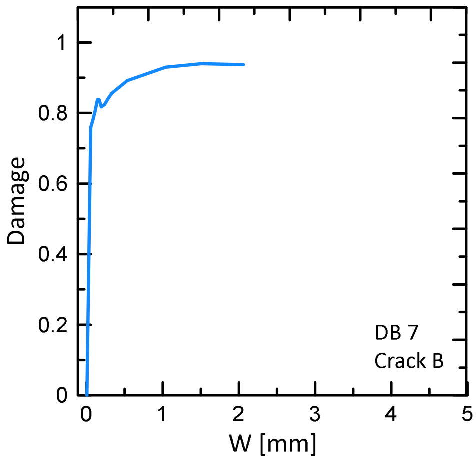

(c)

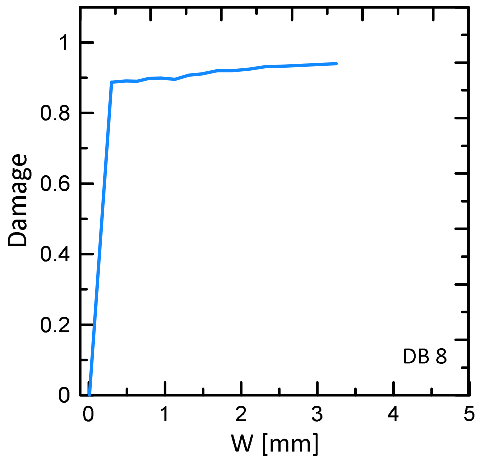

(d)

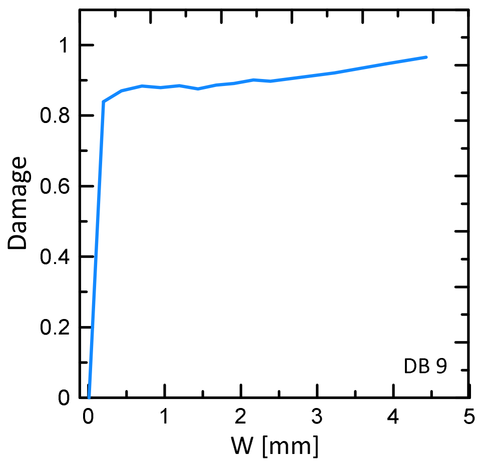

(e)

Figure 73 – Damage evolution curves for the tensile cyclic tests for dogbone specimens DB6 (a), DB7 (b) and (c), DB8 (d) and DB9 (e).

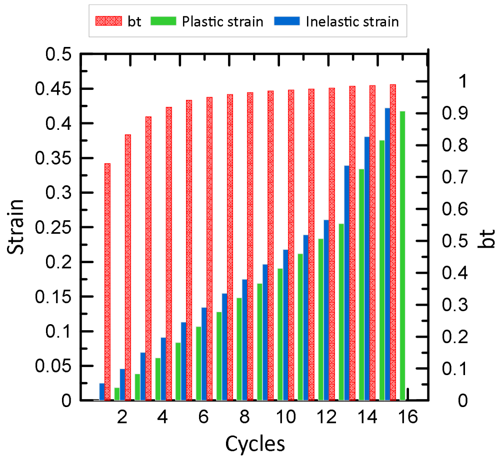

(a)

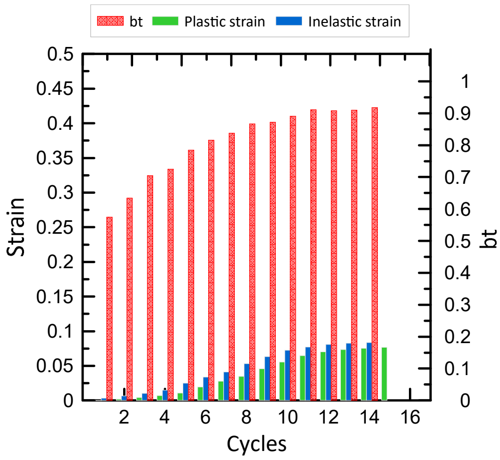

(b)

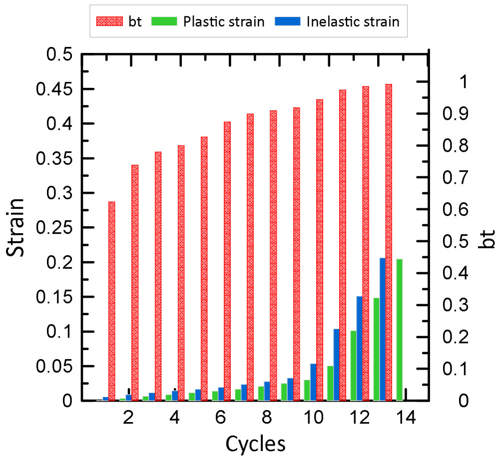

(c)

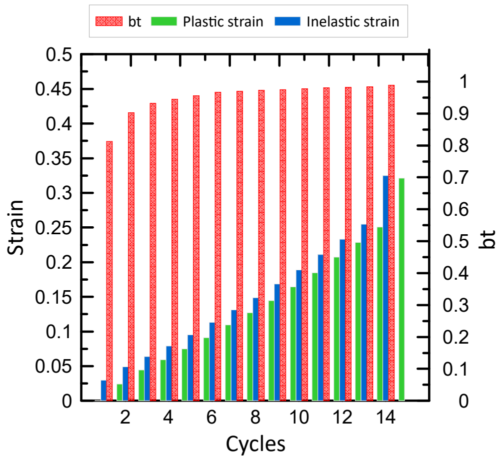

(d)

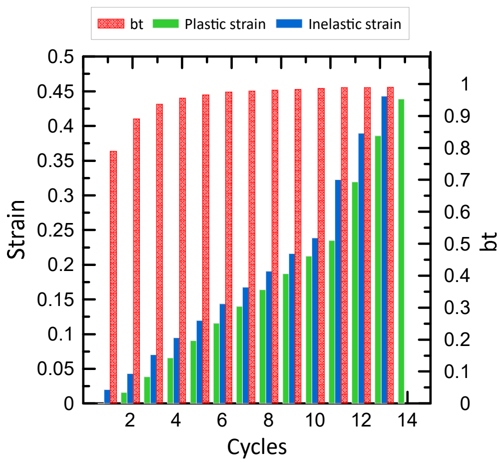

(e)

Figure 74 – Evolution of the bt parameter obtained at each cycle by the relation between plastic and inelastic strains at each cycle for dogbone specimens DB6 (a), DB7 (b) and (c), DB8 (d) and DB9 (e).

Figure 73 shows the experimental damage evolution obtained through the stiffness degradation at each cycle. As observed for the cyclic tests in compression, the bt parameters interpolated from the relationship between the plastic and inelastic strains also resulted in a variation with a growing tendency (Figure 74). Because of that. A fit was also made for the determination of the bt parameter in tension.

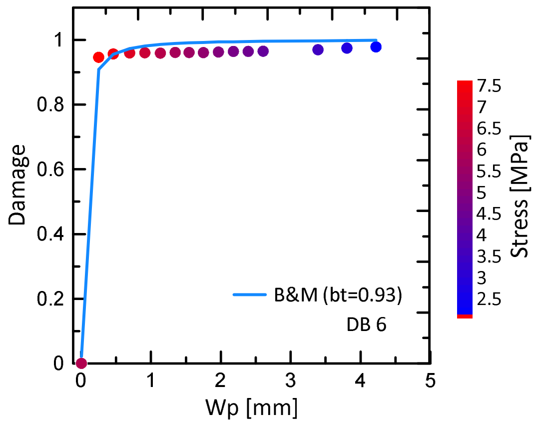

(a)

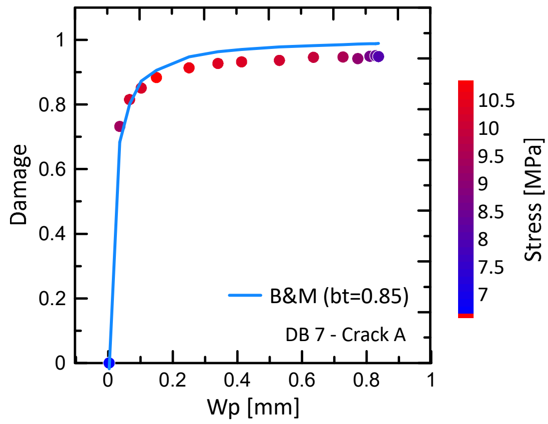

(b)

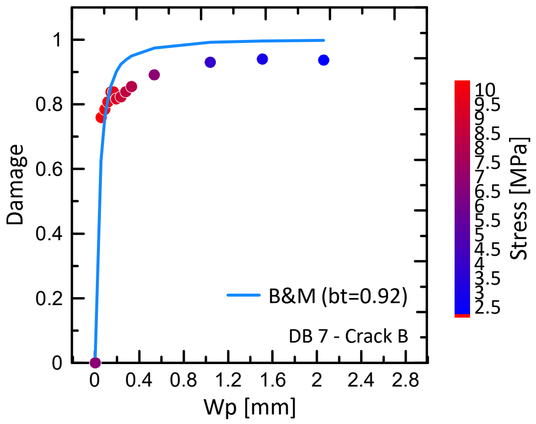

(c)

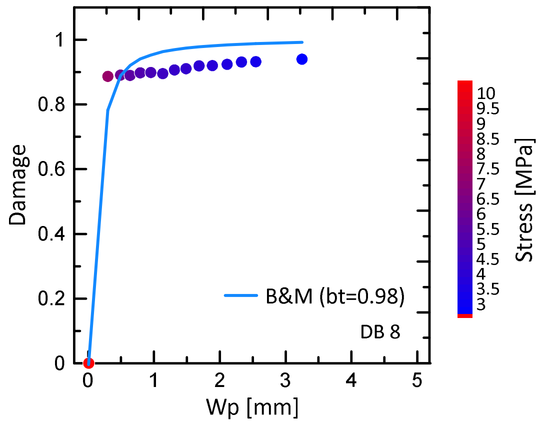

(d)

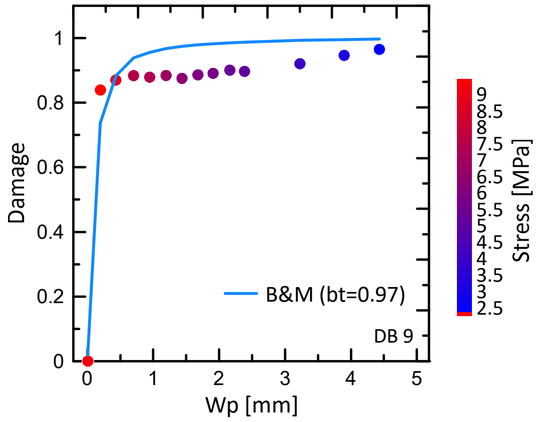

(e)

Figure 75 – Superposition of the experimental damage at each cycle and resulting interpolation of Birtel and Mark's [78] model with resulting bt parameter for dogbone specimens DB6 (a), DB7 (b) and (c), DB8 (d) and DB9 (e).

After the determination of the experimental damage evolution for each cycle, the damage value, stress value and plastic strains at each cycle were used as input parameters for the interpolation the Birtel and Mark's model for the determination of the bt parameter that resulted in the best fit to the experimental data. Figure 75 shows the superposition of the experimental damage and the interpolated curves.

For the interpolation, the correspondence between strains and crack openings was made by adopting the mesh size of 10 mm for the relation between crack opening and the inelastic strain. Interpolations were made for the curve presented in Figure 75 with characteristic lengths of 5 and 20 mm, resulting in interpolated values of 0.964 and 0.87, indicating that smaller mesh values correspond to higher bt parameters. Because of that, all correspondences used in this work used this value for characteristic length and the meshes presented in Chapter 6 also adopt this value.

Figure 75 (b) and (c) correspond to the dogbone tests presented in Figure 69 (g) with two cracks and presenting lower bt values. These curves were ignored and the final bt value obtained experimentally was the average of the curves presented in Figure 75 (a), (d) and (e), resulting in a bt parameter of 0.96.

Figure 76 shows the comparison between the envelope of the cyclic tests and the monotonic tests, showing the tendency for the cyclic tests to have the same format as the monotonic tests. For the curves displayed, the most discrepant ones are the curves obtained from the dogbone with two cracks (curves 2 and 3).

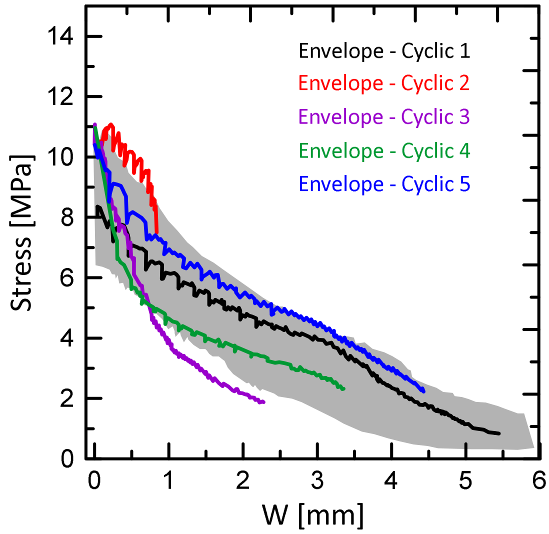

Figure 76 – Comparison of the envelope of the cyclic tests and the monotonic tests.

4.3.3 Structural tests

DIC analysis was performed to verify the longitudinal strains at the peak load. Figure 77 shows that the beams exhibited non-homogeneous deformations at the non-linear regime. The main reason is the material variability. The localization of the failure happened on spots where the beams exhibited higher strain values prior to cracking.

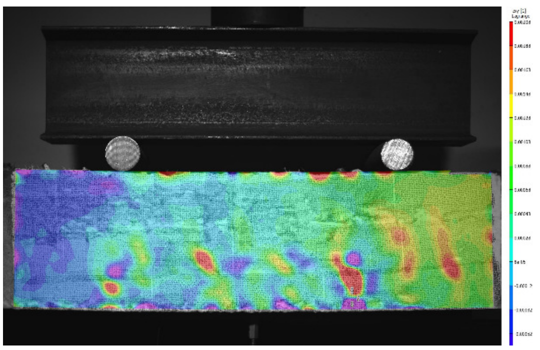

(a)

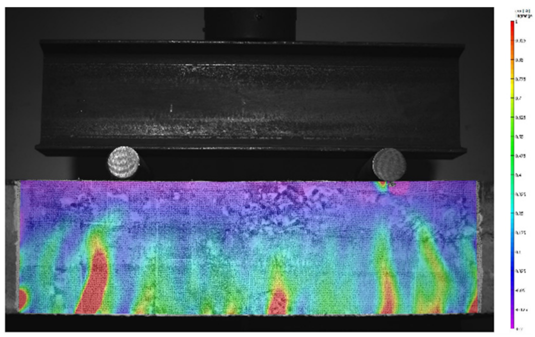

(b)

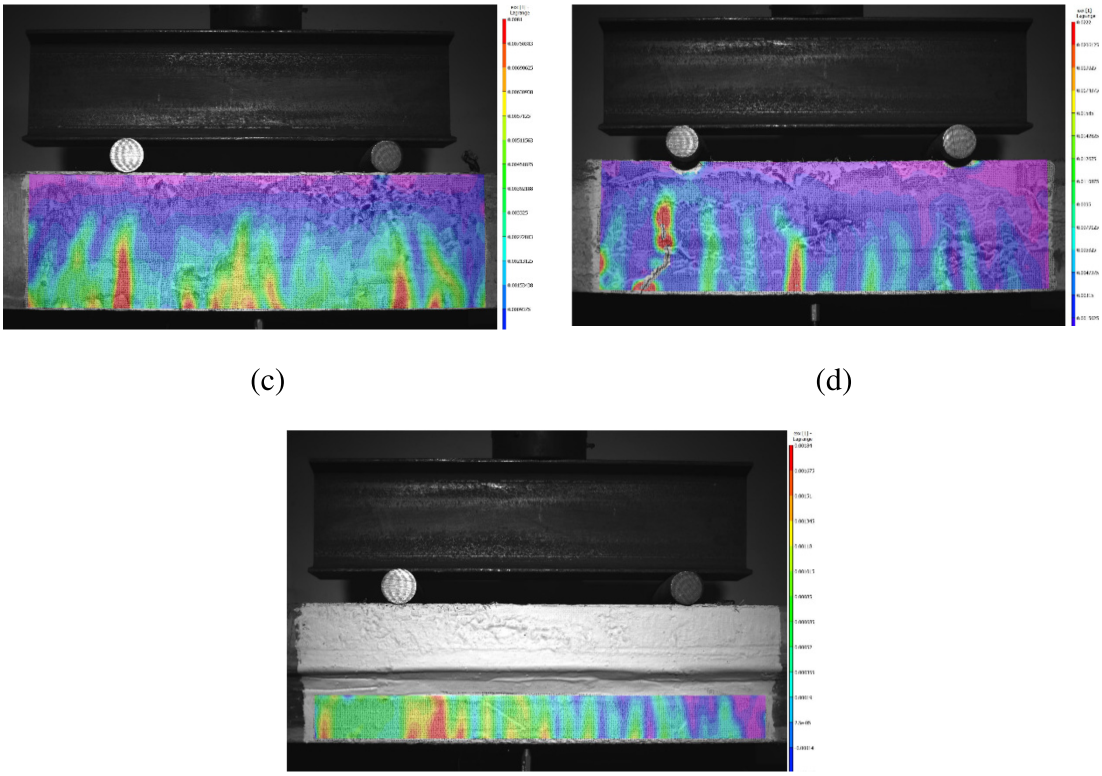

(c) (d)

(e)

Figure 77 - Longitudinal strains at peak load for the unreinforced beam (a), full section beam (b), intermediate beam (c), half section beam (d) and T section beam (e).

Figure 78 (a) shows the results for the load-displacement curves obtained from the four-point load bending tests. The curves show that the increase of the beams' cross-section lead to an increase in the peak load but also, a general trend for the post-peak drop to be more inclined due to the reduction in reinforcement ratio. The reference un-reinforced beam exhibited the most prominent post-peak drop. Figure 78 (a) shows a linear elastic branch in the pre-cracking phase of the load-displacement curves, with displacement hardening until peak-load and finally a softening phase when fibers enter pull-out phase.

The moment-curvature curves shown in Figure 78 (b) show and increase in the cracking moment with the increase in the cross-section's width. In the post-cracking regime, the beams with the same reinforcement area exhibited almost the same inclination of the moment curvature relation.

The moment-strain curves (Figure 78 (c)) for the strain gauges fixed to the longitudinal reinforcements show the tendency for higher moments corresponding to lower strains in beams with thicker cross-sections. Another phenomenon that can be noticed in this graph is that while some beams show a rapid growth of the strains after reaching the peak moment, others show a stagnation of those strains. This leads to the conclusion that the strain-gauges which were fixed to the locations close to the localized failure reflected in growing strains while for the strain gauges located outside the localization zone, strain increments stopped.

For the strain gauges fixed to the transversal reinforcements (Figure 78 (d)) all curves showed first a slight compression in the transversal reinforcement until a certain shear value and then these reinforcements finally enter a tensile phase, showing that at a first phase, shear is resisted by the concrete.

Figure 78 (e) shows the moment – crack opening curves for the tested beams. Is can be observed that although greater widths resulted in greater cracking moments, the lower reinforcement ratios also resulted in greater post-cracking drops in moment.

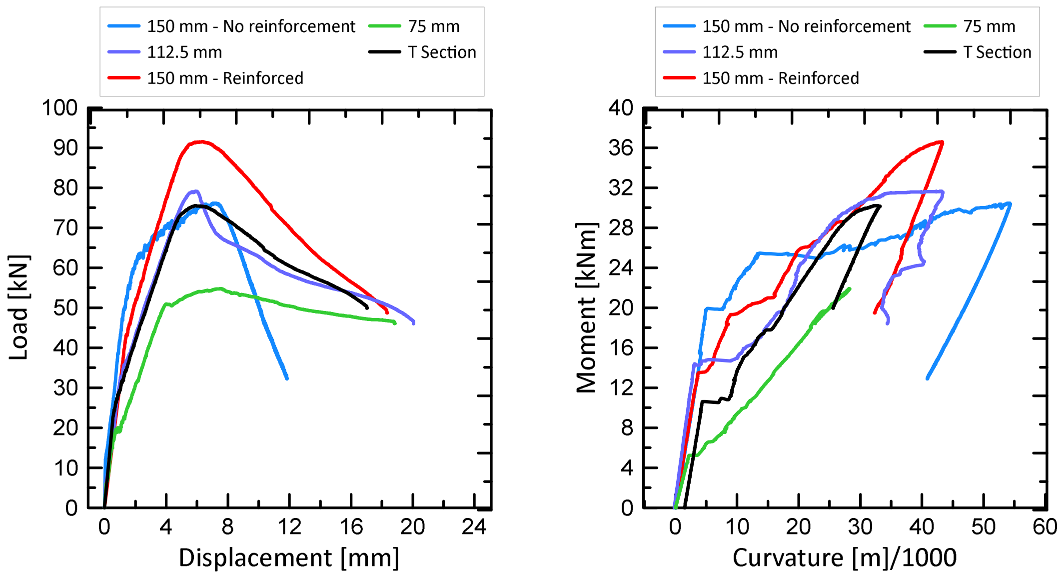

(a) (b)

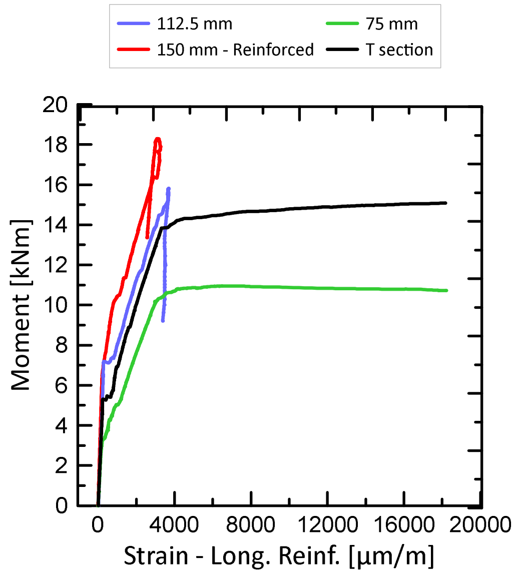

(c)

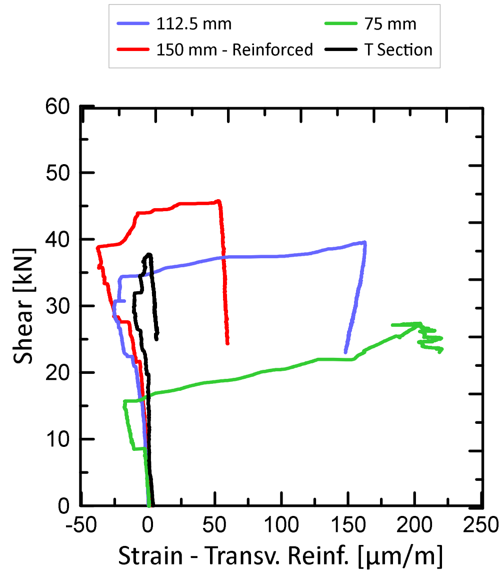

(d)

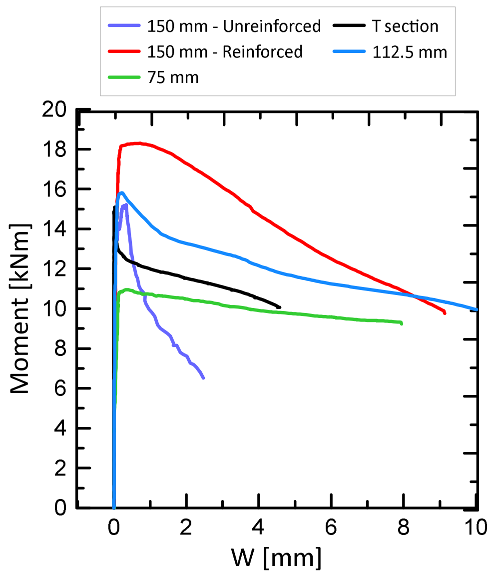

(e)

Figure 78 - Results for the tested beams with corresponding load-displacement (a), moment curvature (b), moment-train for longitudinal reinforcement (c), moment-train for transversal reinforcement (d) and moment-crack opening (e).

Figure 79 (c) shows that the strain gauges positioned at the section where the localization occurred presented large longitudinal deformations while the ones located at the uncracked zone stopped strain increments after reaching the peak load. Figure 79 shows the comparisons obtained through DIC analysis for the longitudinal strains at the failure localization section and at the midspan of the beam outside the cracked zone.

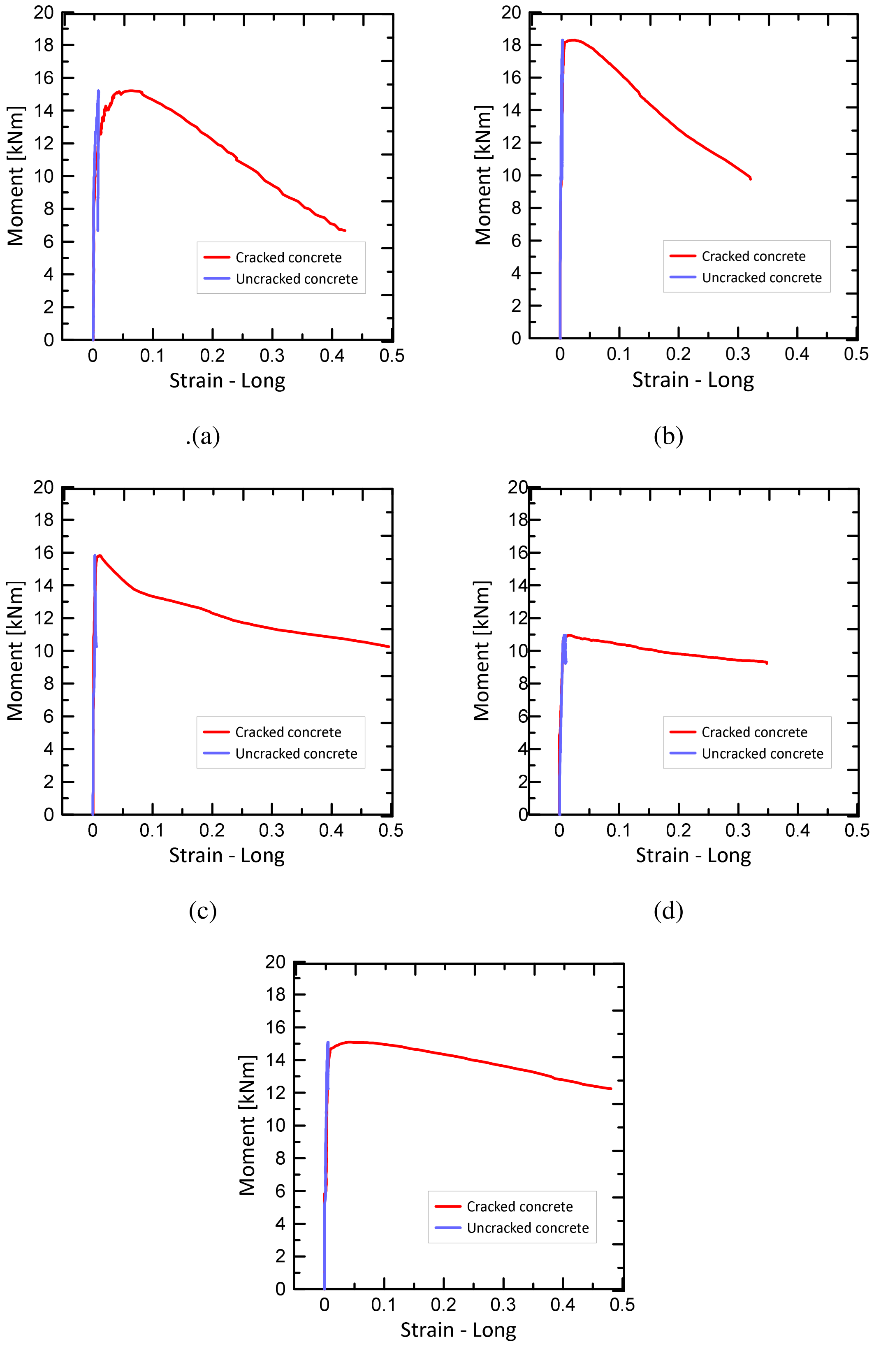

Figure 79 – Comparison of longitudinal strains for the main crack and the uncracked concrete for unreinforced beam (a), full section beam (b), Intermediate section beam (c), half section beam (d) and T section beam (e).

Figure 80 shows the failure modes for each beam. All the beams exhibited flexural failure, with a major crack localizing when the beams entered the displacement softening phase of the tests. Regarding the number of cracks, the beams with the original section, both reinforced and unreinforced exhibited 1 main crack and no minor cracks. The intermediate rectangular beam exhibited one major crack and one minor crack and the beam with half the section exhibited one major crack and two minor cracks. The T-girder exhibited only one major crack.

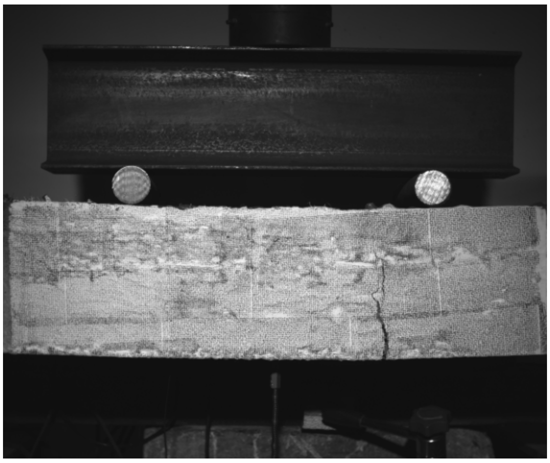

(a)

(b)

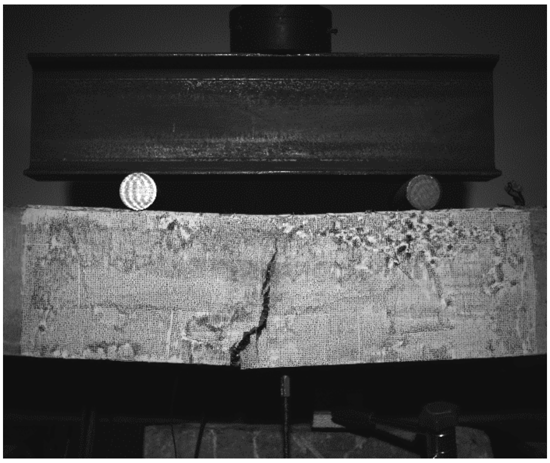

(c)

(d)

(e)

Figure 80 - Failure modes of the beams without reinforcement (a), with the full section (b), intermediate section (c) half section (d) and T-section (e).

The comparison between Figure 77 (peak) and Figure 80 (failure) shows the clear tendency where until peak-load no major cracks were formed while after-peak load the cracks localized resulting in major cracks associated with fiber pull-out. The combination of these two stages result in the aspect show in Figure 78 (a) for the load-displacement curves, with a non-linear regime until peak-load and softening when fiber enter pull-out phase associated with failure localization.

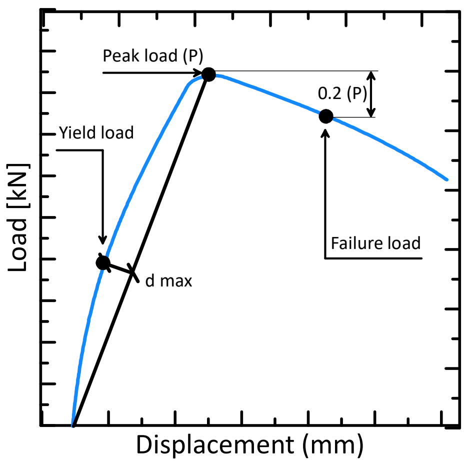

Figure 81 – Points required to calculate the ductility by the method defined by Song et al. [65].

The ductility of the tested beams was calculated through the method presented by Song et al. [65], which defines the ductility by the relation between the failure displacement over the yield displacement (Figure 81). The results are shown in Figure

82. The results for the half section beam are not shown because the 20% post-peak drop was not observed before the ending of the test.

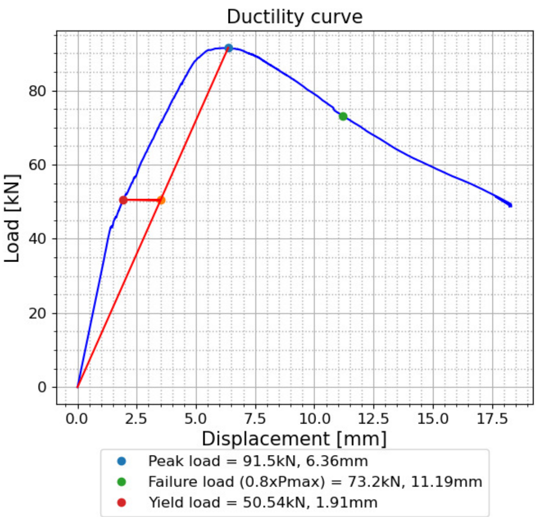

(a)

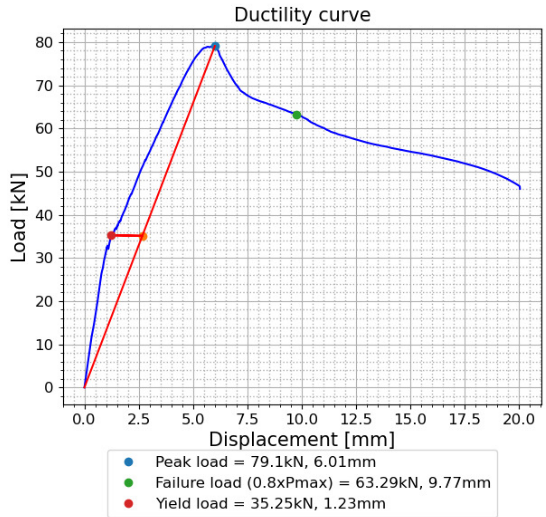

(b)

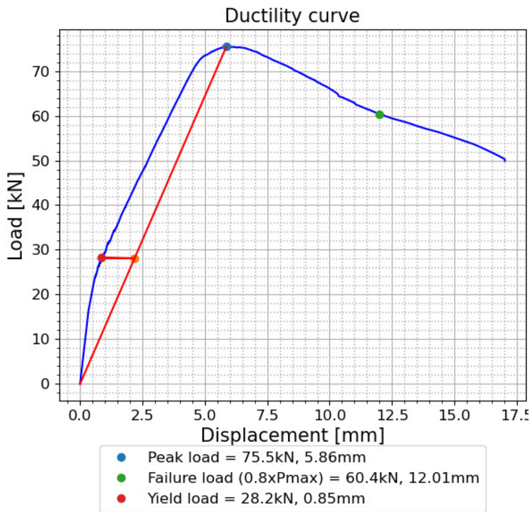

(c)

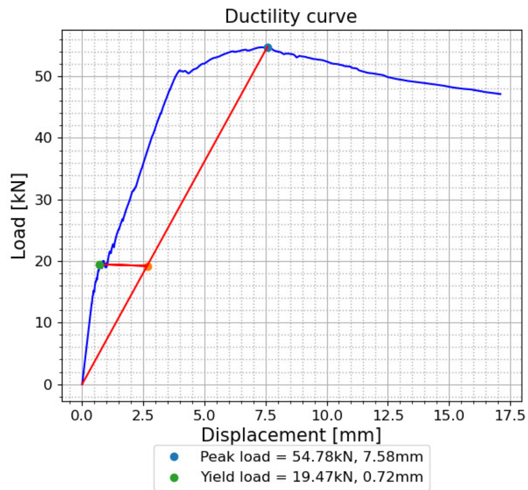

(d)

Figure 82 – Ductility calculation for the full-section beam (a), intermediate beam (b) and T-section beam (c), half section beam (d).

Table 24 - Results for the reinforced beams.

Result	150 mm - reinforced	112.5 mm	75 mm	T section
Load capacity [kN]	91.5	79.1	54.78	75.5
Yield load [kN]	50.54	35.25	19.3	28.2
Cracking load [kN]	91.3	78.32	50.82	63.89
Ductility	5.848	7.923	-	14.106

Table 24 shows the results for load capacity, yield load, cracking load and ductility for the reinforced beams. It can be observed that as expected for the rectangular beams, an increase in the width of the cross-section results in increase in the load capacity of the beams, with the intermediate section representing a 44% increase and the original section an increase of 67%whereas the width increment was of 50% and 100% respectively. The T section beam had a load capacity approximately equal to its equivalent intermediate beam.

For the yield load, the beam with half the original section had a correction, with the yield load determined by the method defined by Song et al. [65] resulting in an overestimation with the yield load in the nonlinear regime of the load-displacement curve. For this case, the yield load was determined by the change in inclination in Figure 82 (d) so that the yield load showed the same behavior as for the other beams. It was observed that the yield load increased with the width of the cross-section, not only in absolute values but also normalized by the peak load. The half section beam presenting a yield load of 35.2%, the intermediate beam of 44.6 % and the full section beam of 55.3 % of the peak load. For the T section, this ratio was of 37.4 %, resulting in a reduction when compared to its equivalent rectangular beam.

For the cracking load, an increment can be observed with an increase of the cross-sections' width. The change in the cross-section's format resulted in a change in the cracking load relative to the peak load, with the rectangular beams all presenting cracking loads over 92% of the load capacity. For the T section, this value was of 84.6%, being the beam with the biggest post cracking increase in load.

Finally, for the ductility factor, it can be observed that the larger the width of the cross-section, the lower the ductility of the beam. This can be related to higher reinforcement ratios, resulting in lower post-peak drops in the load-displacement curves, but also with the reduction of the normalized relation between yield-load and peak-load, resulting in a higher ratio between the deflections corresponding to failure load, defined as a 20% post-peak drop and the yield-load. The T section presented a considerable increase in ductility compared to the equivalent rectangular section, however the relation between ductility may have been compromised by the premature post-peak drop presented by the intermediate beam.

5 NUMERICAL MODELING

A new set of models based on novel calibration techniques is presented. The calibration of the uniaxial models and damage evolution models in compression and tension is conducted based on the results of the monotonic and cyclic tests of the material characterization. The CDP parameters are calibrated by material level models so that these models result in the same curves obtained in the experimental program. Finally, the calibration is compared to the curves obtained experimentally for the five beams through a new set of beam models.

A total of four models are made for each beam, with two damage evolution models in homogeneous and heterogeneous models. The effects of the random material properties are discussed in each case.

5.1 Calibration of the CDP parameters

The results of the compression characterization tests indicated that the concrete exhibits an elastic modulus close to the estimate provided by the Mansur method. To create uniaxial compression curves, equiation 11 was adopted, relating compressive strength to the elastic modulus. The only variables left to be determined are the compressive strength and the volume of fibers. The Mansur model was calibrated based on the peak strain to better fit the post-peak experimental data. A peak strain of 1.10 fc/Ei was adopted. The resulting curve is shown in Figure 83 (a). For compression damage, Birtel and Mark's [78] model was adopted with a coefficient bc equal to 0.7, as determined from experimental data.

Figure 83 (b) illustrates the overlay of the theoretical damage evolution model with the envelope of damage vs. plastic strain curves. It is observed that for damage values less than 0.8, the curve results in a good match to the experimentally obtained damage evolution.

To calibrate the parameters of the CDP model, several attempts were made on a representative model for the compression tests. While for the uniaxial and damage evolution models the results of the material characterization were used to select the models that resulted in the best fit, for the CDP parameters were adjusted using a novel calibration technique. In these attempts, values for the dilation angle and viscosity were adjusted, with the other parameters having less influence on the results. Thus, the same values as Lima et al [2] were adopted for the other parameters, with 0.1 for eccentricity, 1.16 for the biaxial ratio, 0.6667 for the shape factor, and 0.2 for the Poisson's ratio.

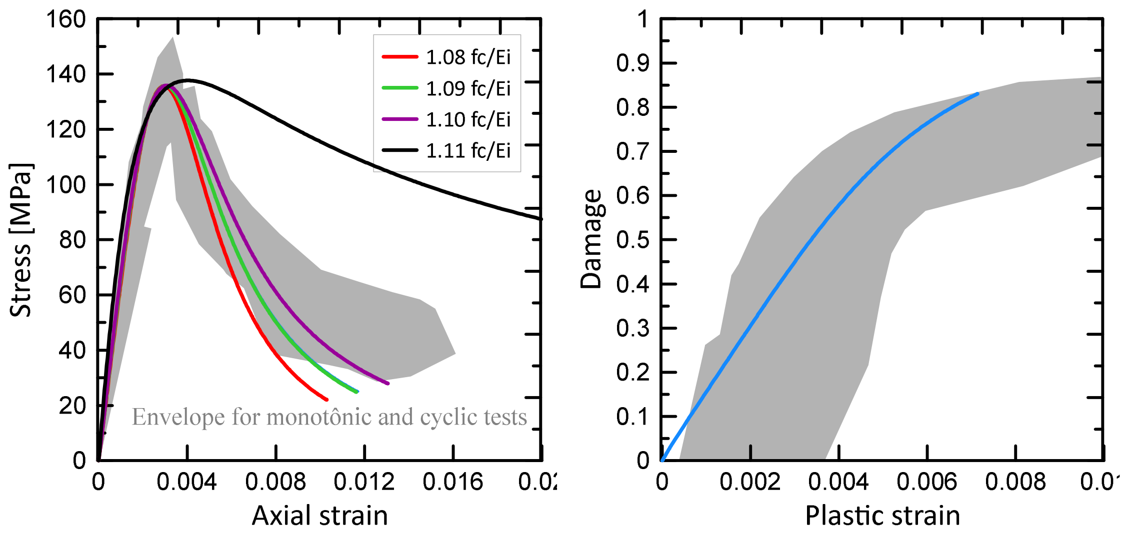

(a) (b)

Figure 83 - Comparison of the calibrated uniaxial (a) and damage evolution models (b) to the experimental results.

$$E_i = (10300 - 400Vf) \times \left(fc^{\frac{1}{3}}\right) \quad 11$$

The calibration of the CDP parameters was performed by varying the dilation angle between 30º and 55º, examining the effect on the axial and transversal stress-strain curves. Once the dilation angle was determined, the viscosity parameter was varied to assess its influence on the obtained results.

Figure 86 (a) shows the comparison of numerically obtained vertical stress-strain curves and the envelope of monotonic tests. It is observed that the model resulting in the best fit had a dilation angle of 55º. Wosatko et al. [114] associate the dilation of concrete to the increase in volume when a particle constituted material is subjected to shear causing the rearrangement of its particles, resulting in plastic strains. In this sense, the higher packing density of UHPC should result in higher dilatancy when its particles are rearranged. From this model, the viscosity factor was varied, and it was found that it had little influence on the uniaxial behavior, however, Hongbing et al. [115] showed that lower viscosity parameters generate a greater localization tendency of the failure in the model. For that reason, the lower value of 0.0001 was adopted.

Figure 84 depicts the radial stress-strain behavior obtained in monotonic tests. A mean curve was interpolated from the experimental curves. It is observed that this curve exhibits a change in slope for points with horizontal strain greater than 0.005 due to excessive opening of cracks in the specimens, resulting in horizontal asymptotic behavior. Figure 84 (b) shows a specimen subjected to circumferential control tests with a detached part in contact with the chain connected to the horizontal LVDT that controls the test. Although this control was effective for conducting the test, the measured values for more developed crack opening resulted in an overestimated radial strain. For characterizing the post-cracking behavior, the branch of the curve corresponding to horizontal strains less than 0.005 was selected. From this section of the mean curve, the mean slope was determined and adopted as the radial strain rate in the post-peak section.

Grassl [116] related the dilation of concrete to the inelastic lateral expansion of concrete with microcracks in inclined planes leading to force transfer through shear stresses, thus relating the lateral strains to the dilation angle. In this study, however, the concrete specimens were confined in steel tubes, preventing the excessive sliding shown in Figure 84 (b).

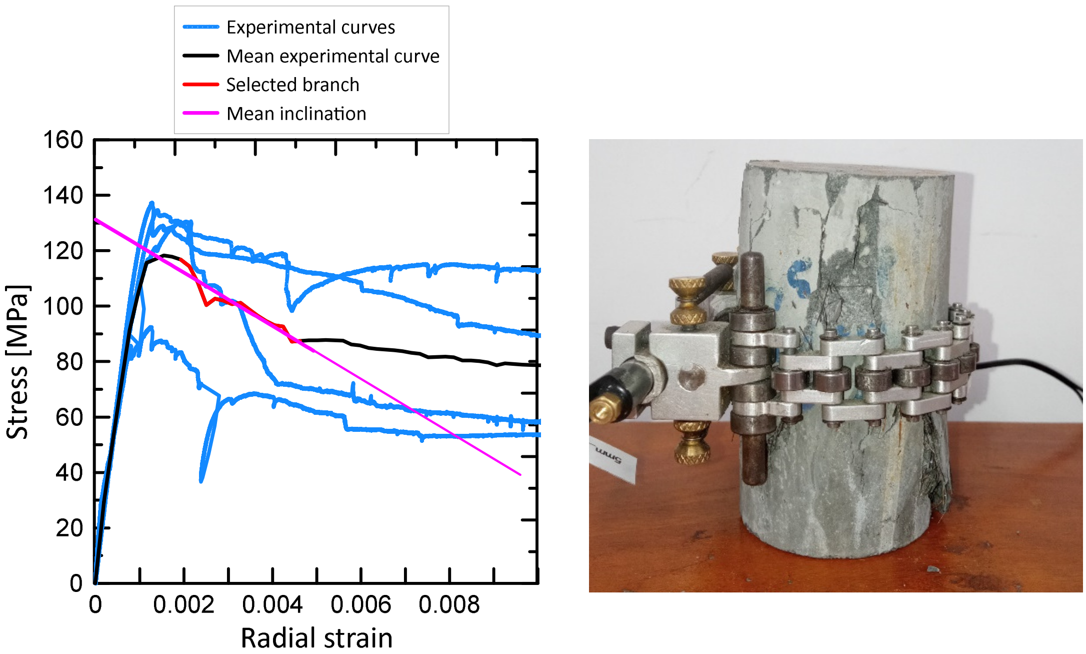

(a) (b)

Figure 84 - Mean curve for horizontal strains (a) and detachment of layer in contact with the control chain (b).

Figure 87 (a) shows the two types of models used in the investigation of the CDP parameters calibration. Figure 85 (a) shows a homogeneous model where the uniaxial and damage evolution law were obtained from the average material properties obtained in the material characterization phase. Figure 85 (b) shows a heterogeneous model where the material properties were generated from the average values and standard deviation values obtained from the material characterization.

(a) (b)

Figure 85 - Compression tests simulations with homogeneous (a) and heterogeneous material properties (b).

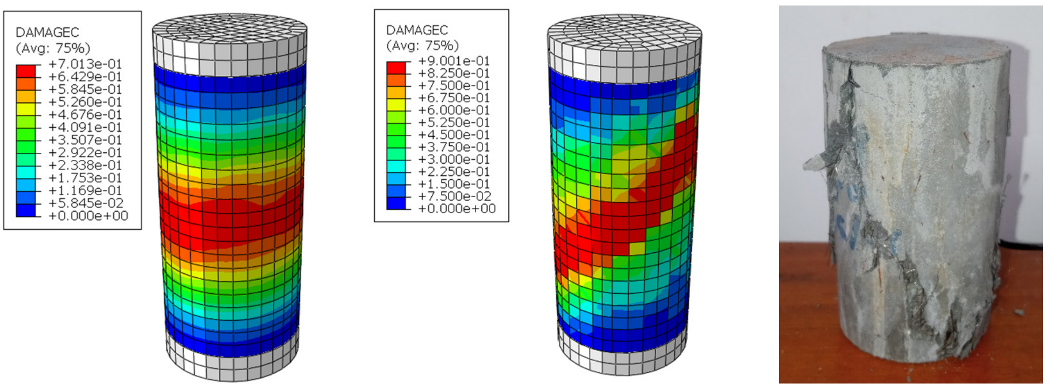

(a) (b) (c)

Figure 86 - Comparison between the failure modes of the homogeneous model (a), heterogeneous model (b) and the experimentally exhibited failure mode (c).

The radial strain in the linear elastic range is governed by the Poisson's ratio, whereas in the post-peak region, its behavior is dictated by the parameters adopted for the CDP model. Figure 87 (b) shows the comparison of curves obtained for each tested model and the mean slope obtained in Figure 84. It was observed that the models with dilation angle of 55° also resulted in the best fit in terms of radial strains.

Figure 86 illustrates the comparison between the model with homogeneous properties and the model adopting random variation of properties within the volume of the compression cylinder. The division was made so that each cell had the approximate sized of one fiber length. The cracking pattern was observed in the model by plotting the DamageC variable. Figure 86 (a) displays the failure pattern for the model with homogeneous properties, exhibiting a horizontal failure pattern, with the cross-section crushing all at once. Figure 86 (b) presents the inclined fracture pattern for the model considering variable properties, which is closer to the fracture pattern observed experimentally in Figure 86 (c).

Mier [117] attributes the inclined failure in compression, among other causes, to imperfections that lead to micro-cracking. These micro-cracks will never be oriented in a perfect vertical plane. These will lead to crack opening under sliding. The process here presented can be viewed an analogy to internal imperfections in the specimen, resulting in the same failure pattern.

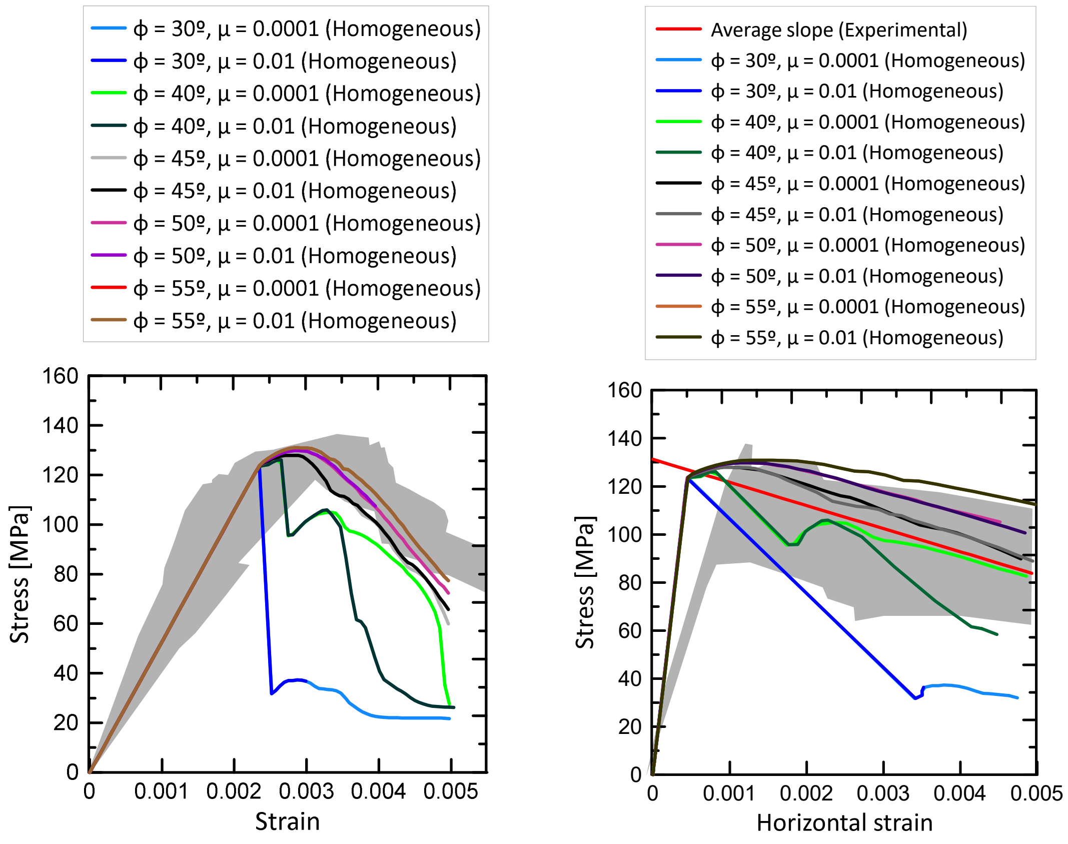

(a) (b)

Figure 87 - Stress - vertical strain a (a) and stress-radial strain (b) curves for the homogeneous models.

The adoption of random material properties, besides generating a fracture pattern closer to the one observed experimentally, resulted in an approximation of the post-peak slope in the radial stress-strain curve. In the vertical stress-strain graph, this method led to a more accelerated drop in the post-peak region, with the cells with lower compressive strength and rapid damage evolution resulting in earlier development of plastic strains and damage evolution, reducing the stiffness of the model. The variation of the viscosity parameter showed little influence, with curves for different viscosity parameters also overlapping for the radial strain curves.

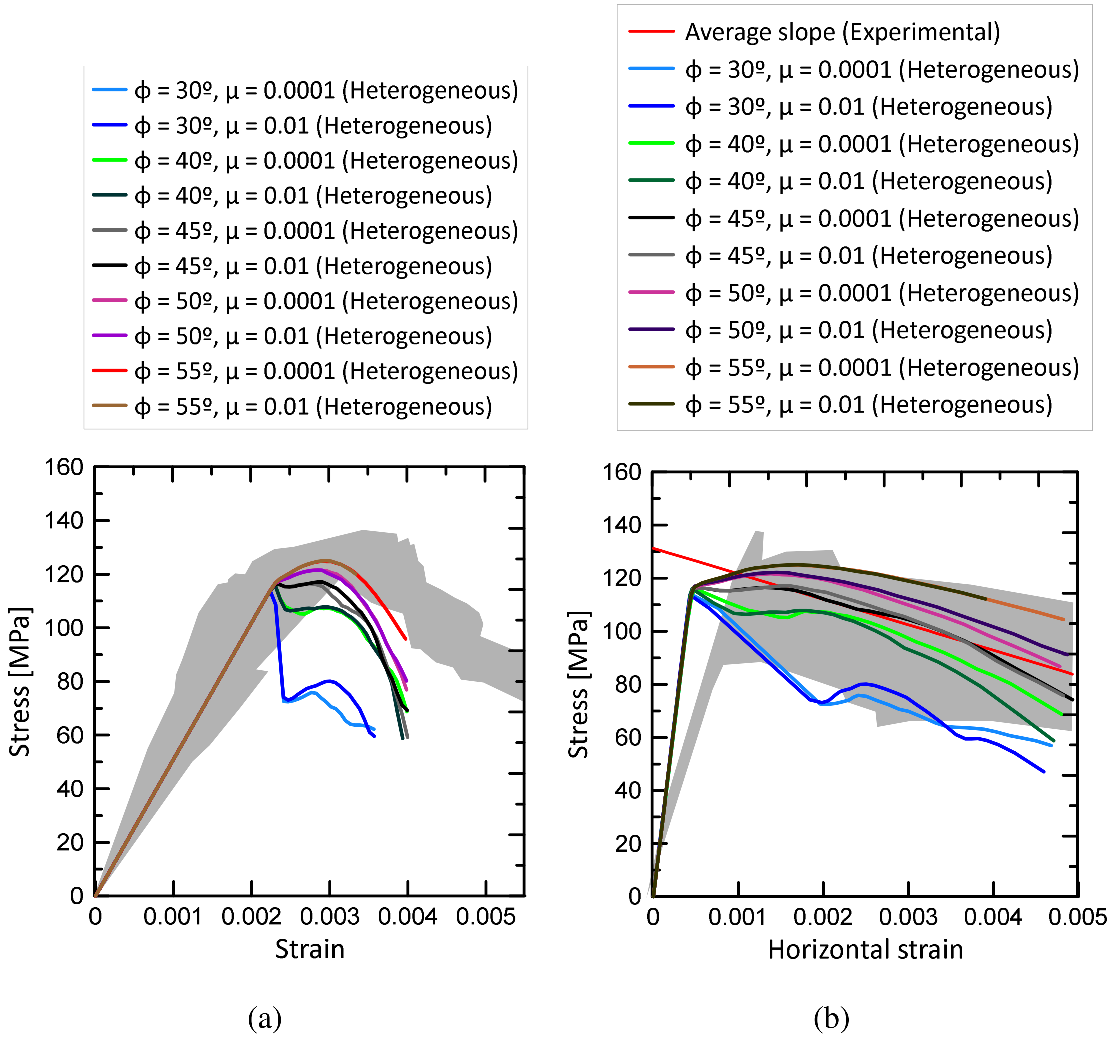

Figure 88 - Stress - vertical strain a (a) and stress-radial strain (b) curves for the heterogeneous models.

The tensile behavior was defined by adopting the results of direct tensile tests as the tensile strength of the matrix in the pre-cracking phase. In the post-cracking phase, the Pyfl [89] model calibrated to obtain the best correlation with the tensile tests was adopted. The comparison of the experimental stress-crack opening curves with theoretical uniaxial models led to a change in the originally used constitutive model to the one shown in Equation 12, resulting in a slight modification to the equation describing the behavior of the fibers after the opening corresponding to the maximum activation (w0) with the crack opening corresponding to a zero value stress in the original model being one fourth of the fiber length whereas the new model presents a crack opening of half the fiber length. Figure 88 shows the overlap of the adopted constitutive model considering the matrix strength and cracking energy obtained experimentally and the stress-crack opening curve obtained by DIC analysis.

$$\sigma_f(w) = \begin{cases} \sigma_{f0}\left(2\sqrt{\frac{w}{w_0}} - \frac{w}{w_0}\right) \text{ for } w \leq w_0 \\ \sigma_{f0}\left(1 - \frac{2w}{L_f}\right)^2 \text{ for } w > w_0 \end{cases} \tag{12}$$

Figure 89 (a) shows the constitutive models calibrated to match the experimentally obtained curves. The first attempt with the theoretical value for W0 resulted in a high peak after cracking. W0 was then calibrated to better match the experimental results and the final calibration for the tensile uniaxial model is shown.

Figure 89 (b) shows the overlapping of the experimentally observed damage evolution curves with the interpolated model based on Birtel and Mark's [78] model with the interpolated bt parameter. It can be noted that the analytical model resulted in a high damage evolution right after cracking, reaching values close to 1, while the experimental curves did not reach 1.

Another calibration of the bt parameter was made based on finite element models to reproduce the tensile tests. In this calibration, bt values, starting from the experimentally obtained value, were tested and the resulting load-displacement curves for the dogbone models were compared to the experimental curves to verify which value produces the best fit. Figure 89 (b) shows the final damage evolution model calibrated through this method.

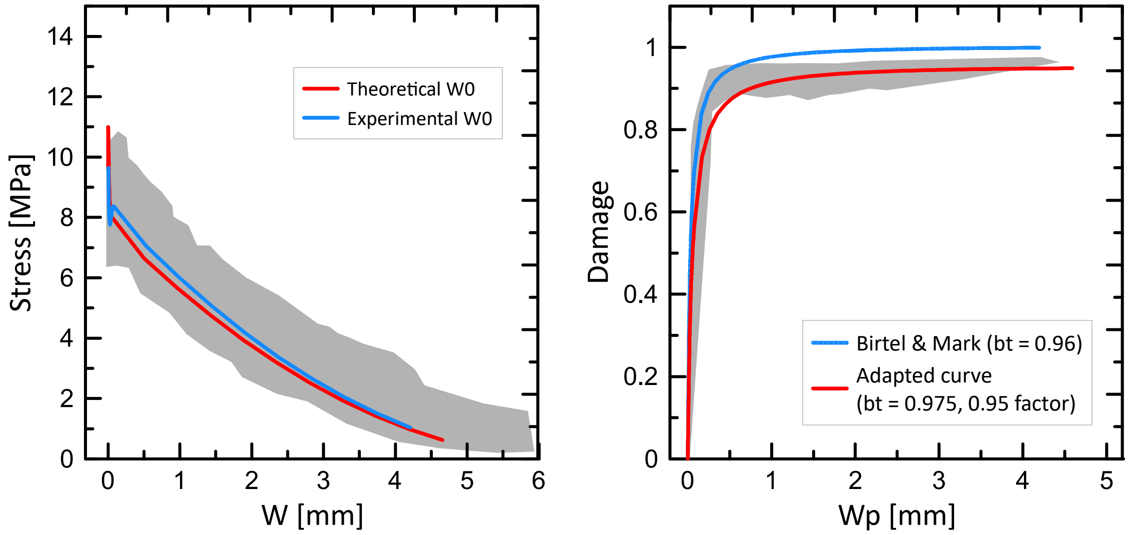

(a) (b)

Figure 89 - Comparison of the uniaxial tensile constitutive models with calibrated w0 (a) and damage evolution models (b) with the experimental curves.

For the calibration of the CDP parameters, two sets of dogbone models were made. Figure 90 (a) shows the model with homogeneous material properties while Figure 90 (c) shows the model with horizontal partitions to which different material properties were assigned. The partition length was adopted to match the length of the fibers.

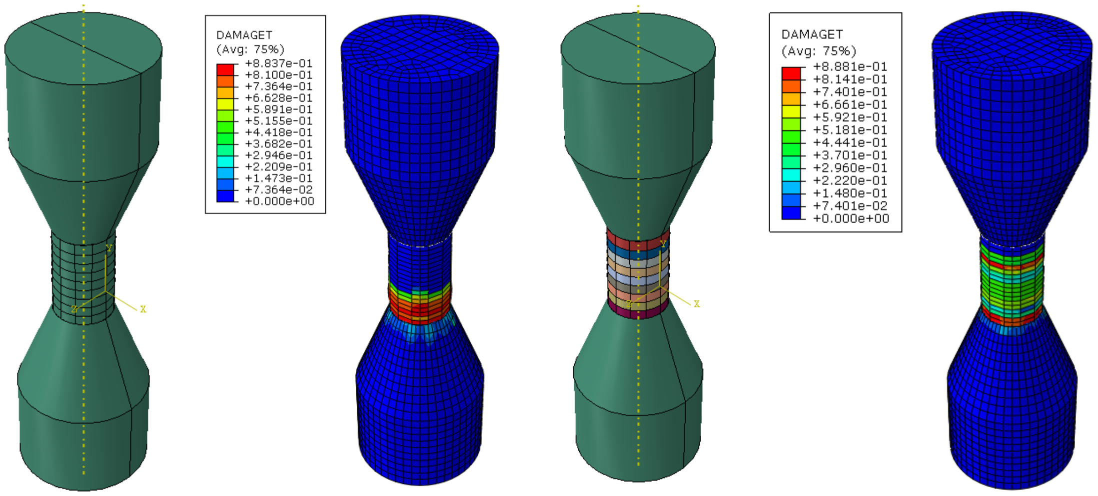

(a) (b) (c) (d)

Figure 90 - Homogeneous dogbone model (a) and corresponding damageT distribution (b) and heterogeneous dogbone model (c) with corresponding damageT distribution (d).

The comparison of models in Figure 90 shows that the change in the modelling strategy resulted in a change in the damage distribution in the model. For the homogeneous models, a larger portion of the model exhibited high damage values while the heterogeneous model showed lower damage values distributed through the specimen and high damage values confined in certain partitions of the model. In this way, the heterogeneity of the model served to contain the damage evolution to restricted parts of the model.

Figure 91 shows the comparison of the displacements between the top and bottom faces of the dogbone specimens. The load-displacement curves for homogeneous and heterogeneous models with tensile damage evolution curves based on Birtel and Mark's model with bt values ranging from 0.85 (interpolated from the cyclic tensile tests) and 0.975 are shown. From the curves, it can be noted that lower bt values resulted in faster drops in the post-cracking regime. For values over 0.968, the model showed little influence in an increase in the specified value. Figure 91 shows the results for two curves obtained through heterogeneous models with a bt value of 0.968 and one curve with a bt value of 0.975, with these three curves being inside the area defined by the envelope of the experimental results.

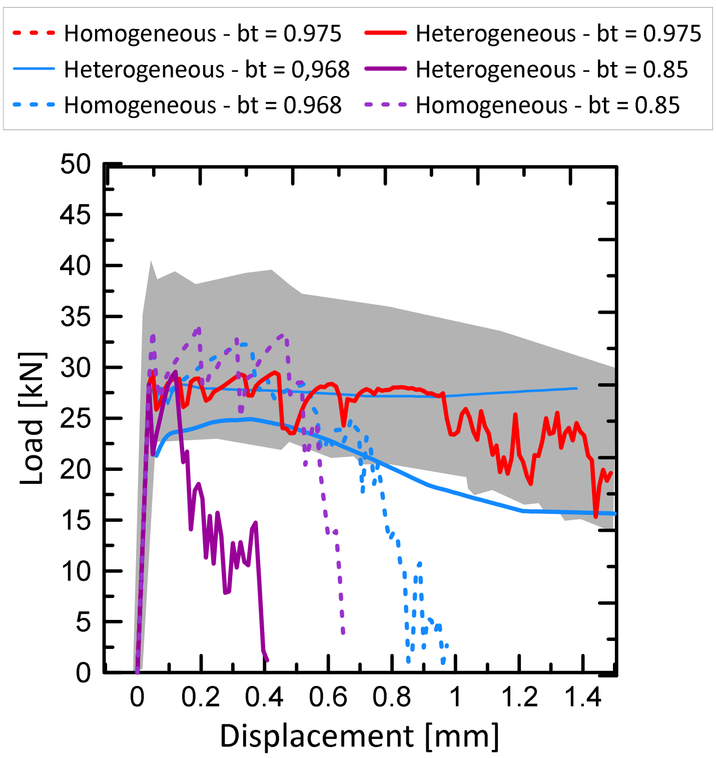

Figure 91 - Results for the calibration of the bt parameter through the dogbone models.

Regarding the comparison between homogeneous and heterogeneous models, the homogeneous models exhibited a more abrupt drop due to the generalized evolution of the damage variable in the model resulting in total degradation of the model's stiffness. For the heterogeneous models, the confined evolution of the tensile damage resulted in more stable models resulting in better fit for the load-displacement curves.

Figure 92 shows that the flexural model resulted in a more sensible analysis for the bt parameters. Load displacement curves for four-point load bending tests on heterogeneous models are shown for bt values ranging from 0.95 to the final value of 0.975. The values of 0.975 was specified for the bt parameter being the one that resulted in the best overall fit in both the tensile test models and the beam models, both reinforced and unreinforced and still resulting in a good agreement with the experimental damage evolution as show in Figure 89 (b).

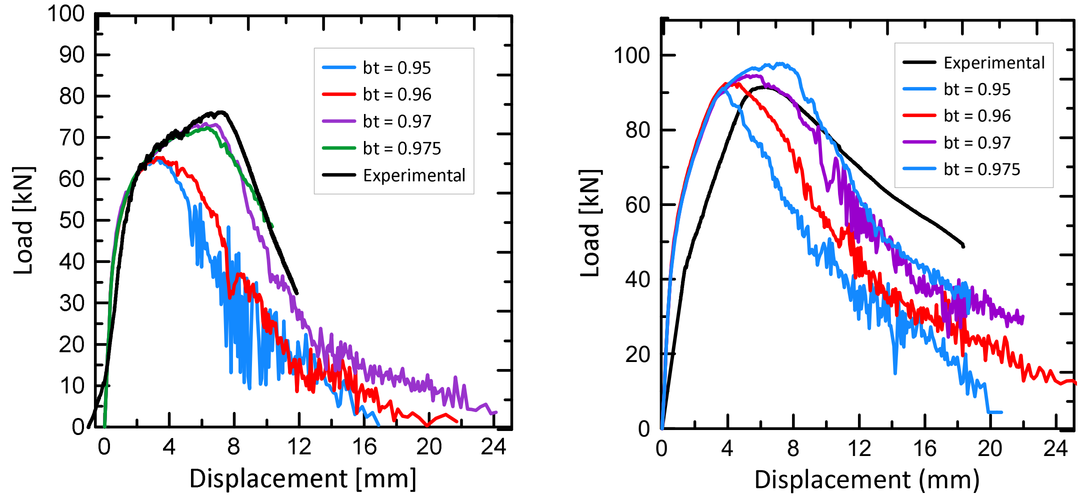

(a) (b)

Figure 92 - Results for the calibration of the bt parameter through the unreinforced beam (a) and reinforced beam (b)

5.2 Numerical models for the tested beams

As a way to compare the effects of the chosen damage evolution model over the UHPC beams' models, a set of four models were made for each of the five tested beams. For each beam, one homogeneous model and one heterogeneous model using both the simplified damage model used by Lima et al. [2] and the calibrated Birtel and Mark's [78] model according to the methodology here presented. The results for the load-displacement curves are shown in Figure 93.

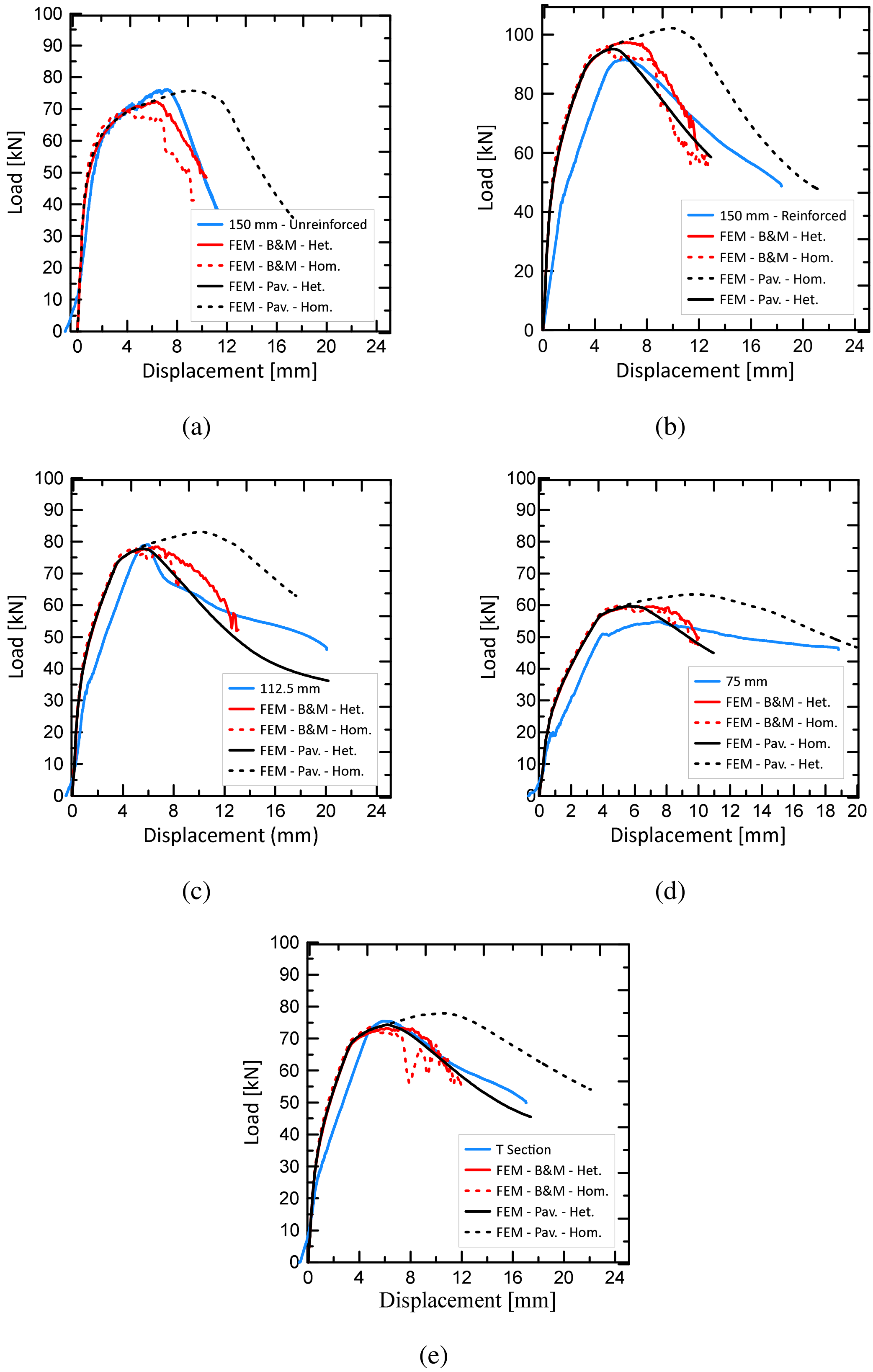

Figure 93 - Load displacement comparison between the experimental results and the numerical models with different cross-sections and damage evolution models for the unreinforced beam (a), the original cross-section beam (b), the intermediate beam (c), half cross-section beam (d) and the T-girder (e).

During the calibration of the modelling parameters, the tensile damage evolution model was the curve which presented most of the changes in the models' results. The experimental evolution of the tensile damage showed a high damage evolution right after the formation of the crack. Although the beam model using simplified model used by Lima et al. [2] resulted in a good agreement with the experimental results, the damage evolution analytical model did not represent what was experimentally observed. The adopted model adopted in that study resulted in lower damage evolution model in relation to the experimental damage evolution curves.

The curves in Figure 93 show that both sets of models behave in distinct ways considering the introduction of the heterogeneous material properties in the modelling technique. For a damage evolution model which the tensile damage evolves in a lower speed, the homogeneous models represent higher stiffness in the post peak regime while the heterogeneous model accelerated the damage variable evolution resulting in the localization of the damage in the model. The heterogeneous model represents a better fit to the experimental curve because it can reproduce higher damage values than the homogeneous model.

For models that result in a faster damage evolution, the homogeneous models represented a faster drop in the model stiffness because a generalized damage evolution was observed in the models that led to a general drop in stiffness. The consideration of the random material properties made the damage evolution more stable, with some locations serving lower damage points and raising the post-peak stiffness of the model, representing an opposite effect to what had been observed by Lima et al. [2].

Regarding the stability of the stiffness of the model in the post-peak regime, the beam models based in Pavlovic's [93] tensile damage evolution model exhibited a lower stiffness at the peak load. However, these models presented a longer lasting stability, with the curves remaining stable until higher displacement values. The models based on the calibration of Birtel and Mark's [78] presented a better correspondence to the experimental curves closer to the peak load but lost the damage localization for higher displacement values. In addition, the stiffness of these models presented a rapid degradation due to fast damage evolution. The curves presented in Figure 93 are shown until the last stable point.

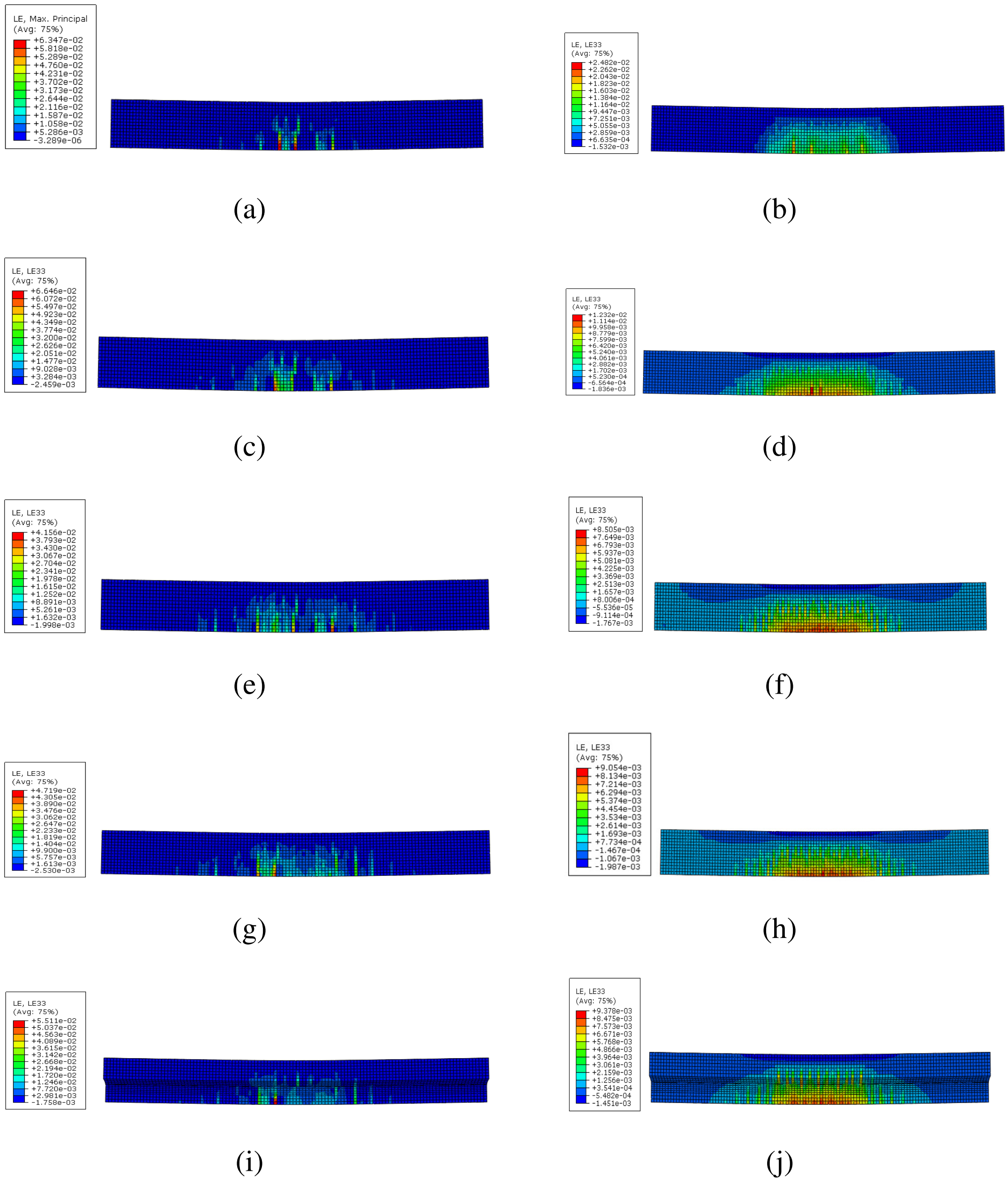

Figure 94 - Heterogeneous and homogeneous models for unreinforced beam (a and b), original section beam (c and d), intermediate beam (e and f), half section beam (g and h) and T-girder (I and j).

The comparison between homogeneous and heterogeneous models also showed that when same damage evolution expressions specified are compared, the simulations based on Birtel and Mark's [78] showed less difference between homogeneous and heterogeneous models. The reason for this, as was shown in Chapter 2, is that Pavlovich's damage model is able to represent a wider range of damage evolution curves.

Figure 94 shows the comparison of longitudinal strains for the heterogeneous beams at the peak load. It can be noted that the heterogeneous models resulted in variations in the longitudinal strains while the homogeneous models resulted in continuous strains with no concentrations. When observing the zones with strain concentrations, it can be noted that the beams with higher reinforcement ratios resulted in a more distributed strain pattern than the beam with no reinforcement or the beam with the original section.

6 CONCLUSIONS

Genetic algorithm optimization showed that a T-section resulted in the best result for load capacity while maintaining the minimum drift capacity ratio, both strongly influenced by the thickness of the beam's cross-section subjected to tensile stresses. I-shaped cross-section beams exhibited high load capacity and low ductility, while beams with a smaller bottom width showed higher ductility and lower load capacity. The optimized beam, according to simulations, had 20,42% higher load capacity than the rectangular beam with minimum ductility and 17.54%% greater ductility than the rectangular beam with the same load capacity. Regarding the experimental results, the ductility relations were also verified, with an increase in ductility with reinforcement ratio, and with the T-section beam presenting a higher ductility than its rectangular counterpart.

The modeling technique based on the calibrated parameters showed good correspondence with the structural tests, being an adequate way to represent load-displacement curves of beams subjected to four-point load bending tests. All models resulted in a good benchmark to experimental curves considering both pre and post-peak branches of load displacement curves, but also load capacity. For the half-section beam, however the model could not sustain the post-peak stiffness for a large displacement as observed in the experimental results.

Regarding the failure pattern, the material models applied by Lima et al. [2] represented a higher localization tendency for the DamageT variable due to the greater variability of Pavlovic's [93] damage evolution for tensile damage evolution.

The material level models resulted in a novel method for the calibration of CDP parameters resulting in good correspondence to material level tests. This method can now be used to justify choosing of CDP parameters for numerical models.

6.1 FUTURE WORKS

For future works, the measurement of dilation through cyclic tests in confined concrete can present a correlation of damage and dilation of UHPC.

For the direct tensile tests, it would be beneficial to redo the tests with the displacement control made with LVDTs and the crack opening measured with DIC, so that the initial damage evolution can be better recorded.

The experimental assessment of other beams presented in the preliminary numerical assessment could present interesting results, higher load capacities and material reduction or higher ductility's

The experimental correlation of the fiber distribution inside the specimen's volume could be used to determine the material properties in each partition cell to verify if the damage pattern can reproduce the cracking patterns observed experimentally.

Regarding the heterogeneous modelling technique, applications in models subjected to fatigue and dynamic loads are still to be investigated.

When comparing the CC elements to UHPC, the cost analysis and life cycle analysis from cradle to end-of-life could show how well UHPC does compared to CC in financial terms, if the reduction on the cross-section can compensate the higher cost of this material, and also take into account the environmental effects of this material. The comparison between the higher cement consumption and the reduction in material consumption to resist the same load capacities is still to be investigated through a life cycle approach.

7 REFERENCES

[1] R. Ding, Y.-T. Sun, X. Nie, and D.-Q. Chen, “Experimental study on seismic behaviour of an unreinforced precast wall-slab structure based on UHPC sandwich panels,” *J. Build. Eng.*, vol. 68, p. 106197, Jun. 2023, doi: 10.1016/j.jobe.2023.106197.

[2] P. B. De Lima, P. A. Krahl, F. A. Silva, and D. C. T. Cardoso, “A modeling strategy for the flexural performance prediction of UHPC beams accounting for variability of properties,” *Compos. Struct.*, vol. 322, p. 117374, Oct. 2023, doi: 10.1016/j.compstruct.2023.117374.

[3] “UHPC cladding panel FClad: thickness and performance.” Accessed: Jan. 31, 2024. [Online]. Available: https://fehrgroup.com/en/cladding-panels/

[4] “TAKTL® Architectural UHPC | TAKTL Architectural UHPC | Facade + Wall Panels, Rainscreen Cladding, Custom Elements.” Accessed: Jan. 31, 2024. [Online]. Available: https://www.taktl-llc.com/

[5] “Fiber Concrete / UHPC | ECO Cladding.” Accessed: Jan. 31, 2024. [Online]. Available: https://www.ecocladding.com/system/fiber-concrete-uhpc

[6] M. A. Bajaber and I. Y. Hakeem, “UHPC evolution, development, and utilization in construction: a review,” *J. Mater. Res. Technol.*, vol. 10, pp. 1058–1074, Jan. 2021, doi: 10.1016/j.jmrt.2020.12.051.

[7] M. Aria and C. Cuccurullo, “bibliometrix : An R-tool for comprehensive science mapping analysis,” *J. Informetr.*, vol. 11, no. 4, pp. 959–975, Nov. 2017, doi: 10.1016/j.joi.2017.08.007.

[8] N. J. Van Eck and L. Waltman, “Software survey: VOSviewer, a computer program for bibliometric mapping,” *Scientometrics*, vol. 84, no. 2, pp. 523–538, Aug. 2010, doi: 10.1007/s11192-009-0146-3.

[9] ASTM, “C1856/C1856M-17 - Standard Practice for Fabricating and Testing Specimens of Ultra-High Performance Concrete.” 2017.

[10] CSA, “A23.1/A23.2 Concrete materials and methods of concrete construction/Test methods and standard practices for concrete.” 2019.

[11] “Swiss Standard SIA 2052 UHPFRC: Materials, Design and Application.” 2016.

[12] AFNOR, “NFP 18 470.” 2016.

[13] JSCE, “Recommendations for Design and Construction of Ultra High Strength Fiber Reinforced Concrete Structures.”

[14] Office of Research, Development, and Technology, “Design and Construction of UHPC-Based Bridge Preservation and Repair Solutions”, doi: 10.21949/1521867.

[15] N. M. Azmee and N. Shafiq, “Ultra-high performance concrete: From fundamental to applications,” *Case Stud. Constr. Mater.*, vol. 9, p. e00197, Dec. 2018, doi: 10.1016/j.cscm.2018.e00197.

[16] “Projects.” Accessed: Jan. 31, 2024. [Online]. Available: https://www.ductal.com/en/projects

[17] G. Zhang and B. A. Graybeal, “Development of UHPC Pi-Girder Sections for Span Length up to 41 m,” *J. Bridge Eng.*, vol. 20, no. 3, p. 04014068, Mar. 2015, doi: 10.1061/(ASCE)BE.1943-5592.0000653.

[18] V. T. Nguyen and V. C. Mai, “Flexural behavior of 60 m UHPC pre-stressed box girder,” 2022, doi: 10.34910/MCE.112.12.

[19] C. Li, Z. Feng, R. Pan, L. Ke, J. He, and S. Dong, “Experimental and Numerical Investigation on the Anchorage Zone of Prestressed UHPC Box-Girder Bridge,” *J.*

Bridge Eng., vol. 25, no. 6, p. 04020028, Jun. 2020, doi: 10.1061/(ASCE)BE.1943-5592.0001556.

[20] J. Zhu, X. Guo, J. Kang, M. Duan, and Y. Wang, "Numerical and theoretical research on flexural behavior of steel-UHPC composite beam with waffle-slab system," *J. Constr. Steel Res.*, vol. 171, p. 106141, Aug. 2020, doi: 10.1016/j.jcsr.2020.106141.

[21] X. Liu, J. Zhang, Z. Cheng, and M. Ye, "Experimental and Numerical Studies on the Negative Flexural Behavior of Steel-UHPC Composite Beams," *Adv. Civ. Eng.*, vol. 2021, pp. 1–15, Jan. 2021, doi: 10.1155/2021/8828175.

[22] J.-L. Xiao, T.-Y. Yang, X. Nie, B.-Y. Li, J.-S. Fan, and B.-A. Shu, "Experimental and numerical investigation on mechanical performance of continuous steel-UHPC composite slabs," *Eng. Struct.*, vol. 270, p. 114804, Nov. 2022, doi: 10.1016/j.engstruct.2022.114804.

[23] Z. Wan, Z. Fang, L. Liang, S. He, and X. Sun, "Structural performance of steel–concrete composite beams with UHPC overlays under hogging moment," *Eng. Struct.*, vol. 270, p. 114866, Nov. 2022, doi: 10.1016/j.engstruct.2022.114866.

[24] H. Wang, T. Sun, X. Shao, C. Tang, and L. Yang, "Static behavior of a steel-ultra high performance concrete continuous composite box girder," *Struct. Infrastruct. Eng.*, vol. 18, no. 8, pp. 1120–1137, Aug. 2022, doi: 10.1080/15732479.2021.1876739.

[25] D. Kruszewski, A. E. Zaghi, and K. Wille, "Finite element study of headed shear studs embedded in ultra-high performance concrete," *Eng. Struct.*, vol. 188, pp. 538–552, Jun. 2019, doi: 10.1016/j.engstruct.2019.03.035.

[26] Y. Ma, B. Zhang, A. Peng, and L. Wang, "Experimental and analytical investigation on shear mechanism of steel-UHPC composite T-Perfobond shear connectors," *Eng. Struct.*, vol. 286, p. 116061, Jul. 2023, doi: 10.1016/j.engstruct.2023.116061.

[27] Z. Fang, L. Hu, H. Jiang, S. Fang, G. Zhao, and Y. Ma, "Shear performance of high-strength friction-grip bolted shear connector in prefabricated steel–UHPC composite beams: Finite element modelling and parametric study," *Case Stud. Constr. Mater.*, vol. 18, p. e01860, Jul. 2023, doi: 10.1016/j.cscm.2023.e01860.

[28] Z. Fang, S. Fang, and F. Liu, "Experimental and Numerical Study on the Shear Performance of Short Stud Shear Connectors in Steel–UHPC Composite Beams," *Buildings*, vol. 12, no. 4, p. 418, Mar. 2022, doi: 10.3390/buildings12040418.

[29] J. Qi, Y. Hu, J. Wang, and W. Li, "Behavior and strength of headed stud shear connectors in ultra-high performance concrete of composite bridges," *Front. Struct. Civ. Eng.*, vol. 13, no. 5, pp. 1138–1149, Oct. 2019, doi: 10.1007/s11709-019-0542-6.

[30] A. Baghdadi, M. Heristchian, L. Ledderose, and H. Kloft, "Experimental and numerical assessment of new precast concrete connections under bending loads," *Eng. Struct.*, vol. 212, p. 110456, Jun. 2020, doi: 10.1016/j.engstruct.2020.110456.

[31] E.-F. Deng *et al.*, "Experimental study on flexural behavior of UHPC wet joint in prefabricated multi-girder bridge," *Eng. Struct.*, vol. 275, p. 115314, Jan. 2023, doi: 10.1016/j.engstruct.2022.115314.

[32] W. Xue, X. Hu, and J. Song, "Experimental study on seismic behavior of precast concrete beam-column joints using UHPC-based connections," *Structures*, vol. 34, pp. 4867–4881, Dec. 2021, doi: 10.1016/j.istruc.2021.10.067.

[33] S. Mahdi, M. S. M. Ali, A. H. Sheikh, M. Elchalakani, and T. Xie, "An investigation into the feasibility of normal and fibre-reinforced ultra-high performance concrete multi-cell and composite sandwich panels," *J. Build. Eng.*, vol. 41, p. 102728, Sep. 2021, doi: 10.1016/j.jobe.2021.102728.

[34] W. Ge *et al.*, "Flexural performance of prefabricated U-shaped UHPC permanent formwork–concrete composite beams reinforced with FRP bars," *Arch. Civ. Mech. Eng.*, vol. 23, no. 2, p. 108, Apr. 2023, doi: 10.1007/s43452-023-00644-4.

[35] D. H. H. Phan, V. I. Patel, Q. Q. Liang, H. Al Abadi, and H.-T. Thai, "Numerical investigations of circular double-skin steel tubular slender beam-columns filled with ultra-high-strength concrete," *Eng. Struct.*, vol. 254, p. 113814, Mar. 2022, doi: 10.1016/j.engstruct.2021.113814.

[36] W. Qin, Z. Zhang, Z. Xi, and D. Wang, "Experimental investigation on the progressive collapse resistance of UHPC-RC composite beam-column structures," *Eng. Struct.*, vol. 284, p. 115737, Jun. 2023, doi: 10.1016/j.engstruct.2023.115737.

[37] H. Cai and Y. Yan, "UHPC-Filled Rectangular Steel Tubular Beam–Column: Numerical Study and Design," *Buildings*, vol. 12, no. 11, p. 1882, Nov. 2022, doi: 10.3390/buildings12111882.

[38] M. T. Marvila, A. R. G. Azevedo, and S. N. Monteiro, "Verification of the application potential of the mathematical models of lyse, abrams and molinari in mortars based on cement and lime," *J. Mater. Res. Technol.*, vol. 9, no. 4, pp. 7327–7334, Jul. 2020, doi: 10.1016/j.jmrt.2020.04.077.

[39] F.-W. Shi, C.-H. Sun, X.-G. Liu, H. Wang, and L. Zong, "Flexural behavior of prefabricated composite beam with cast-in-situ UHPC: Experimental and numerical studies," *Structures*, vol. 45, pp. 670–684, Nov. 2022, doi: 10.1016/j.istruc.2022.09.048.

[40] H. M. Elsanadedy, H. Abbas, T. H. Almusallam, and Y. A. Al-Salloum, "Hybrid UHPC/NSM CFRP strips vs. traditional systems for flexural upgrading of RC beams – Experimental and FE study," *Compos. Struct.*, vol. 261, p. 113291, Apr. 2021, doi: 10.1016/j.compstruct.2020.113291.

[41] A. H. Selim, F. Mahmoudi, J. A. Abdalla, R. A. Hawileh, F. Abed, and M. Kyaure, "Finite Element Modeling of Engineered Cementitious Composite (ECC) Prisms and Beams," in *2022 Advances in Science and Engineering Technology International Conferences (ASET)*, Dubai, United Arab Emirates: IEEE, Feb. 2022, pp. 1–6. doi: 10.1109/ASET53988.2022.9734820.

[42] H. Yin, K. Shirai, and W. Teo, "Numerical model for predicting the structural response of composite UHPC–concrete members considering the bond strength at the interface," *Compos. Struct.*, vol. 215, pp. 185–197, May 2019, doi: 10.1016/j.compstruct.2019.02.040.

[43] *Ultra-high-performance concrete: an emerging technology report (ACI 239R-18)*. Farmington Hills, MI: American Concrete Institute, 2018.

[44] S. A. Paschalis and A. P. Lampropoulos, "Developments in the use of Ultra High Performance Fiber Reinforced Concrete as strengthening material," *Eng. Struct.*, vol. 233, p. 111914, Apr. 2021, doi: 10.1016/j.engstruct.2021.111914.

[45] M. Singh, A. H. Sheikh, M. S. Mohamed Ali, P. Visintin, and M. C. Griffith, "Experimental and numerical study of the flexural behaviour of ultra-high performance fibre reinforced concrete beams," *Constr. Build. Mater.*, vol. 138, pp. 12–25, May 2017, doi: 10.1016/j.conbuildmat.2017.02.002.

[46] A. A. Bahraq, M. A. Al-Osta, S. Ahmad, M. M. Al-Zahrani, S. O. Al-Dulaijan, and M. K. Rahman, "Experimental and Numerical Investigation of Shear Behavior of RC Beams Strengthened by Ultra-High Performance Concrete," *Int. J. Concr. Struct. Mater.*, vol. 13, no. 1, p. 6, Dec. 2019, doi: 10.1186/s40069-018-0330-z.

[47] H. Li, L. Li, X. Fan, M. Ye, X. Shao, and L. Yi, "Experimental and numerical investigation on the flexural behavior of a large-scale prestressed UHPC T-Shaped

girder," *Eng. Struct.*, vol. 272, p. 115027, Dec. 2022, doi: 10.1016/j.engstruct.2022.115027.

[48] Z. Feng, C. Li, L. Ke, and D.-Y. Yoo, "Experimental and numerical investigations on flexural performance of ultra-high-performance concrete (UHPC) beams with wet joints," *Structures*, vol. 45, pp. 199–213, Nov. 2022, doi: 10.1016/j.istruc.2022.09.029.

[49] Q. Sun and C. Liu, "Experimental study and calculation method on the flexural resistance of reinforced concrete beam strengthened using high STRAIN-HARDENING ultra high performance concrete," *Struct. Concr.*, vol. 22, no. 3, pp. 1741–1759, Jun. 2021, doi: 10.1002/suco.202000592.

[50] A. Basha, S. Fayed, and G. Elsamak, "Flexural Behavior of Cracked RC Beams Retrofitted with Strain Hardening Cementitious Composites," *KSCE J. Civ. Eng.*, vol. 23, no. 6, pp. 2644–2656, Jun. 2019, doi: 10.1007/s12205-019-1874-4.

[51] Q. Wang, Q. Li, X. Yin, S. Xu, Z. Su, and H. Xie, "Fracture behavior and size effect of UHPFRC: Experimental and meso-scale numerical investigation," *Eng. Fract. Mech.*, vol. 283, p. 109197, Apr. 2023, doi: 10.1016/j.engfracmech.2023.109197.

[52] X.-L. Gao and J.-Y. Wang, "Experimental and numerical study on the tensile behaviours of wet joints in steel-UHPC composite decks using a novel tensile test setup," *Mater. Struct.*, vol. 54, no. 2, p. 93, Apr. 2021, doi: 10.1617/s11527-021-01686-x.

[53] S. Yuan, Z. Liu, T. Tong, and J. Liu, "Experimental, analytical, and numerical investigation on flexural behavior of hybrid beams consisting of ultra-high performance and normal-strength concrete," *Eng. Struct.*, vol. 268, p. 114725, Oct. 2022, doi: 10.1016/j.engstruct.2022.114725.

[54] M. M. A. Kadhim, A. Jawdhari, and A. Peiris, "Development of hybrid UHPC-NC beams: A numerical study," *Eng. Struct.*, vol. 233, p. 111893, Apr. 2021, doi: 10.1016/j.engstruct.2021.111893.

[55] M. A. Sakr, A. A. Sleemah, T. M. Khalifa, and W. N. Mansour, "Shear strengthening of reinforced concrete beams using prefabricated ultra-high performance fiber reinforced concrete plates: Experimental and numerical investigation," *Struct. Concr.*, vol. 20, no. 3, pp. 1137–1153, Jun. 2019, doi: 10.1002/suco.201800137.

[56] J. Yang, B. Chen, J. Su, G. Xu, D. Zhang, and J. Zhou, "Effects of fibers on the mechanical properties of UHPC: A review," *J. Traffic Transp. Eng. Engl. Ed.*, vol. 9, no. 3, pp. 363–387, Jun. 2022, doi: 10.1016/j.jtte.2022.05.001.

[57] A. Hussein Ali Al-Ahmed, A. Al-Rumaithi, A. A. Allawi, and A. El-Zohairy, "Mesoscale analysis of Fiber-Reinforced concrete beams," *Eng. Struct.*, vol. 266, p. 114575, Sep. 2022, doi: 10.1016/j.engstruct.2022.114575.

[58] Rots, Jan, and Blaauwendraad, "Crack Models for Concrete, Discrete or Smeared? Fixed, Multi-Directional or Rotating?," *Crack Models Concr. Discrete Smeared Fixed Multi-Dir. Rotating*, 1989.

[59] N. Hrebenkach, "ATENA Program Documentation Part".

[60] L. J. Malvar, J. E. Crawford, J. W. Wesevich, and D. Simons, "A plasticity concrete material model for DYNA3D," *Int. J. Impact Eng.*, vol. 19, no. 9, pp. 847–873, Oct. 1997, doi: 10.1016/S0734-743X(97)00023-7.

[61] Hrynyk and Vecchio, "VecTor4 User's Manual." 2019.

[62] J. Lubliner, J. Oliver, S. Oller, and E. Oñate, "A plastic-damage model for concrete," *Int. J. Solids Struct.*, vol. 25, no. 3, pp. 299–326, 1989, doi: 10.1016/0020-7683(89)90050-4.

[63] R. Franssen, S. Guner, L. Courard, and B. I. Mihaylov, "Numerical modeling approach for UHPFRC members including crack spacing formulations," *Eng. Struct.*, vol. 238, p. 112179, Jul. 2021, doi: 10.1016/j.engstruct.2021.112179.

[64] Y. Zhang, Z. Yang, T. Xie, and J. Yang, "Flexural behaviour and cost effectiveness of layered UHPC-NC composite beams," *Eng. Struct.*, vol. 273, p. 115060, Dec. 2022, doi: 10.1016/j.engstruct.2022.115060.

[65] Y. Song, S. Yao, and L. Liu, "Flexural Reinforcement of Over-Reinforced Beam by Ultrahigh Performance Concrete Layer," *Math. Probl. Eng.*, vol. 2022, pp. 1–15, Dec. 2022, doi: 10.1155/2022/9171300.

[66] W. Mansour, B. A.Tayeh, and L. Tam, "Finite element analysis of shear performance of UHPFRC-encased steel composite beams: Parametric study," *Eng. Struct.*, vol. 271, p. 114940, Nov. 2022, doi: 10.1016/j.engstruct.2022.114940.

[67] A. M. Mahdi, "Impact of Failure-surface Parameters of Concrete Damage Plasticity Model on the Behavior of Reinforced Ultra-high Performance Concrete Beams," *Period. Polytech. Civ. Eng.*, Feb. 2023, doi: 10.3311/PPci.21345.

[68] *CEB-FIP Model Code 90*. 1993.

[69] W. Zheng, L. Li, and S. Lu, "Experimental research on mechanical performance of normal section of reinforced reactive powder concrete beam," *Jianzhu Jiegou XuebaoJournal Build. Struct.*, vol. 32, no. 6, pp. 125–134, 2011.

[70] Z.-H. Lu and Y.-G. Zhao, "Empirical stress-strain model for unconfined high-strength concrete under uniaxial compression," *J. Mater. Civ. Eng.*, vol. 22, no. 11, pp. 1181–1186, 2010, doi: 10.1061/(ASCE)MT.1943-5533.0000095.

[71] P. R. Prem, A. Ramachandra Murthy, and B. H. Bharatkumar, "Influence of curing regime and steel fibres on the mechanical properties of UHPC," *Mag. Concr. Res.*, vol. 67, no. 18, pp. 988–1002, Sep. 2015, doi: 10.1680/macr.14.00333.

[72] Yang, "Flexural behavior of ultra-high performance concrete beams prestressed with CFRP tendons," Hunan University, Changsha, China, 2007.

[73] M. A. Mansur, M. S. Chin, and T. H. Wee, "Stress-Strain Relationship of High-Strength Fiber Concrete in Compression," *J. Mater. Civ. Eng.*, vol. 11, no. 1, pp. 21–29, Feb. 1999, doi: 10.1061/(ASCE)0899-1561(1999)11:1(21).

[74] E. Osorio, J. M. Bairán, and A. R. Marí, "Lateral behavior of concrete under uniaxial compressive cyclic loading," *Mater. Struct.*, vol. 46, no. 5, pp. 709–724, May 2013, doi: 10.1617/s11527-012-9928-9.

[75] RILEM, "RILEM TC 148-SSC: STRAIN SOFTENING OF CONCRETE - TEST METHODS FOR COMPRESSIVE SOFTENING123003." 2000.

[76] D. C. Jansen and S. P. Shah, "Effect of Length on Compressive Strain Softening of Concrete," *J. Eng. Mech.*, vol. 123, no. 1, pp. 25–35, Jan. 1997, doi: 10.1061/(ASCE)0733-9399(1997)123:1(25).

[77] N. Pressmair, F. Brosch, M. Hammerl, and B. Kromoser, "Non-linear material modelling strategy for conventional and high-performance concrete assisted by testing," *Cem. Concr. Res.*, vol. 161, p. 106933, Nov. 2022, doi: 10.1016/j.cemconres.2022.106933.

[78] V. Birtel and P. Mark, "Parameterised Finite Element Modelling of RC Beam Shear Failure," 2006.

[79] B. A. Graybeal, "Material Property Characterization of Ultra-High Performance Concrete".

[80] Graybeal, "Compressive Behavior of Ultra-High-Performance Fiber-Reinforced Concrete," *ACI Mater. J.*, vol. 104, no. 2, 2007, doi: 10.14359/18577.

[81] Carreira and Chu, *Model Code 2010. 1.* in Bulletin / Fédération Internationale du Béton, no. 55. Lausanne: International Federation for Structural Concrete (fib), 2010.
[82] P. A. Krahl, G. De Miranda Saleme Gidrão, and R. Carrazedo, “Compressive behavior of UHPFRC under quasi-static and seismic strain rates considering the effect of fiber content,” *Constr. Build. Mater.*, vol. 188, pp. 633–644, Nov. 2018, doi: 10.1016/j.conbuildmat.2018.08.121.
[83] Zhang, Shao, Li, Zhu, and Chen, “Axial Tensile Behavior Test of Ultra High Performance Concrete.” 2015.
[84] D. A. Hordjijk, “Tensile and fatigue behaviour of concrete; experiments, modelling and analyses,” *Tensile and fatigue behaviour of concrete; experiments, modelling and analyses*, 1992.
[85] A. Hillerborg, M. Modéer, and P.-E. Petersson, “Analysis of crack formation and crack growth in concrete by means of fracture mechanics and finite elements,” *Cem. Concr. Res.*, vol. 6, no. 6, pp. 773–781, Nov. 1976, doi: 10.1016/0008-8846(76)90007-7.
[86] Z. P. Bažant and B. H. Oh, “Crack band theory for fracture of concrete,” *Matér. Constr.*, vol. 16, no. 3, pp. 155–177, May 1983, doi: 10.1007/BF02486267.
[87] Aveston and Kelly, “Single and multiple fracture. In: The Prop. fibre Compos.Conf. proceedings, Natl. Phys. Lab., Guilford: IPC Science and Technology Press Ltd; 1971. p. 15–26.,” 1971.
[88] V. C. Li and C. K. Y. Leung, “Steady-State and Multiple Cracking of Short Random Fiber Composites,” *J. Eng. Mech.*, vol. 118, no. 11, pp. 2246–2264, Nov. 1992, doi: 10.1061/(ASCE)0733-9399(1992)118:11(2246).
[89] Pyfl, “Tragverhalten von Stahlfaserbeton,” Zurich, 2003.
[90] E. Fehling, M. Schmidt, J. C. Walraven, T. Leutbecher, and S. Fröhlich, Eds., *Ultra-high performance concrete UHPC: fundamentals - design - examples*. in Beton-Kalender Series. Berlin: Ernst & Sohn, 2014.
[91] G. H. Mahmud, Z. Yang, and A. M. T. Hassan, “Experimental and numerical studies of size effects of Ultra High Performance Steel Fibre Reinforced Concrete (UHPFRC) beams,” *Constr. Build. Mater.*, vol. 48, pp. 1027–1034, Nov. 2013, doi: 10.1016/j.conbuildmat.2013.07.061.
[92] P. A. Krahl, R. Carrazedo, and M. K. El Debs, “Mechanical damage evolution in UHPFRC: Experimental and numerical investigation,” *Eng. Struct.*, vol. 170, pp. 63–77, Sep. 2018, doi: 10.1016/j.engstruct.2018.05.064.
[93] M. Pavlović, Z. Marković, M. Veljković, and D. Buđevac, “Bolted shear connectors vs. headed studs behaviour in push-out tests,” *J. Constr. Steel Res.*, vol. 88, pp. 134–149, Sep. 2013, doi: 10.1016/j.jcsr.2013.05.003.
[94] X. Tian, Z. Fang, T. Zhou, and Y. Xiang, “Behavior and constitutive model of ultra-high-performance concrete under monotonic and cyclic tensile loading,” *Constr. Build. Mater.*, vol. 389, p. 131634, Jul. 2023, doi: 10.1016/j.conbuildmat.2023.131634.
[95] B. Alfarah, F. López-Almansa, and S. Oller, “New methodology for calculating damage variables evolution in Plastic Damage Model for RC structures,” *Eng. Struct.*, vol. 132, pp. 70–86, Feb. 2017, doi: 10.1016/j.engstruct.2016.11.022.
[96] A. N. Dancygier and E. Berkover, “Cracking localization and reduced ductility in fiber-reinforced concrete beams with low reinforcement ratios,” *Eng. Struct.*, vol. 111, pp. 411–424, Mar. 2016, doi: 10.1016/j.engstruct.2015.11.046.

[97] A. N. Dancygier and Y. S. Karinski, “Probabilistic model of the crack localization in axially loaded fibrous reinforced concrete bars,” *Eng. Struct.*, vol. 79, pp. 417–426, Nov. 2014, doi: 10.1016/j.engstruct.2014.07.043.

[98] Yang and Xu, “A heterogeneous cohesive model for quasi-brittle materials considering spatially varying random fracture properties,” *Heterog. Cohesive Model Quasi-Brittle Mater. Considering Spatially Varying Random Fract. Prop.*, 2008, doi: https://doi.org/10.1016/j.cma.2008.03.027.

[99] Y. Shao and S. L. Billington, “Impact of UHPC Tensile Behavior on Steel Reinforced UHPC Flexural Behavior,” *J. Struct. Eng.*, vol. 148, no. 1, p. 04021244, Jan. 2022, doi: 10.1061/(ASCE)ST.1943-541X.0003225.

[100] A. V. Benedito, “UNIVERSIDADE ESTADUAL DE MARINGÁ CENTRO DE TECNOLOGIA DEPARTAMENTO DE ENGENHARIA CIVIL PROGRAMA DE PÓS-GRADUAÇÃO EM ENGENHARIA CIVIL”.

[101] “Abaqus Analysis User’s Manual, vol3”.

[102] M. Melanie, “An Introduction to Genetic Algorithms”.

[103] M. Lepˇs, “Applying genetic algorithms to optimization of reinforced concrete beam”.

[104] K. Sastry, D. Goldberg, and G. Kendall, “Genetic Algorithms,” in *Search Methodologies*, E. K. Burke and G. Kendall, Eds., Boston, MA: Springer US, 2005, pp. 97–125. doi: 10.1007/0-387-28356-0_4.

[105] T. Adibaskoro and M. Suarjana, “Prestressed Concrete I-Girder Optimization via Genetic Algorithm,” *J. Eng. Technol. Sci.*, vol. 51, no. 2, pp. 170–183, Apr. 2019, doi: 10.5614/j.eng.technol.sci.2019.51.2.2.

[106] S. Malasri, D. A. Halijan, and M. L. Keough, “Concrete Beam Design Optimization with Genetic Algorithms,” vol. 48, 1994.

[107] C. A. Coello Coello, A. D. Christiansen, and F. S. Hern�ndez, “A simple genetic algorithm for the design of reinforced concrete beams,” *Eng. Comput.*, vol. 13, no. 4, pp. 185–196, Dec. 1997, doi: 10.1007/BF01200046.

[108] S. T. Yousif and R. M. Najem, “OPTIMUM COST DESIGN OF REINFORCED CONCRETE BEAMS USING GENETIC ALGORITHMS,” 2012.

[109] ABNT, “NBR 5739 (ABNT/MB 3) de 05/2018 - Concreto - Ensaio de compressão de corpos de prova cilíndricos.” 2018.

[110] S. Wang, L. Xu, C. Yin, Z. Chen, and Y. Chi, “Experimental investigation on the damage behavior of ultra-high performance concrete subjected to cyclic compression,” *Compos. Struct.*, vol. 267, p. 113855, Jul. 2021, doi: 10.1016/j.compstruct.2021.113855.

[111] D. L. Nguyen, G. S. Ryu, K. T. Koh, and D. J. Kim, “Size and geometry dependent tensile behavior of ultra-high-performance fiber-reinforced concrete,” *Compos. Part B Eng.*, vol. 58, pp. 279–292, Mar. 2014, doi: 10.1016/j.compositesb.2013.10.072.

[112] K. Wille, S. El-Tawil, and A. E. Naaman, “Properties of strain hardening ultra high performance fiber reinforced concrete (UHP-FRC) under direct tensile loading,” *Cem. Concr. Compos.*, vol. 48, pp. 53–66, Apr. 2014, doi: 10.1016/j.cemconcomp.2013.12.015.

[113] K. Wille, D. J. Kim, and A. E. Naaman, “Strain-hardening UHP-FRC with low fiber contents,” *Mater. Struct.*, vol. 44, no. 3, pp. 583–598, Apr. 2011, doi: 10.1617/s11527-010-9650-4.

[114] A. Wosatko, A. Winnicki, M. A. Polak, and J. Pamin, “Role of dilatancy angle in plasticity-based models of concrete,” *Arch. Civ. Mech. Eng.*, vol. 19, no. 4, pp. 1268–1283, Aug. 2019, doi: 10.1016/j.acme.2019.07.003.

[115] H. Chen, B. Xu, J. Wang, T. Zhou, X. Nie, and Y. L. Mo, “Parametric analysis on compressive strain rate effect of concrete using mesoscale modeling approach,” *Constr. Build. Mater.*, vol. 246, p. 118375, Jun. 2020, doi: 10.1016/j.conbuildmat.2020.118375.

[116] P. Grassl, “Modelling of dilation of concrete and its e ect in triaxial compression,” *Finite Elem. Anal. Des.*, 2004.

[117] J G M van Mier, “FAILURE OF CONCRETE UNDER UNIAXIAL COMPRESSION: AN OVERVIEW. Proceedings FRAMCOS-3. AEDIFICATIO Publishers, D-79104 Freiburg, Germany,” *FAILURE OF CONCRETE UNDER UNIAXIAL COMPRESSION: AN OVERVIEW.*

[118] M. Pimentel Tinoco, “COMPORTAMENTO MECÂNICO DE COMPÓSITOS CIMENTÍCIOS DO TIPO SHCC UTILIZANDO REFORÇOS HÍBRIDOS,” MESTRE EM ENGENHARIA CIVIL, PONTIFÍCIA UNIVERSIDADE CATÓLICA DO RIO DE JANEIRO, Rio de Janeiro, Brazil, 2020. doi: 10.17771/PUCRio.acad.49421.

8 ANNEX A – REHOLOGY STABILIZATION OF THE UHPC MIX

The mix design was adapted from a first UHPC mix originally conceived without fibers. The mix was composed of cement CP-V ARS according to Brazilian standards, industrialized pre-dried sand, fly ash, quatz powder, micro-silica, water reducing agent and water. Table 25 shows the material consumption per cubic meter.

Table 25 - Material consumption for the original UHPC mix.

Materials	Consumption (kg/m³)
Cement CPV-ARI RS	800.00
Industrialized Sand AG50/60	846.20
Pozofly fly Ash	80.00
Quartz powder SM325	200.00
Micro-silica 920U	80.00
Water	166.20
MasterGlenium 51 Super plasticizer	40.00

The concrete mixing was performed in a planetary mixer with total capacity of 30L, with a total concrete formation time of approximately 25 minutes. The mixing procedure involved placing the dry materials in the mixer and mixing for approximately five minutes. Subsequently, half of the water, the superplasticizer, and the remaining water were added. After adding the water and the additive, approximately 10 minutes followed until the concrete was finally formed in the mixer. Finally, the fibers were added through a fine pour to ensure they were incorporated into the mixture without clusters that could result in voids inside the concrete mass. The time that the concrete remained in the mixer after the addition of the fibers was approximately 5 minutes. A total of 33 liters of concrete were molded divided in two batches, corresponding to ten cylindrical specimens and four dog bone-type specimens with 500 mm size. Figure 95 shows the molded specimens and the spread obtained in the mini-slump test and a mean spread of 310 mm.

(a) (b)

Figure 95 - Cylindrical and dog-bone type specimens (a) and spread obtained in the minislump test (b).

(a) (b)

Figure 96 - Failure mode of the three specimens without fibers in the failure section (a) and failure mode of the dogbone with fibers (b).

The tensile tests resulted in brittle failure, with three specimens showing no post-cracking resistance (Figure 97). Figure 96 (a) displays the failure sections of specimens that did not exhibit post-cracking resistance, and Figure 96 (b) shows the specimen with fibers in the failure section, resulting in post-cracking resistance. Three of the four dog bone specimens not presenting residual strength with no fibers in the cracked section indicated a rheology problem which caused the fibers to not present an adequate distribution throughout the specimens' volume.

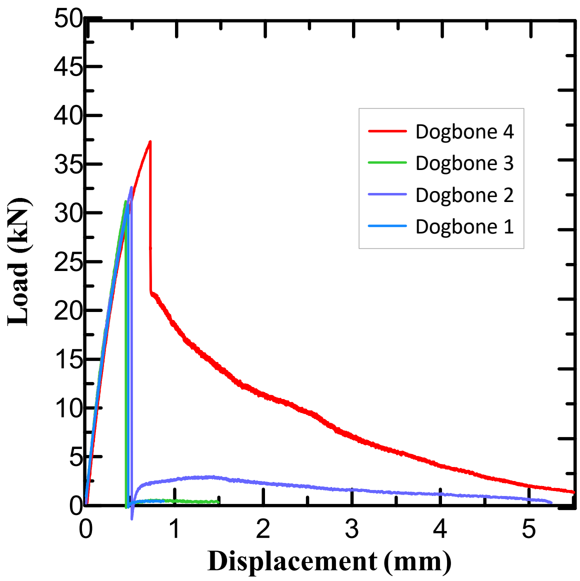

Figure 97 - Load displacement curves for the first four tested dog bones.

The specimens were then opened with hammers to investigate the distribution of fibers along their heights. Figure 98 shows the inspection results, revealing that the fibers had segregated and concentrated at the bottom of the specimens while the top of the specimens remained without fibers.

(a)

(b)

Figure 98 - Fibers concentrated in the bottom part of the speciments (a) while the top part showed no fibers (b).

For the correction of the fiber segregation, a modification of the rheology of the mix was carried through the reduction of the superplasticizer and using viscosity modifying agent (VMA). The VMA used was MastersBuilders MMatrix VMA 358. Mixtures were prepared as specified in Table 26 in smaller volumes sufficient to produce four compression test specimens and conduct a spread table test with the mini-slump cone. The mixtures were molded in a 5L mixer and tested using a Controls model MCC8 machine with force control and a loading rate of 0.25 MPa/s.

Table 26 - Compressive strength at seven days' age for mixes with different amounts os superplasticizer and viscosity-modifying agent.

Mix	SP	VMA	Age (days)	fc (average) [MPa]	Standard deviation	β	fc (7 days) [MPa]
M 1	3%	0	7	104.86	6.92	0.82	104.86
M 2	2.50%	0	10	119.38	11.93	0.87	111.83
M 3	2.50%	0.25%	10	118.19	7.95	0.87	110.71
M 4	2.25%	0.25%	10	125.69	2.55	0.87	117.74

For each mix with a defined amount of superplasticizer and VMA, spread and compression tests were carried out. Table 26 presents the compression strength results obtained for each tested mix. The compression strengths were all converted to equivalent strengths at seven days using the expression provided by NBR 6118:2014, multiplying the compression strength at ten days by the beta coefficient corresponding to seven days divided by the beta at ten days. The relationship that provides the beta coefficient is given by the expression 13, where s = 0.20 for CPV (ARI) cement concretes, and t is the concrete’s age in days.

$$\beta = e^{s \times \left(1 - \left(\frac{28}{t}\right)\right)} \tag{13}$$

The initial studies started with a VMA dosage of 0.25% of the cement mass [118] . It is observed that the changes made in the mix did not result in a loss of compressive strength of the concrete when comparing strengths at younger ages. The comparison of spreads, conducted with mini-slump tests, aimed to ensure the workability of the concrete, and no significant spread losses were observed, maintaining a measured diameter between 27 cm and 30 cm.

A supplementary mixture with a 2% content of superplasticizer was prepared however, the concrete did not remain self-consolidating, showing unsatisfactory spread. Among the four mixtures presented in Table 26, the M3 mix was selected for the production of two new dog bone-shaped specimens to verify fiber segregation. A considerable improvement was observed, with fiber distribution becoming homogeneous in the section where the cross-section reduction occurs, and segregation occurring so that only the top of the specimens in the outermost layer did not contain fibers.

A final mixture test was conducted based on M3, increasing the VMA content by 50%, resulting in 0.375% of the cement mass. Two additional specimens were prepared and broken the next day with a hammer to verify the dispersion of fibers in the matrix.

The distribution of fibers along the specimens is shown in Figure 80. It is observed that the modifications were effective, with the specimens presenting fibers in both the upper and intermediate/lower sections.

(a) (b) (c)

Figure 99 - Fiber distribution the the dogbones casted using the final mix.

9 Annex B – Fiber distribution in the failure section of the dogbones

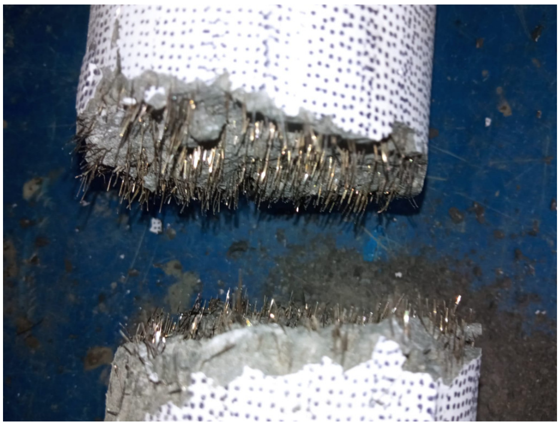

(a)

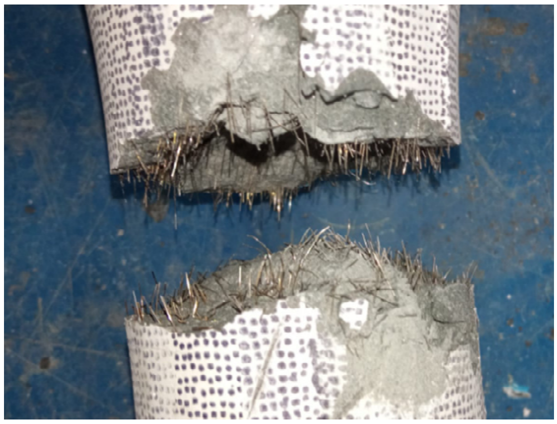

(b)

(c)

(d)

(e)

(f)

(g)

(h)

(i)

10 ANNEX C – PYTHON CODES

10.1 RANDOM MATERIAL PROPERTIES GENERATOR

```
# -*- coding: utf-8 -*-
"""
Created on Fri Apr 21 14:33:55 2023

@author: Paulo Feghali
"""


import numpy as np
import pickle


def Rel_Const (Num_Part_Vert, Num_Part_Hor,Num_Part_Trans):


    import random
    import numpy as np
    import matplotlib.pyplot as plt
    import math as m
    import warnings


    #Propriedades do concreto
    fcm = 135
    Desvio_Padrao_fcm = 8.37

    #Entradas do método de Carreira e Chu a compressão

    bc = 0.7
    Num_pontos_C = 30

    Ef = 200000
    df = 0.2
    Lf = 13

    #Entradas para o método li e leung

    Num_pontos_T1 = 20
    Num_pontos_T2 = 50
    Largura_Elementos = 10
    bt = 0.975


    ####################################################
    #Definição do concreto a compressão################
    ####################################################


    Numero_Particoes = Num_Part_Vert*Num_Part_Hor*Num_Part_Trans


    Curvas_Tensao_Dano_Compressao = []
```

```
    Curvas_Tensao_Dano_Tracao = []
    Lista_fc_Ei = []
    Lista_Beta = []

    for i in range (Numero_Particoes):

        Fator_BT = 0.95

        Dano_Max = 0.93*Fator_BT

        #Curva Tensão-Deformação na compressão

        #Metodo de Carreira e Chu adaptado por Mansur para corpos de
prova
        #cilindricos

        fc = random.gauss(fcm, Desvio_Padrao_fcm)

        Vf = random.gauss(0.02, 0.001)

        Ei = (10300-400*Vf)*(fc**(1/3))

        Def_Pico = 1.1*fc/Ei

        Beta = 1 / (1 - fc/(Def_Pico*Ei))

        k1 = ((50/fc)**3)*(1+2.5*(Vf*Lf/df)**2.5)

        k2 = ((50/fc)**1.3)*(1-0.11*(Vf*Lf/df)**-1.1)


        #Determinação do limite de proporcionalidade pela Deformação
inelástica


        Lim_Elastico = 0.4*fc/Ei

        Def_Inelastica_Lim_Elast = 0

        while Def_Inelastica_Lim_Elast <= 0:

            Lim_Elastico = Lim_Elastico + Def_Pico/100

            Sigma_Lim_Elast =
fc*(k1*Beta*(Lim_Elastico/Def_Pico))/(k1*Beta-1+
            (Lim_Elastico/Def_Pico)**(k2*Beta))

            Def_Inelastica_Lim_Elast = Lim_Elastico -
Sigma_Lim_Elast/Ei


        #Determinação do limite de dano

        Dano_Lim = 0

        Def_Lim = Def_Pico
```

```
        while Dano_Lim < Dano_Max:

            Def_Lim = Def_Lim + (Def_Pico/1000)

            Sigma_Lim = fc*(k1*Beta*(Def_Lim/Def_Pico))/(k1*Beta-
1+(Def_Lim/Def_Pico)**(k2*Beta))

            Def_Inelastica_Lim = Def_Lim - Sigma_Lim/Ei


            Def_Plastica_Lim = bc * Def_Inelastica_Lim

            Dano_Lim = 1 - (Sigma_Lim/Ei)/(Def_Plastica_Lim*(1/bc -
1)+Sigma_Lim/Ei)


        Def_C1 = np.linspace
(Lim_Elastico,Def_Pico,int(Num_pontos_C/2))

        Def_C2 = np.linspace (Def_Pico,Def_Lim,int(Num_pontos_C/2))

        Def_C = np.append(Def_C1,Def_C2[1:int(Num_pontos_C/2)])

        Sigma_C = fc*(k1*Beta*(Def_C/Def_Pico))/(k1*Beta-
1+(Def_C/Def_Pico)**(k2*Beta))

        Def_Inelastica = Def_C[1:] - Sigma_C[1:] /Ei

        Def_Plastica = bc*Def_Inelastica

        Def_Inelastica = np.append(np.array(int(0)),Def_Inelastica)

        Def_Plastica = np.append(np.array(int(0)),Def_Plastica)

        Dano_C = 1 - (Sigma_C/Ei)/(Def_Plastica*(1/bc -1)+Sigma_C/Ei)

        Curvas_Tensao_Dano_Compressao.append ([Sigma_C,Def_Inelastica,
Dano_C])

        Lista_fc_Ei.append([fc,Ei])

        plt.subplot(2,2,1)

        plt.plot(Def_C, Sigma_C)

        plt.subplot(2,2,2)

        plt.plot(Def_Plastica, Dano_C)


    #####################################################
    #Definição do concreto a tração#####################
    #####################################################

        #Inserção das propriedades aleatórias por ensaios

        fct = random.gauss(9.55, 0.852)#
```

```
        Teq = random.gauss(8, 1.6)#

        #Estimativas das propriedades aleatórias

        Gf = random.gauss(0.212, 0.059) #ok

        #W0 = 0.078
        #W0 = Teq*(Lf**2)/(Ef*df)
        W0 = 0

        while (W0 < 0.005) or  (W0 > 0.132):

            W0 = random.gauss(0.078, 0.04)

        n = random.gauss(1, 0.1)

        Sigma_F0 = n*(Lf/df)*Teq*Vf #ok

        Dano = 0

        W_Lim = float(0)

        W_max = Lf/2 #ok

        Sigma_Max = 0

        while Dano < Dano_Max:

            W_Lim = W_Lim + W_max/1000

            if W_Lim < W0:

                Sigma_F = Sigma_F0*(2*m.sqrt(W_Lim/W0)-W_Lim/W0)

            else:

                Sigma_F = Sigma_F0*(1-2*W_Lim/Lf)**2

            Sigma_M = fct*np.exp(-2*fct*W_Lim/Gf)

            Sigma = Sigma_M + Sigma_F

            Def_Inelastica = W_Lim/Largura_Elementos

            Def_Plastica = bt*Def_Inelastica

            Dano = Fator_BT*(1 - (Sigma/Ei)/(Def_Plastica*(1/bt -
1)+Sigma/Ei))
```

```
        if W_Lim > W0:

            W_1 = np.linspace(0,W0,Num_pontos_T1)

            W_2 = np.linspace(W0,W_Lim,Num_pontos_T2)

            W= np.append(W_1,W_2[1:Num_pontos_T2])

            Sigma_F1 = Sigma_F0*(2*np.sqrt(W_1/W0)-W_1/W0)

            Sigma_F2 = Sigma_F0*(1-2*W_2/Lf)**2

            Sigma_M = fct*np.exp(-2*fct*W/Gf)

            Sigma =  np.append(Sigma_F1,Sigma_F2[1:Num_pontos_T2]) +
Sigma_M

        else:

            W= np.linspace(0,W_Lim,Num_pontos_T1)

            Sigma_F1 = Sigma_F0*(2*np.sqrt(W/W0)-W/W0)

            Sigma_M = fct*np.exp(-2*fct*W/Gf)

            Sigma =  Sigma_F1 + Sigma_M


        Sigma_Max = max(Sigma)

        Dano_T1=np.array(0)

        Def_Inelastica = W/Largura_Elementos

        Def_Plastica = bt*Def_Inelastica

        Dano_T2 = Fator_BT*(1 - (Sigma[1:]/Ei)/(Def_Plastica[1:]*(1/bt
-1)+Sigma[1:]/Ei))

        Dano_T =  np.append(Dano_T1,Dano_T2)

        plt.subplot(2,2,3)

        plt.plot(W, Sigma)

        plt.subplot(2,2,4)

        plt.plot(W, Dano_T)


        Curvas_Tensao_Dano_Tracao.append ([Sigma,W, Dano_T])

    plt.subplot(2,2,1).grid()
    plt.subplot(2,2,2).grid()
    plt.subplot(2,2,3).grid()
    plt.subplot(2,2,4).grid()
```

```
    plt.subplot(2,2,1).title.set_text('Curvas Tensao-Deformaçao 
Compressão')
    plt.subplot(2,2,1).set_xlabel('Deformacao')
    plt.subplot(2,2,1).set_ylabel('Tensao')
    plt.subplot(2,2,2).set_xlabel('Deformacao plastica')
    plt.subplot(2,2,2).set_ylabel('Dano')
    plt.subplot(2,2,2).title.set_text('Dano-Deformaçao Plastica')
    plt.subplot(2,2,3).title.set_text('Curvas Tensao-Abertura de 
fissuras')
    plt.subplot(2,2,3).set_xlabel('W(mm)')
    plt.subplot(2,2,3).set_ylabel('Tensao')
    plt.subplot(2,2,4).title.set_text('Dano-Abertura de fissuras')
    plt.subplot(2,2,4).set_xlabel('W(mm)')
    plt.subplot(2,2,4).set_ylabel('Dano')

    plt.show()
    plt.tight_layout()


    return 
([Lista_fc_Ei,Curvas_Tensao_Dano_Compressao,Curvas_Tensao_Dano_Tracao]
)



Rel_Const_Geradas = Rel_Const (20,5,5)
with open("Arquivo_Relacoes_Constitutivas","wb") as Arq:
    pickle.dump(Rel_Const_Geradas, Arq, protocol=2)
```

10.2 HETEROGENEOUS BEAM GENERATOR CODE

```
# -*- coding: utf-8 -*-
"""
Created on Thu Apr 20 17:24:59 2023

@author: Paulo Feghali
"""

from abaqus import *
from part import *
from material import *
from section import *
from assembly import *
from step import *
from interaction import *
from load import *
from mesh import *
from optimization import *
from job import *
from sketch import *
from visualization import *
from connectorBehavior import *
import numpy as np
import regionToolset
from abaqusConstants import *
import random
import math as m
session.journalOptions.setValues(replayGeometry=COORDINATE,
recoverGeometry=COORDINATE)
import pickle
from abaqus import backwardCompatibility
backwardCompatibility.setValues(reportDeprecated=False)


#Criação do modelo

myModel = mdb.Model(name='Model-1')

Arquivo_Relacoes_Constitutivas =
open("Arquivo_Relacoes_Constitutivas","rb")


####################################################
#Dados de entrada###################################
####################################################


#Numero de divisoes da viga
Num_Part_Vert = 20
Num_Part_Hor = 5
Num_Part_Trans = 5

#Dimensoes da viga
Comprimento_Viga = 1200
```

```
Altura_Viga = 150
Largura_Viga = 150


#Informações CDP
Poisson = 0.2
Angulo = 55
Excentricidade = 0.1
Fb0_fc0 = 1.16
K = 0.6667
Viscosidade = 0.0001


#####################################################
#Criacao das partes##################################
#####################################################

#Criação da parte da viga de concreto

Sketch_Secao = myModel.Sketch(name='Sketch_Secao', sheetSize=200.0)


Coords_Secao_Viga = ((-Largura_Viga/2, 0), (Largura_Viga/2, 0),
(Largura_Viga/2, Altura_Viga),
    (-Largura_Viga/2, Altura_Viga),(-Largura_Viga/2, 0))

for i in range(len(Coords_Secao_Viga)-1):
    Sketch_Secao.Line(point1=Coords_Secao_Viga[i],
        point2=Coords_Secao_Viga[i+1])


Parte = myModel.Part(name='Viga', dimensionality=THREE_D,
    type=DEFORMABLE_BODY)

Parte.BaseSolidExtrude(sketch=Sketch_Secao, depth=Comprimento_Viga)


#Criação dos datum Planes

for i in range (1,Num_Part_Vert):
    p = mdb.models['Model-1'].parts['Viga']
    p.DatumPlaneByPrincipalPlane(principalPlane=XYPLANE,
offset=i*Comprimento_Viga/Num_Part_Vert)

for i in range (1,Num_Part_Hor):
    p = mdb.models['Model-1'].parts['Viga']
    p.DatumPlaneByPrincipalPlane(principalPlane=XZPLANE,
offset=i*Altura_Viga/Num_Part_Hor)

for i in range (1,Num_Part_Trans):
    p = mdb.models['Model-1'].parts['Viga']
    p.DatumPlaneByPrincipalPlane(principalPlane=YZPLANE, offset=-
Largura_Viga/2 + i*Largura_Viga/Num_Part_Trans)

#Criação das partições

p = mdb.models['Model-1'].parts['Viga']
```

```
c = p.cells
pickedCells = c.getSequenceFromMask(mask=('[#1 ]', ), )
d = p.datums
p.PartitionCellByDatumPlane(datumPlane=d[2], cells=pickedCells)



for i in range (1,Num_Part_Vert-1):

    p = mdb.models['Model-1'].parts['Viga']
    c = p.cells
    pickedCells = c.getByBoundingBox(-10000, -10000, -10000, 10000,
10000, 10000)
    d1 = p.datums
    p.PartitionCellByDatumPlane(datumPlane=d1[i+2], cells=pickedCells)

for i in range (1,Num_Part_Hor):

    p = mdb.models['Model-1'].parts['Viga']
    c = p.cells
    pickedCells = c.getByBoundingBox(-10000, -10000, -10000, 10000,
10000, 10000)
    d1 = p.datums
    p.PartitionCellByDatumPlane(datumPlane=d1[Num_Part_Vert+i],
cells=pickedCells)

for i in range (1,Num_Part_Trans):

    p = mdb.models['Model-1'].parts['Viga']
    c = p.cells
    pickedCells = c.getByBoundingBox(-10000, -10000, -10000, 10000,
10000, 10000)
    d1 = p.datums

p.PartitionCellByDatumPlane(datumPlane=d1[Num_Part_Vert+Num_Part_Hor+i
-1], cells=pickedCells)


session.viewports['Viewport:
1'].partDisplay.geometryOptions.setValues(
    datumPlanes=OFF)


######################################################
#Coordenadas das celulas##############################
######################################################
Pos_Long = 0
Pos_Trans = 0
Pos_Vert = 0

Coords_Celulas = []

for Pos_Vert in range(Num_Part_Hor):
    for Pos_Long in range (Num_Part_Vert):
        for Pos_Trans in range (Num_Part_Trans):
```

```
            Coord_Trans = -Largura_Viga/2 +
Pos_Trans*Largura_Viga/Num_Part_Trans +
0.5*Largura_Viga/Num_Part_Trans
            Coord_Vert = Pos_Vert*Altura_Viga/Num_Part_Hor +
0.5*Altura_Viga/Num_Part_Hor
            Coord_Long = Pos_Long*Comprimento_Viga/Num_Part_Vert +
0.5*Comprimento_Viga/Num_Part_Vert

            Coords_Celulas.append([Coord_Trans,Coord_Vert,Coord_Long])


######################################################
#Criação das propriedades aleatórias do concreto######
######################################################

#Rel_Const =  Rel_Const (Num_Part_Vert,Num_Part_Hor ,Num_Part_Trans)

Rel_Const = pickle.load(open("Arquivo_Relacoes_Constitutivas", "rb"))


######################################################
#Criação das propriedades no Abaqus##################
######################################################


for i in range (Num_Part_Vert*Num_Part_Hor*Num_Part_Trans):

    #Definição de cada uma das propriedades

    Nome_Material = "Concreto_"+str(i)

    Modulo_Elast = Rel_Const[0][i][1]

    Tensao_Compressao = tuple(Rel_Const[1][i][0])

    Deformacao_inelastica = tuple(Rel_Const[1][i][1])

    Dano_Compressao = tuple(Rel_Const[1][i][2])

    Tensao_Tracao = tuple(Rel_Const[2][i][0])

    Abertura_Fissura = tuple(Rel_Const[2][i][1])

    Dano_Tracao = tuple(Rel_Const[2][i][2])

    #Criação das tabelas para inserção nas abas do CDP

    Tabela_Tensao_Deformacao_Compressao = []

    Tabela_Tensao_Deslocamento_Tracao = []

    Tabela_Dano_Compressao_Deformacao = []

    Tabela_Dano_Tracao_Deslocamento = []

    for j in range (len(Tensao_Compressao)):
```

```
Tabela_Tensao_Deformacao_Compressao.append((Tensao_Compressao[j],Defor
macao_inelastica[j]))

    Tabela_Tensao_Deformacao_Compressao = tuple
(Tabela_Tensao_Deformacao_Compressao)

    for j in range (len(Tensao_Tracao)):

       Tabela_Tensao_Deslocamento_Tracao.append((
Tensao_Tracao[j],Abertura_Fissura[j]))

    Tabela_Tensao_Deslocamento_Tracao = tuple
(Tabela_Tensao_Deslocamento_Tracao)


    for j in range (len(Dano_Compressao)):

       Tabela_Dano_Compressao_Deformacao.append((
Dano_Compressao[j],Deformacao_inelastica[j]))

    Tabela_Dano_Compressao_Deformacao = tuple
(Tabela_Dano_Compressao_Deformacao)


    for j in range (len(Dano_Tracao)):

       Tabela_Dano_Tracao_Deslocamento.append((
Dano_Tracao[j],Abertura_Fissura[j]))

    Tabela_Dano_Tracao_Deslocamento = tuple
(Tabela_Dano_Tracao_Deslocamento)

    #Cração dos materiais no Abaqus

    mdb.models['Model-1'].Material(name=Nome_Material)


    mdb.models['Model-
1'].materials[Nome_Material].Elastic(table=((Modulo_Elast, Poisson),
))

    mdb.models['Model-
1'].materials[Nome_Material].ConcreteDamagedPlasticity(table=((Angulo,
Excentricidade, Fb0_fc0, K, Viscosidade), ))

    mdb.models['Model-
1'].materials[Nome_Material].concreteDamagedPlasticity.ConcreteCompres
sionHardening(
    table= Tabela_Tensao_Deformacao_Compressao)

    mdb.models['Model-
1'].materials[Nome_Material].concreteDamagedPlasticity.ConcreteTension
Stiffening(
    table=Tabela_Tensao_Deslocamento_Tracao, type=DISPLACEMENT)
```

```
    mdb.models['Model-
1'].materials[Nome_Material].concreteDamagedPlasticity.ConcreteCompres
sionDamage(
    table= Tabela_Dano_Compressao_Deformacao)


    mdb.models['Model-
1'].materials[Nome_Material].concreteDamagedPlasticity.ConcreteTension
Damage(
    table=Tabela_Dano_Tracao_Deslocamento)
    mdb.models['Model-
1'].materials[Nome_Material].concreteDamagedPlasticity.concreteTension
Damage.setValues(
    type=DISPLACEMENT)


    #Criação das seções no Abaqus

    Nome_secao = "Secao_"+str(i)
    mdb.models['Model-1'].HomogeneousSolidSection(name=Nome_secao,
    material=Nome_Material, thickness=None)


    CoordX=Coords_Celulas[i][0]
    CoordY=Coords_Celulas[i][1]
    CoordZ=Coords_Celulas[i][2]


    p = mdb.models['Model-1'].parts['Viga']
    c = p.cells
    cells = c.findAt(((CoordX, CoordY, CoordZ), ))
    region = regionToolset.Region(cells=cells)
    p = mdb.models['Model-1'].parts['Viga']
    p.SectionAssignment(region=region, sectionName=Nome_secao,
offset=0.0,
    offsetType=MIDDLE_SURFACE, offsetField='',
    thicknessAssignment=FROM_SECTION)
```

11 Annex D – Individual results for the genetic algorithm optimization

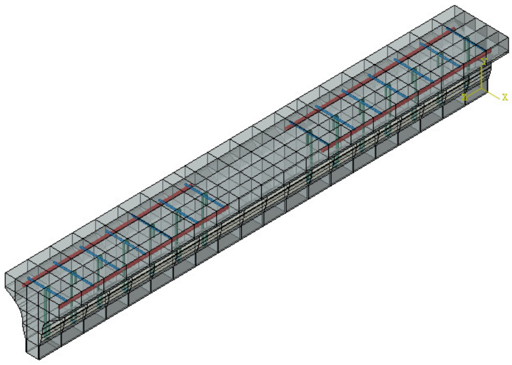

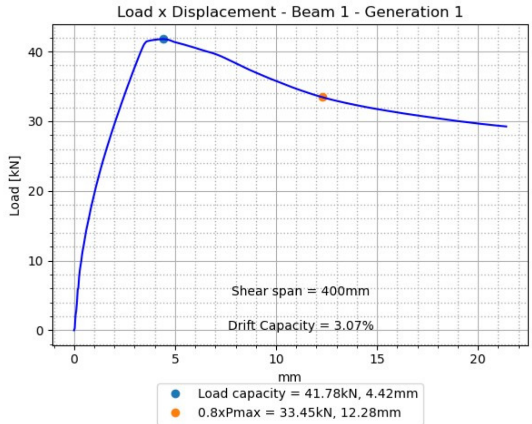

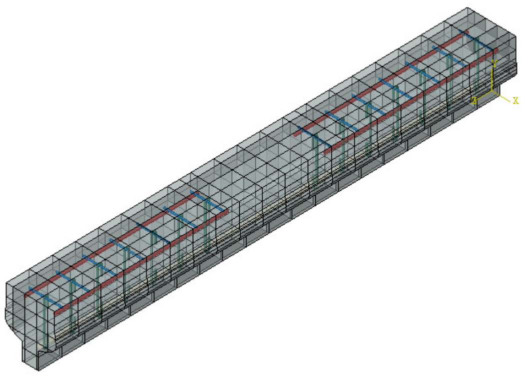

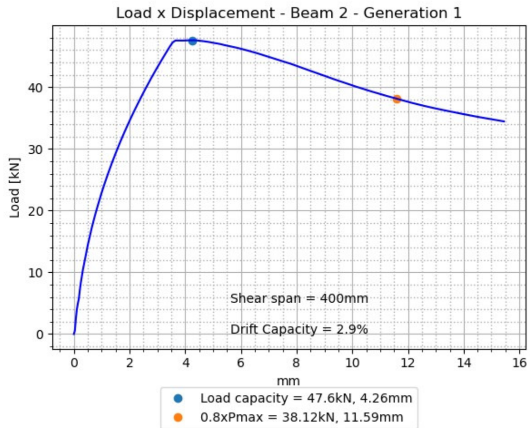

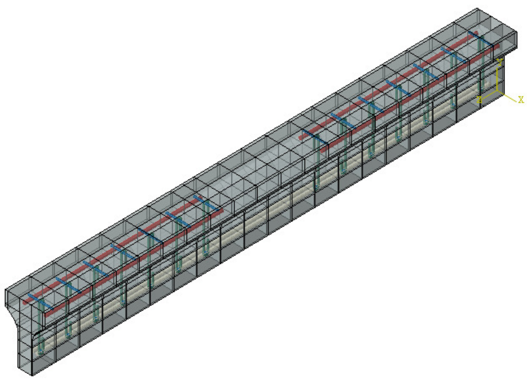

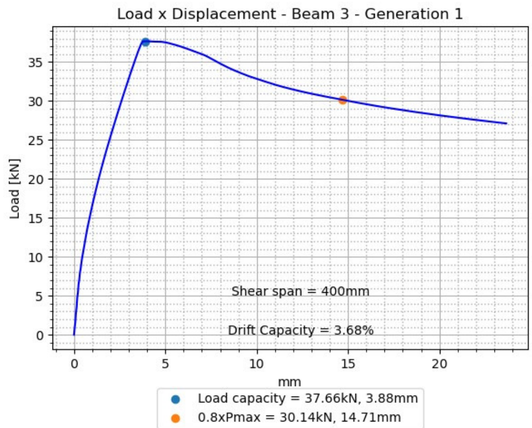

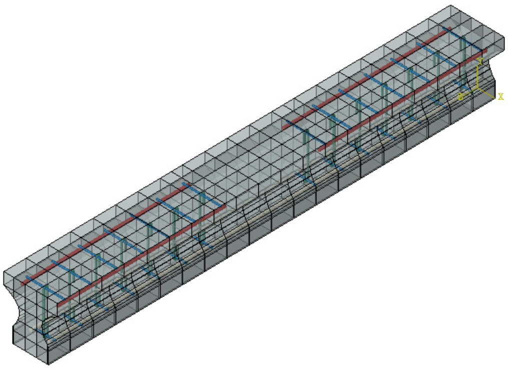

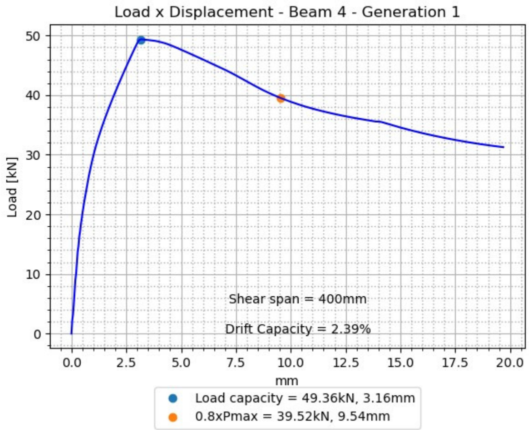
Load x Displacement - Beam 4 - Generation 1
Load [kN]
mm
Shear span = 400mm
Drift Capacity = 2.39%
Load capacity = 49.36kN, 3.16mm
0.8xPmax = 39.52kN, 9.54mm

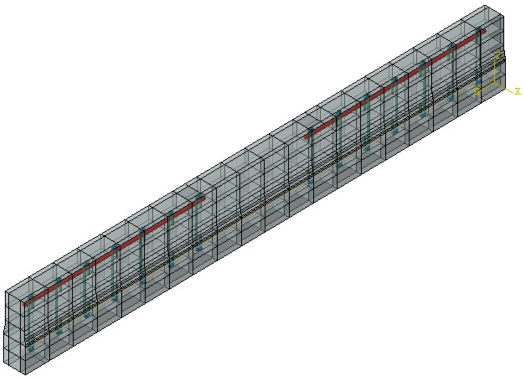

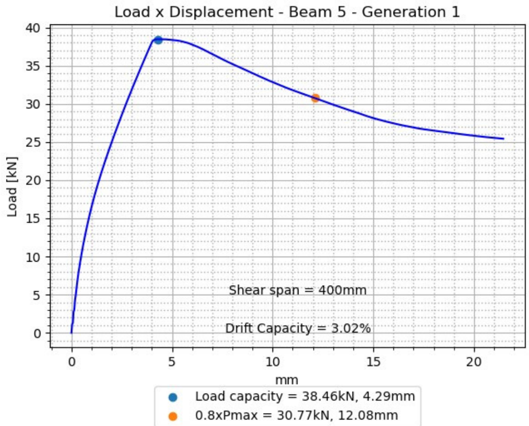
Load x Displacement - Beam 5 - Generation 1
Load [kN]
mm
Shear span = 400mm
Drift Capacity = 3.02%
Load capacity = 38.46kN, 4.29mm
0.8xPmax = 30.77kN, 12.08mm

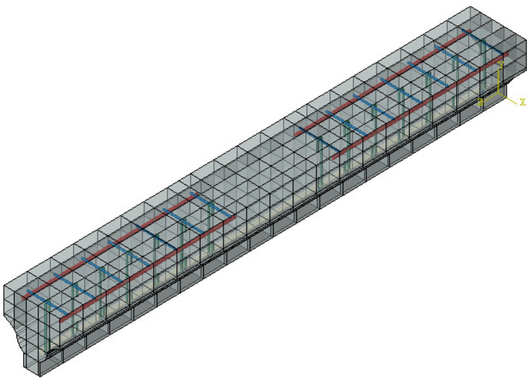

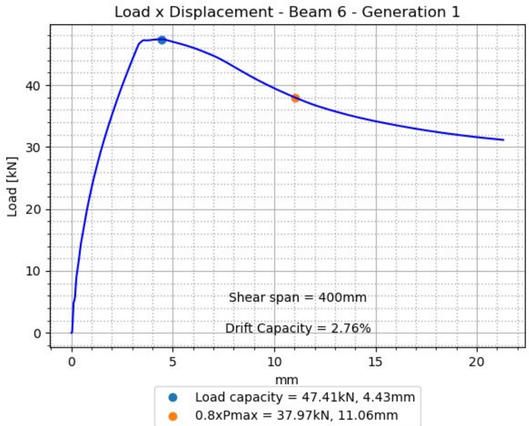
Load x Displacement - Beam 6 - Generation 1
Load [kN]
mm
Shear span = 400mm
Drift Capacity = 2.76%
Load capacity = 47.41kN, 4.43mm
0.8xPmax = 37.97kN, 11.06mm

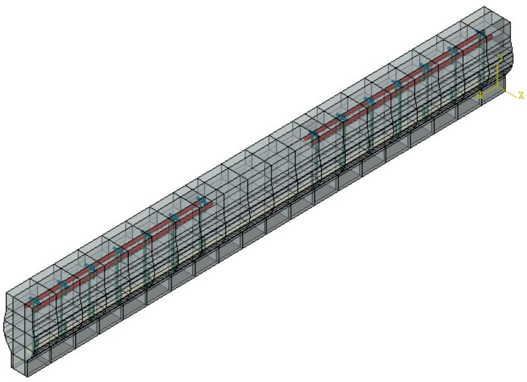

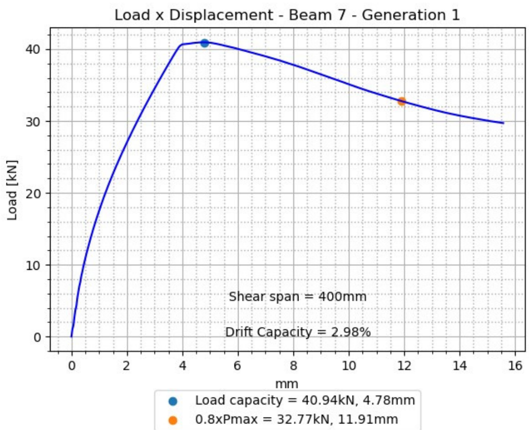
Load x Displacement - Beam 7 - Generation 1
Load [kN]
mm
Shear span = 400mm
Drift Capacity = 2.98%
Load capacity = 40.94kN, 4.78mm
0.8xPmax = 32.77kN, 11.91mm

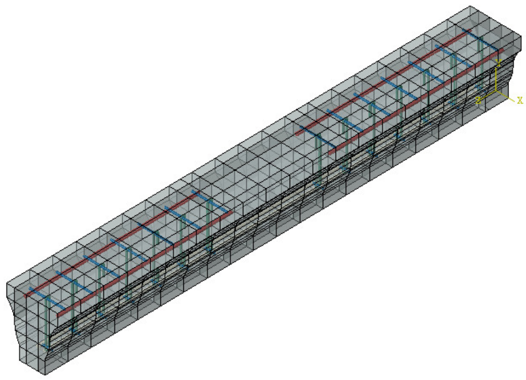

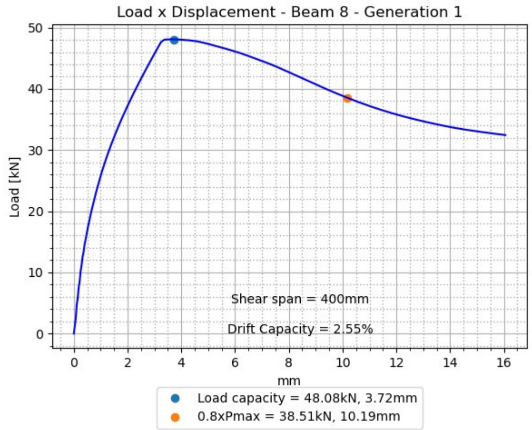
Load x Displacement - Beam 8 - Generation 1
Load [kN]
mm
Shear span = 400mm
Drift Capacity = 2.55%
Load capacity = 48.08kN, 3.72mm
0.8xPmax = 38.51kN, 10.19mm

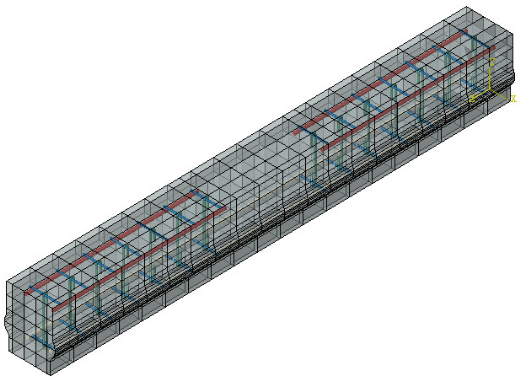

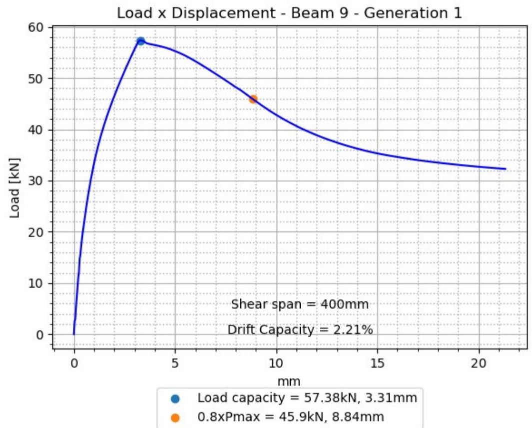
Load x Displacement - Beam 9 - Generation 1
Load [kN]
mm
Shear span = 400mm
Drift Capacity = 2.21%
Load capacity = 57.38kN, 3.31mm
0.8xPmax = 45.9kN, 8.84mm

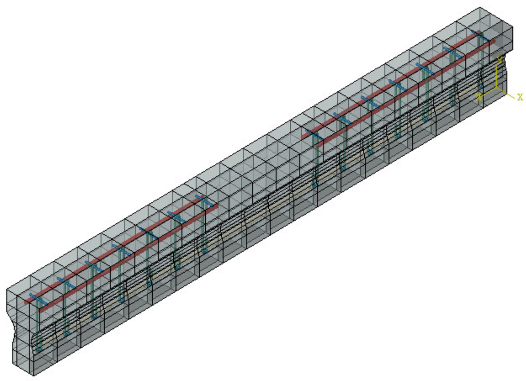

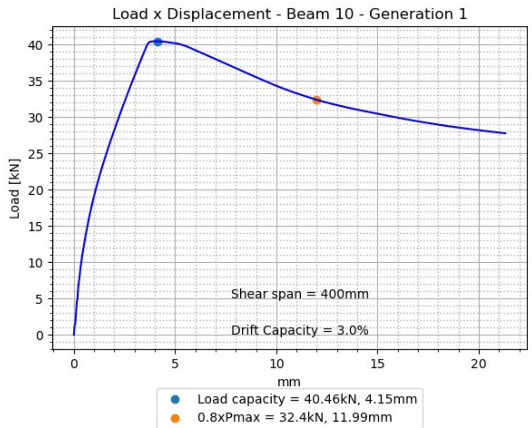
Load x Displacement - Beam 10 - Generation 1
Load [kN]
mm
Shear span = 400mm
Drift Capacity = 3.0%
Load capacity = 40.46kN, 4.15mm
0.8xPmax = 32.4kN, 11.99mm

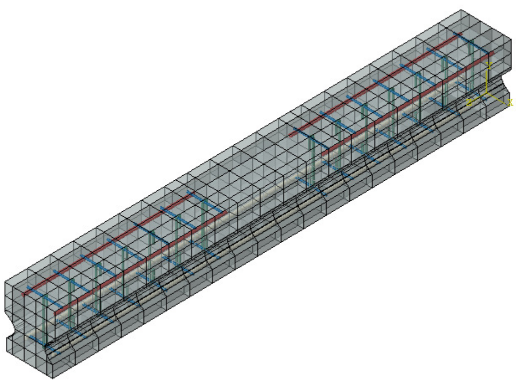

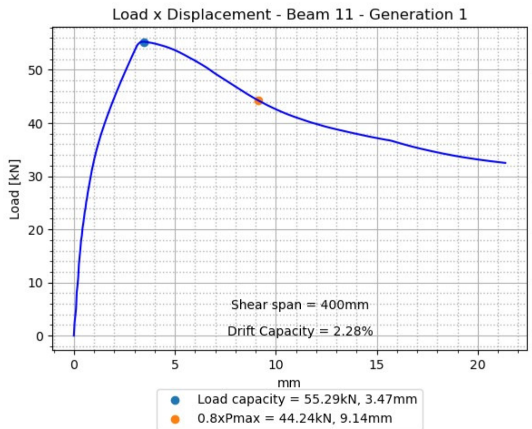
Load x Displacement - Beam 11 - Generation 1
Load [kN]
mm
Shear span = 400mm
Drift Capacity = 2.28%
Load capacity = 55.29kN, 3.47mm
0.8xPmax = 44.24kN, 9.14mm

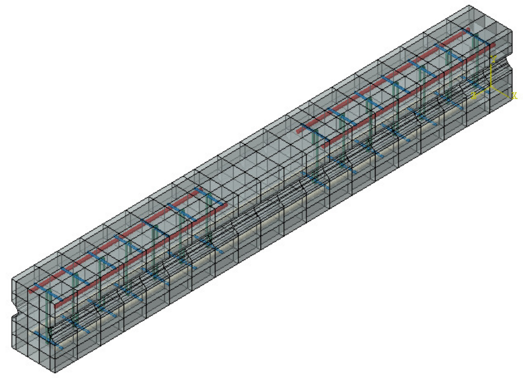

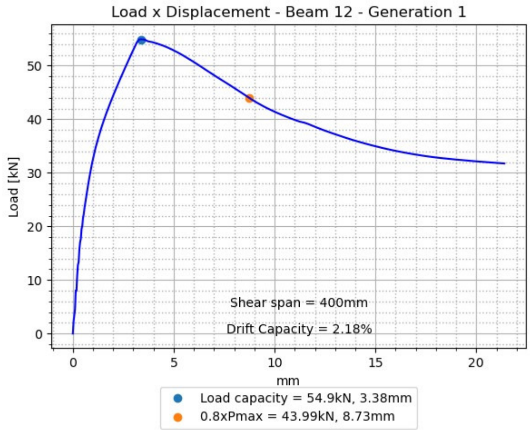
Load x Displacement - Beam 12 - Generation 1
Load [kN]
mm
Shear span = 400mm
Drift Capacity = 2.18%
Load capacity = 54.9kN, 3.38mm
0.8xPmax = 43.99kN, 8.73mm

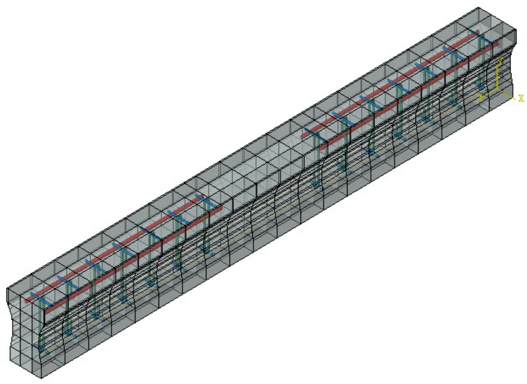

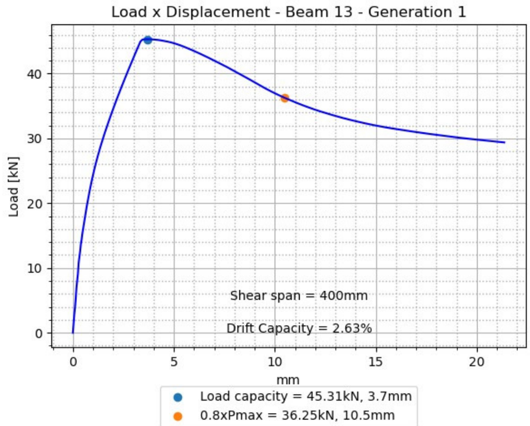
Load x Displacement - Beam 13 - Generation 1
Load [kN]
mm
Shear span = 400mm
Drift Capacity = 2.63%
Load capacity = 45.31kN, 3.7mm
0.8xPmax = 36.25kN, 10.5mm

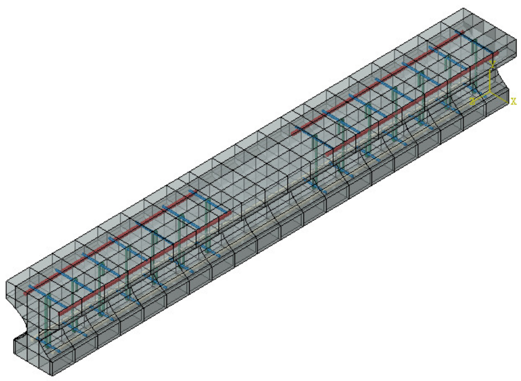

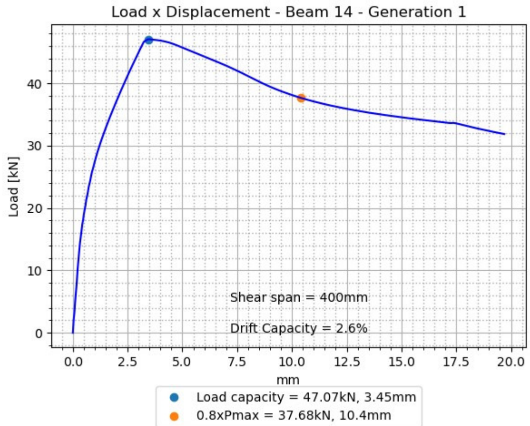
Load x Displacement - Beam 14 - Generation 1
Load [kN]
mm
Shear span = 400mm
Drift Capacity = 2.6%
Load capacity = 47.07kN, 3.45mm
0.8xPmax = 37.68kN, 10.4mm

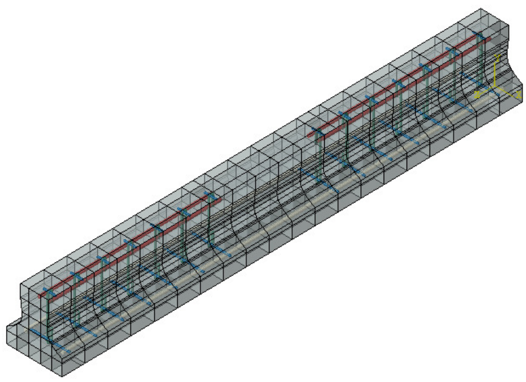

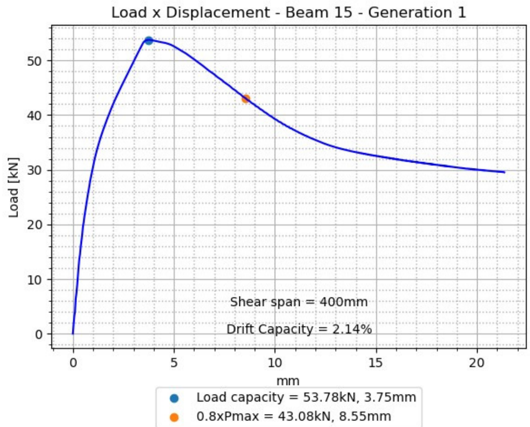
Load x Displacement - Beam 15 - Generation 1
Load [kN]
mm
Shear span = 400mm
Drift Capacity = 2.14%
Load capacity = 53.78kN, 3.75mm
0.8xPmax = 43.08kN, 8.55mm

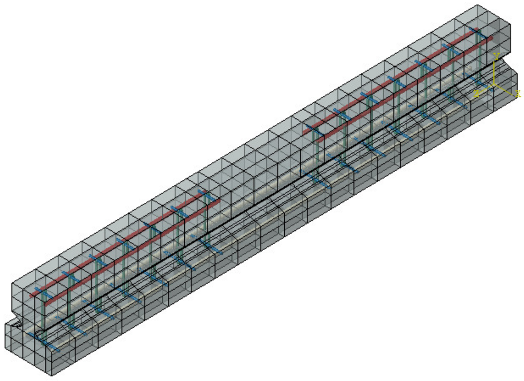

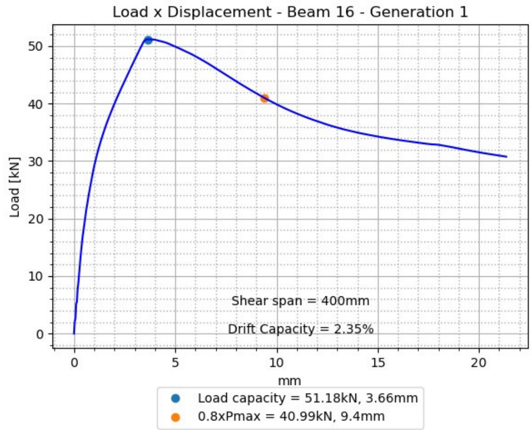
Load x Displacement - Beam 16 - Generation 1
Load [kN]
mm
Shear span = 400mm
Drift Capacity = 2.35%
Load capacity = 51.18kN, 3.66mm
0.8xPmax = 40.99kN, 9.4mm

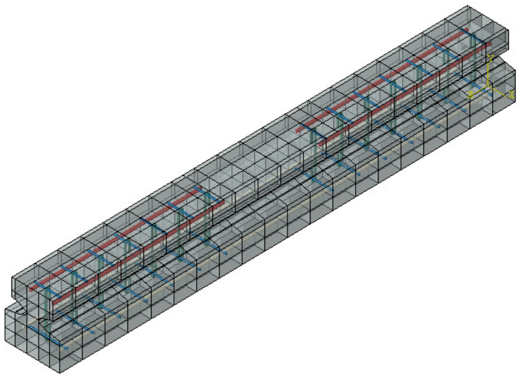

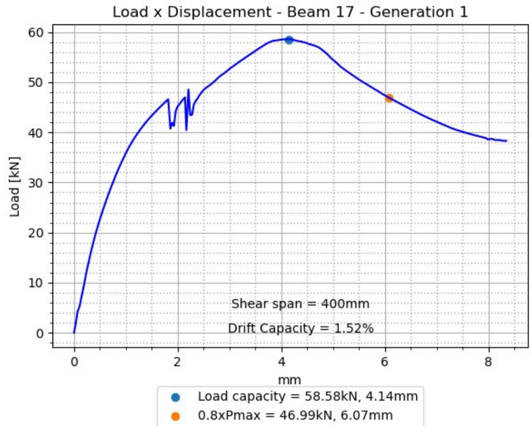
Load x Displacement - Beam 17 - Generation 1
Load [kN]
mm
Shear span = 400mm
Drift Capacity = 1.52%
Load capacity = 58.58kN, 4.14mm
0.8xPmax = 46.99kN, 6.07mm

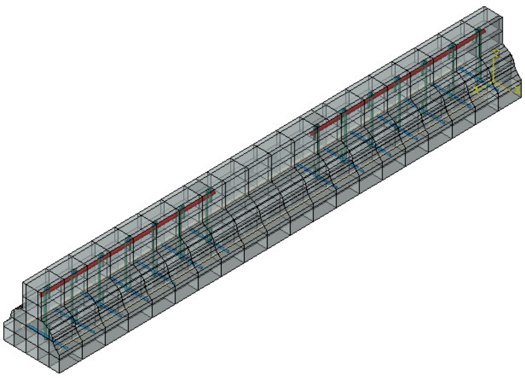

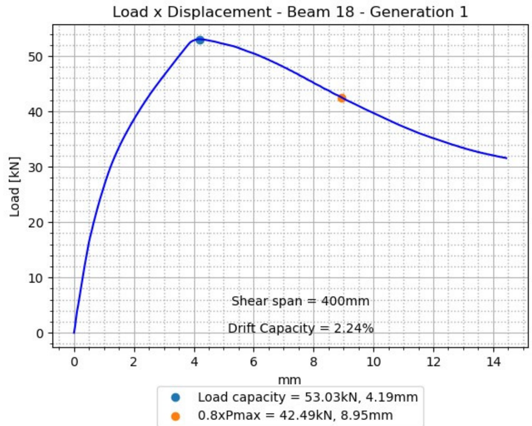
Load x Displacement - Beam 18 - Generation 1
Load [kN]
mm
Shear span = 400mm
Drift Capacity = 2.24%
Load capacity = 53.03kN, 4.19mm
0.8xPmax = 42.49kN, 8.95mm

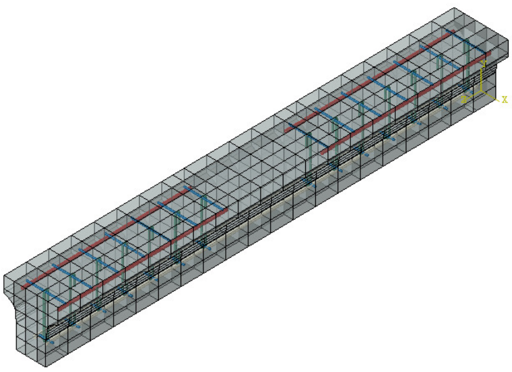

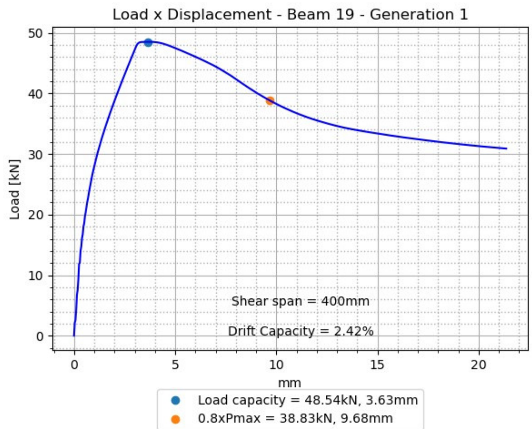
Load x Displacement - Beam 19 - Generation 1
Load [kN]
mm
Shear span = 400mm
Drift Capacity = 2.42%
Load capacity = 48.54kN, 3.63mm
0.8xPmax = 38.83kN, 9.68mm

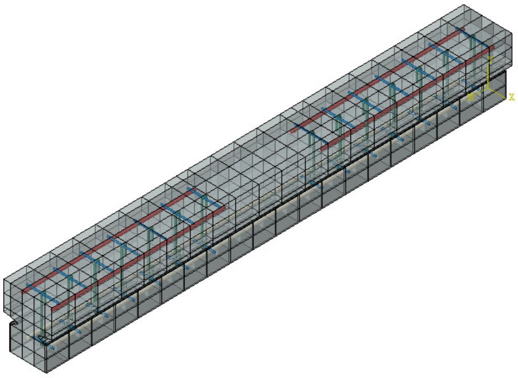

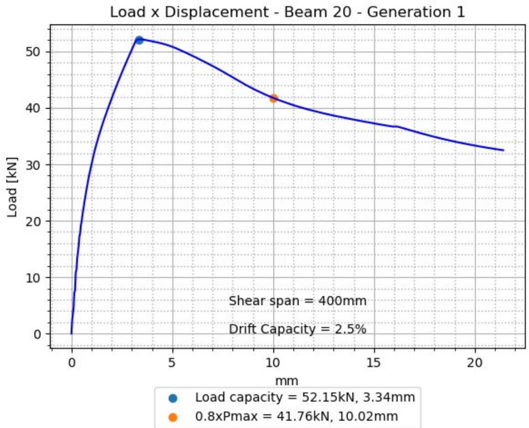

Load x Displacement - Beam 20 - Generation 1
Load [kN]
mm
Shear span = 400mm
Drift Capacity = 2.5%
Load capacity = 52.15kN, 3.34mm
0.8xPmax = 41.76kN, 10.02mm

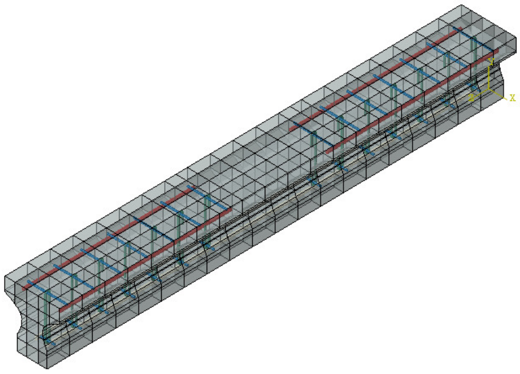

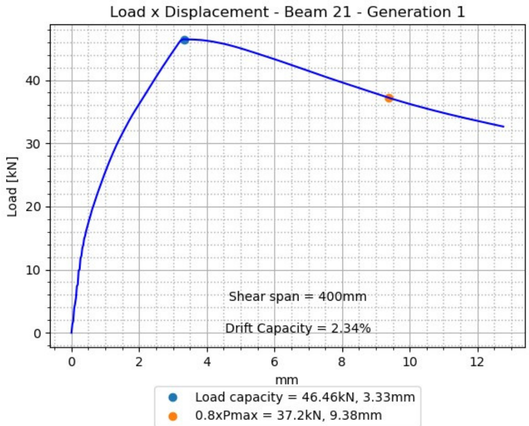

Load x Displacement - Beam 21 - Generation 1
Load [kN]
mm
Shear span = 400mm
Drift Capacity = 2.34%
Load capacity = 46.46kN, 3.33mm
0.8xPmax = 37.2kN, 9.38mm

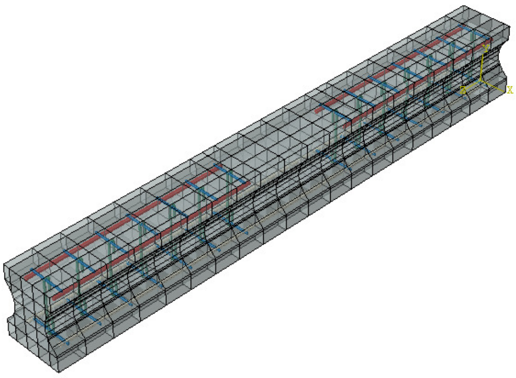

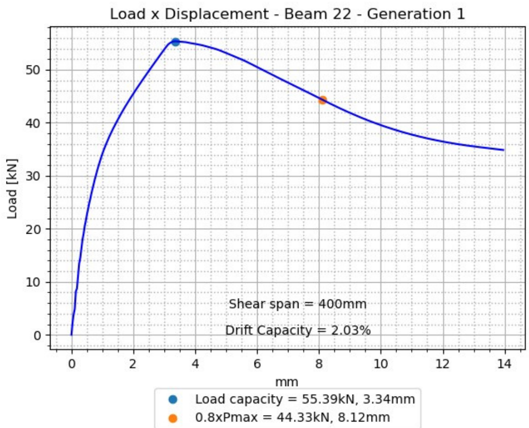

Load x Displacement - Beam 22 - Generation 1
Load [kN]
mm
Shear span = 400mm
Drift Capacity = 2.03%
Load capacity = 55.39kN, 3.34mm
0.8xPmax = 44.33kN, 8.12mm

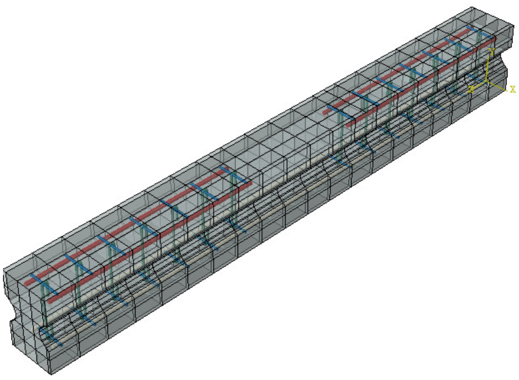

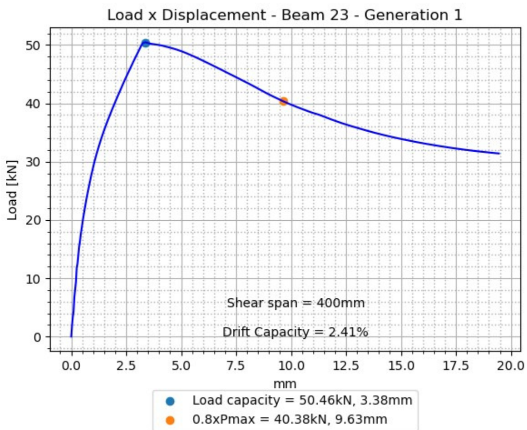

Load x Displacement - Beam 23 - Generation 1
Load [kN]
mm
Shear span = 400mm
Drift Capacity = 2.41%
Load capacity = 50.46kN, 3.38mm
0.8xPmax = 40.38kN, 9.63mm

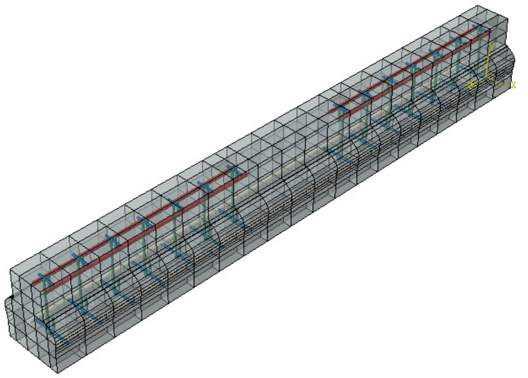

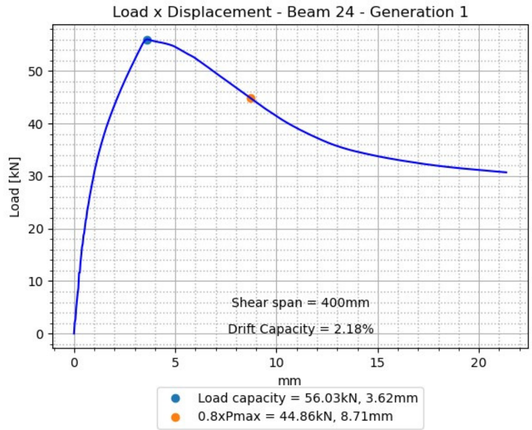

Load x Displacement - Beam 24 - Generation 1
Load [kN]
mm
Shear span = 400mm
Drift Capacity = 2.18%
Load capacity = 56.03kN, 3.62mm
0.8xPmax = 44.86kN, 8.71mm

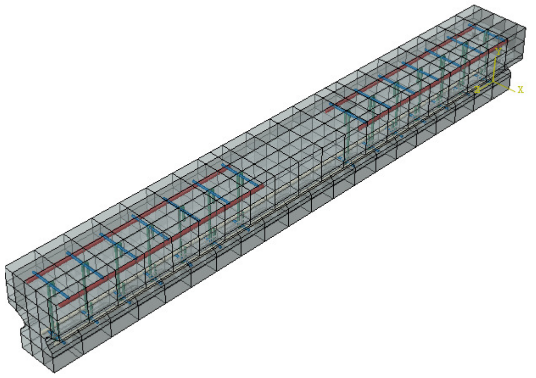

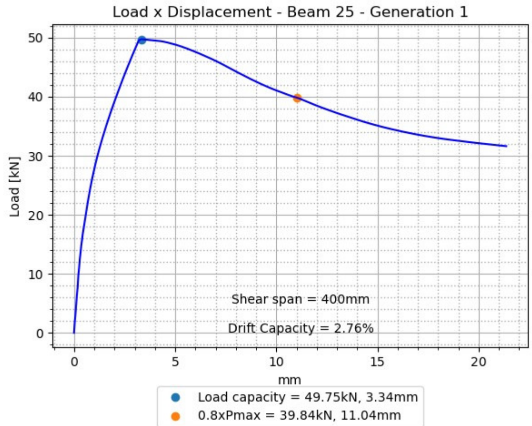

Load x Displacement - Beam 25 - Generation 1
Load [kN]
mm
Shear span = 400mm
Drift Capacity = 2.76%
Load capacity = 49.75kN, 3.34mm
0.8xPmax = 39.84kN, 11.04mm

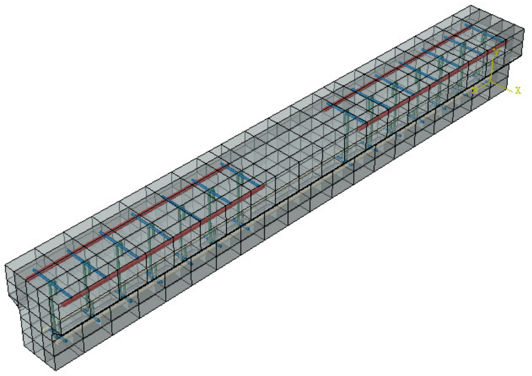

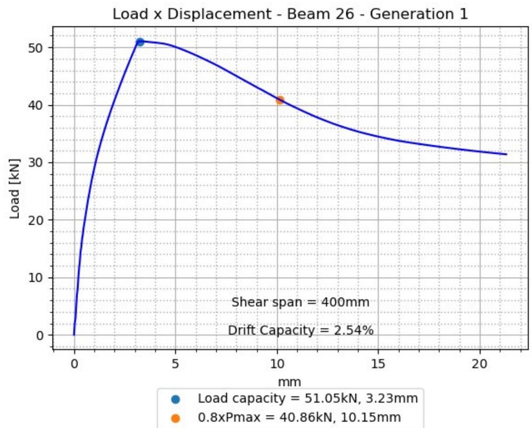

Load x Displacement - Beam 26 - Generation 1
Load [kN]
mm
Shear span = 400mm
Drift Capacity = 2.54%
Load capacity = 51.05kN, 3.23mm
0.8xPmax = 40.86kN, 10.15mm

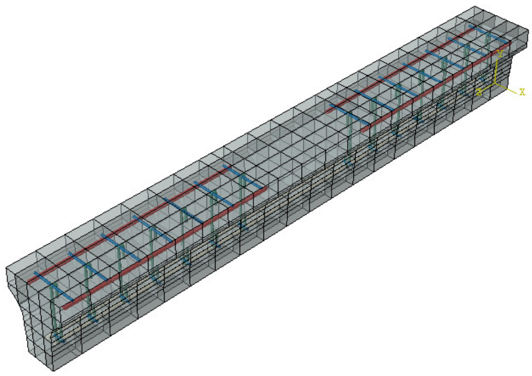

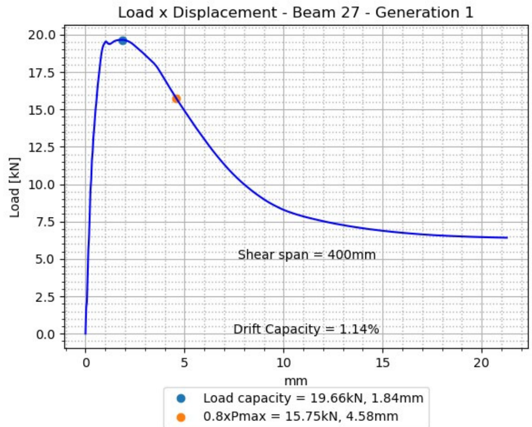

Load x Displacement - Beam 27 - Generation 1
Load [kN]
mm
Shear span = 400mm
Drift Capacity = 1.14%
Load capacity = 19.66kN, 1.84mm
0.8xPmax = 15.75kN, 4.58mm

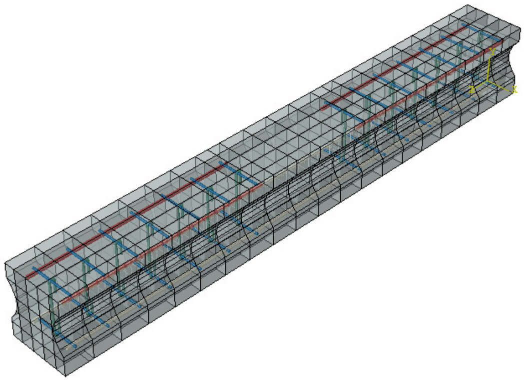

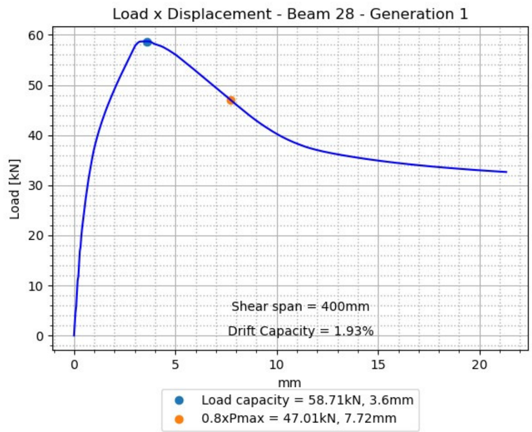
Load x Displacement - Beam 28 - Generation 1
Load [kN]
mm
Shear span = 400mm
Drift Capacity = 1.93%
Load capacity = 58.71kN, 3.6mm
0.8xPmax = 47.01kN, 7.72mm

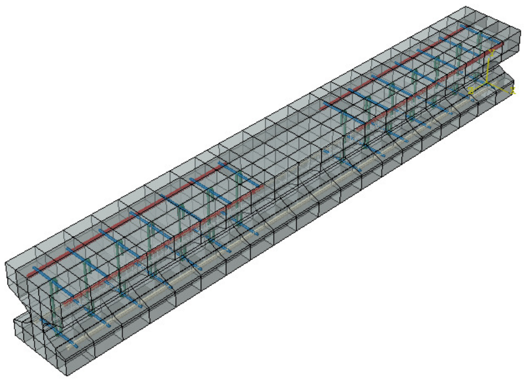

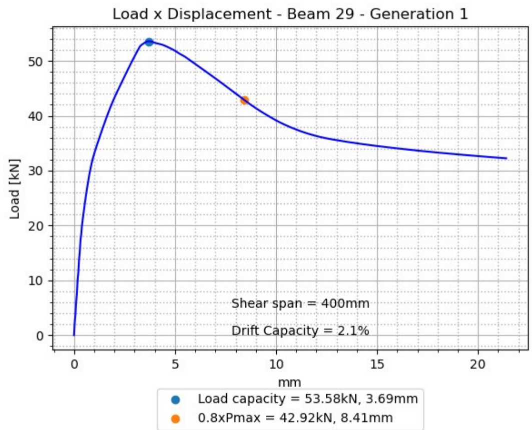
Load x Displacement - Beam 29 - Generation 1
Load [kN]
mm
Shear span = 400mm
Drift Capacity = 2.1%
Load capacity = 53.58kN, 3.69mm
0.8xPmax = 42.92kN, 8.41mm

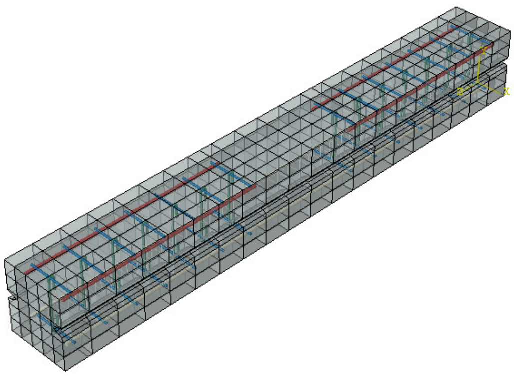

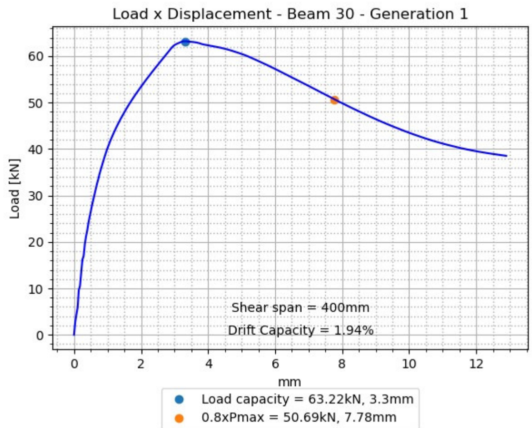
Load x Displacement - Beam 30 - Generation 1
Load [kN]
mm
Shear span = 400mm
Drift Capacity = 1.94%
Load capacity = 63.22kN, 3.3mm
0.8xPmax = 50.69kN, 7.78mm

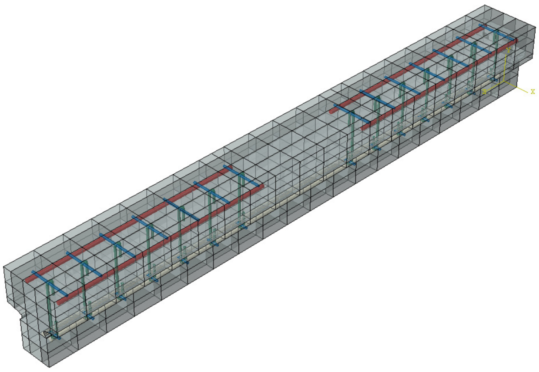

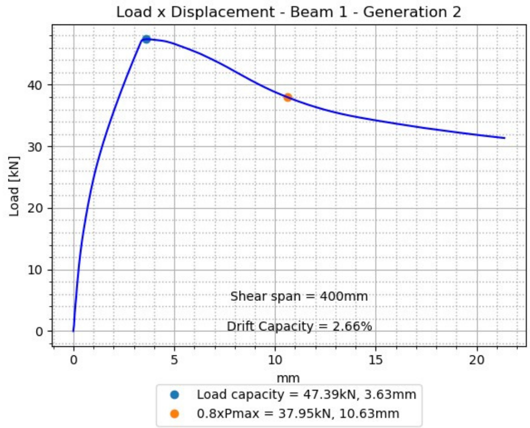
Load x Displacement - Beam 1 - Generation 2
Load [kN]
mm
Shear span = 400mm
Drift Capacity = 2.66%
Load capacity = 47.39kN, 3.63mm
0.8xPmax = 37.95kN, 10.63mm

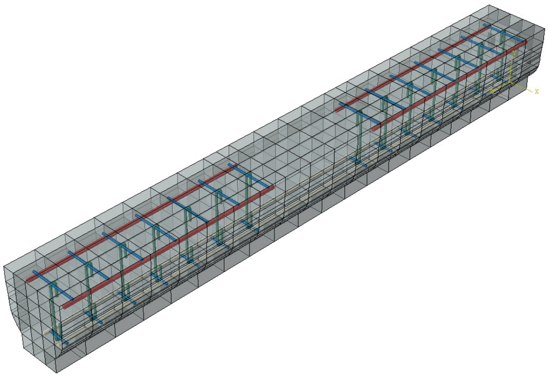

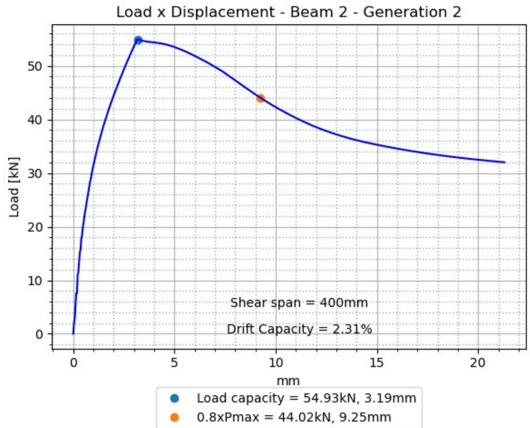
Load x Displacement - Beam 2 - Generation 2
Load [kN]
mm
Shear span = 400mm
Drift Capacity = 2.31%
Load capacity = 54.93kN, 3.19mm
0.8xPmax = 44.02kN, 9.25mm

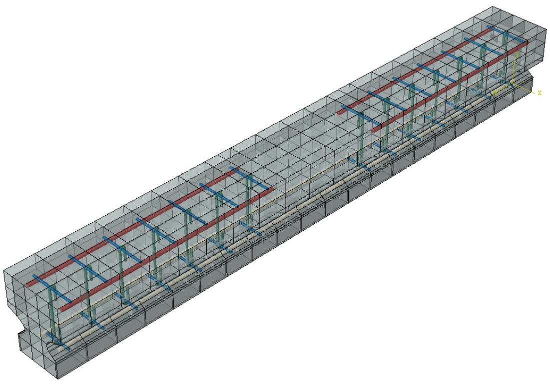

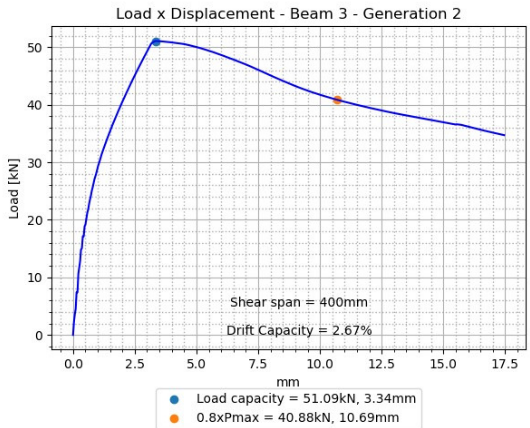
Load x Displacement - Beam 3 - Generation 2
Load [kN]
mm
Shear span = 400mm
Drift Capacity = 2.67%
Load capacity = 51.09kN, 3.34mm
0.8xPmax = 40.88kN, 10.69mm

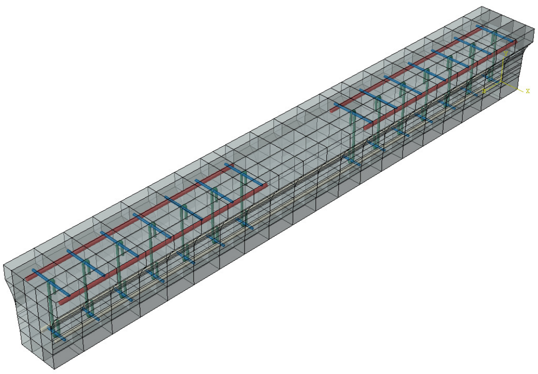

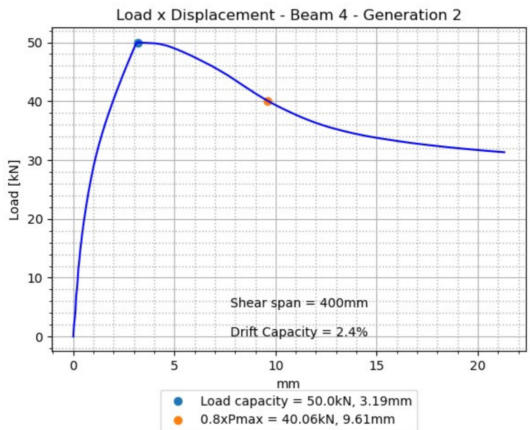
Load x Displacement - Beam 4 - Generation 2
Load [kN]
mm
Shear span = 400mm
Drift Capacity = 2.4%
Load capacity = 50.0kN, 3.19mm
0.8xPmax = 40.06kN, 9.61mm

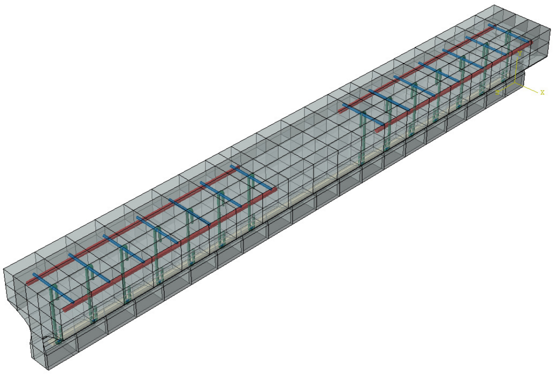

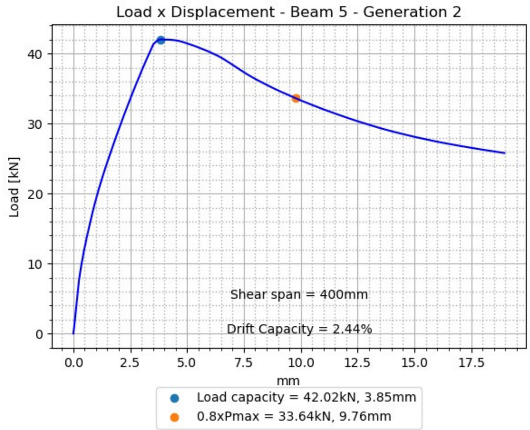
Load x Displacement - Beam 5 - Generation 2
Load [kN]
mm
Shear span = 400mm
Drift Capacity = 2.44%
Load capacity = 42.02kN, 3.85mm
0.8xPmax = 33.64kN, 9.76mm

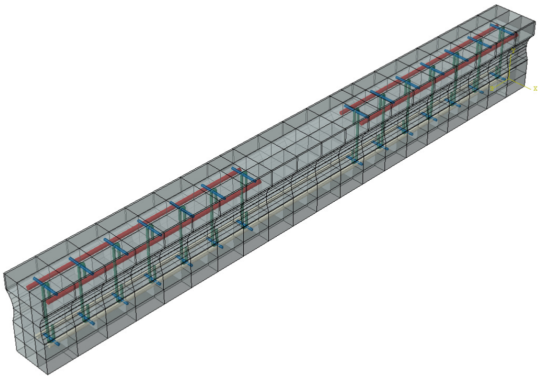

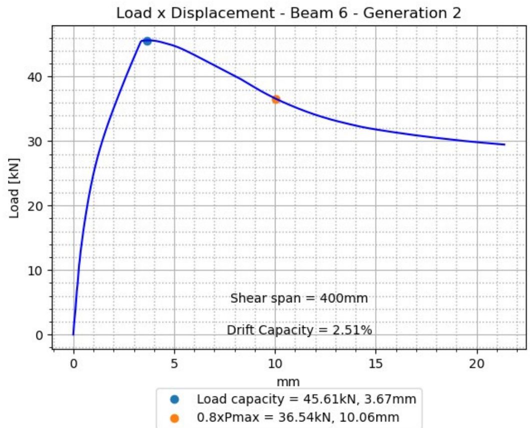
Load x Displacement - Beam 6 - Generation 2
Load [kN]
mm
Shear span = 400mm
Drift Capacity = 2.51%
Load capacity = 45.61kN, 3.67mm
0.8xPmax = 36.54kN, 10.06mm

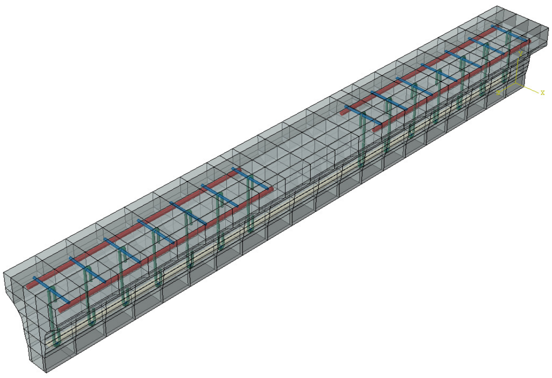

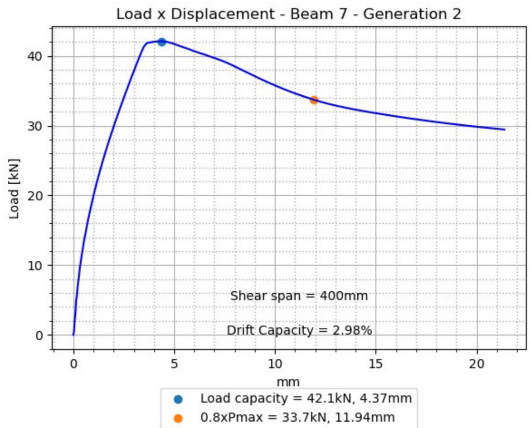
Load x Displacement - Beam 7 - Generation 2
Load [kN]
mm
Shear span = 400mm
Drift Capacity = 2.98%
Load capacity = 42.1kN, 4.37mm
0.8xPmax = 33.7kN, 11.94mm

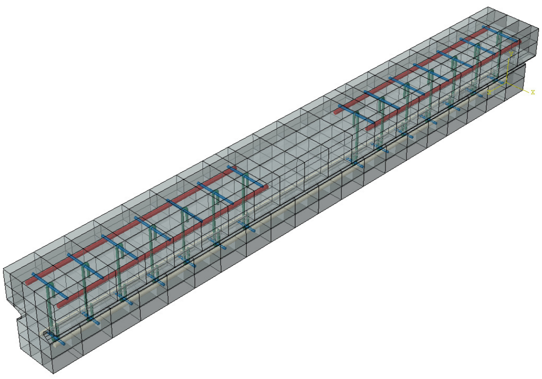

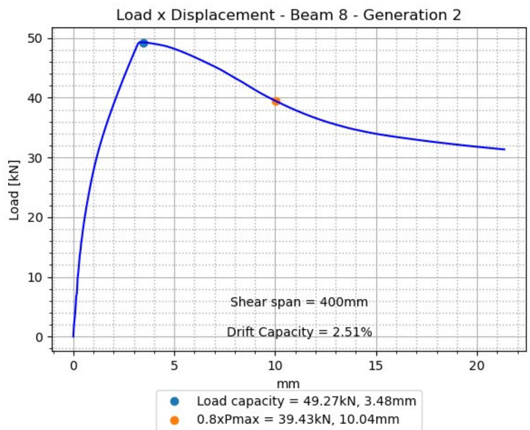
Load x Displacement - Beam 8 - Generation 2
Load [kN]
mm
Shear span = 400mm
Drift Capacity = 2.51%
Load capacity = 49.27kN, 3.48mm
0.8xPmax = 39.43kN, 10.04mm

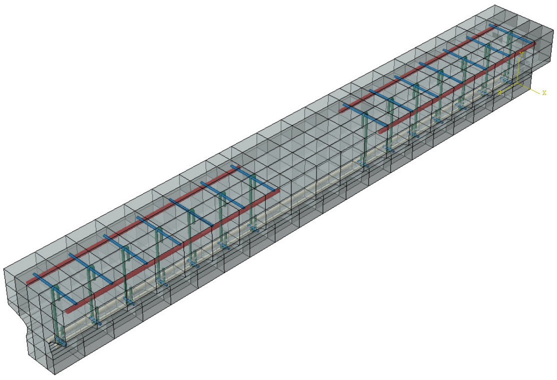

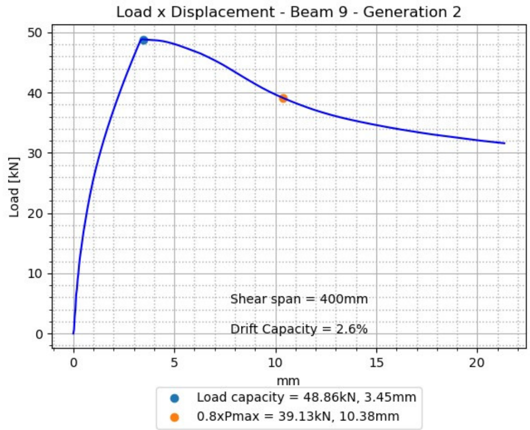
Load x Displacement - Beam 9 - Generation 2
Load [kN]
mm
Shear span = 400mm
Drift Capacity = 2.6%
Load capacity = 48.86kN, 3.45mm
0.8xPmax = 39.13kN, 10.38mm

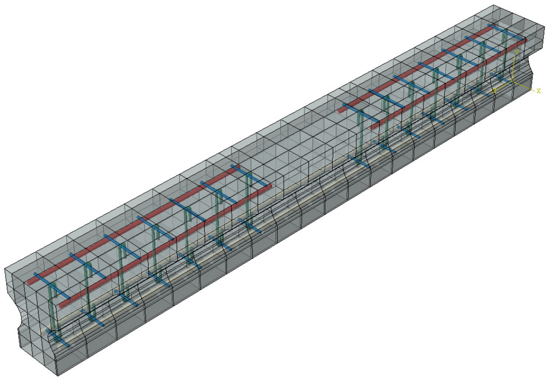

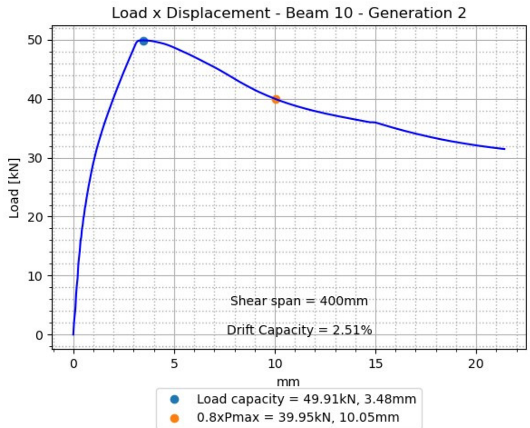
Load x Displacement - Beam 10 - Generation 2
Load [kN]
mm
Shear span = 400mm
Drift Capacity = 2.51%
Load capacity = 49.91kN, 3.48mm
0.8xPmax = 39.95kN, 10.05mm

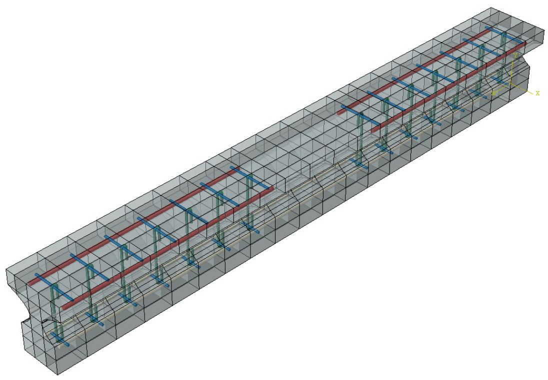

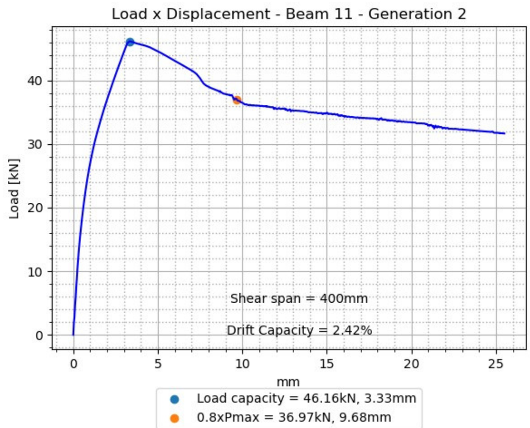
Load x Displacement - Beam 11 - Generation 2
Load [kN]
mm
Shear span = 400mm
Drift Capacity = 2.42%
Load capacity = 46.16kN, 3.33mm
0.8xPmax = 36.97kN, 9.68mm

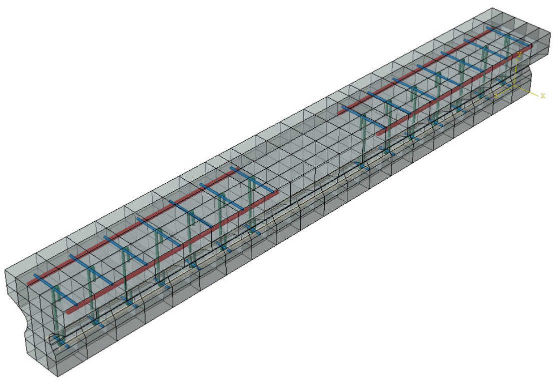

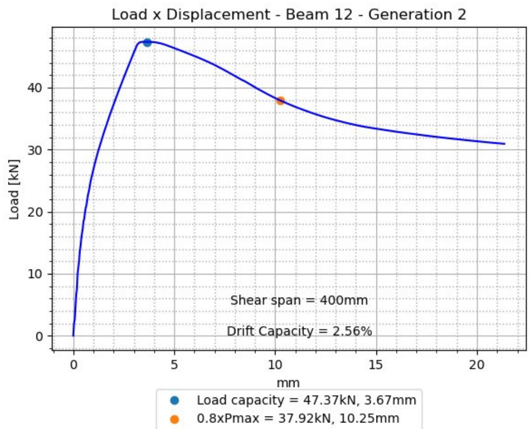
Load x Displacement - Beam 12 - Generation 2
Load [kN]
mm
Shear span = 400mm
Drift Capacity = 2.56%
Load capacity = 47.37kN, 3.67mm
0.8xPmax = 37.92kN, 10.25mm

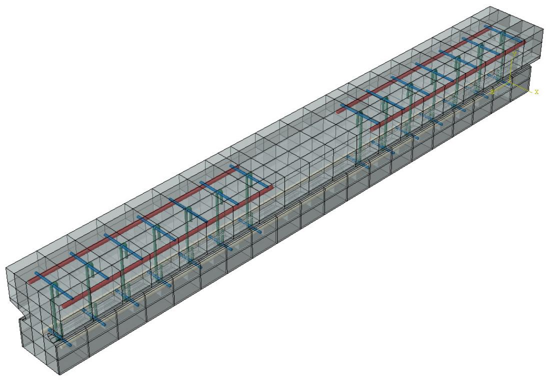

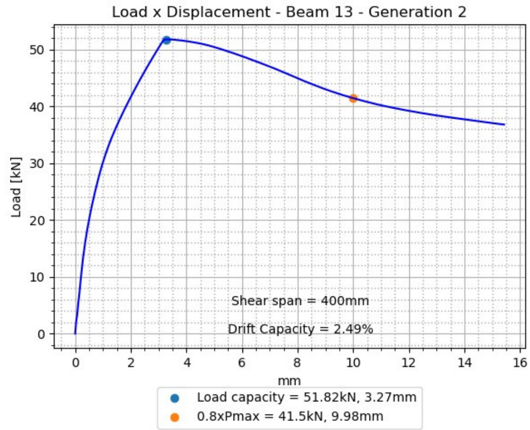

Load x Displacement - Beam 13 - Generation 2
Load [kN]
mm
Shear span = 400mm
Drift Capacity = 2.49%
Load capacity = 51.82kN, 3.27mm
0.8xPmax = 41.5kN, 9.98mm

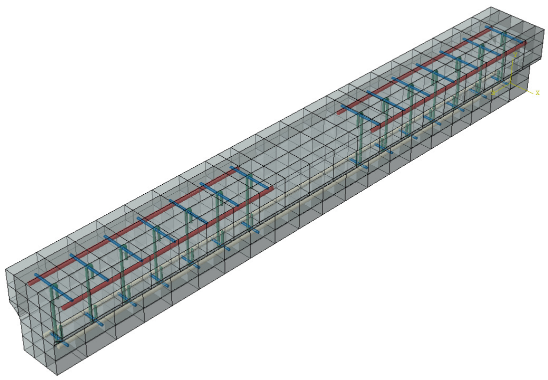

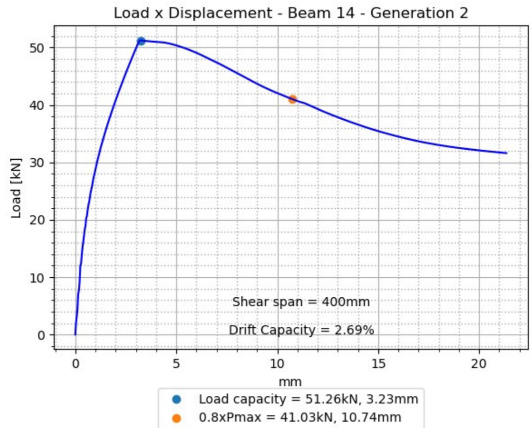

Load x Displacement - Beam 14 - Generation 2
Load [kN]
mm
Shear span = 400mm
Drift Capacity = 2.69%
Load capacity = 51.26kN, 3.23mm
0.8xPmax = 41.03kN, 10.74mm

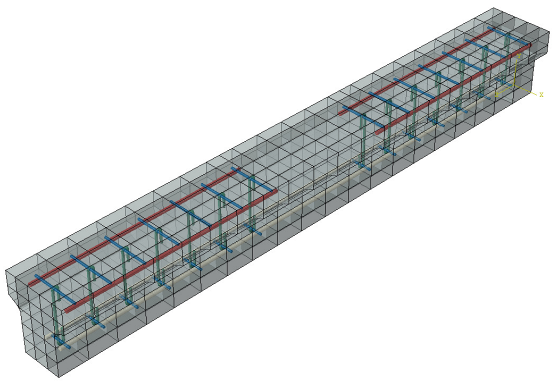

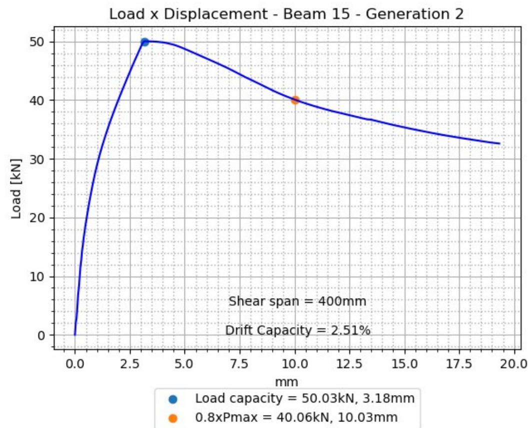

Load x Displacement - Beam 15 - Generation 2
Load [kN]
mm
Shear span = 400mm
Drift Capacity = 2.51%
Load capacity = 50.03kN, 3.18mm
0.8xPmax = 40.06kN, 10.03mm

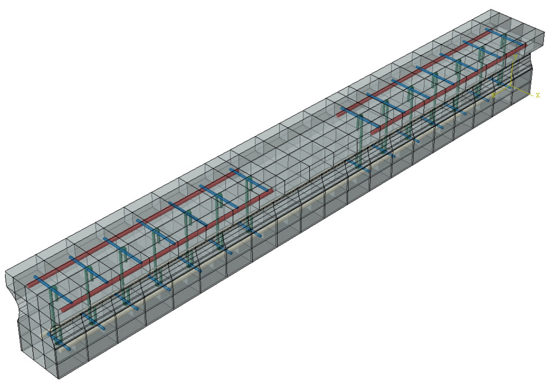

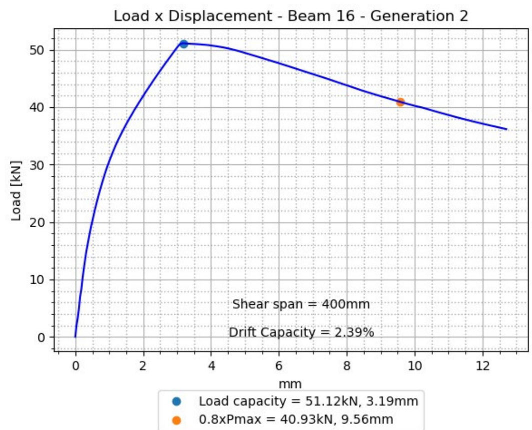

Load x Displacement - Beam 16 - Generation 2
Load [kN]
mm
Shear span = 400mm
Drift Capacity = 2.39%
Load capacity = 51.12kN, 3.19mm
0.8xPmax = 40.93kN, 9.56mm

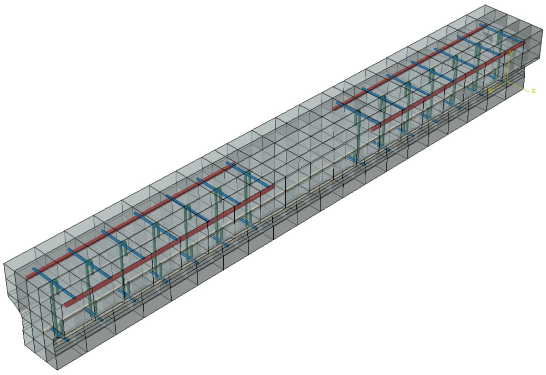

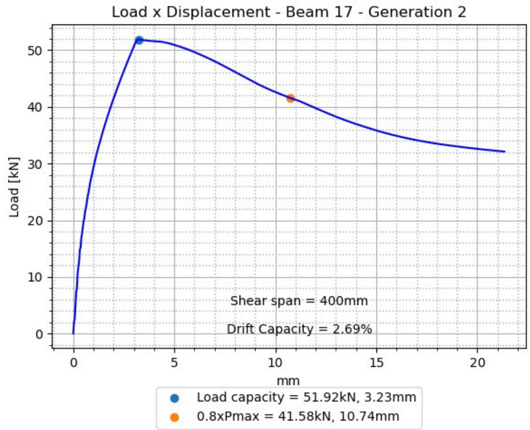
Load x Displacement - Beam 17 - Generation 2
Load [kN]
mm
Shear span = 400mm
Drift Capacity = 2.69%
Load capacity = 51.92kN, 3.23mm
0.8xPmax = 41.58kN, 10.74mm

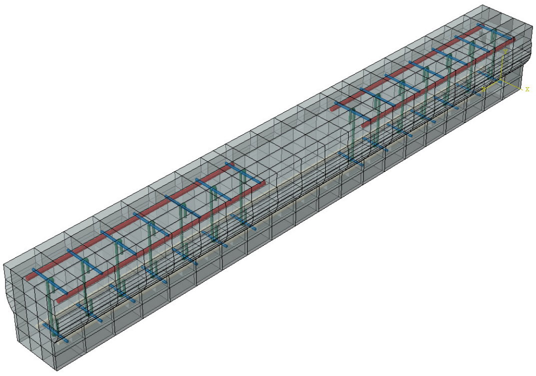

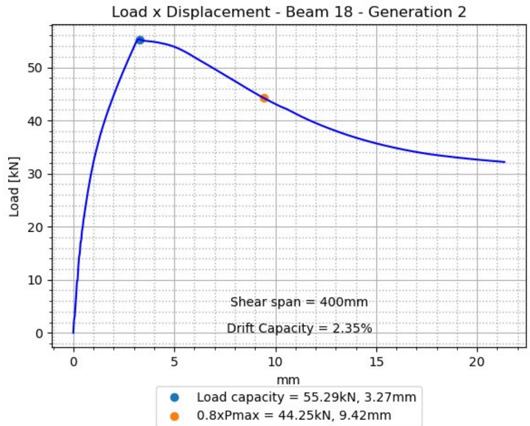
Load x Displacement - Beam 18 - Generation 2
Load [kN]
mm
Shear span = 400mm
Drift Capacity = 2.35%
Load capacity = 55.29kN, 3.27mm
0.8xPmax = 44.25kN, 9.42mm

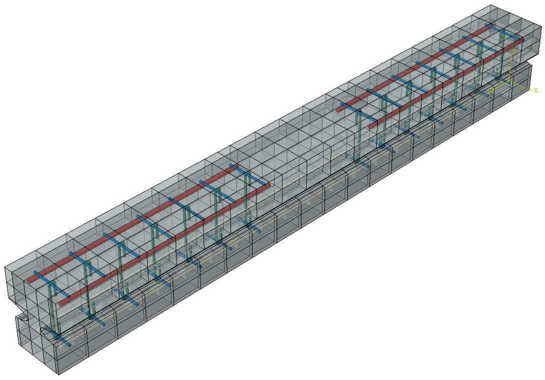

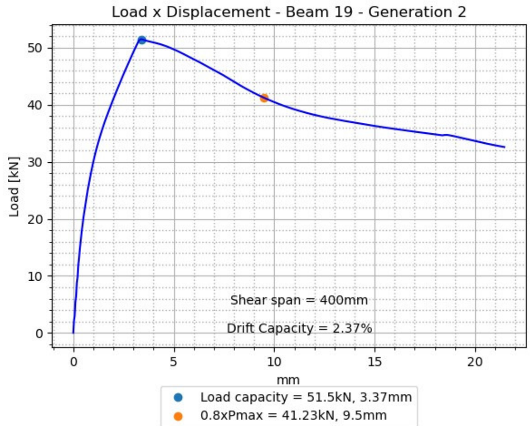
Load x Displacement - Beam 19 - Generation 2
Load [kN]
mm
Shear span = 400mm
Drift Capacity = 2.37%
Load capacity = 51.5kN, 3.37mm
0.8xPmax = 41.23kN, 9.5mm

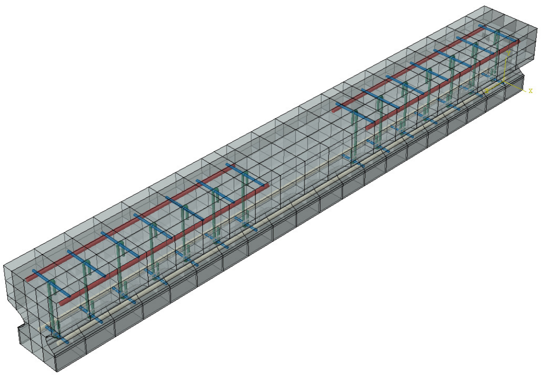

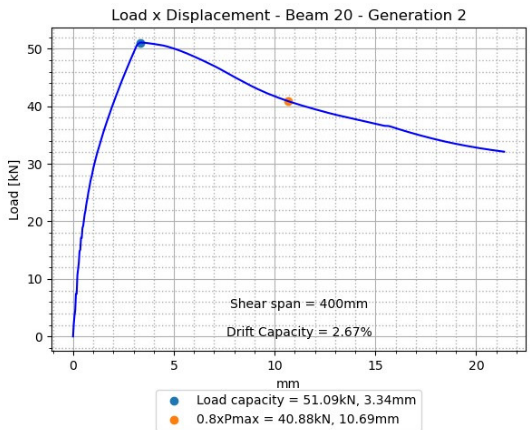
Load x Displacement - Beam 20 - Generation 2
Load [kN]
mm
Shear span = 400mm
Drift Capacity = 2.67%
Load capacity = 51.09kN, 3.34mm
0.8xPmax = 40.88kN, 10.69mm

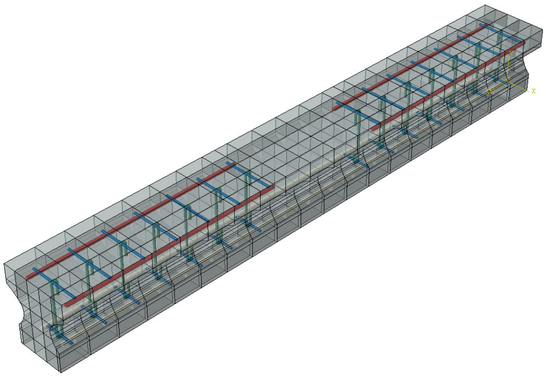

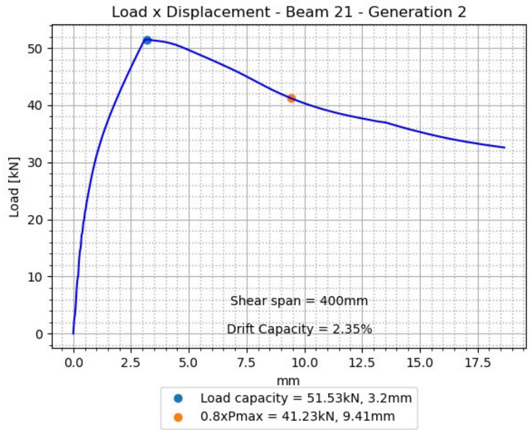
Load x Displacement - Beam 21 - Generation 2
Load [kN]
mm
Shear span = 400mm
Drift Capacity = 2.35%
Load capacity = 51.53kN, 3.2mm
0.8xPmax = 41.23kN, 9.41mm

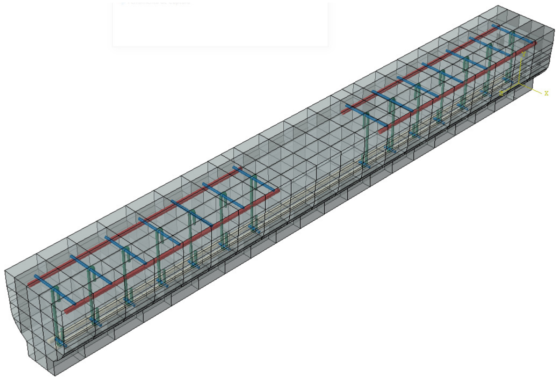

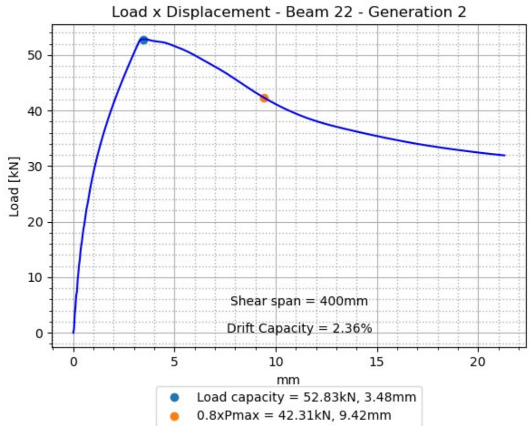
Load x Displacement - Beam 22 - Generation 2
Load [kN]
mm
Shear span = 400mm
Drift Capacity = 2.36%
Load capacity = 52.83kN, 3.48mm
0.8xPmax = 42.31kN, 9.42mm

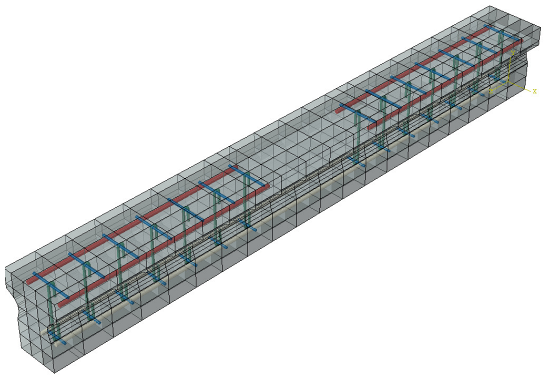

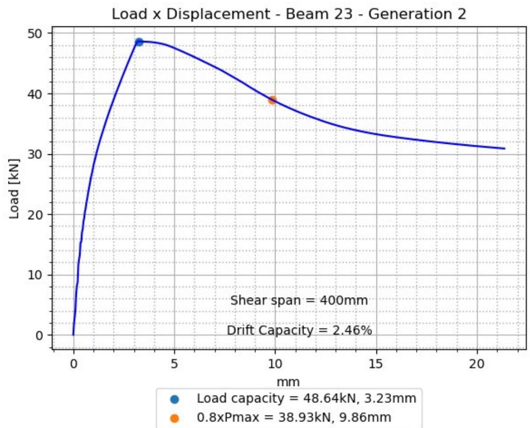
Load x Displacement - Beam 23 - Generation 2
Load [kN]
mm
Shear span = 400mm
Drift Capacity = 2.46%
Load capacity = 48.64kN, 3.23mm
0.8xPmax = 38.93kN, 9.86mm

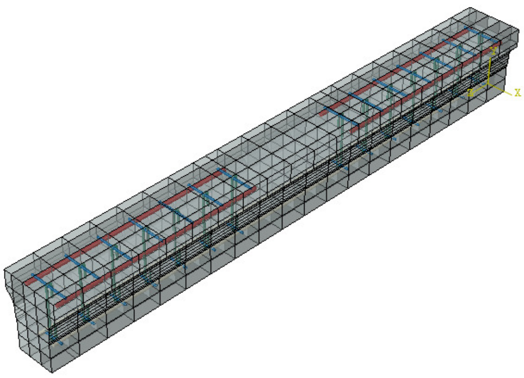

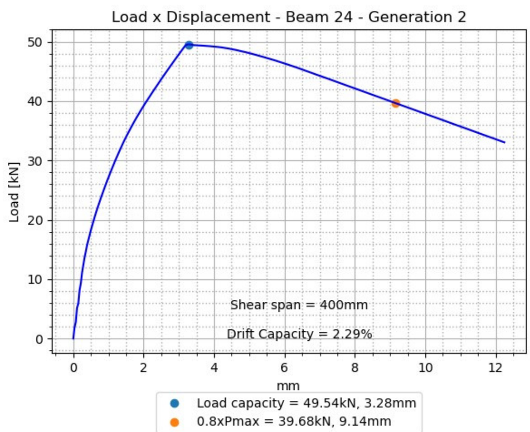
Load x Displacement - Beam 24 - Generation 2
Load [kN]
mm
Shear span = 400mm
Drift Capacity = 2.29%
Load capacity = 49.54kN, 3.28mm
0.8xPmax = 39.68kN, 9.14mm

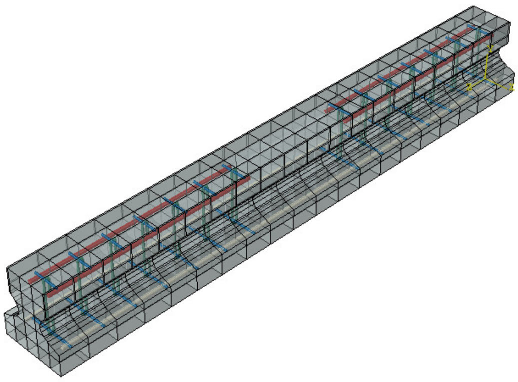

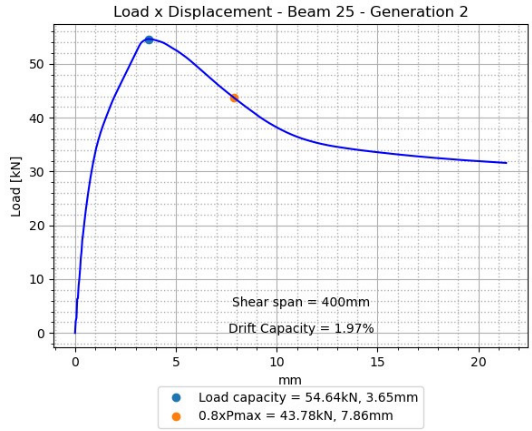

Load x Displacement - Beam 25 - Generation 2
Load [kN]
mm
Shear span = 400mm
Drift Capacity = 1.97%
Load capacity = 54.64kN, 3.65mm
0.8xPmax = 43.78kN, 7.86mm

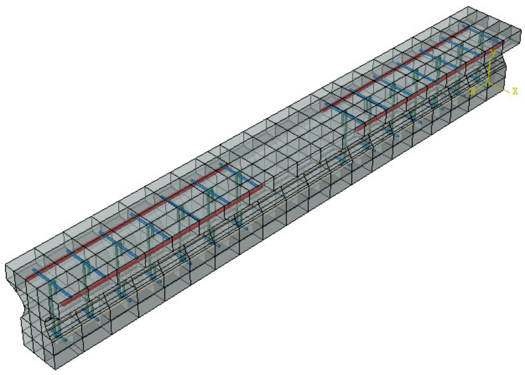

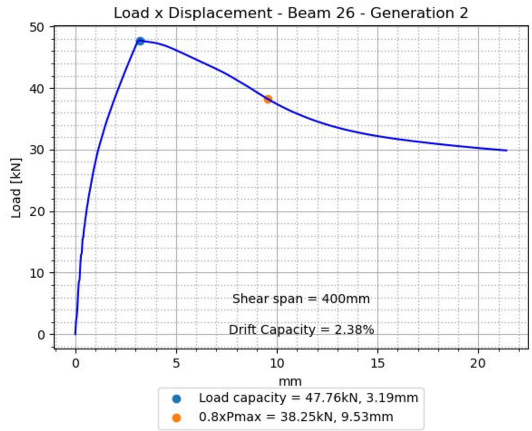

Load x Displacement - Beam 26 - Generation 2
Load [kN]
mm
Shear span = 400mm
Drift Capacity = 2.38%
Load capacity = 47.76kN, 3.19mm
0.8xPmax = 38.25kN, 9.53mm

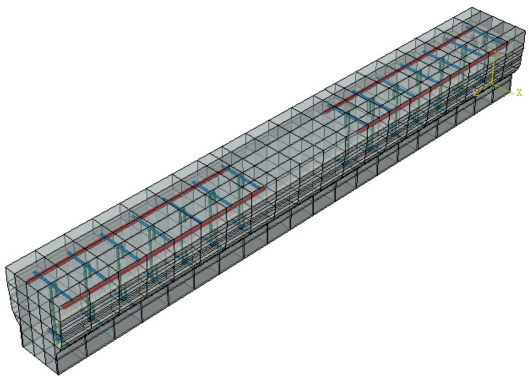

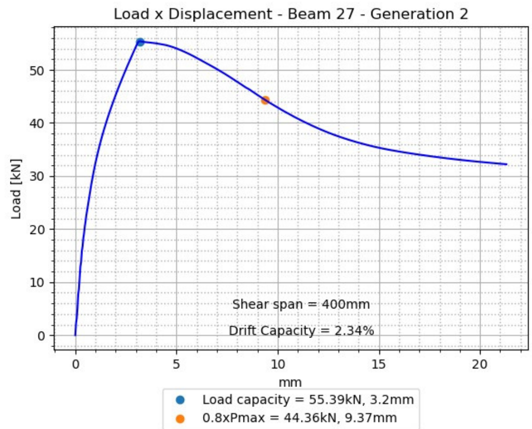

Load x Displacement - Beam 27 - Generation 2
Load [kN]
mm
Shear span = 400mm
Drift Capacity = 2.34%
Load capacity = 55.39kN, 3.2mm
0.8xPmax = 44.36kN, 9.37mm

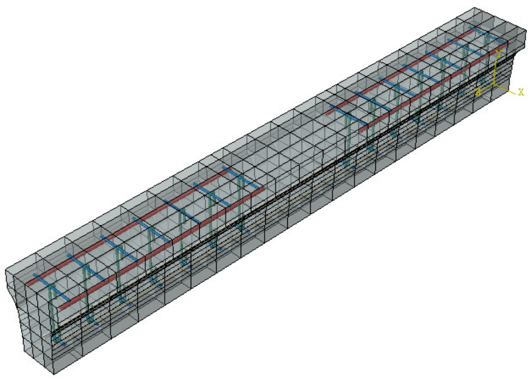

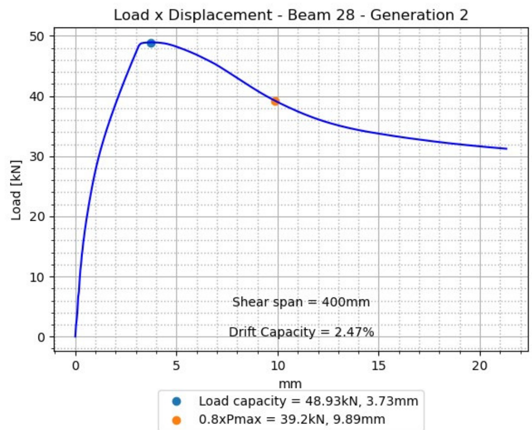

Load x Displacement - Beam 28 - Generation 2
Load [kN]
mm
Shear span = 400mm
Drift Capacity = 2.47%
Load capacity = 48.93kN, 3.73mm
0.8xPmax = 39.2kN, 9.89mm

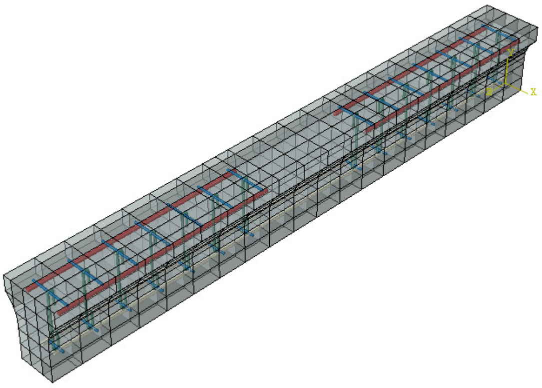

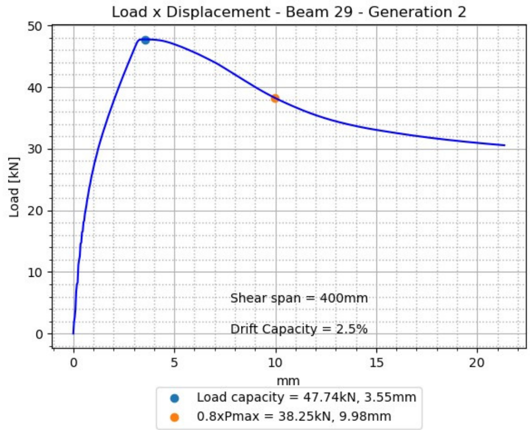
Load x Displacement - Beam 29 - Generation 2
Load [kN]
mm
Shear span = 400mm
Drift Capacity = 2.5%
Load capacity = 47.74kN, 3.55mm
0.8xPmax = 38.25kN, 9.98mm

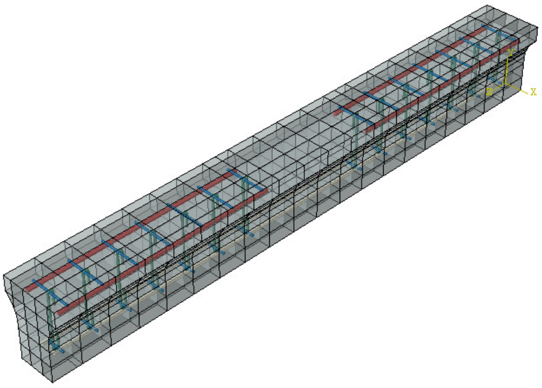

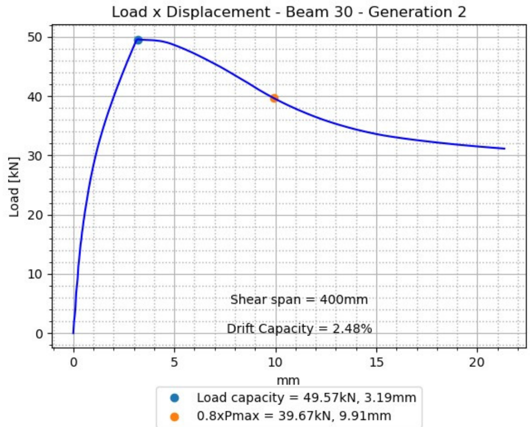
Load x Displacement - Beam 30 - Generation 2
Load [kN]
mm
Shear span = 400mm
Drift Capacity = 2.48%
Load capacity = 49.57kN, 3.19mm
0.8xPmax = 39.67kN, 9.91mm

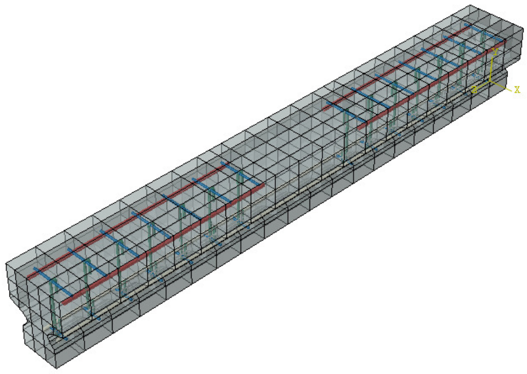

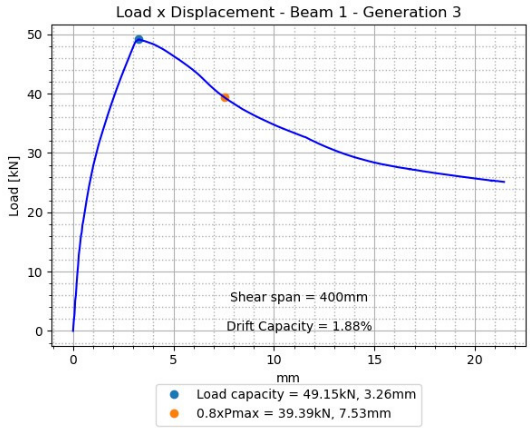
Load x Displacement - Beam 1 - Generation 3
Load [kN]
mm
Shear span = 400mm
Drift Capacity = 1.88%
Load capacity = 49.15kN, 3.26mm
0.8xPmax = 39.39kN, 7.53mm

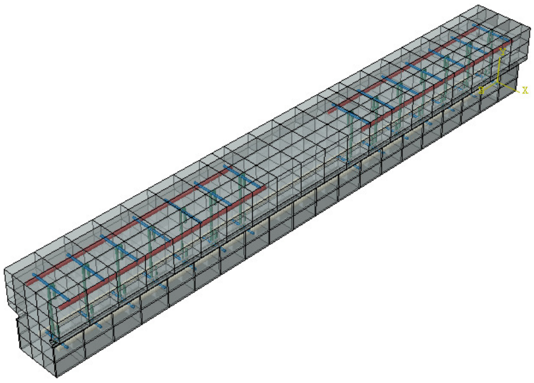

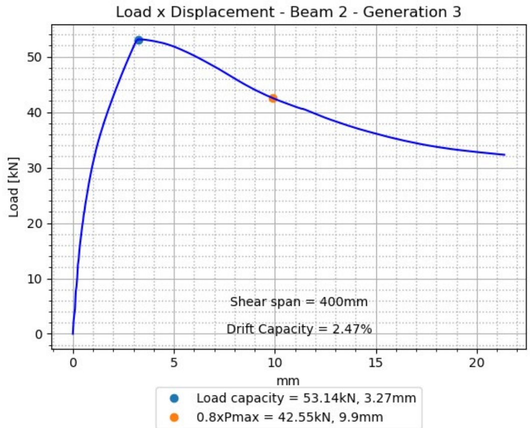
Load x Displacement - Beam 2 - Generation 3
Load [kN]
mm
Shear span = 400mm
Drift Capacity = 2.47%
Load capacity = 53.14kN, 3.27mm
0.8xPmax = 42.55kN, 9.9mm

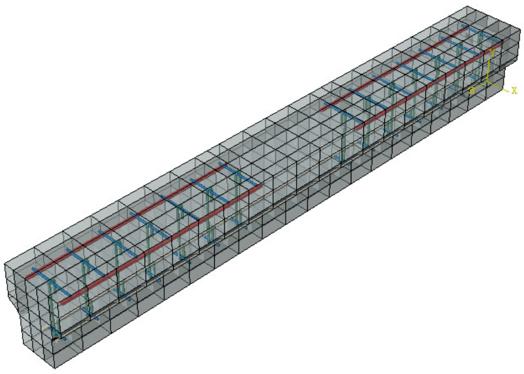

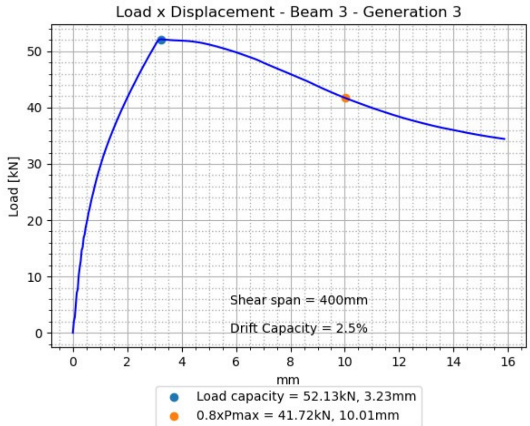
Load x Displacement - Beam 3 - Generation 3
Load [kN]
mm
Shear span = 400mm
Drift Capacity = 2.5%
Load capacity = 52.13kN, 3.23mm
0.8xPmax = 41.72kN, 10.01mm

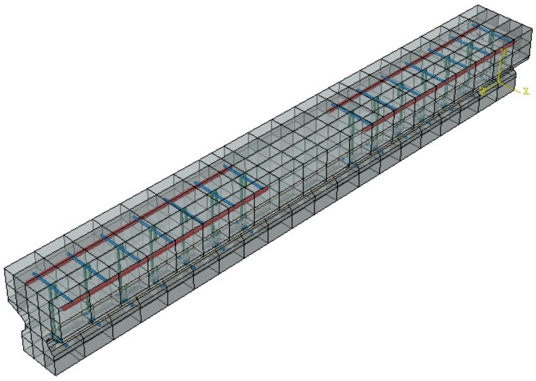

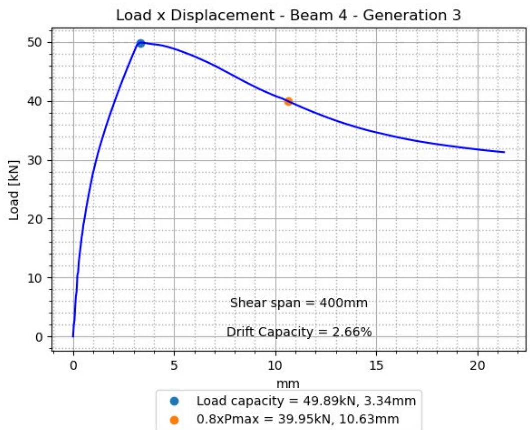
Load x Displacement - Beam 4 - Generation 3
Load [kN]
mm
Shear span = 400mm
Drift Capacity = 2.66%
Load capacity = 49.89kN, 3.34mm
0.8xPmax = 39.95kN, 10.63mm

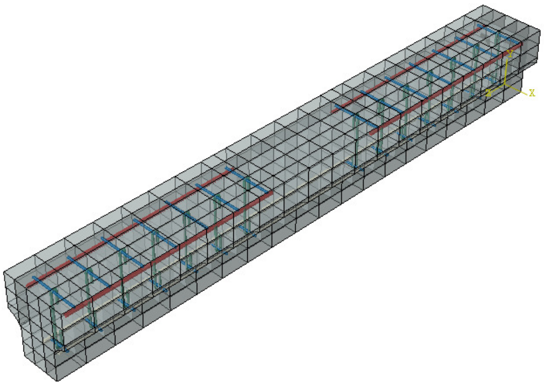

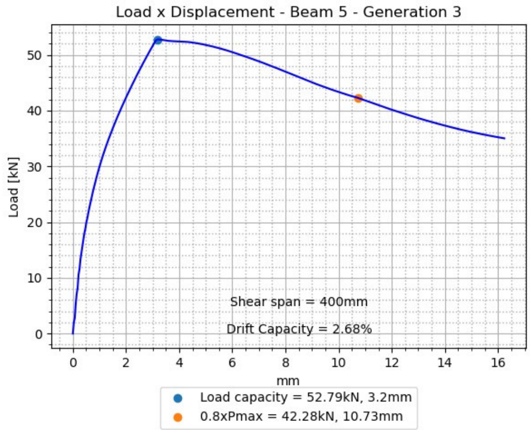

Load x Displacement - Beam 5 - Generation 3
Load [kN]
mm
Shear span = 400mm
Drift Capacity = 2.68%
Load capacity = 52.79kN, 3.2mm
0.8xPmax = 42.28kN, 10.73mm

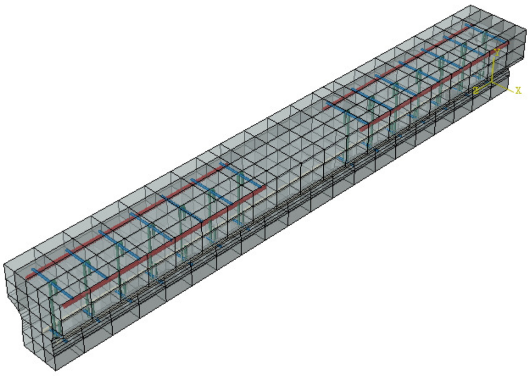

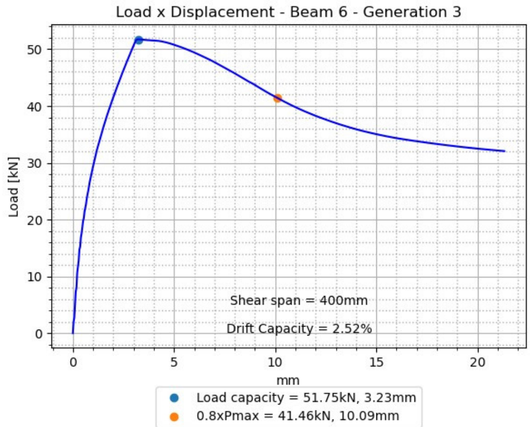

Load x Displacement - Beam 6 - Generation 3
Load [kN]
mm
Shear span = 400mm
Drift Capacity = 2.52%
Load capacity = 51.75kN, 3.23mm
0.8xPmax = 41.46kN, 10.09mm

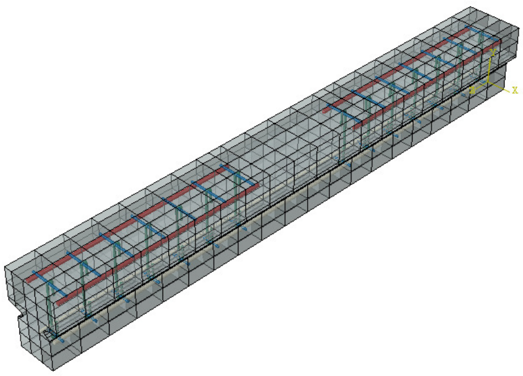

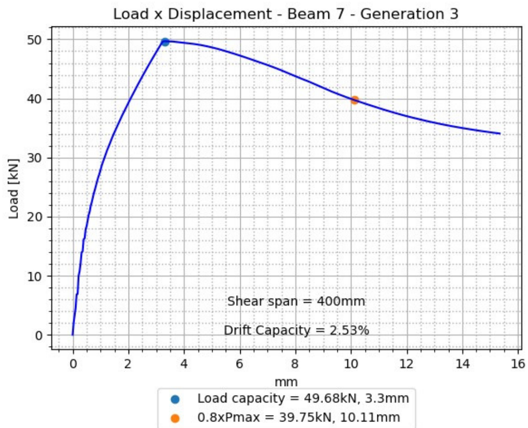

Load x Displacement - Beam 7 - Generation 3
Load [kN]
mm
Shear span = 400mm
Drift Capacity = 2.53%
Load capacity = 49.68kN, 3.3mm
0.8xPmax = 39.75kN, 10.11mm

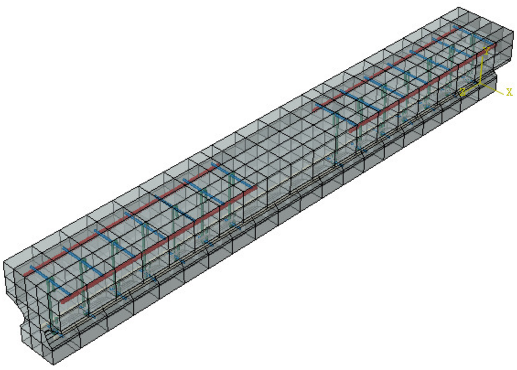

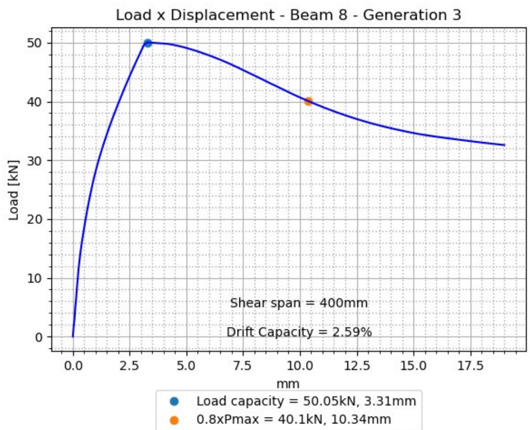

Load x Displacement - Beam 8 - Generation 3
Load [kN]
mm
Shear span = 400mm
Drift Capacity = 2.59%
Load capacity = 50.05kN, 3.31mm
0.8xPmax = 40.1kN, 10.34mm

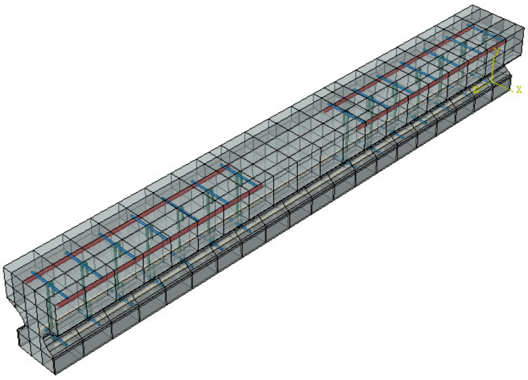

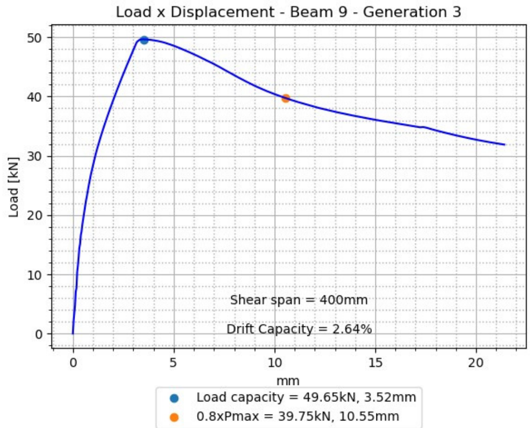
Load x Displacement - Beam 9 - Generation 3
Load [kN]
mm
Shear span = 400mm
Drift Capacity = 2.64%
Load capacity = 49.65kN, 3.52mm
0.8xPmax = 39.75kN, 10.55mm

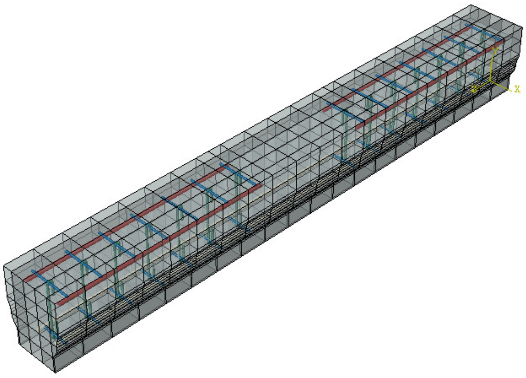

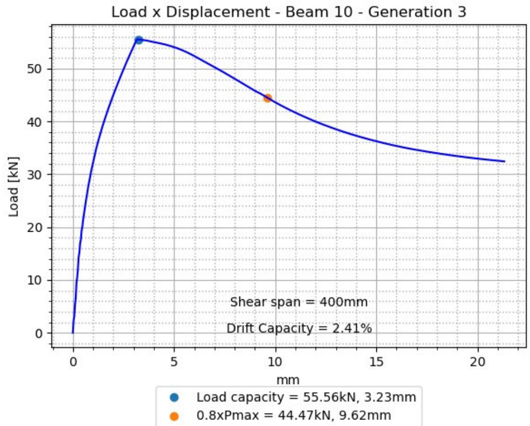
Load x Displacement - Beam 10 - Generation 3
Load [kN]
mm
Shear span = 400mm
Drift Capacity = 2.41%
Load capacity = 55.56kN, 3.23mm
0.8xPmax = 44.47kN, 9.62mm

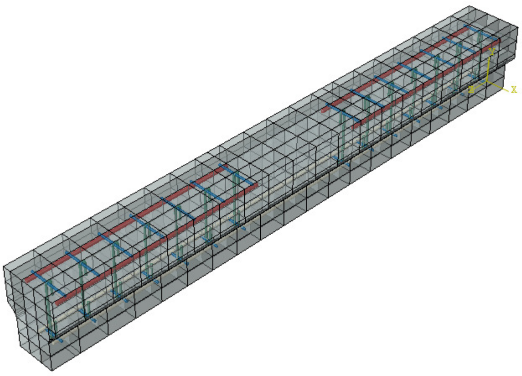

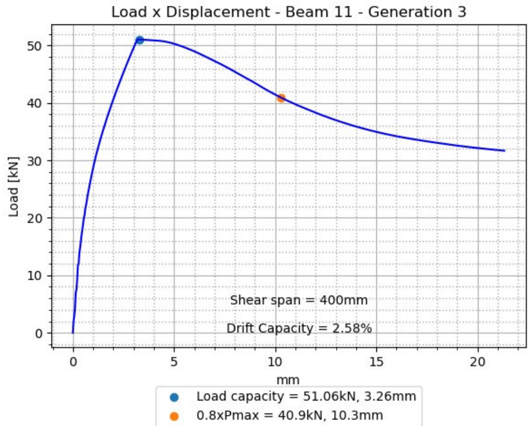
Load x Displacement - Beam 11 - Generation 3
Load [kN]
mm
Shear span = 400mm
Drift Capacity = 2.58%
Load capacity = 51.06kN, 3.26mm
0.8xPmax = 40.9kN, 10.3mm

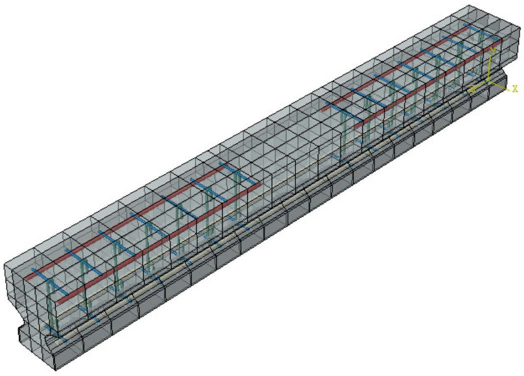

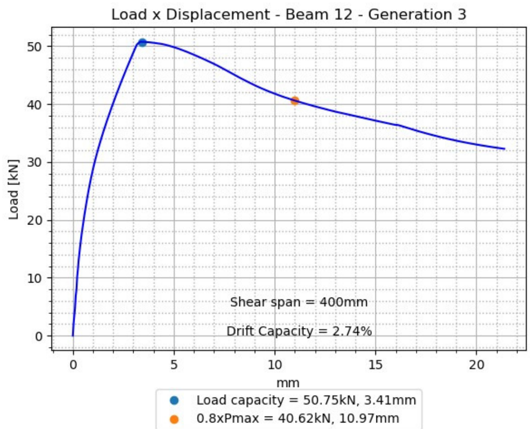
Load x Displacement - Beam 12 - Generation 3
Load [kN]
mm
Shear span = 400mm
Drift Capacity = 2.74%
Load capacity = 50.75kN, 3.41mm
0.8xPmax = 40.62kN, 10.97mm

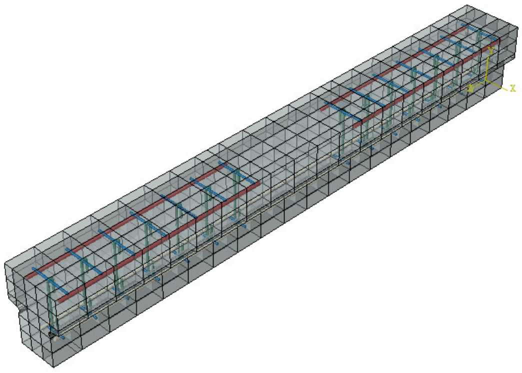

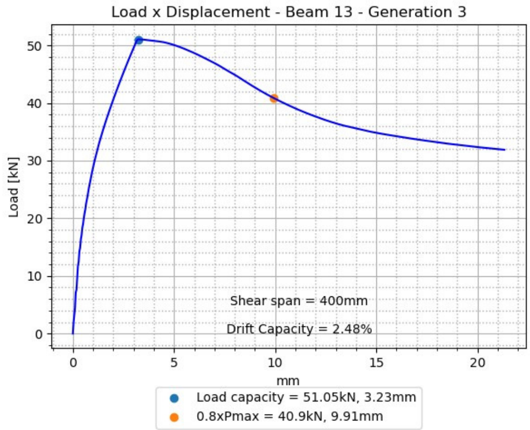
Load x Displacement - Beam 13 - Generation 3
Load [kN]
mm
Shear span = 400mm
Drift Capacity = 2.48%
Load capacity = 51.05kN, 3.23mm
0.8xPmax = 40.9kN, 9.91mm

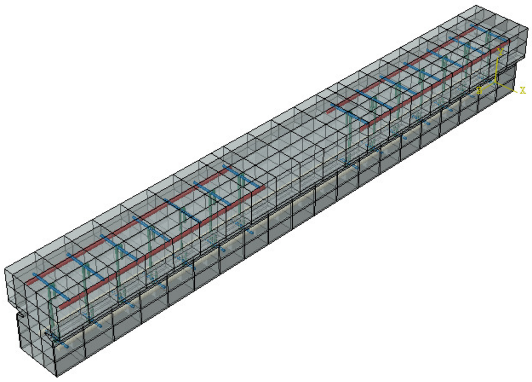

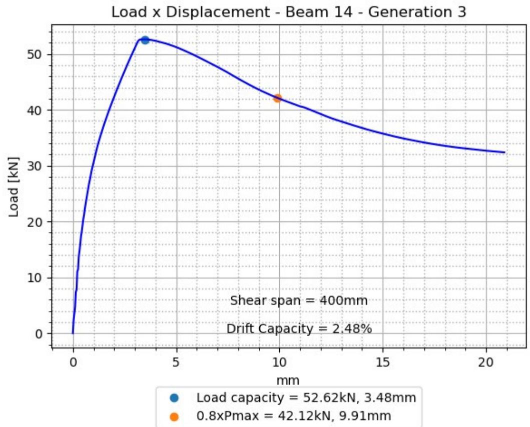
Load x Displacement - Beam 14 - Generation 3
Load [kN]
mm
Shear span = 400mm
Drift Capacity = 2.48%
Load capacity = 52.62kN, 3.48mm
0.8xPmax = 42.12kN, 9.91mm

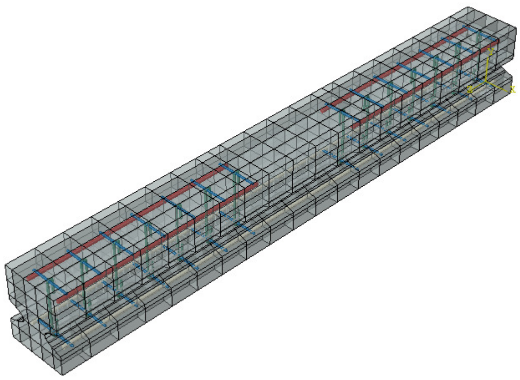

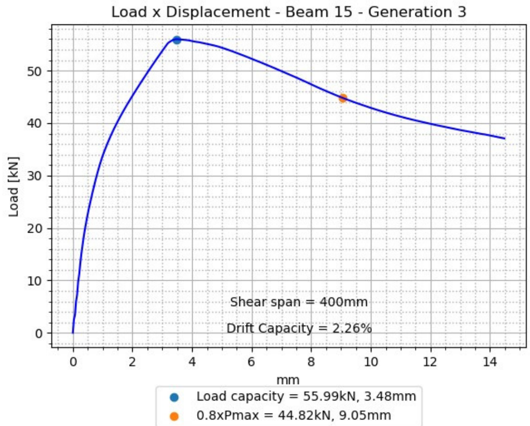
Load x Displacement - Beam 15 - Generation 3
Load [kN]
mm
Shear span = 400mm
Drift Capacity = 2.26%
Load capacity = 55.99kN, 3.48mm
0.8xPmax = 44.82kN, 9.05mm

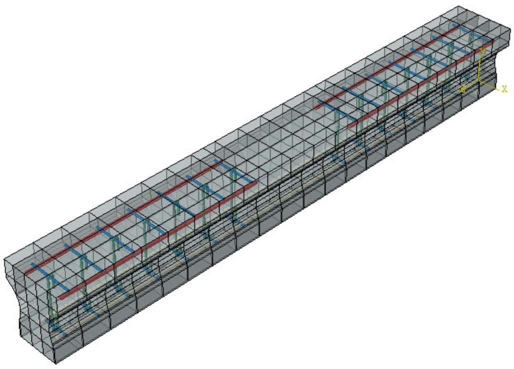

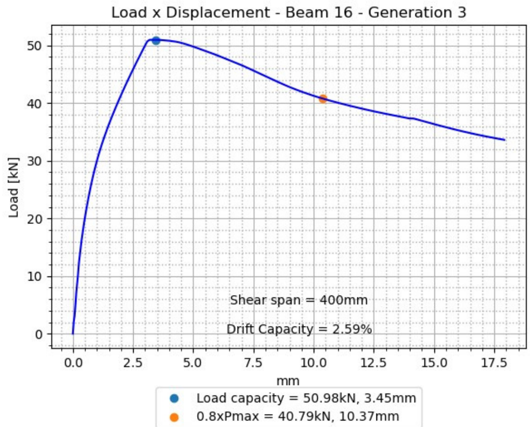
Load x Displacement - Beam 16 - Generation 3
Load [kN]
mm
Shear span = 400mm
Drift Capacity = 2.59%
Load capacity = 50.98kN, 3.45mm
0.8xPmax = 40.79kN, 10.37mm

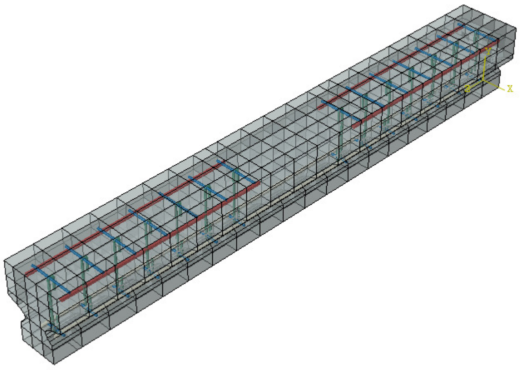

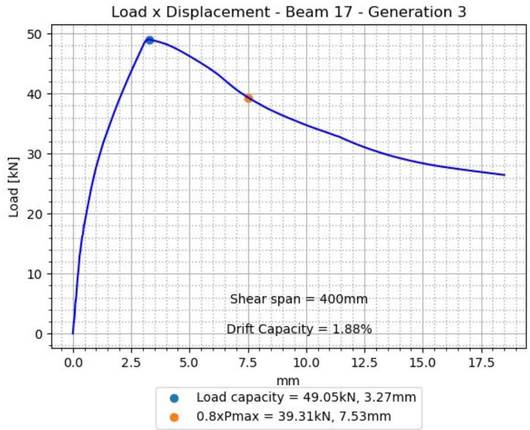
Load x Displacement - Beam 17 - Generation 3
Load [kN]
mm
Shear span = 400mm
Drift Capacity = 1.88%
Load capacity = 49.05kN, 3.27mm
0.8xPmax = 39.31kN, 7.53mm

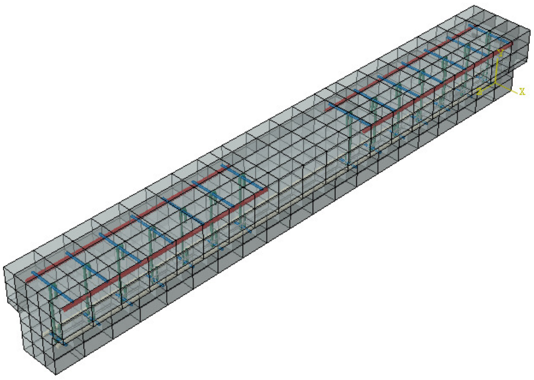

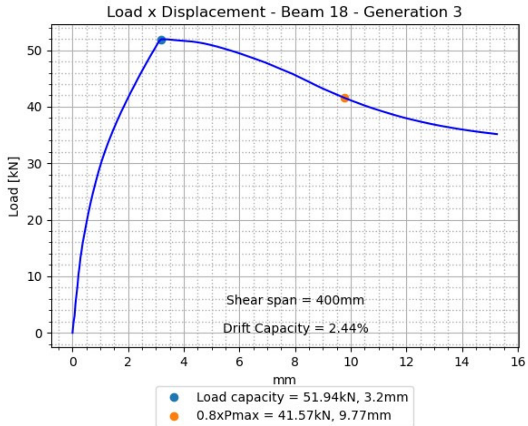
Load x Displacement - Beam 18 - Generation 3
Load [kN]
mm
Shear span = 400mm
Drift Capacity = 2.44%
Load capacity = 51.94kN, 3.2mm
0.8xPmax = 41.57kN, 9.77mm

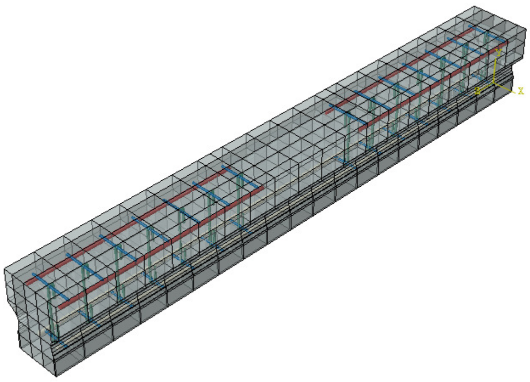

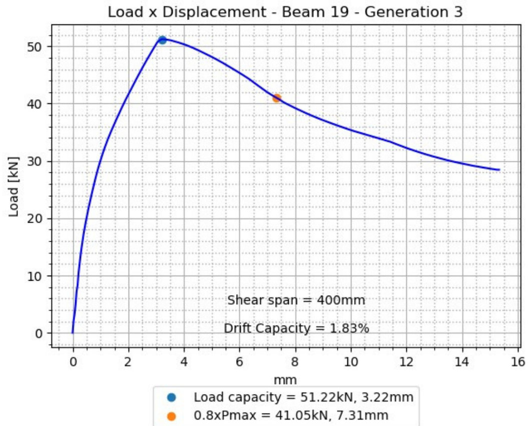
Load x Displacement - Beam 19 - Generation 3
Load [kN]
mm
Shear span = 400mm
Drift Capacity = 1.83%
Load capacity = 51.22kN, 3.22mm
0.8xPmax = 41.05kN, 7.31mm

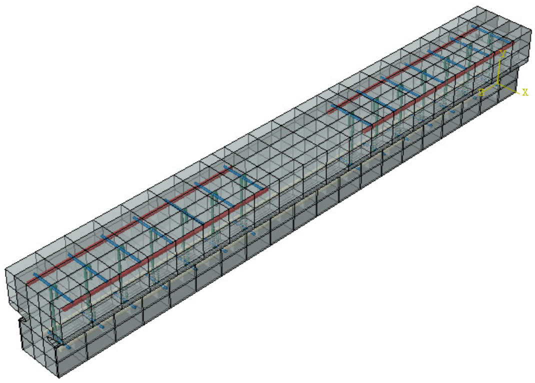

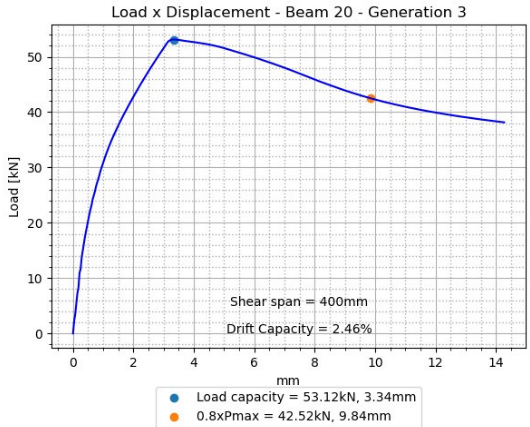
Load x Displacement - Beam 20 - Generation 3
Load [kN]
mm
Shear span = 400mm
Drift Capacity = 2.46%
Load capacity = 53.12kN, 3.34mm
0.8xPmax = 42.52kN, 9.84mm